Probing Topological States of Matter using Scanning Tunneling Microscopy and Spectroscopy

Dissertation

zur Erlangung des Doktorgrades der Naturwissenschaften
(Dr. rer. nat.)

der

Naturwissenschaftlichen Fakultät II
Chemie, Physik und Mathematik

der Martin-Luther-Universität
Halle-Wittenberg

vorgelegt von

Herrn **Souvik Das**

Gutachter:
Prof. Dr. Stuart S.P. Parkin
Prof. Dr. Wolf Widdra
Prof. Dr. Wulf Wulfhekel

Tag der öffentlichen Verteidigung:
03.12.2025

Abstract

The principle of bulk-boundary correspondence states that the topological properties of a material's bulk determine the existence and nature of the edge or surface states. In this thesis, I investigate the nature of these edge states in two distinct topological materials: a topological crystalline insulator (TCI) and a topological superconductor. Since these edge states are localized at the boundary, detecting them requires surface-sensitive techniques with high spatial resolution. To this, low-temperature high-resolution scanning tunneling microscopy and spectroscopy (STM/STS) techniques are ideal, as they offer the surface sensitivity and spatial resolution necessary to visualize these localized edge states.

In the first part of this thesis, I investigate correlated electronic states arising from one-dimensional flat bands at a step edge of a TCI $Pb_{0.7}Sn_{0.3}Se$. Using the STM/STS techniques, I demonstrate that the half-unit cell step edge of $Pb_{0.7}Sn_{0.3}Se$ features one-dimensional edge modes. These edge modes have a flat-band-like dispersion, which manifests as a peak in the local density of states at the energy of the Dirac point ($E = 125$ meV). Since the flat band at the step edge is located far above the Fermi level, electron-electron interactions are weak since the kinetic energy scale is predominant. However, it is possible to enhance these interactions by positioning the energy of the 1D flat band close to the Fermi level. The key idea is that, as the kinetic energy is quenched, electron correlations can become the dominant energy scale. To shift the Dirac point to the Fermi level, I use an approach of surface doping, where small amounts of 3d transition elements are doped on the surface of the $Pb_{0.7}Sn_{0.3}Se$ crystal. I observe that as the Dirac point is tuned to the Fermi level, the single peak of the 1D flat band, which also shifts coherently, splits into multiple components and opens a gap in the local density of states at the Fermi level. Theoretical modeling, supported by Hartree-Fock analysis, rationalizes these experimental results in terms of electron-electron interactions that are significantly enhanced since the 1D flat band is energetically localized close to the Fermi level. These interactions cause a splitting of the peak associated with the flat band, resulting in up to four states that spontaneously break time-reversal symmetry and stabilize a flat band Stoner ferromagnetism at the step edge.

In the second part, I use STM/STS to probe an unconventional topological superconducting phase at the interface between a monolayer ferromagnet, $CrCl_3$, and a superconductor, $NbSe_2$. The high-resolution STS measurements reveal a fully gapped interfacial superconducting state in the $CrCl_3/NbSe_2$ heterostructure that remains resilient under strong out-of-plane magnetic fields, contrary to conventional expectations for a ferromagnet-superconductor hybrid. Furthermore, I observe an enhancement in the local density of states at the Fermi energy along the boundaries of the $CrCl_3$ islands, suggesting the presence of edge modes. Theoretical analysis attributes these features to an intrinsic helical p-wave superconducting state at the $CrCl_3/NbSe_2$ interface, stabilized by interfacial Rashba spin-orbit coupling, which explains both the anomalous magnetic field resilience and the emergence of topological edge excitations.

Together, these findings demonstrate how strategic material engineering, from the surface modifications in topological crystalline insulators to precisely assembled van der Waals heterostructures, can create and control exotic quantum states. The one-dimensional correlated states in $Pb_{0.7}Sn_{0.3}Se$ offer a new platform for studying interaction-driven topology, while the unconventional interfacial topological superconductivity in the $CrCl_3/NbSe_2$ heterostructure provides a unique system for exploring non-Abelian anyons and their potential applications in quantum computing.

Contents

Abstract i

Acknowledgments vii

List of Figures viii

List of Tables xi

List of Abbreviations xiii

I Introduction 1

1 Introduction and Scope of Thesis 2

II Experimental Methods 10

2 Experimental Methods 11

- 2.1 Scanning Tunneling Microscope . . . 11
  - 2.1.1 Tunneling Current . . . 12
  - 2.1.2 Types of STM measurements . . . 16
    - 2.1.2.1 STM topography . . . 16
    - 2.1.2.2 Spectroscopy . . . 18
  - 2.1.3 ^{3}He STM system . . . 20
- 2.2 Tip preparation . . . 22
  - 2.2.1 DC etching in solution . . . 23
  - 2.2.2 DC etching using the lamella technique . . . 27
- 2.3 Sample preparation . . . 28
  - 2.3.1 Cleaving of $Pb_{1-x}Sn_xSe$ single crystals . . . 28
  - 2.3.2 Sputtering and Annealing . . . 30
  - 2.3.3 Molecular Beam Epitaxy . . . 32

III Probing interaction effects in a Topological Crystalline Insulator 35

3 Pathway to Topological Crystalline Insulator 36

- 3.1 Quantum Hall Effect . . . 36
- 3.2 Quantum Spin Hall Effect . . . 40

3.3 $\mathcal{Z}_2$ Topological Insulators 42
3.4 3D Topological Insulators 44
3.5 Topological Crystalline Insulators 49
  3.5.1 Strong Electron-Electron Correlations 67

4 Interaction effects at the step edges of $Pb_{1-x}Sn_xSe$ 69
4.1 Experimental demonstration of edge states in $Pb_{1-x}Sn_xSe$ 70
4.2 Tuning interactions in the 1D flat band by surface doping 79
4.3 Theoretical interpretation of the 1D flat band splitting 92
  4.3.1 Theoretical understanding of the edge modes 93
  4.3.2 1D flat-band Stoner ferromagnetism 96
4.4 Conclusion 104

IV Unconventional topological superconductivity in a van der Waals heterostructure 105

5 Superconductivity and Magnetism 106
5.1 Overview of Superconductivity 107
  5.1.1 London penetration depth 108
  5.1.2 Pippard's coherence length 110
  5.1.3 The Ginzburg-Landau theory 111
  5.1.4 The BCS theory 115
    5.1.4.1 Mathematical formalism of the BCS theory 119
5.2 The gap function for different pairing states 123
5.3 p-wave superconductivity 129
  5.3.1 Mathematical formalism for a p-wave gap function 129
  5.3.2 Chiral p-wave vs. Helical p-wave superconductors 131
5.4 Rashba Spin-Orbit-Coupling 134
5.5 2D van der Waals materials 134
  5.5.1 $CrCl_3$: a 2D in-plane van der Waals ferromagnet 136
  5.5.2 $NbSe_2$: a 2D van der Waals superconductor 138

6 Helical edge states in a van der Waals heterostructure 141
6.1 STM topography of the vdW heterostructure $CrCl_3/NbSe_2$ 142
6.2 Edge states in the $CrCl_3/NbSe_2$ heterostructure 145
6.3 Robust interfacial superconductivity under an out-of-plane field . . . 148
6.4 XMCD measurements on the $CrCl_3/NbSe_2$ heterostructure 152
6.5 Theory of the edge states and the superconducting gap in the $CrCl_3/NbSe_2$ heterostructure 153
6.6 Conclusion 161

V Conclusion and Outlook 162

7 Conclusion and Outlook 163

VI Appendix **166**

Bibliography **167**

List of Publications **189**

Curriculum Vitae **192**

Declaration **193**

Dedicated to Maa and Baba

Acknowledgements

I want to begin by expressing my sincere gratitude to my supervisor, Prof. Dr. Stuart S.P. Parkin. His guidance, patience, and constant support were essential throughout my research journey. His insightful feedback and encouragement were invaluable learning experiences, and I am particularly grateful for the opportunity to work in world-class research facilities under his direction.

True to the saying that science is a team effort, I want to express my heartfelt gratitude to Felix Küster and Paolo Sessi in the STM lab. Their guidance in learning this wonderful technique was essential. The long months we spent together, wrestling with and ultimately mastering our ^{3}He STM, will remain a cherished memory.

In the spirit of the fruitful connection between theory and experiment, I am deeply grateful to Prof. Marcel Franz from the University of British Columbia, Prof. Titus Neupert from the University of Zurich, and Prof. Ronny Thomale from the Julius-Maximillians-Universität Würzburg. Their insightful theoretical contributions were pivotal to my research and significantly broadened my theoretical knowledge. Furthermore, I extend my gratitude to the Postdocs and PhD students in their groups, especially Benjamin Zhou, Niclas Heinsdorf, and Glenn Wagner, for their theoretical contributions, which were invaluable to my research. My gratitude extends to Prof. Tomasz Story's experimental group at the Polish Academy of Sciences for supplying the high-quality single crystals essential to our research. I also thank Prof. Matthias Bode's STM group at the Julius-Maximillians-Universität Würzburg for their generous contribution of data sets, which significantly supported our experiments. I am grateful to Anshuman Padhi and Jingrong Ji for their crucial role in providing samples during my PhD research.

I am also grateful to Banabir Pal for the numerous productive sessions we had on tight-binding calculations, as well as for his insightful scientific discussions. I'm also incredibly grateful to Prof. Binoy Krishna Hazra, Prof. Rana Saha, Avanindra K Pandeya, Abhay Srivastava, Jagannath Jena, Anirban Chakraborty, Pranava K Sivakumar, Ankit Sharma, Arpit Sharma, Ajesh K Gopi, Kajal Tiwari, Samiran Choudhury, and Bimalesh Giri for the amazing time and memories created during my PhD. I also thank Rima, Dipu, Tanushree, and Twinkle for the truly enjoyable time we shared. I would also like to thank Ishika, who was a constant source of

support during the writing of this thesis.

I am grateful to Banabir Pal, Mihir Date, Pranava K Sivakumar, Jitul Deka, Sagar Gambhira, and Anshuman Padhi, who generously dedicated their time to proofread my thesis. Their insightful feedback was invaluable in shaping the final version.

My appreciation goes to the technical and administrative staff of the NISE department for their assistance with resources, equipment, and logistics, without which this work would not have been possible. Furthermore, I thank the Max Planck Gesellschaft and the International Max Planck Research School for Science and Technology of Nano-Systems for funding my research.

I owe a debt of gratitude to my family, especially my parents, Sharmistha Das and Dipak Kumar Das, for their endless love, sacrifices, and belief in my abilities. Their encouragement kept me going even during the most demanding times.

List of Figures

2.1 Schematic of the tunneling junction 13
2.2 Schmeatic of a STM and Friedel oscillations in Ag(111) 17
2.3 Examples of dI/dV spectrum and dI/dV maps 19
2.4 He_3 STM system 20
2.5 Schematic of the ^{3}He cryostat 21
2.6 Schematic illustration of tip etching techniques 24
2.7 Demonstration of scanning with sharp and blunt tips 26
2.8 Domain structure of Fe double layer on W(110) probed by a spin-polarized Cr tip 27
2.9 Demonstration of cleaving a sample under ambient conditions 29
2.10 Sputtering of an Ag(111) surface 30
2.11 Sputtering and annealing of single crystals of PdGa(001) and RhSi(001) 31
2.12 Schematic illustration of MBE 33

3.1 Hall Effect 37
3.2 Geometry to realize the QHE 38
3.3 Geometry to realize the QSHE 41
3.4 Electron Dispersion of a $\mathcal{Z}_2$ TI 43
3.5 CECs for weak and strong 3D TI 45
3.6 Band structure of $\mathrm{Bi}_{1-x}\mathrm{Sb}_x$ 46
3.7 Experimental detection of surface dispersion of $\mathrm{Bi}_{0.9}\mathrm{Sb}_{0.1}$ 47
3.8 Experimental observation of Dirac cone for $\mathrm{Bi}_2\mathrm{Te}_3$, $\mathrm{Bi}_2\mathrm{Se}_3$ and $\mathrm{Sb}_2\mathrm{Te}_3$ 48
3.9 Theoretical model for TCI 50
3.10 Tight binding results for the TCI 51
3.11 Crystal Structure and Bulk Brillouin zone of SnTe 52
3.12 Surface band dispersion for PbTe and SnTe 53
3.13 SSs on SnTe surface along $\overline{\Gamma}$-$\overline{\mathrm{X}}$ 57
3.14 Lifshitz transition in the band structure of SnTe 59
3.15 Spin texture of the Dirac SSs on the SnTe surface 61
3.16 Evolution of the band gap for the substitutional alloy $\mathrm{Pb}_{1-x}\mathrm{Sn}_x\mathrm{Se}$ at different temperatures 63

4.1 2D and 3D STM topography of the cleaved (001) surface of $\mathrm{Pb}_{0.7}\mathrm{Sn}_{0.3}\mathrm{Se}$ 71
4.2 Arrangement of atoms mimicking the side view of the unit-cell and half-unit cell step 73
4.3 STM Topography and line profile of the (001) surface of $\mathrm{Pb}_{1-x}\mathrm{Sn}_x\mathrm{Se}$ 74
4.4 Edge states at the half-unit cell step in the pristine $\mathrm{Pb}_{1-x}\mathrm{Sn}_x\mathrm{Se}$ crystals 75
4.5 Spatial mapping of the DOS at energies above and below the Dirac point energy in the pristine samples 77

4.6 Absence of backscattering at the edges 78
4.7 STS measurements on the terrace, half-unit cell and unit-cell step after the 1^{st} step of Cr doping 81
4.8 Spatial mapping of the DOS at energies above and below the Dirac point 82
4.9 STS measurements on the terrace, half-unit cell and unit-cell step after the 3^{rd} step of Cr doping 84
4.10 STS measurements on the terrace, half-unit cell and unit-cell step after the 3^{rd} step of Cr doping 85
4.11 Recovery of the 1D flat band when doped below the Fermi energy . . 87
4.12 Splitting of the 1D flat band for doping with Mn 88
4.13 Splitting of the 1D flat band for doping with Fe 89
4.14 Splitting of the 1D flat band for doping with Cu 89
4.15 Splitting magnitude as a function of different 3d-dopants 91
4.16 Splitting of the 1D flat band into 4 peaks 92
4.17 Toy model for the edge modes 94
4.18 Schematic of spin-polarized 1D flat bands 95
4.19 Hartree-Fock results 101
4.20 Evolution of the splitting of the 1D flat band as a function of increasing interaction strength 102

5.1 Critical field as a function of temperature 108
5.2 Boundary between superconducting and normal domains 112
5.3 GL parameter for a clean and dirty superconductor 113
5.4 Dependence of the critical field as a function of temperature in a type-II superconductor 114
5.5 Fermi surface instability 116
5.6 Formation of Cooper pairs mediated by phonons 117
5.7 Schematic illustration of the quasiparticle spectrum 120
5.8 Classification of superconducting correlations following from the Pauli exclusion principle 124
5.9 Examples of the form of the gap function for different pairing symmetries 125
5.10 Schematic illustration of the chiral and helical p-wave pairing 132
5.11 Crystal structure of $CrCl_3$ 137
5.12 Crystal structure of $NbSe_2$ 138
5.13 Electronic structure of bulk and monolayer $NbSe_2$ 139

6.1 STM topography of the $CrCl_3/NbSe_2$ heterostructure 142
6.2 STM topography of the $NbSe_2$ surface 144
6.3 Edge states in the $CrCl_3/NbSe_2$ heterostructure 145
6.4 Zero-bias peaks from impurities 146
6.5 Superconducting gap estimation 147
6.6 Robust superconductivity in $CrCl_3$ 148
6.7 Vortex on the $NbSe_2$ substrate 149
6.8 Vortex nucleation on the $CrCl_3$ island and edge 150
6.9 Field dependence of superconducting gap on $NbSe_2$ and $CrCl_3$ 151
6.10 Magnetic hysteresis loop on the $CrCl_3/NbSe_2$ heterostructure 152
6.11 Electrostatic field due to the $CrCl_3$ ML 155

6.12 Estimation of Rashba SOC strength 156
6.13 Bogoliubov-de Gennes quasi-particle spectrum 159
6.14 Helical edge states in the excitation spectrum 160

List of Tables

6.1 Irreducible Representations and Superconducting order parameters . 158

List of Abbreviations

QHE	Quantum Hall Effect
QSHE	Quantum Spin Hall Effect
QHS	Quantum Hall State
TI	Topological Insulator
TCI	Topological Crystalline Insulator
LDOS	Local Density of States
VHS	van Hove singularity
STM	Scanning Tunneling Microscopy
STS	Scanning Tunneling Spectroscopy
ARPES	Angle-resolved photoemission spectroscopy
FWHM	Full width at half maxima
FFT	Fast Fourier Transform
HF	Hartree-Fock
CEC	Constant Energy Contours
FIM	Focused Ion Milling
DC	Direct Current
0D	zero-dimensional
1D	one-dimensional
2D	two-dimensional
3D	three-dimensional
DI	deionized
QPI	Quasiparticle interference
GL	Ginzburg and Landau
SOC	Spin-orbit coupling

MBE	Molecular beam epitaxy
SS	Surface states
MBS	Majorana Bound States
MZM	Majorana zero modes
TSC	Topological Superconductivity
CDW	Charge density wave
vdW	van der Waals
XMCD	X-ray magnetic circular dichroism
ML	monolayer
TMDC	transition-metal dichalcogenide
DFT	Density functional theory

Part I

Introduction

1 Introduction and Scope of Thesis

The concept of topology stems from mathematics, where it is used to describe the property of a geometric object that is preserved under continuous deformations such as twisting, bending, and stretching, the straightforward example being the transformation of a doughnut into a coffee cup. Over the years, this concept has also emerged as a powerful tool for understanding diverse phenomena in condensed matter physics. The discovery of the Quantum Hall Effect (QHE) by Klaus von Klitzing (Nobel Prize 1985) marked the first observation of a topological state in this field. Klaus von Klitzing, through his pioneering work, demonstrated that electrons confined in a two-dimensional (2D) geometry under the influence of strong perpendicular magnetic fields exhibit quantized Hall conductance, a unique topological state characterized by an insulating bulk and chiral edge states. Motivated by this experimental work, Thouless *et al.* [1] in 1982 introduced the TKNN invariant (n), a topological index distinguishing the QHE state ($n = 1$) from a conventional insulator ($n = 0$). Of significant interest are the chiral edge states in the QHE, which lead to one-dimensional (1D) edge currents that are dissipationless, and robust against scattering by impurities and therefore hold promises toward technological applications in low-power electronics, novel spintronic devices, topological quantum computing, etc. However, such 1D conducting edge currents are not exclusive to the QHE. Kane and Mele [2] as well as Bernevig *et al.* [3] theoretically proposed the Quantum Spin Hall Effect (QSHE), which exhibits 1D conducting channels even in the absence of any external field. This effect was attributed to the spin-orbit coupling (SOC), which replaces the role of the magnetic field, causing a spin-dependent force to act on the electrons moving through the lattice. Unlike the QHE, the edge states in the QSHE are spin-momentum-locked. The propagation of such spin-momentum-locked electrons leads to helical currents at the edges. The QSHE was predicted in HgTe/CdTe quantum wells [4], followed by the experimental realization by Koenig *et al.* in non-local transport measurements [5], marking the discovery of the first 2D $\mathcal{Z}_2$ TI. The 2D $\mathcal{Z}_2$ TI was predicted alongside the QSHE by Kane and Mele [6], where the role of SOC and time-reversal ($\mathcal{T}$) symmetry was highlighted. As the name suggests, this class of materials is insulating in the bulk with $\mathcal{T}$ symmetry-protected gapless edge states located inside the bulk gap. The initial 2D $\mathcal{Z}_2$ TIs involved QSH materials, which were mostly semiconducting heterostructures. However, experiments on these systems had a major drawback in the sense that there was a lack of direct evidence of the 1D topological edge states. This motivated the search for novel experimental systems and the implementation of high-resolution spatial detection techniques, such as scanning tunneling microscopy, which would allow for direct spatial visualization of these 1D edge states. This technique was subsequently used to visualize 1D topological edge states in various 2D TIs, such as bilayer-Bismuth [7, 8], $ZrTe_5$ [9, 10], $Ta_2Pd_3Te_5$ [11], Bi/SiC(0001) [12], etc.

The concept of a 2D $\mathcal{Z}_2$ TI was later extended to three dimensions, with the theoretical prediction of three-dimensional (3D) TIs, arising from the generalization of the QSHE, which was a 2D phenomenon, to the 3D case. This breakthrough was independently proposed by three research groups, establishing the foundation for 3D TIs [13–15]. While the 2D TIs host 1D gapless edge states, the 3D TIs exhibit 2D surface states (SSs) with a Dirac-Cone-like dispersion. These SS are protected by $\mathcal{T}$ symmetry. Such Dirac-cone-like SSs were demonstrated experimentally for the first time in the 3D semiconducting alloy $Bi_{1-x}Sb_x$ using angle-resolved photoemission spectroscopy (ARPES) [16]. Shortly thereafter, extensive efforts were devoted to realizing the 3D TI phase in the chalcogenide compounds namely, Bi_2Te_3 [17], Bi_2Se_3 [18] and Sb_2Te_3 [19].

The topological materials discovered until the late 2000s involved the 2D and 3D TIs, where the major symmetry, protecting the edge states and SSs was the $\mathcal{T}$ symmetry. However, in 2011, Liang Fu predicted a new 3D topological class that featured SSs protected by crystal point group symmetries. This new 3D class was termed "Topological Crystalline Insulator" (TCI) [20]. This class of materials was theoretically predicted to host multiple spin-polarized SS, which are protected by crystalline symmetries. The initial theoretical prediction of this topological phase was made in the mirror-symmetric alloy SnTe [21], with subsequent experimental confirmation achieved through ARPES [22]. To distinguish this 3D TCI phase in SnTe, Hsieh *et al.* further introduced a topological invariant, the mirror Chern number: n_M = -2. The family of 3D TCIs grew with the identification of this phase in $Pb_{1-x}Sn_xTe$ [23] and $Pb_{1-x}Sn_xSe$ [24], further expanding the class of materials exhibiting this topological state. Following the experimental confirmation of the 3D TCI phase in these materials, extensive STM studies were conducted, revealing Dirac surface states [25, 26], Landau quantization [27], quasiparticle interference patterns [28, 29], one-dimensional edge states [26, 30] etc. Particularly noteworthy was the observation of robust one-dimensional spin-polarized edge states exhibiting a flat-band dispersion at half-unit-cell step edges of $Pb_{1-x}Sn_xSe$ (001). In Part II (Chapter 4) of this thesis, the evolution of the electronic properties of this 1D flat band residing at the step edges of $Pb_{1-x}Sn_xTe$ is investigated under surface doping with 3d transition metals by employing high-resolution STM/STS. In conventional 3D TIs, the Coulomb interactions are too weak to spontaneously break $\mathcal{T}$ symmetry in the 2D SSs [31], and in $Pb_{1-x}Sn_xSe$, electron correlation effects are usually ignored due to its large dielectric constant [32], which screens electron-electron interactions. However, in the present case, since the bands are flat, they are characterized by a large DOS, making them susceptible to Stoner ferromagnetism. The spectroscopic measurements presented in this work reveal that the single peak of the 1D flat band splits into multiple peaks once the 1D flat band is shifted to the Fermi level, accompanied by an opening of a gap in the electronic spectrum near the Fermi level.

These experimental findings are interpreted as signatures of enhanced electron correlations, attributed to the spatially localized 1D flat band residing in the vicinity of the Fermi level. Depending on the strength of the interactions, defined as the ratio of the Coulomb energy and the kinetic energy, the single peak splits into a maximum of four peaks, which spontaneously break $\mathcal{T}$ symmetry and stabilize a Stoner ferromagnetic state in the 1D flat band along the half-unit cell step edge.

In parallel with developments in TCIs, the late 2000s saw fundamental advances in understanding topological superconductors through the seminal works of Kitaev [33], Schnyder *et al.* [34], and Qi *et al.* [35], who established the classification schemes for superconducting systems. Topological superconductors represent a class of quantum materials that combine topological electronic structure with superconductivity, offering significant potential for both fundamental research and quantum technologies. While conventional s-wave superconductors, described by BCS theory, emerge from the condensation of spin-singlet Cooper pairs with opposite momenta, topological superconductors arise from a complex interplay of SOC, electronic band topology, and proximity effects. These systems develop a superconducting gap characterized by a non-trivial topological invariant, which governs both the bulk electronic properties and the emergence of gapless boundary states [36–38]. In the past decade, substantial efforts have focused on identifying material platforms capable of hosting these topological superconducting states, motivated by their potential to harbor Majorana fermions. These exotic quasiparticles, first predicted by Ettore Majorana, are characterized by their self-conjugate nature (acting as their own antiparticles) and non-Abelian exchange statistics [38–40]. Such remarkable properties make them potential candidates for fault-tolerant topological quantum computing.

Multiple experimental routes to realize topological superconductors have been established in recent years [36]. A particularly successful approach has been the proximity-induced superconductivity method, where Cooper pairs from a conventional s-wave superconductor are induced into the topological SSs of an adjacent 3D TI [41–43]. This hybrid system creates an effective 2D $p + ip$ topological superconducting state capable of hosting Majorana-bound states (MBS) within vortex cores [41–43]. Experimental signatures of these MBSs were detected in STM measurements, appearing as a zero-bias conductance peak localized at the vortex cores in $Bi_2Se_3/NbSe_2$ heterostructures [44–46]. This 2D paradigm was subsequently extended to 1D systems, where topological superconductivity (TSC) was realized in semiconductor nanowires with strong SOC proximitized to conventional superconductors [47]. Here, rather than vortex-confined states, the MBS manifests as robust zero-energy states localized at the end of the nanowire. Electrical transport measurements on InSb nanowires coupled to NbTiN superconducting electrodes revealed zero-bias conductance peaks consistent with Majorana zero modes (MZM) [48].

A foundational theoretical framework for 1D topological superconductors was proposed by Alexei Kitaev, who considered a model for a 1D chain of spinless fermions coupled to an s-wave superconductor with strong SOC [49]. This model predicts that the pairing symmetry due to the interaction between the 1D chain and the superconductor acquires an effective p-wave character, which facilitates the emergence of Majorana fermions at opposite ends of the chain. The experimental realization of this model was first achieved in the seminal work of Nadj-Perge *et al.*, who observed localized MZMs at both ends of a ferromagnetic Fe atomic chain grown on a superconducting Pb substrate [50]. This breakthrough sparked extensive research into 1D magnetic chains coupled with various superconductors to engineer 1D topological superconductors hosting 0D MZMs [51–54]. From these experimental and theoretical studies [38, 55], three essential ingredients were identified for creating a 1D topological superconductor with effective p-wave pairing: (i) out-of-plane magnetism, (ii) superconductivity, and (iii) strong Rashba SOC. This framework was also later extended to 2D systems, where magnetic islands coupled to superconductors were shown to host 1D chiral propagating Majorana edge modes along the boundary of the islands. In contrast to 0D MZMs, which have a flat energy-momentum dispersion, these 1D Majorana edge modes are characterized by a linear energy-momentum dispersion located within the topological superconducting gap.

One such experimental evidence of these 1D chiral Majorana edge modes was found in a 2D topological superconductor composed of a monolayer (ML) Pb film deposited on magnetic Co-Si islands fabricated on a Si(111) surface, where the 1D Majorana edge mode is localized around the edge of the Co-Si islands [56].

More recently, van der Waals (vdW) heterostructures, combining 2D ferromagnets with 2D superconductors, have evolved as a potential platform for 2D $p+ip$ TSC, capable of harboring 1D chiral Majorana edge modes. TSC has been demonstrated in the vdW heterostructure comprising a ML out-of-plane ferromagnet, $CrBr_3$, on top of the superconductor, $NbSe_2$. The study revealed 1D chiral Majorana edge modes propagating along the boundary of the $CrBr_3$ islands [57]. A critical finding across these studies is that establishing a TSC state requires the ferromagnetic exchange coupling (J) to dominate both the Rashba SOC and the superconducting gap (Δ). In contrast to the above, in Chapter 6 of this thesis, an unconventional p-wave Rashba TSC, which does not have the stringent requirement of a $J > \Delta$, has been demonstrated in the heterostructure combining MLs of an in-plane 2D vdW ferromagnet, $CrCl_3$, on top of $NbSe_2$. Specifically, the interface of the $CrCl_3/NbSe_2$ heterostructure exhibits a superconducting gap, which remains resilient even under an out-of-plane magnetic field. This is a surprising observation, since magnetic fields typically suppress superconductivity. Moreover, the boundary between the ML $CrCl_3$ island and the $NbSe_2$ substrate features an enhancement in the local density of states (LDOS) at the Fermi energy (E_F), strongly suggesting the presence of topological edge states. Although the observed edge states resemble those previously reported in $CrBr_3/NbSe_2$ heterostructures [57], the conventional TSC framework fails to account for their emergence in the $CrCl_3/NbSe_2$ system. In conventional TSC, while magnetization is typically essential, the exceptionally weak exchange coupling in $CrCl_3$ ($J < \Delta$) renders the magnetization irrelevant. Theoretical calculations indicate that the fully gapped superconducting state observed at the $CrCl_3/NbSe_2$ interface, along with its gapless edge modes, can be attributed to a topological p-wave Rashba superconducting phase, which hosts helical edge states.

This discovery paves the way for designing topological p-wave superconductors with robust Rashba SOC, offering exciting prospects for topological quantum computing and cryogenic spintronics applications.

Scope of thesis

This thesis investigates two distinct topological systems, so it has been divided into parts. Part II, which includes chapter 2, details the experimental techniques employed throughout this work. Part III (comprising Chapters 3 and 4) investigates interaction effects in a TCI. Chapter 3 establishes the theoretical framework of TCIs by tracing their conceptual evolution from fundamental discoveries, including the QHE, QSHE, $\mathcal{Z}_2$ TIs, and 3D TIs, with specific attention given to the TCI, $Pb_{1-x}Sn_xSe$. Building on this foundation, Chapter 4 presents experimental and theoretical studies of interaction effects in a 1D flat band at the step edges of $Pb_{1-x}Sn_xSe$, beginning with the experimental demonstration of edge states and the associated 1D flat band, followed by the realization of interaction effects within these confined electronic systems, and concluding with theoretical modeling that reconciles the experimental observations. Part IV (Chapters 5 and 6) explores an unconventional TSC in the vdW heterostructure $CrCl_3/NbSe_2$. Chapter 5 outlines the theoretical foundations relevant to this work, beginning with conventional BCS superconductivity and progressing to p-wave superconductivity, including a mathematical description and an example gap function to introduce the concept of TSC. The chapter concludes with a brief overview of Rashba SOC and 2D vdW materials. Chapter 6 investigates the vdW heterostructure composed of $CrCl_3$ and $NbSe_2$, focusing on the edge states and the helical p-wave pairing at the interface. It begins with a structural characterization of the heterostructure, followed by a detailed examination of the observed edge states using the STS technique. The chapter then explores the robust superconductivity exhibited by the interface between $CrCl_3$ and $NbSe_2$ under an out-of-plane magnetic field. A theoretical framework is presented to explain the nature of the edge states and the pairing symmetry of the superconducting gap at the interface of the $CrCl_3/NbSe_2$ heterostructure. Finally, the key findings of this chapter are summarized in the conclusion. Chapter 7 concludes this thesis by summarizing the work presented here and providing future research directions.

Part II

Experimental Methods

2 Experimental Methods

2.1 Scanning Tunneling Microscope

The scanning tunneling microscope was first realized in 1981 through the groundbreaking work of Gerd Binnig and Heinrich Rohrer at IBM Zurich Research Laboratory. Their pioneering experiment successfully demonstrated vacuum tunneling between a sharp tungsten tip and a platinum surface, marking the first direct observation of electron tunneling in a controllable, spatially resolved manner [58]. This groundbreaking discovery represented a monumental advancement in scientific instrumentation, enabling unprecedented atomic-scale probing of conductive materials. In recognition of its profound impact, Binnig and Rohrer were awarded the Nobel Prize in Physics in 1986, just five years after their seminal discovery. The scientific community's fascination with STM has grown exponentially due to its remarkable versatility, enabling atomic-scale visualization of material surfaces, surface defects, electronic standing wave patterns, magnetic spin textures such as skyrmions, etc. Furthermore, STM's unparalleled capacity for atomic manipulation has opened new frontiers in nanoscience, enabling the precise positioning of individual atoms to construct artificial nanostructures, including 2D atomic lattices and quantum corrals, that reveal fundamental quantum phenomena. Beyond conventional imaging, the technique's spectroscopic applications, ranging from LDOS measurements to inelastic electron tunneling spectroscopy, provide unprecedented insights into electronic and vibrational properties, complemented by emerging time-resolved studies of dynamic surface processes. Unlike conventional microscopes, which rely on classical wave optics or particle scattering, the operation of STM is fundamentally rooted in quantum mechanics. The STM, while conceptually straightforward in principle, presents formidable experimental challenges that demand cutting-edge instrumentation. Achieving atomic-resolution imaging and spectroscopy requires maintaining atomically clean surfaces under ultra-high vacuum conditions while simultaneously implementing sophisticated vibration isolation systems to ensure sub-picometer stability. The technique's extraordinary sensitivity relies on ultra-low-noise electronics capable of detecting faint tunneling currents on the order of femtoamperes, coupled with advanced cryogenic systems that reach millikelvin temperatures to achieve ultra-high energy resolution. Over the years, with technological advancement, STMs have achieved unprecedented performance approaching fundamental quantum limits. State-of-the-art systems now operate down to mK temperatures and under high magnetic fields, while maintaining exceptional stability. These advanced instruments combine ultra-low electrical noise with sub-microelectronvolt energy resolution, enabling the investigation of delicate quantum phenomena that were previously inaccessible. While STM has its roots in condensed matter physics, the technique has successfully crossed into biological and molecular research. It now enables scientists to visualize conjugated organic molecules and observe self-assembly processes in action. Furthermore, modern STM applications can track atomic-scale transformations during actual chemical processes - from catalytic reactions to electrochemical changes at surfaces - providing exciting views of dynamic molecular behavior.

2.1.1 Tunneling Current

Tunneling is one of the most striking manifestations of quantum mechanics, where particles traverse classically forbidden barriers. While often illustrated by macroscopic analogies—such as objects passing through walls—this phenomenon is strictly confined to the quantum realm, governing the behavior of electrons. Unlike classical particles, electrons are described by a wave function $\Psi(r)$, with their spatial probability distribution given by $|\Psi(r)|^2$. Near a metal surface, electrons at the E_F encounter a potential barrier defined by the material's work function (Φ), which would classically prevent their escape. However, their wavefunctions extend into the

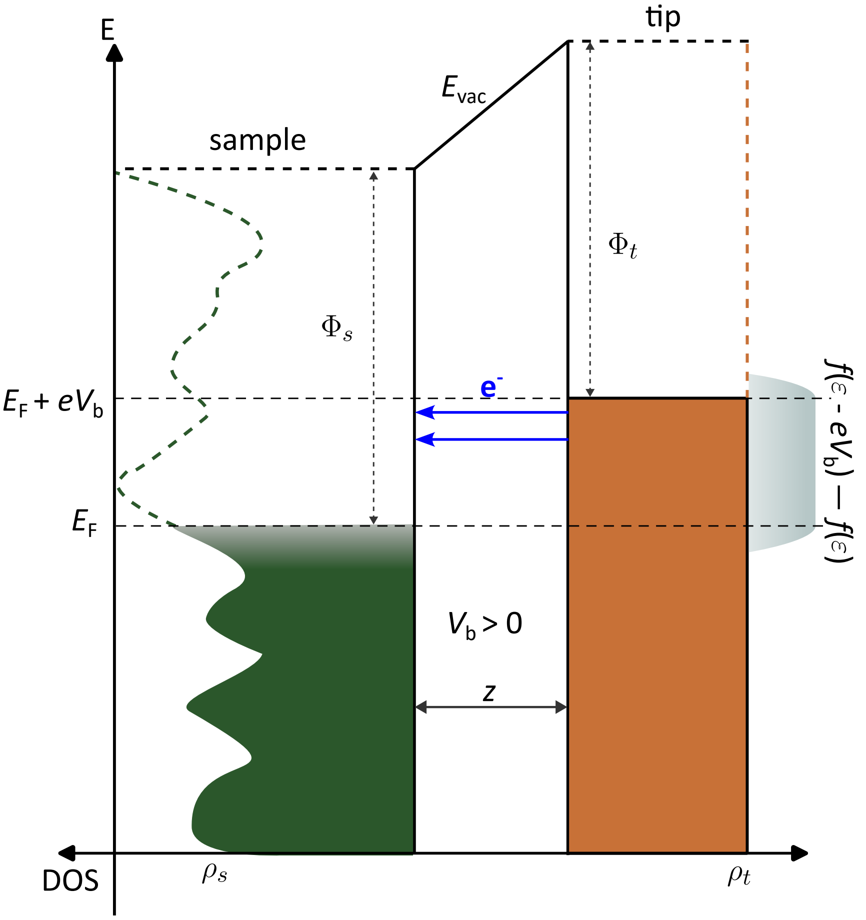

Figure 2.1: Schematic of the tunneling junction. A positive bias voltage V_{b} is applied between the tip and the sample which shifts down the Fermi level of the sample with respect to that of the tip causing electrons to tunnel from the occupied states of the tip to the unoccupied states of the sample across a vaccum barrier of width z. The DOS of the tip and the sample are denoted by ρ_t and ρ_s, respectively, which are filled up to the Fermi level. The electrons tunnel within an energy window defined by the Fermi-Dirac distribution $f(\varepsilon)$ through the vacuum barrier E_{vac}.

vacuum with an exponential decay. Interestingly, when a second conducting surface, which is the STM tip, is brought within nanometers of the sample, the tail of the electron's wavefunction overlaps with available electronic states in the tip. If a bias voltage (V_{b}) is applied, electrons can tunnel elastically across the gap without ever truly occupying the vacuum—effectively, transitioning directly from the energy band of one solid to another. This process generates a measurable tunneling current (I_{t}), despite the absence of physical contact. The tunneling current is governed by three key factors: (i) **Exponential Distance Dependence**: I_{t} decays exponentially with the tip-sample separation (z), as the overlap of the electronic wave functions of the tip and the sample diminishes rapidly. (ii) **Energy window of tunneling**: Only electrons within an energy range defined by E_F and $E_\mathrm{F} + eV_\mathrm{b}$, contribute to the tunneling process, requiring occupied states on one side and vacant states on the other. (iii) **Density of states**: The number of accessible electronic states in the tip ($\rho_t(\varepsilon)$) and the sample ($\rho_s(\varepsilon)$) at the relevant energies ($\varepsilon = E - E_\mathrm{F}$) governs the tunneling current. A generalized schematic of the tunneling junction is illustrated in figure 2.1, where the tip and sample possess uniform and non-uniform DOS, respectively. For the rest of the discussion, the suffixes in V_b and I_t will be dropped and referred to as just V and I respectively. An expression for the tunneling current can be obtained using the first-order time-dependent perturbation theory [59]. A brief derivation of the tunneling current is as follows: first, one needs to consider the individual contribution to the tunneling current from the tip to the sample and vice versa at an energy ε:

$$i_{tip \rightarrow sample} = -2e\frac{2\pi}{\hbar}|M|^2(\rho_t(\varepsilon - eV) \cdot f(\varepsilon - eV)) \cdot (\rho_s(\varepsilon)[1 - f(\varepsilon)]) \tag{2.1}$$

$$i_{sample \rightarrow tip} = -2e\frac{2\pi}{\hbar}|M|^2(\rho_s(\varepsilon) \cdot f(\varepsilon)) \cdot (\rho_t(\varepsilon - eV)[1 - f(\varepsilon - eV)]) \tag{2.2}$$

where $\rho_s(\varepsilon)$ and $\rho_t(\varepsilon)$ are the DOS of the sample and tip respectively, $f(\varepsilon) = \frac{1}{1+exp(\frac{\varepsilon}{k_B T})}$ is the Fermi-Dirac distribution function. At T = 0 K, $f(\varepsilon) = 1$, for $\varepsilon < 0$, implying that all states below E_F are occupied, while $f(\varepsilon) = 0$, for $\varepsilon > 0$, implying that all states above E_F are empty. However, for finite T, there is a smearing of the Fermi-Dirac distribution function, causing some states above E_F to be occupied and vice versa. The tunneling matrix or the transfer function M considers the quantum mechanical coupling between the tip and the sample, introducing several non-trivial dependencies. The matrix element modulates the tunneling probability across the energy window defined by the bias voltage, effectively acting as a transmission filter. While the overall current decays as $\mathrm{e}^{-2\kappa z}$, M further refines this dependence by accounting for subtle variations in wave function overlap. The atomic-scale morphology of the tip and sample, along with the spatial symmetry of their respective wavefunctions, critically influence M. For instance, a sharp tip with *d*-orbital character may enhance tunneling to specific sample states compared to a tip with an *s*-type orbital. Having defined the essential factors affecting the tunneling current, one can write down the expression for the current measured by the STM, which is given by the sum of the above equations and integrated over all energies:

$$I = \frac{4\pi e}{\hbar} \int_{-\infty}^{\infty} |M|^2 \rho_s(\varepsilon)\rho_t(\varepsilon - eV)\Big(f(\varepsilon - eV) - f(\varepsilon)\Big)d\varepsilon \tag{2.3}$$

For measurements conducted at cryogenic temperatures, T $\sim$ 1.8 K, the thermal broadening is minimal, reducing the integral to:

$$I \approx \frac{4\pi e}{\hbar} \int_{0}^{eV} |M|^2 \rho_s(\varepsilon)\rho_t(\varepsilon - eV)d\varepsilon \tag{2.4}$$

For small applied biases, the electron wavefunctions, and thus the tunneling matrix element $|M|^2$, remain essentially constant across the narrow energy window. In this regime, the tunneling current reflects the convolution of the sample's and tip's LDOS:

$$I \approx \frac{4\pi e}{\hbar} |M|^2 \int_{0}^{eV} \rho_s(\varepsilon)\rho_t(\varepsilon - eV)d\varepsilon \tag{2.5}$$

Standard STM configurations typically employ tungsten (W) or platinum-iridium (PtIr) alloy tips, which exhibit a nearly constant DOS near the Fermi level. This characteristic is routinely verified through high-bias field-emission spectroscopy on noble metal surfaces (e.g., Ag or Cu(111)), where current-voltage (I-V) measurements should not yield any unexpected features apart from the surface states. Under these conditions, the tip's DOS $\rho_t(\varepsilon – eV)$ becomes effectively energy-independent, simplifying to $\rho_t(0)$. Hence, I can be written as:

$$I \approx \frac{4\pi e}{\hbar} \rho_t(0) |M|^2 \int_{0}^{eV} \rho_s(\varepsilon)d\varepsilon \tag{2.6}$$

As mentioned previously, the matrix $|M|^2$ has a very complex form, which would depend on the particularities of the system. For a square potential barrier between the tip and the sample, the matrix element can be approximated by the WKB approximation:

$$|M|^2 \approx e^{-2\frac{z}{\hbar}\sqrt{2m\varphi}} \tag{2.7}$$

where m is the effective electron mass, z is the width of the potential barrier, φ is the effective local barrier height, given as $\varphi = \Phi_s + \Phi_t - (2\varepsilon - eV)$. Substituting the form $|M|^2$ in eq. 2.6, I reduces to:

$$I \approx \frac{4\pi e}{\hbar} e^{-z\sqrt{\frac{8m\varphi}{\hbar^2}}} \rho_t(0) \int_0^{eV} \rho_s(\varepsilon) d\varepsilon \tag{2.8}$$

This expression for the tunneling current I describes the measured signal in STM experiments under applied bias V, revealing that I is directly proportional to the integral of the DOS of the sample from the Fermi energy to eV. Moreover, this expression also correctly captures the exponential decay of the current with the width of the vacuum barrier.

2.1.2 Types of STM measurements

2.1.2.1 STM topography

A foundational principle underpinning STM's extraordinary ability to map surfaces at the atomic scale is the pronounced sensitivity of the tunneling current to the tip-sample separation z, mathematically expressed as $I \propto e^{-\kappa z}$ (where κ is a constant). This exponential relationship dictates that even a minuscule vertical displacement of the tip, of the order of an Å, can induce a tenfold change in the tunneling current for typical metallic work functions. This translates into a vertical resolution of the order of a few picometres, enabling a sharp tip, as it traverses a sample surface, to effortlessly resolve the atomic steps and the individual atoms in the lattice. To precisely move the tip across the surface, it's attached to a piezotube that uses the piezoelectric effect. This means applying a voltage makes the tube expand or shrink in a controlled way. By using three separate high-voltage controls, the tip can be translated in the x, y, and z directions with extremely high precision. To detect a measurable tunneling current (of the order of pA), the scanning probe must be

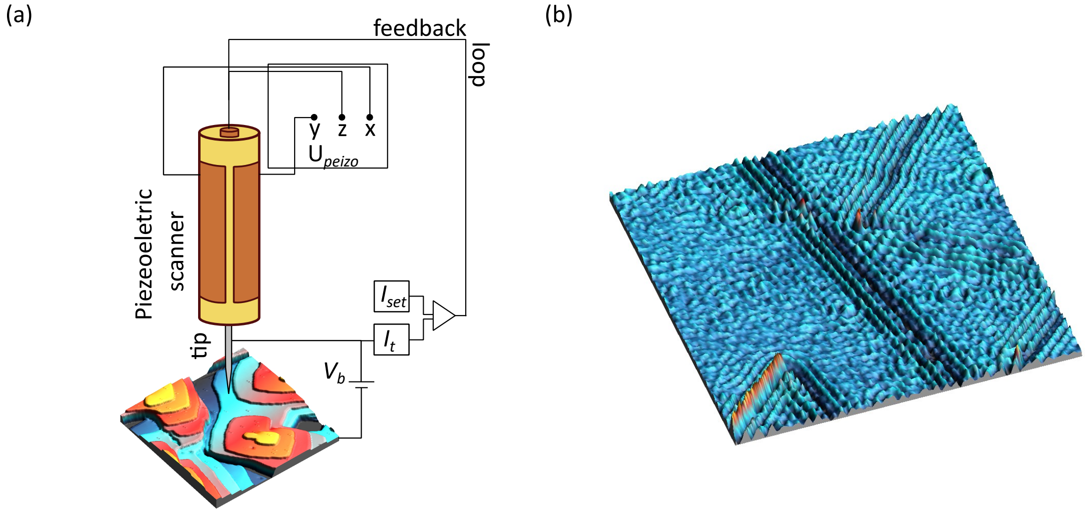

Figure 2.2: (a) Schematic illustration of the core components of an STM. A voltage V_b is applied between a sharp tip and a sample. The motion of the tip on the xy plane, as well as the vertical z motion, is precisely controlled by a 3D piezoelectric scanner using a feedback loop. The image shown is a 3D constant current topography of a SnTe sample. (b) Computer-generated image of a 2D matrix containing the z values acquired over a 120 x 120 nm region on Ag(111), revealing monoatomic steps. Friedel oscillations are also visible, which are correlated to the electronic structure.

positioned extremely close to the sample surface ($\sim$ 10 Å). This controlled approach involves a coarse motor that moves the entire tube scanner in discrete steps smaller than the scanner's total z-range. In most of the STM systems, this coarse motion is achieved using piezoelectric stacks operating in a "slip-stick" mode. After each coarse step, the scanner performs a fine sweep across its full z-range before the coarse motor advances again. This iterative process continues until a tunneling current is detected. To stabilize the z-position of the tip, a rapid electronic feedback loop dynamically adjusts the z-scanner voltage, ensuring that the tunneling current remains locked at a user-defined setpoint.

Surface topography is typically visualized using a technique known as "constant current operation". Here, the x and y piezo voltages drive the tip in a raster pattern across the sample surface, scanning a 2D area line by line along the fast scan direction (at speeds around 50 nm s^{-1}). Simultaneously, the feedback system continuously adjusts the tip height z to maintain the tunneling current I_t at the desired setpoint (I_set). The STM topography is generated by the z-trajectory of the tip, which effectively maps the surface contour. The STM topography in the schematic in figure 2.2a is a constant-current scan of a SnTe sample. It is critical to select appropriate operating parameters, as excessively high scan speeds can overwhelm the feedback system's response time, potentially leading to unintended mechanical contact between the tip and the sample. It is important to note that for a sample with homogeneous DOS, the recorded variations in the tip's z-position directly mirror the surface's topographic structure; however, the spatial inhomogeneity of the DOS in most materials implies that the STM topographic images of such materials reflect a combination of both surface geometry and electronic structure. For instance, the scattering of surface state quasiparticles at the step edges and defects on a Ag(111) surface gives rise to characteristic Friedel oscillations, as exemplified in figure 2.2b.

2.1.2.2 Spectroscopy

Beyond its renowned capability for atomic-scale topographic imaging, STM serves as a powerful spectroscopic tool that can reveal the electronic DOS across an energy range spanning several electron volts, encompassing both occupied and unoccupied states. This spectroscopic measurement is performed by first stabilizing the tip at a fixed height above the surface (by disabling the feedback loop) and then sweeping the applied bias voltage while recording the resulting tunneling current $I(V)$. The fundamental relationship between the tunneling current and electronic structure becomes apparent when one considers eq. 2.8. By numerically differentiating the I, one can extract the sample's DOS at a specific energy eV:

$$\frac{dI}{dV} \propto \rho_s(eV) \tag{2.9}$$

However, in practice, direct numerical differentiation of experimental I(V) data introduces significant noise that often obscures the relevant spectroscopic features. To overcome this limitation, a lock-in detection technique is usually employed that provides much cleaner spectroscopic data with a high signal-to-noise ratio. This method involves superimposing a small AC modulation V_{mod} (typically a few μV

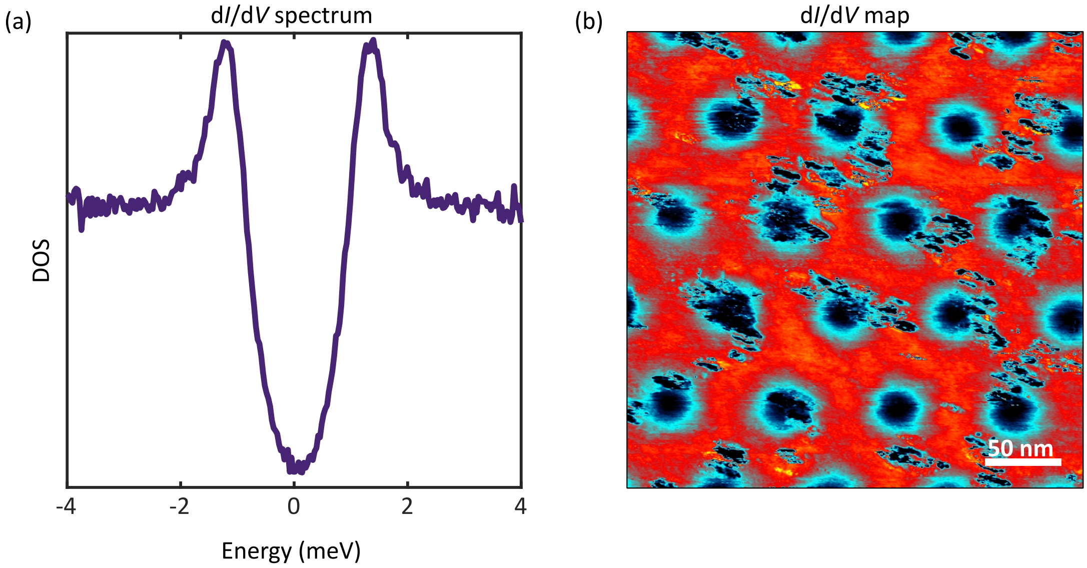

Figure 2.3: (a) A typical dI/dV spectrum on a superconductor featuring a gap in the DOS. (b) A dI/dV map on a superconductor showing a variation in the DOS at a particular bias.

to mV) at a frequency f_{mod} on the DC bias voltage and measuring the change in the tunneling current dI, to obtain dI/dV. However, the successful implementation of the lock-in technique requires careful attention to two critical experimental parameters. Firstly, the STM junction's capacitive coupling and stray capacitances in the wiring introduce phase-shifted artifacts at the modulation frequency f_{mod}. Precise phase matching is therefore essential to isolate the actual tunneling current response from these spurious capacitive contributions. Secondly, the amplitude of the bias modulation sets a lower limit for the energy resolution given by $\approx \mathrm{e}V_{\text{mod}}$, therefore, the chosen V_{mod} must be significantly smaller than V ($V_{\text{mod}} << V$). This ensures that the modulation acts as a differential probe rather than averaging over finite energy ranges. Figure 2.3b shows a typical dI/dV spectrum on the surface of a NbSe_2 crystal, revealing the superconducting gap in the DOS.

Utilizing the lock-in technique during topographic scans allows mapping the LDOS in real space at a specific energy, $U = eV$, providing insights into the spatial distribution of the DOS. These maps are commonly referred to as dI/dU maps. Furthermore, a dI/dU map can be obtained from a densely packed grid of points over a line or an area, allowing for the visualization of the DOS in 1D or 2D. Figure

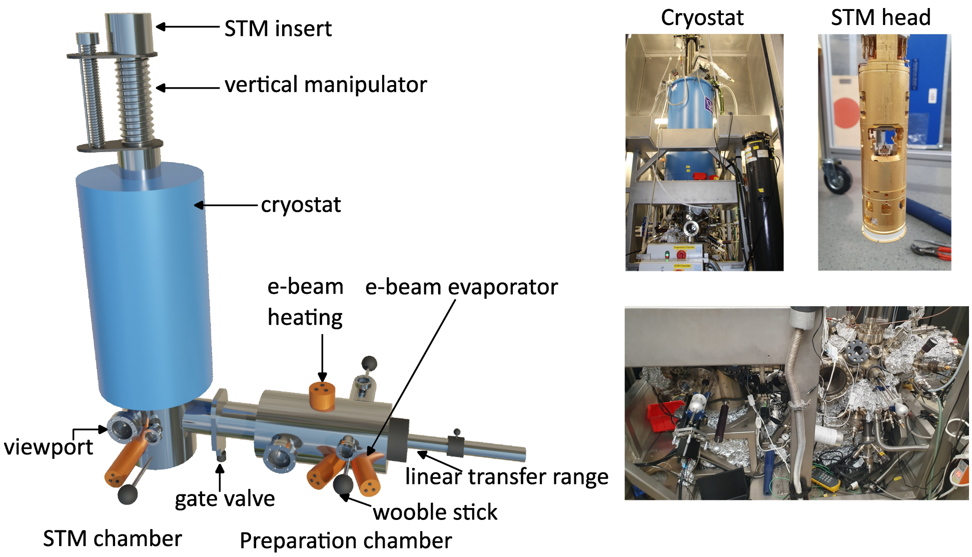
STM insert
vertical manipulator
cryostat
e-beam heating
e-beam evaporator
viewport
gate valve
linear transfer range
wooble stick
STM chamber
Preparation chamber
Cryostat
STM head

Figure 2.4: On the left is the schematic of the He_3 STM system in the laboratory. The cryostat, STM chamber, and preparation chamber, along with all the components, are indicated in the figure. The STM system is enclosed within an acoustic isolation housing and installed on a dedicated vibration-damped platform. For enhanced mechanical decoupling, the entire assembly is supported by pneumatic vibration isolation legs that can be actively pressurized to float the system, protecting against mechanical vibrations. The right side of the figure shows photographs of the Oxford cryostat, the STM head, and the UHV chambers in the lab.

2.3b shows a typical $\mathrm{d}I/\mathrm{d}V$ map acquired at a particular bias, revealing magnetic vortices on the surface of a superconductor $NbSe_2$.

All the spectroscopic data presented in this work will be accompanied by the relevant experimental parameters, I_t, V_b, and V_{mod} to enable proper interpretation. The spectroscopic data ($\mathrm{d}I/\mathrm{d}U$)has been plotted as a function of the energy w.r.t the Fermi energy (E-E_{F}).

2.1.3 ^{3}He STM system

The experimental results presented in this thesis have been obtained using a low-temperature ultra-high vacuum (UHV) STM. Figure 2.4 shows a schematic of the He_3 STM system in the laboratory. The system features a Scienta Omicron "Tribus" STM head integrated with an Oxford Instruments bath cryostat. The cryogenic system comprises a 70 L liquid N_2 jacket, a 100 L ^{4}He reservoir, a 1K pot, and a ^{3}He refrigerator [60, 61], that enables ∼6 days of continuous operation at a base temperature 1.8 K and ∼24 hrs at 550 mK in a single-shot ^{3}He mode (see figure 2.5).

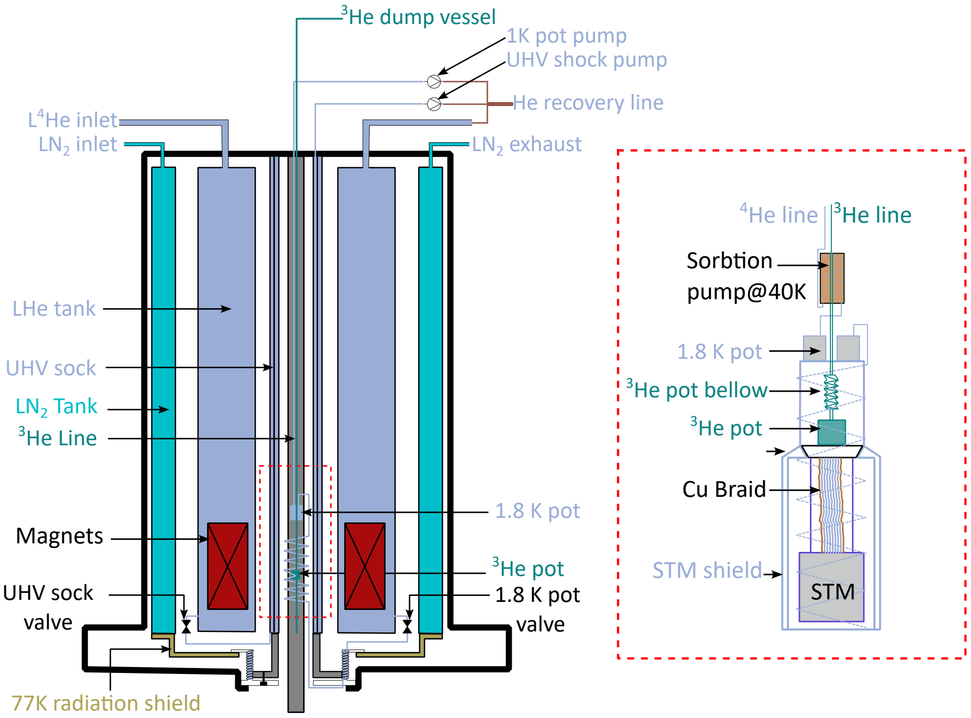
^{3}He dump vessel
1K pot pump
UHV shock pump
He recovery line
L^{4}He inlet
LN$_2$ inlet
LN$_2$ exhaust
LHe tank
UHV sock
LN$_2$ Tank
^{3}He Line
Magnets
UHV sock valve
77K radiation shield
1.8 K pot
^{3}He pot
1.8 K pot valve
^{4}He line
^{3}He line
Sorbtion pump@40K
1.8 K pot
^{3}He pot bellow
^{3}He pot
Cu Braid
STM shield
STM

Figure 2.5: Schematic of the ^{3}He cryostat system containing a 100L LHe tank which supplies LHe to the 1 K pot (connected to the STM shield) and the UHV sock (in contact with the inner wall of the cryostat) which are pumped to cool down below 4K. A tank of LN$_2$ acts as a thermal shield against radiation from the bottom and sides of the cryostat. The magnified version of the variable temperature insert is shown in the red dotted box, consisting of the 1 K pot fixed to the STM shield, the sorption pump, the ^{3}He pot fixed to the STM head, and the ^{3}He bellow. The ^{3}He in the dump vessel condenses into the ^{3}He pot, which is cooled by the 1K pot via the STM shield. The sorption pump is maintained at 40 K by heating to keep the pressure in the ^{3}He pot high so that the bellow remains extended, providing sufficient thermal contact between the cone (attached to the ^{3}He pot) and the counter-cone on the STM shield which allows the STM head to cold down to 1.8 K. On switching the heater of the sorption pump, the pressure in the bellow reduces so it contracts, which decouples the ^{3}He pot from the shields, causing the ^{3}He to evaporate, thereby cooling the pot to 550 mK.

Superconducting solenoids embedded in the helium tank enable application of both in-plane ($B_{x,y} \leq 1.2$ T) and out-of-plane ($B_z \leq 6$ T) magnetic fields. The cryostat is coupled to the STM chamber (see figure 2.4). The STM head is fixed to a variable temperature insert, which can be accessed using the motorized vertical manipulator that lowers the insert into the STM chamber, where the thermal shields encompassing the STM head are opened, for sample and tip exchange. The STM chamber is equipped with a wobble stick that facilitates tip and sample exchange. The STM chamber is additionally equipped with two electron-beam evaporators aligned toward the sample stage, allowing for in situ material/atom deposition directly onto the sample stage. The preparation chamber, connected to the STM chamber via a gate valve, facilitates sample cleaning through argon ion sputtering, e-beam annealing, as well as resistive annealing. To maintain pristine conditions, the system employs turbo-molecular, ion getter, and titanium sublimation pumps, sustaining pressures of 1.8 x 10^{-10} mbar in both the STM chamber and preparation chamber. The linear travel range was optimized by colleagues to minimize degassing during sample transfer. The volume of the inner bore of the cryostat where the STM insert is located is additionally pumped by a small ion-getter pump. At the bottom of the cryostat are gate flaps that act as a radiation shield for the inner bore of the cryostat. The cryostat's inner wall is thermally coupled to the specialized UHV sock assembly. This UHV shock functions as an efficient cryopump when cooled below 4 K by pumping on liquid helium circulation, creating an ultra-clean measurement environment inside the inner bore of the cryostat. This results in a local pressure near the tip-sample junction, substantially lower than the base chamber pressure, enabling stable measurements of highly reactive samples for extended durations with minimal adsorbate accumulation.

The STM is operated using the Nanonis control system (SPECS Zurich), which integrates dedicated electronics with a comprehensive software package for measurement automation and data acquisition. All experimental data presented in this work were processed and analyzed using a combination of WSxM software [62] for topographic image analysis and MATLAB for advanced numerical processing and visualization.

2.2 Tip preparation

The preparation of atomically sharp tips made of different materials, such as Tungsten, Platinum-Iridium, Chromium, etc., is important for achieving high spatial resolution, which ultimately allows the clear visualization of different atomic species in the STM topographic images. An atomically sharp (ideal case) STM tip is expected to have just one atom at the tip apex which is primarily responsible for the tunneling phenomena, however this is not the case most of the time as there could be more than one atom or a cluster of atoms at the tip apex, implying varying asperities at the tip apex which can affect the spatial resolution. There are, in principle, two steps to tip preparation: the first one is the ex-situ method, followed by in-situ treatment. Different methods of ex-situ tip preparation have been proposed in the past, the most popular of which are electrochemical etching [63, 64] and mechanical etching techniques, and the more sophisticated ones involve electron beam deposition [65, 66], focused ion milling (FIM) techniques [67, 68], and others. The electrochemical tip-etching and mechanical tip-etching techniques are easily feasible in lab experiments, are cost-effective, and are known to produce tips of desirable quality. The STM measurements presented in this thesis are performed with tips made by the electrochemical etching and mechanical etching methods hence, the discussion will be limited to just those two techniques. At first, the electrochemical etching technique will be discussed. Electrochemical etching can be performed in two ways: the direct current (DC) etching in solution and the DC etching using the lamella method. The subsections below provide detailed descriptions of these methods.

2.2.1 DC etching in solution

Figure 2.6 shows a schematic illustration of the DC etching in solution technique used for preparing W tips. As can be seen, the main components are a DC biasing circuit combined with a cut-off circuit, a 5-8 % NaOH solution, a vertically controllable tip holder, a polycrystalline W rod acting as the anode, and a ring-shaped electrode made out of Copper/Gold which acts as the cathode. The initial step involves preparing a 5-8 % NaOH solution by dissolving 5-8 gm of NaOH pellets in 100 mL deionized (DI) water and leaving it overnight for the pellets to be dissolved completely. Once the NaOH solution is prepared, it is poured into a small beaker where the etching occurs. A 10-15 mm long W wire having a diameter of 0.35 mm is fixed to the tip micropositioner. The tip holder, which acts as the anode, is connected to the positive terminal of the bias setup. A 1 mm thick gold wire is shaped into

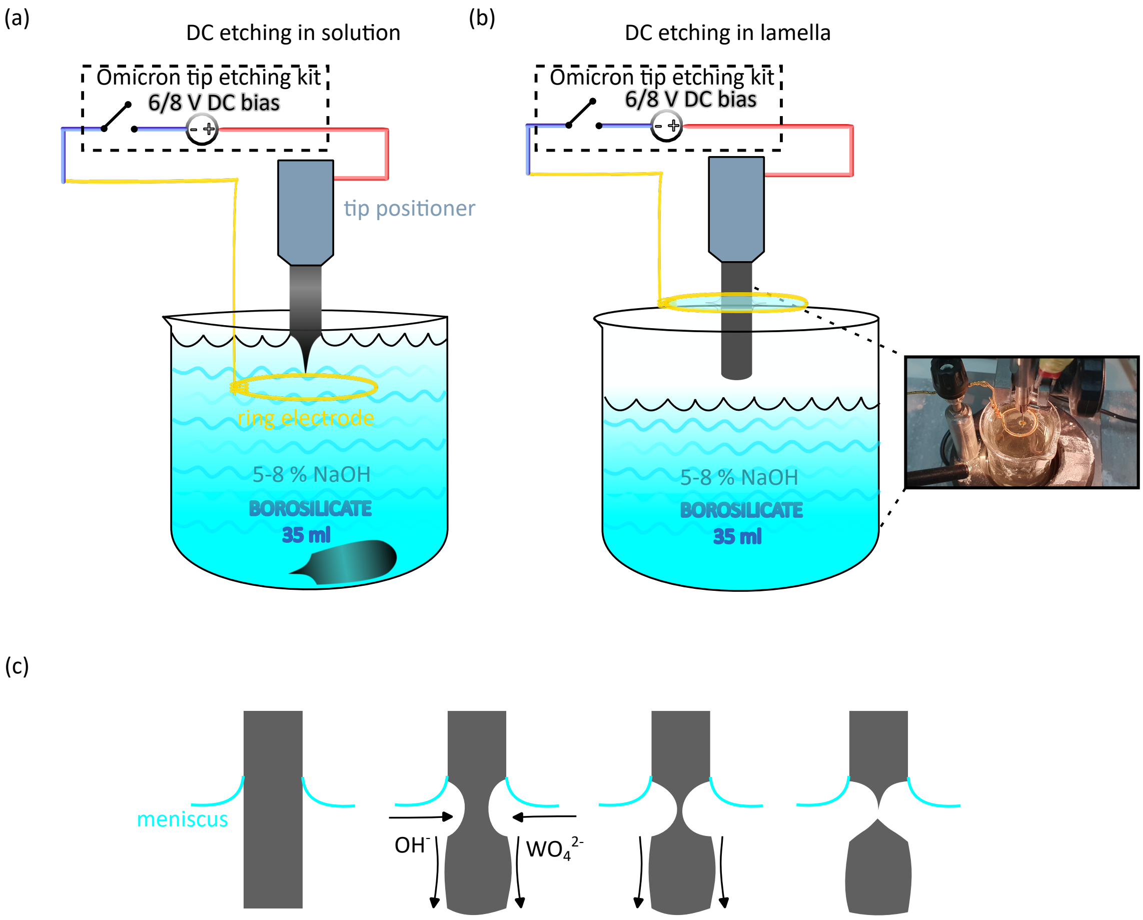
(a)
DC etching in solution
Omicron tip etching kit
6/8 V DC bias
tip positioner
ring electrode
5-8 % NaOH
BOROSILICATE
35 ml
(b)
DC etching in lamella
Omicron tip etching kit
6/8 V DC bias
5-8 % NaOH
BOROSILICATE
35 ml
(c)
meniscus
OH-
WO42-

Figure 2.6: (a) DC etching in solution with the W wire submerged in the NaOH solution. The situation shown here is after the etching process has been completed. (b) DC etching using the lamella method. (c) Gradual etching of the tip close to the meniscus formed around the W rod. Part (c) adapted from ref. [69].

a ring as demonstrated in the schematic in figure 2.6, submerged into the solution, and connected to the negative terminal acting as the cathode. In the next step, the W wire is lowered into the solution through the center of the gold wire ring and extended 3-4 mm underneath the plane of the ring. Once the voltage bias is switched on, the etching process is initiated. An Omicron tip etching toolkit performs the entire tip etching process controllably, allowing one to change the voltage and set a threshold value of the current below which the etching circuit is broken. A high-magnification tabletop optical microscope monitors the etching process. The OH$^-$ ions produced at the cathode due to the dissociation of NaOH into Na$^+$ and OH$^-$, flow towards the electrolyte-air interface where the etching begins. The OH$^-$ reacts with the W rod, causing its oxidation and forming WO$_4^{2-}$, which flows downwards from the electrolyte-air interface and collects near the bottom part of the submerged rod, forming a thick layer around it. At the beginning of the etching process, the rate is initially higher close to the electrolyte-air interface, causing a necking of the W rod just below the interface, as shown in figure 2.6c. As the necking happens, the amount of W available for etching is substantially reduced leading to a reduction in the etching rate. Simultaneously, the bottom part of the submerged wire gets heavier due to the deposition of $WO_4^{2^-}$. At a certain point, the weight of the submerged part acts against the thin neck formed due to the etching, and the bottom part of the wire drops into the solution, leaving a cone-shaped tip (see figure2.6a). Figure 2.6c demonstrates this step-wise necking and breaking process of the W wire. The etching toolkit measures the current flowing, which has now fallen below the threshold value, and switches off the circuit. The top part of the wire with a cone-shaped apex is removed from the micropositioner and cleaned with DI water to remove the oxide layer at the apex of the tip. It should be noted that the shape of the tip formed depends mainly on the meniscus formed by the NaOH solution around the W rod [64]. In an extensive thesis on the preparation of tips by different methods [69], it has been demonstrated that, depending on different bias voltages, the length of the cone and the aspect ratio of the tip can be controlled [69].

The as-prepared tips are unsuitable for STM measurements since the apex of the tip would still be very blunt and might have multiple asperities. Therefore, further in-situ treatment of the as-prepared tips is required. Several methods of in-situ tip preparation have been proposed, such as e-beam heating, sputtering-annealing cycles, field emission against the surface of a noble metal, etc. In the present thesis, the as-prepared tips have been prepared by mostly treating them on a freshly prepared Ag(111) crystal surface (refer to sec. 2.3.2). The quality of a tip can be judged by performing topographic scans and looking at any defects, adatoms, or step edges. To achieve reasonably sharp tips, small voltage pulses in the range of ±5 V are applied. During the pulsing, the tip might drop contaminants loosely bound to the tip apex or pick up a cluster of Ag atoms from the Ag surface. This pick-up

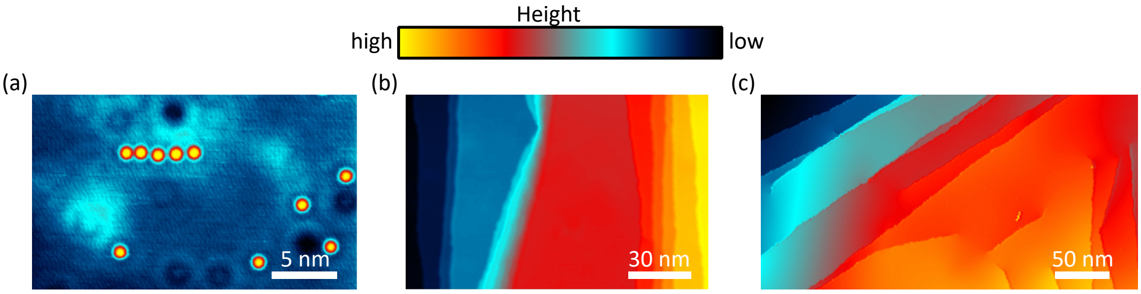

Figure 2.7: (a) Atomically sharp tip can image the Cr atoms on the Ag(111) substrate, (b) Scanning the Ag(111) surface with a blunt tip causes the step edges to appear blunt, (c) Scanning the Ag(111) with a sharp tip due to which step edges appear sharp.

or drop manifests as a change in the tip height. Following the application of voltage pulses, STM topographic scans are acquired to judge the quality of the tips. This procedure of pulsing is repeated several times until reasonably sharp features can be seen in the topographic images (defects and adatoms usually appear spherically symmetric in shape, and the step edges appear pretty sharp). Even after several pulsing cycles, if the tip remains blunt, the tip is gently drawn 0.5-1 nm into the sample, keeping the feedback off. This method is called poking which sometimes helps in shaping the tip apex to yield sharp tips. Another method of in-situ tip preparation that can also be applied is deep crashing the tip against the Ag(111) surface using the z-coarse motion. This involves dipping a few nanometres into the surface of Ag(111). The heat generated during the hard crash between the tip and sample helps to shape the tip apex. This method was seen to work robustly and usually produces extremely sharp tips. It is to be noted that although it is commonly mentioned that W tips are used for STM measurements, generally the tip apex will have a cluster of Ag atoms because it is conditioned on the Ag(111) surface. Figure 2.7 demonstrates STM topographic images acquired using sharp and blunt tips. Figure 2.7(a) shows that scanning with an atomically sharp tip allows the visualization of Cr atoms on the surface of Ag(111). As shown in figure 2.7b, scanning the Ag(111) surface with a blunt tip i.e., a tip with a cluster of atoms, can obscure the sharpness of the step edges. However, the advantage of scanning with a sharp tip is apparent from figure 2.7c, which shows sharp step edges on the Ag(111) surface.

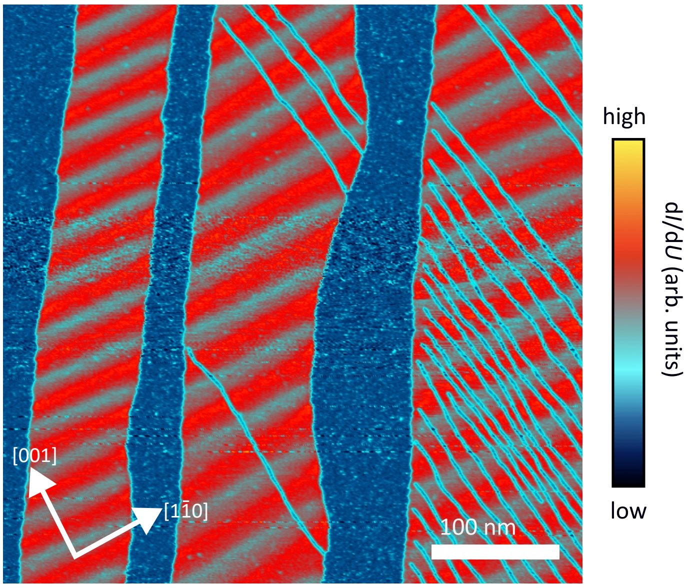

Figure 2.8: Spin polarized dI/dU map acquired on Fe double layer on W(110) using a bulk Cr tip at zero magnetic field demonstrating the spin spiral state.

2.2.2 DC etching using the lamella technique

The DC etching using the lamella method involves utilizing a lamella of the NaOH solution to perform the etching. Unlike the etching in solution technique, in this case, the ring made out of the gold wire acting as the cathode is not submerged in the solution. It remains 5-7 mm above the solution as shown in figure 2.6b. For the etching process, the same components as those mentioned in the previous subsection are used. The first step is to lower the metal wire to be etched using the micropositioner so that it passes 3-4 mm below the center of the ring. In the next step, a lamella of the solution is formed in the ring by lifting the beaker of NaOH solution until the ring is submerged into the solution and then brought down. A real image of a lamella during tip preparation is depicted in figure 2.6b. Once a lamella his prepared, the bias voltage is applied using the Omicron tip preparation kit, and the etching process commences. In this method, the chemical reactions involved in the etching and the necking of the wire are similar to those mentioned in the previous subsection. The etching occurs at the air-electrolyte interface, and the lamella's meniscus plays an important role in shaping the tip (the length of the cone and the aspect ratio). Although this method is known to yield tips of similar quality to the previous approach, it is significantly more time-consuming. This is because the lamella breaks several times during the etching process, so it has to be reprepared from time to time. This also implies that constant monitoring is required till the end of the etching process. However, this process is beneficial for preparing spin-polarized tips out of Chromium rods, which tend to etch from the bulk instead of the surface. As a test, the method in the previous section was applied to prepare Cr tips, and it could be seen visually that the end of the tip was blunt. Following the etching of the tips, they are cleaned using DI water followed by the in-situ treatment discussed in the previous section. Figure 2.8 shows a spin-polarized $\mathrm{d}I/\mathrm{d}U$ map acquired on Fe bilayer on W(110) showing a spin spiral state, obtained using a bulk antiferromagnetic Cr tip prepared by the lamella method. The red and sky blue stripes depict the spin spiral state as demonstrated by Meckler *et al.* [70].

2.3 Sample preparation

STM is a highly surface-sensitive technique demanding an atomically smooth surface to obtain the best results. Since the quantum phenomena of quasiparticle tunneling from the tip to the sample and vice versa occur on a length scale of a few angstroms, any surface roughness of a similar scale arising from poor sample preparation or contaminants on the surface could be extremely detrimental to scanning and spectroscopy. Therefore, it is important to prepare atomically flat and contaminant-free surfaces. The following subsections present an overview of the different sample preparation methods employed to obtain high-quality samples.

2.3.1 Cleaving of $\mathrm{Pb}_{1-x}\mathrm{Sn}_x\mathrm{Se}$ single crystals

The $\mathrm{Pb}_{1-x}\mathrm{Sn}_x\mathrm{Se}$ single crystals used in our experiments were provided by collaborators from the Institute of Physics and International Research Centre MagTop, Institute of Physics, Polish Academy of Sciences. The samples obtained are air-exposed so they are heavily contaminated, hence unsuitable for scanning in their as-obtained form with surface-sensitive techniques like STM, which demands ultra-clean and atomically flat surfaces to achieve the best results. To successfully perform

STM measurements on these crystals, a fresh contaminant-free surface needs to be exposed in the ultrahigh-vacuum environment. To accomplish this the single crystal of $\mathrm{Pb}_{1-x}\mathrm{Sn}_x\mathrm{Se}$ was fixed with low-temperature compatible silver paste (EPO-TEK H20E Electrical Conducting Adhesive Two-part) on the Omicron sample plate. In the next step, a 7 mm long stainless steel rod was fixed on the top of the crystal with a vacuum-compatible resin (Torr Seal low vapor pressure resin sealant). After this, the sample was inserted into the load lock and pumped for several hours until the pressure reached the 10^{-10} mbar range. Then the sample was transferred to the sample storage of the STM chamber, where the sample, along with the cleaving rod, faces downwards. At this point, the cleaving step was performed at room temperature with the help of the wobble stick. Firstly, the rod was grabbed with the pincer grip and pushed against the closed end of the sample garage with sufficient force till the rod was knocked off the sample. By doing this, a fresh surface free from contaminants, with optically visible flat sample regions, was exposed. The optically flat sample regions are important for the safe approach of the STM tip and for performing the measurements smoothly. The sample was immediately inserted into the STM to cool down and perform subsequent measurements. It is worth mentioning that, since $\mathrm{Pb}_{1-x}\mathrm{Sn}_x\mathrm{Se}$ single crystals are 3D in nature, several trials of cleaving were required before a reasonably flat surface could be identified using the optical camera installed in the STM chamber.

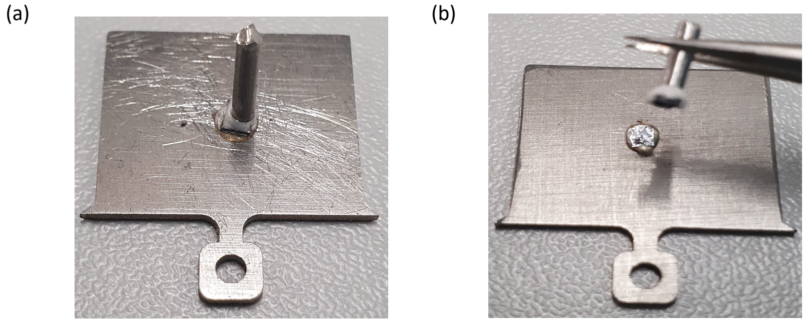

Figure 2.9: (a) Rod fixed to a sample on an Omicron-style sample plate. (b) After cleaving the sample using a tweezer, the shiny surface of the crystal is visible.

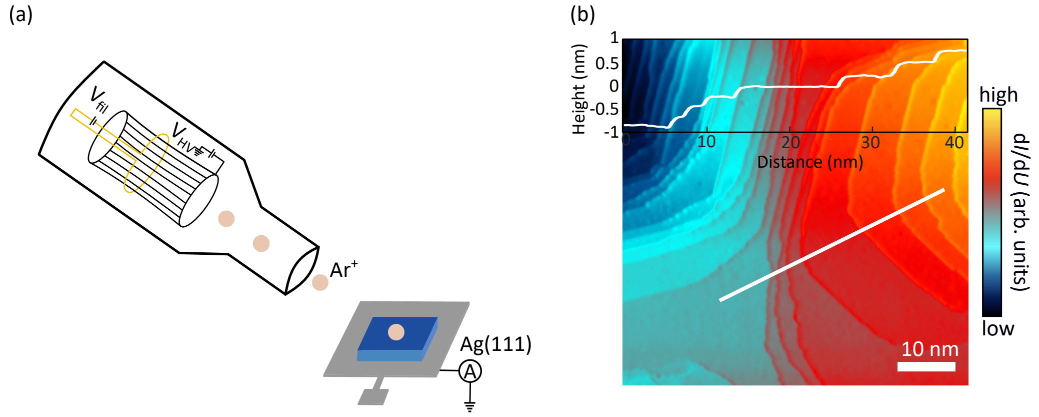

Figure 2.10: (a) Schematic of the sputtering setup. (b) Topography of an Ag(111) surface just after sputtering, revealing numerous steps separated by narrow terraces.

2.3.2 Sputtering and Annealing

It is well known that the surface of noble metals like Au(111), Ag(111), and Cu(111) can be prepared by bombarding the surface with Argon ions, followed by a subsequent annealing step. The process of bombarding the surface with argon ions to remove contaminants such as C, CH, O, etc. is known as sputtering. This method has been applied to prepare the Ag(111) surface for tip conditioning. Additionally, this method can be applied to prepare the surface of certain single crystals to investigate the electronic properties by performing quasiparticle interference (QPI) measurements. This section provides a brief overview of the sputtering-annealing process. In sputtering, the vacuum chamber is initially filled with Ar gas from a bottle of compressed gas ($Westfalen$ UN 1950 aerosol Argon 5.0) via a DN16CF flange until its partial pressure reaches $p_{Argon} = 3 \times 10^{-6}$ mbar. Next, the Ar atoms in the chamber are ionized by a commercial sputter gun from $SPECS$ (IQE 11/35). The sputter gun contains a Yttrium-coated Iridium filament that emits electrons, which are accelerated by a high voltage (up to 3kV) anode cage. These electrons ionize the Ar atoms, which go on to bombard the metal surface due to their kinetic energy. The sample position is adjusted a priori to ensure the direct impact of the ion beam on the sample. The sample must be grounded during the process of sputtering to prevent it from getting charged, which, if not done, results in ineffective sputtering. Figure 2.10a shows a schematic illustration of the sputtering setup. The sputter-

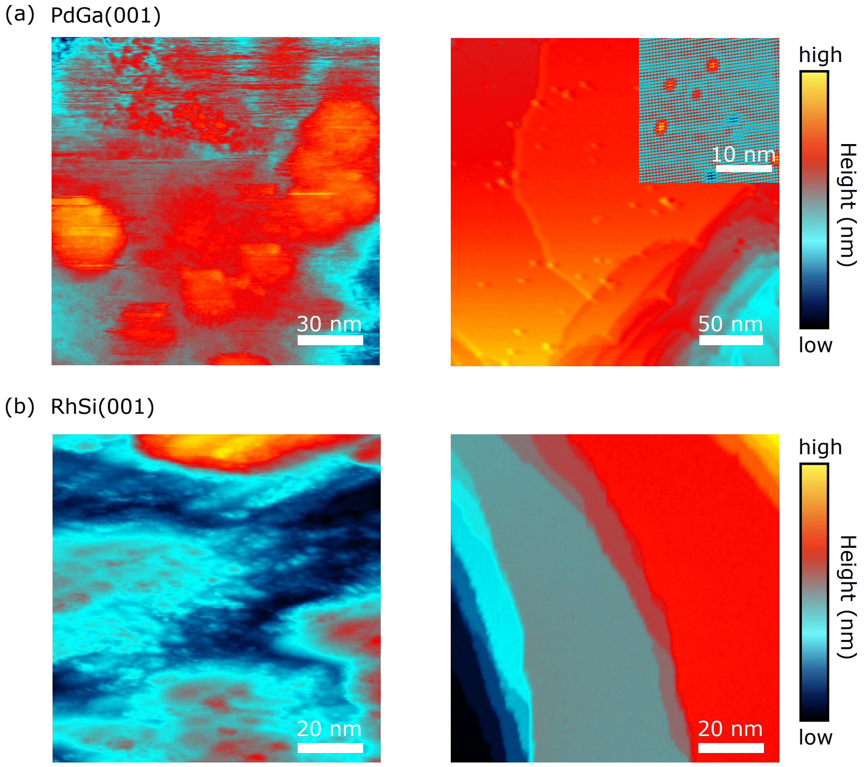

Figure 2.11: (a) STM topography of PdGa(001) single crystal, left panel: after 2 cycles of sputtering and annealing showing a rough and contaminated surface, right panel: after 15 cycles of sputtering and annealing depicting a clean surface with step edges and terraces. Inset shows an atomically resolved image acquired on the terrace. (b) STM topography of a RhSi(001) single crystal, left panel: after few cycles of sputtering and annealing showing a contaminated surface, right panel: after 60 hours of sputtering and annealing revealing a clean surface with flat terraces and step edges.

ing process on metal surfaces is usually carried out for 40 minutes - 1 hr, however, depending on the type of crystal, the duration needs to be optimized. Figure 2.6 depicts the topography of an Ag(111) surface post-sputtering. As evident from the topographic image, the sputtering removes the contaminants from the surface. This surface polishing effect creates a series of steps on the surface separated by small terraces. It is possible to enlarge the terraces by annealing the sample at a certain temperature post-sputtering. Annealing the sample causes the step edges to merge, thereby causing the terraces to become wider and flatter. For preparing the Ag(111) surface, the crystal was annealed at T = 300 °C for 20-30 minutes. Post-annealing flat and clean terraces are obtained, similar to the ones shown in figure 2.7b,c. This sputtering-annealing procedure was also used to prepare single crystals of semimetals such as PdGa(001) and RhSi(001). Figure 2.11 demonstrates the effectiveness of this surface preparation method. The left panel of figure 2.11a shows the STM topography of a PdGa(001) single crystal after a few sputtering-annealing cycles. As can be seen, the surface is rough and covered by contaminants (blood-orange patches). The right panel of figure 2.11a displays the PdGa(001) topography after 15 cycles of sputtering-annealing, demonstrating a substantially cleaner surface exhibiting flat terraces and step edges. The same holds for the RhSi(001) single crystals, which also reveal step edges and contaminant-free terraces after numerous sputtering-annealing cycles (see figure 2.11b).

2.3.3 Molecular Beam Epitaxy

Molecular Beam Epitaxy (MBE) is a highly versatile and precise technique for growing epitaxial thin films and heterostructures of different materials, including semiconductors, metals, insulators, 2D ferromagnetic semiconductors, 2D superconductors, and even organic molecules, with atomic layer control [71]. This growth technique plays a crucial role in materials science and nanotechnology, enabling the fabrication of high-quality materials for a wide range of applications, from microelectronics and optoelectronics to spintronics and quantum computing [72].

Figure 2.12a shows a schematic illustration of the MBE setup with all its essential components such as a vacuum chamber, a rotatable sample stage with a heater for heating the substrate, effusion cells for evaporating the materials, RHEED gun and a fluorescent screen, a mass spectrometer to detect the different gases as well as molecular species, an ion gauge to determine the pressure in the chamber and cryo panels which function as cold traps to adsorb the residual gases and unwanted molecules to prevent them from re-evaporating and contaminating the growth chamber. MBE works typically at a base pressure of $<10^{-10}$ mbar, which helps to reduce contaminants and ensures the growth of high-purity samples. The growth process involves the deposition of elements or molecular species evaporated from an effusion cell or an e-beam evaporator, forming atomic or molecular beams that impinge on a pre-heated substrate. As this beam arrives at the surface of the substrate, it migrates

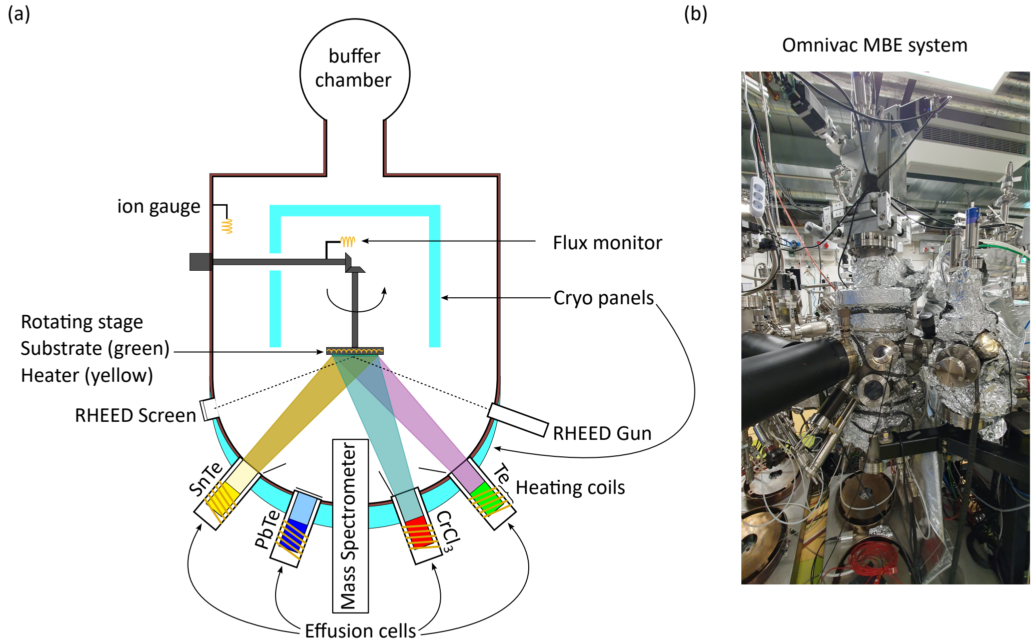
(a)
buffer chamber
ion gauge
Flux monitor
Cryo panels
Rotating stage
Substrate (green)
Heater (yellow)
RHEED Screen
RHEED Gun
SnTe
PbTe
Mass Spectrometer
CrCl$_3$
Te
Heating coils
Effusion cells
(b)
Omnivac MBE system

Figure 2.12: (a) Schematic illustration of a MBE setup highlighting the different components. (b) In-house MBE setup from Omnivac used to grow the CrCl$_3$/NbSe$_2$ samples.

across it and forms atomic layers, leading to highly crystalline thin films. The term “epitaxial” suggests that materials grow on the substrate strictly following the lattice ordering of the substrate. MBE also allows for real-time control of the growth process using an in-situ surface diagnostic tool called Reflection high-energy electron diffraction (RHEED). The RHEED works on the principle of electron diffraction, forming streaky diffraction patterns on a fluorescent screen, which provides information on the surface structure, growth mode, and film quality. From the RHEED oscillations, one can also control the thickness of films down to a ML. The growth process in MBE can occur via different modes depending on how the deposited material and the substrate interact. The different modes are: the Frank-Van der Merwe, Stranski-Krastanov, and the Volmer-Weber [73]. The Frank-Van der Merwe growth mode involves the layer-by-layer growth of MLs, induced by the strong affinity of the adatoms to bond with the substrate. However, in the Volmer-Weber method, the adatoms have a strong affinity to one another, causing them to merge and form 3D islands directly on the substrate surface. In the Stranski-Krastanov growth mode, initially, layer-by-layer growth takes place until a transition to the formation of

3D islands occurs since the strain energy due to the lattice mismatch between the substrate and thin film becomes significant.

The $CrCl_3$/$NbSe_2$ samples investigated in chapter 6 were grown using a multiple source MBE chamber from OMNIVAC. An image of this chamber is shown in figure 2.12b. Initially, a $NbSe_2$ single crystal was cleaved in situ in the load lock of the MBE chamber at a base pressure of 5 x 10^{-10} mbar using the method described in the subsection 2.3.1 and immediately inserted into the main chamber. In the next step, the substrate was degassed slowly by switching on the heater while monitoring the pressure simultaneously, ensuring that the pressure remained within permissible limits. It has been observed that during degassing, the silver paste used to fix the substrate also degasses substantially, making it necessary to wait longer for the pressure to recover. The pressure in the growth chamber was mostly maintained in the low 10^{-9} mbar range during the degassing procedure. Once the substrate was degassed till 350 °C, the temperature was reduced to the growth temperature, 300 °C (previously optimized). For the deposition of $CrCl_3$, the anhydrous powder of $CrCl_3$ was loaded into a Knudsen cell (K-cell) and previously degassed. While the substrate temperature stabilized, the Knudsen cell was heated using a temperature controller to 380 °C at a rate of 19 °C/min. Once the substrate and the source temperature are stabilized, the growth is initiated by opening the shutter of the K-cell. The growth rate was previously calibrated by growing $CrCl_3$ on n-doped 6H-SiC(0001) substrate [74]. The calculated deposition time for ML $CrCl_3$ was 12 minutes, so the K-cell was switched off accordingly, and the substrate was cooled to room temperature. No post-growth annealing was required. Once the sample cooled down to room temperature, it was immediately transferred using an ultra-high vacuum suitcase to the low-temperature STM chamber to avoid any surface contamination.

Part III

Probing interaction effects in a Topological Crystalline Insulator

3 Pathway to Topological Crystalline Insulator

This chapter establishes the theoretical framework for topological crystalline insulators (TCIs) by tracing their conceptual development from fundamental discoveries – including the quantum Hall effect (QHE), quantum spin Hall effect (QSHE), $\mathcal{Z}_2$ topological insulators, and 3D topological insulators – with particular emphasis on the TCI system $Pb_{1-x}Sn_xSe$.

3.1 Quantum Hall Effect

The band theory of solids acts as an effective tool to distinguish between different types of insulators based on their electronic band structure. Ordinary insulators, for example, are characterized by a bulk band gap separating the conduction and valence bands. However, tuning the band structure, for example, by introducing strong SOC can lead to the emergence of different types of insulators. More than a decade ago, it was proposed by Kane and Mele [2] that the incorporation of spin-orbit interactions in a single layer of graphene generates a topologically distinct state from its 2D semimetallic state. The duo considered a model developed by Haldane [75] in graphene, that breaks $\mathcal{T}$ symmetry under the application of a magnetic field which has a net zero flux through the unit cell of the graphene lattice. This resultant state was intriguingly gapped in the bulk but featured the transport of charge and spin currents along the sample's edges, whose directionality was locked to the spin. The formulation of such edge currents was previously theoretically carried out by Halperin [76] in the early 1980s, however unlike Haldane, Halperin considered a

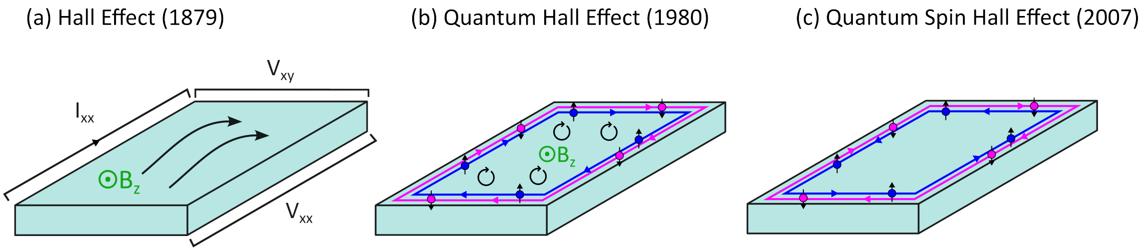
(a) Hall Effect (1879)
(b) Quantum Hall Effect (1980)
(c) Quantum Spin Hall Effect (2007)
V$_{xy}$
I$_{xx}$
⊙B$_z$
V$_{xx}$
⊙B$_z$

Figure 3.1: Schematic illustration of the (a) Hall Effect, (b) Quantum Hall Effect, (c) Quantum Spin Hall effect.

strong magnetic field perpendicular to the 2D surface.

Considering the case of the ordinary Hall effect, when a small perpendicular magnetic field is applied to a sample carrying current along the x direction (I_{xx}), the electrons are deflected to one side of the sample due to the Lorentz force. Due to this, the electrons get collected at the side of the sample, causing a charge accumulation that leads to a potential difference V_{xy} across the sample termed as Hall voltage, as shown in figure 3.1a. According to the formulation of classical mechanics, these electrons at the edges of the sample are static . The dynamics of these edge electrons was accounted for, in the phenomenal discovery of the Noble prize-winning QHE by Klaus von Klitzing [77] (figure 3.1b) in 1980, where he discovered that a 2D electron gas when subjected to extreme quantum conditions i.e., a high magnetic field and low temperature, exhibits quantized Hall resistance given by $\sigma_{xy} = e^2/h$. The QHE, the quantum counterpart of the classical hall effect (as shown in figure 3.1a) was described as electrons moving in quantized circular orbits at a cyclotron frequency $\omega_c = \frac{eB}{m}$ in the presence of a perpendicular magnetic field. The quantization of the electron's orbits forms quantized energy levels, known as Landau levels with an energy $\epsilon_l = \hbar\omega_c(l + \frac{1}{2})$. As the magnetic field is tuned, due to the quantization, some of the Landau levels are filled while the rest are empty. These Landau levels can be interpreted as filled and unfilled bands of a band insulator with a gap in the spectrum separating the filled ones from the empty ones. Unlike an ordinary insulator, the gapped quantum hall state (QHS) is characterized by the emergence of gapless conducting states localized at the edges of the sample. The emergence of this gapless conducting state can be understood in the following manner: due to

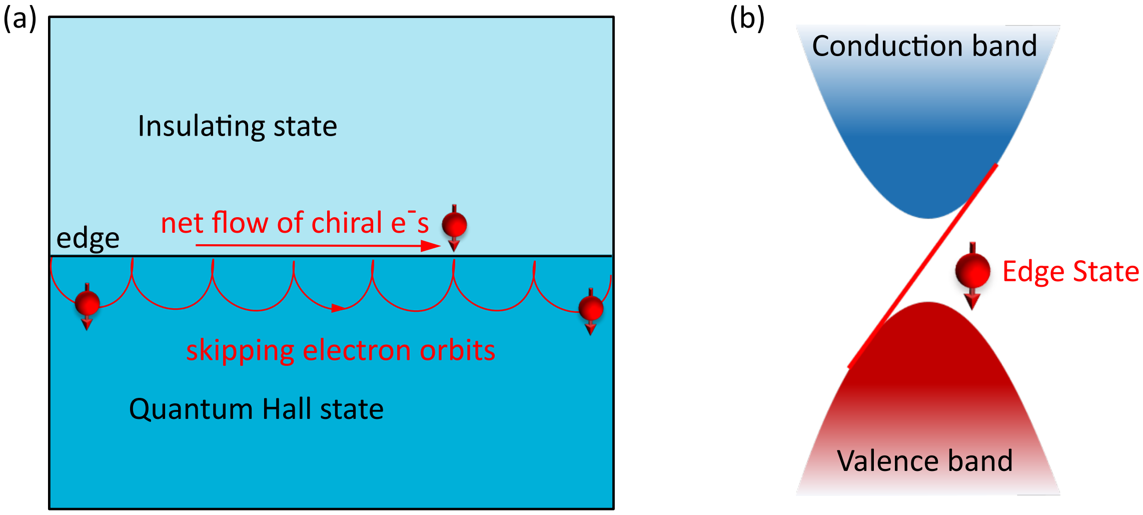

Figure 3.2: Geometry to realize the QHE considering (a) a semi-infinite strip with skipping electron orbits along the edge. (b) A single-edge state with a distinct chirality connects the bulk bands.

the magnetic field while the electrons at the center of the sample form closed orbits (figure 3.1b), the electrons near the edges bounce off, forming skipping orbits (figure 3.2a). These electrons at the edge, which propagate in a skipping orbit give rise to a continuous flow of edge currents as depicted in figure 3.1b. These edge states have a particular chirality that is determined by the direction of the applied field. Intriguingly, these chiral edge states are insensitive to disorder, since there are no available states for the electrons to backscatter.

It has been proposed in Haldane's model [75], that one can theoretically obtain the chiral edge states by solving a particular model for the case of graphene that considers a semi-infinite geometry similar to the one shown in figure 3.2a. The figure shows an edge at y = 0. The fundamental idea is centered around crossing a phase boundary, which in this scenario implies transitioning from the sample's central region, through its edge, and into the insulating vacuum, as illustrated in figure 3.2a. While the center of the sample is in the QHS, the vacuum behaves like an insulator. In 1982, Thouless, Kohmoto, Nightingale, and den Nijs [1] demonstrated that each of these gapped phases can be characterized by a distinct topological invariant known as the TKNN invariant (or Chern number), denoted by the integer n. This invariant is defined as the integral of the Berry curvature [78] across the

Brillouin zone, which for the model Hamiltonian $\mathcal{H}(\vec{k}) = \vec{h}(k) \cdot \vec{\sigma}$ defined for the case of Graphene, can be rewritten as [79] :

$$n = \frac{1}{4\pi} \int d^2\mathbf{k}(\partial_{k_x}\hat{h} \times \partial_{k_y}\hat{h}) \cdot \hat{h} \tag{3.1}$$

since for the above Hamiltonian, the Berry flux is related to the solid angle subtended by $\hat{h} = \vec{h}/|\vec{h}|$. The observation of the edge modes is closely linked to the change in the TKNN invariant going from the $n = 1$ (QHS) to the $n = 0$ (insulating state), where the edge demarcates the two different regions. It is important to note that this Chern number transition is only possible if the contributions from the edge are accounted for. This leads us to the next question: How can the edge contribute? The edge contributes by closing the gap across this Chern number transition, manifesting as low-energy excitations within the bulk gap. These are the often-mentioned edge states in the QHE. One such edge state is sketched in figure 3.2b connecting the bulk conduction and valence band.

Bulk-Boundary Correspondence

From the preceding discussion, it becomes clear that the existence of these metallic edge states is intrinsically linked to the topological properties of the non-trivial bulk material. In essence, these robust SSs are a consequence of the bulk's topological order. Furthermore, while modifications to the Hamiltonian describing the surface can indeed alter the details of the edge state band dispersion and even lead to the emergence of multiple edge states [79], a fundamental constraint remains. Specifically, if one considers the number of edge modes propagating in opposite directions – say, n$_R$ moving right and n$_L$ moving left – their difference, Δn = n$_R$ - n$_L$ is not arbitrary. Instead, Δn is a fixed integer quantity that is fundamentally determined by a topological invariant characterizing the bulk material. This deep connection between the properties of the boundary and the topological characteristics of the bulk is a central theme in the field of topological physics, known as the bulk-boundary correspondence. It signifies that the edge states are not independent entities but rather are guaranteed to exist and possess specific properties due to the underlying topological nature of the bulk. One cannot describe the edge properties in isolation without considering the topological invariants that define the bulk phase. The presence and characteristics of the boundary states serve as a "fingerprint" of the bulk's topological order. For instance, a non-zero value of Δn directly indicates a topologically non-trivial bulk phase, and the magnitude of Δn often corresponds to the value of a specific bulk topological invariant (the Chern number). This correspondence is a powerful tool, allowing one to predict the existence and some properties of SSs simply by analyzing the topological invariants of the bulk material.

3.2 Quantum Spin Hall Effect

As discussed in the previous section, Haldane's model formulated the QHE considering a single layer of graphene with just broken $\mathcal{T}$symmetry but, Kane and Mele [2] based their model on a single layer of graphene in the presence of $\mathcal{T}$ symmetry and additionally incorporated spin-orbit interaction where the spin-orbit term is given by the Hamiltonian $\mathcal{H}_{SO}$:

$$\mathcal{H}_{SO} = \Delta_{SO}\,\Psi^{\dagger}\sigma_z\tau_z s_z\,\Psi \tag{3.2}$$

where Δ_{SO} determines the strength of the interaction, s_z is the Pauli matrix describing the electron spin, σ_z and τ_z describe the states at the graphene sublattice and the K points, respectively. As discussed in the literature [2], this model is equivalent to considering two identical entities of the Haldane model that interact via the spin-orbit term. The resultant effect is electrons with both up and down spins flowing in opposite directions along the boundary of the sample as shown in figure 3.1c. These spin entities come in time-reversed pairs (Kramers doublet), which protects them from back scattering as long as $\mathcal{T}$ symmetry is unbroken. In the presence of an electric field, since the Hall currents due to the up and down spin flow in opposite directions, the net Hall conductivity, σ_{xy} is zero, but there is a non-zero flow of quantized spin current given by, $J_x^{\uparrow} - J_x^{\downarrow} = \sigma_{xy}^{s}E_y$, where $\sigma_{xy}^{s} = e/2\pi$ is the

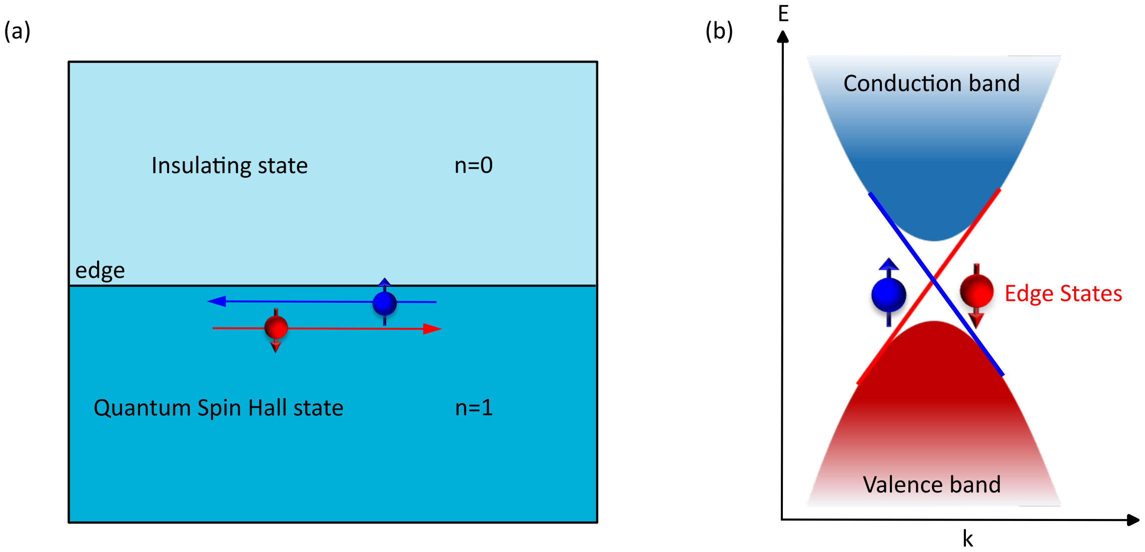

Figure 3.3: Geometry to realize the QSHE considering (a) a semi-infinite strip with electrons of both spin types flowing in opposite directions. (b) Linearly dispersing edge states of opposite chirality connecting the conduction and valence band.

hallmark QSHE. Like the QHS, the QSH state hosts gapless metallic edge states. Importantly, just like the QHE, the existence of these edge states in the QSHE is fundamentally tied to the nontrivial topology of its bulk electronic structure. Given that the topological invariant must also transition from a non-zero value (n=1 in the QSH state) to zero (in the insulating state), this change can only occur if the energy gap closes. This gap closing then manifests physically as low-energy excitations, which are precisely the gapless edge modes. Figure 3.3a depicts this schematically, showing counterpropagating edge states in a semi-infinite geometry, emulating the case of graphene [79]. Figure 3.3b shows the corresponding edge state dispersion with edge states of opposite chirality connecting the bulk bands. Notably, the discussion of the edge states in the QSHE involved only up and down spin electrons corresponding to the z component of the spin S_z, the quantity conserved here. Building upon the understanding of topological invariants and their connection to edge states, Kane and Mele further demonstrated in subsequent work [6] that the edge states in the QSHE possess remarkable robustness, even when spin conservation is not strictly enforced. This resilience arises due to the presence of $\mathcal{T}$ symmetry. A key characteristic of these QSH edge states is their helical nature: electrons with opposite spin orientations propagate in opposite directions along the edge. This spin-momentum locking, or helicity, ensures that backscattering is strongly suppressed, mirroring the situation in the QHE where chiral edge states are not allowed to backscatter. Moreover, through the application of symmetry arguments, Kane and Mele also showed that these helical QSH edge states are topologically protected against localization, even in the presence of significant non-magnetic disorder [2]. This protection stems from the fundamental topological properties of the bulk material, reinforcing the concept of bulk-boundary correspondence.

The QSHE was first experimentally demonstrated in HgTe/CdTe quantum wells by König *et al.* [5], marking a significant advancement in topological materials. This work confirmed theoretical predictions that strong SOC could drive a band inversion, producing helical edge states protected by $\mathcal{T}$ symmetry. The observation of a quantized conductance plateau ($2e^2/h$) at zero magnetic field, unaffected by non-magnetic disorder, provided definitive evidence of the QSH state. These results further established HgTe as the first 2D $\mathcal{Z}_2$ TI, laying the foundation for exploring $\mathcal{T}$ symmetry-protected topology in broader material systems.

3.3 $\mathcal{Z}_2$ Topological Insulators

The discussion of the QSHE motivates a deeper examination of $\mathcal{T}$ symmetry for spin-1/2 particles, which underpins the $\mathcal{Z}_2$ classification of TIs. The $\mathcal{Z}_2$ invariant—taking values 0 (trivial) or 1 (nontrivial), distinguishes these phases by counting the number of Kramers pairs of edge states modulo 2. For such systems, the time-reversal operator Θ satisfies $\Theta^2 = -1$, a signature property of fermionic systems with half-integer spin [80]. This constraint enforces Kramers' degeneracy: every eigenstate of a $\mathcal{T}$-symmetric Bloch Hamiltonian $\mathcal{H}(\mathrm{k})$ must have a degenerate partner at $\mathcal{T}$ invariant momenta. The Hamiltonian obeys $\Theta\mathcal{H}(\mathrm{k})\Theta^{-1} = \mathcal{H}(\text{-k})$, leading to a topological classification where phases with the same $\mathcal{Z}_2$ invariant can be adiabatically connected without closing the bulk gap. For a 2D insulator protected by $\mathcal{T}$ symmetry, the existence of edge states depends on the Hamiltonian's boundary conditions [79].

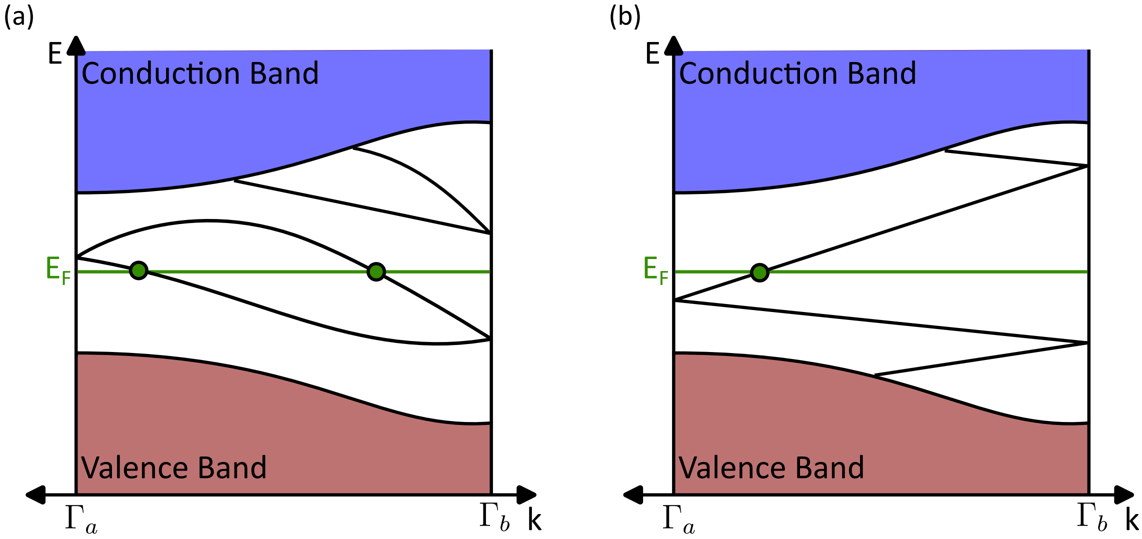

Figure 3.4: Schematic illustration of the electronic dispersion between two boundary Kramers degenerate points $\Gamma_a = 0$ and $\Gamma_b = \pi/a$. In (a) the number of SS crossing the E_F is even, whereas in (b) it is odd. An odd number of crossings leads to topologically protected metallic boundary states. Figure adapted from ref. [79].

However, when present, Kramers' theorem guarantees that these edge states appear in degenerate pairs at $\mathcal{T}$ invariant momenta, $k_x = 0$ and $k_x = \pi/a$ as depicted in figure 3.4. The figure displays one half of the Brillouin zone(0 < k$_x$ <π/a); the other half (-π/a < k$_x$ <0) is related by $\mathcal{T}$ symmetry. While the edge states remain degenerate at $\mathcal{T}$ invariant momenta points, SOC lifts this degeneracy elsewhere in the Brillouin zone. This leads to two distinct scenarios depending on how the edge states at $\Gamma_a = 0$ and $\Gamma_b = \pi/a$ connect. As shown in figure 3.4a, they can connect in pairs, thereby obliterating the edge states by pushing the bound states outside the gap. In this case, the bands cross the E_F between $k_x = 0$ and $k_x = \pi/a$, an even number of times which is the case of a trivial insulator. In the other case as shown in figure 3.4b, the edge states connect in a sawtooth-like trajectory between the two boundary kramers degenerate points, crossing the E$_F$ an odd number of times, corresponding to the case of the 2D $\mathcal{Z}_2$ TI.

Following the pioneering observation of the QSHE effect in HgTe/CdTe quantum wells, which provided the first experimental confirmation of a 2D $\mathcal{Z}_2$ TI phase, subsequent studies have identified this topological state in several other material systems. These include InAs/GaSb quantum wells [81], bismuthene monolayers on

SiC substrates [12], and more recently in the van der Waals compound β-BiBr [82], significantly expanding the family of 2D $\mathcal{Z}_2$ TIs.

3.4 3D Topological Insulators

The QSH insulator features edge states in the 2D limit characterized by a single $\mathcal{Z}_2$ invariant that distinguishes the trivial insulator (n = 0) phase from the QSH insulator (n = 1) phase. This concept naturally extends to three dimensions through four $\mathcal{Z}_2$ invariants $(\nu_0; \nu_1, \nu_2, \nu_3)$, which collectively distinguish between trivial insulators, weak topological insulators, and strong topological insulators. The theoretical foundation for this classification was established in 2006 through independent work by several groups [13–15, 83]. In 3D, the topological insulating phases are characterized by metallic SSs. These SSs can be represented in the momentum space by 2D crystal momentum. Contrary to a 2D $\mathcal{Z}_2$ TI, the 3D TI features 4 $\mathcal{T}$ invariant momenta on the surface Brillouin zone labelled as $\Gamma_1, \Gamma_2, \Gamma_3, \Gamma_4$ (as shown in figure 3.5a and b). As illustrated in figure 3.5a,b, if a surface state is located at any of these points, it will be doubly degenerate (marked by the pink dots), obeying Kramers' theorem. Interestingly, these surface state crossings form 2D Dirac cones at the Kramers' degenerate points. As one moves away from these special points, the spin-orbit interaction splits the degeneracy, similar to the 2D $\mathcal{Z}_2$ TI case.

Qualitatively, the 3D TI can be viewed as a three-dimensional extension of the QSH insulator, constructed by stacking multiple layers of the 2D QSH insulator. This results in the spin-momentum locked edge states in the QSH insulator evolving into 2D SSs. Going back to the discussion on weak 3D TIs, figure 3.5a shows one possible surface Fermi contour corresponding to a weak 3D TI. As can be seen, a single surface band intercepts the E_F between the $\mathcal{T}$ invariant momenta Γ_1 and Γ_2, and Γ_3 and Γ_4. This is equivalent to the scenario of a $\mathcal{Z}_2$ TI, where a single topological edge state crosses the E_F between Γ_a and Γ_b as illustrated in figure 3.4b. A 3D representation of this would be the weak TI characterized by the $\mathcal{Z}_2$ invariant

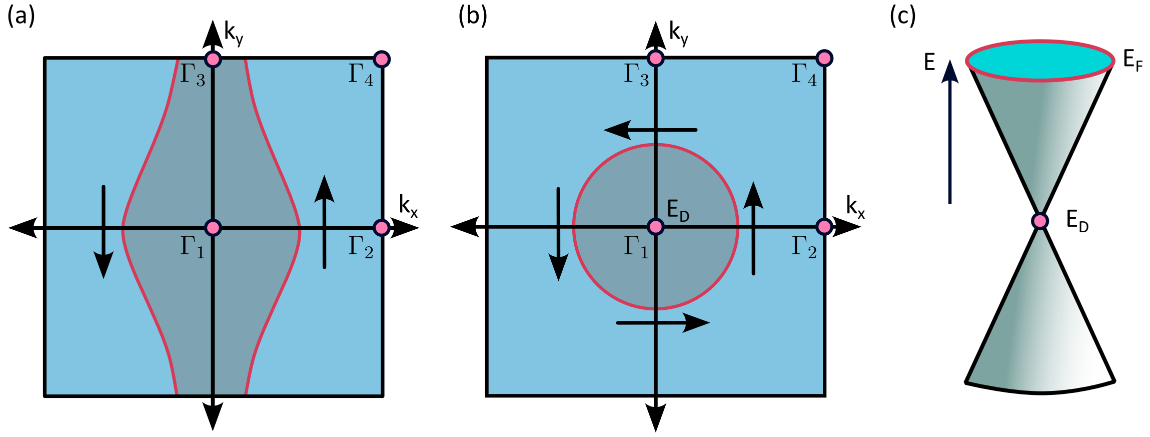

Figure 3.5: Schematic illustration of the Fermi circles in the surface Brillouin zone for (a) a weak topological insulator and (b) a strong topological insulator. (c) A single Dirac cone where the Fermi surface encloses the single Dirac point E_D, the simplest case of a strong topological insulator. Figure adapted from ref. [79].

$\nu_0 = 0$. The term weak stems from the fact that, unlike the 2D helical edge states in the QSH insulator, the SSs here are not protected by $\mathcal{T}$ symmetry [13]. However, the strong TI phase characterized by $\nu_0 = 1$ is not just a simple extrapolation of the 2D QSH to the 3D space. The topological invariant ν_0 plays an important role here as it counts the number of Karmers degenerate points enclosed by the Fermi surface. For the strong TI, as shown in figures 3.5b and 3.5c, an odd number (one in the case shown here)of Kramers degenerate Dirac points is enclosed by the surface Fermi circle. It has been shown that the Hamiltonian corresponding to a massless Dirac fermion on the 2D surface can be written as [37]:

$$\mathcal{H}_{surface} = -i\hbar v_F \sigma.\nabla \tag{3.3}$$

where σ is the Pauli spin matrices and v_F is the Fermi velocity. In contrast to a conventional metal, where every point of the Fermi surface consists of a degenerate distribution of both up and down spins, the SSs of a 3D TI are non-degenerate, displaying a helical spin-momentum locking. As illustrated in figure 3.5b, the electron spins are locked perpendicular to their momentum, resulting in a particular spin texture that winds around the Fermi surface. This spin texture is a direct consequence of strong SOC and $\mathcal{T}$ symmetry protection, distinguishing 3D TI SSs from ordinary

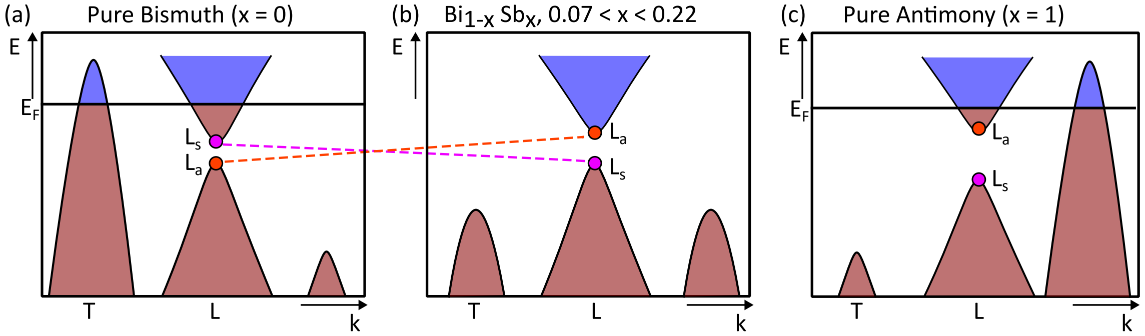

Figure 3.6: Schematic illustration of the band structure of $Bi_{1-x}Sb_x$ as it transforms from the (a) semimetallic state for pure Bi, to the (b) semiconducting state for 0.07 < x < 0.22 and back to the (c) semimetallic state for x > 0.22. Figure adapted from ref. [79].

metallic states. Similar to the QSH insulator, the SSs in the 3D TI are also pretty robust to disorder and protected from backscattering. It has been shown by Nomura *et al.* [84] that these SSs resist localization even under the strongest of perturbations as long as the bulk band gap remains intact, which is ensured by the π Berry phase acquired by the massless Dirac fermions as they encircle the Dirac point. It has been shown that this π Berry phase leads to a negation of the localization effects, causing a logarithmic increase in the conductivity [85], however, the SS transport differs fundamentally from the ballistic edge channels of 2D TIs, exhibiting instead a diffusive regime.

Experimental Discovery of 3D TIs

The first 3D TI phase was discovered in a semiconducting alloy, $Bi_{1-x}Sb_x$ in angle-resolved photoemission spectroscopy (ARPES) experiments. Bi is a semimetal and a material with large SOC, which is believed to have an indirect negative band gap [86]. Figure 3.6a shows a schematic of the band structure of pure Bi, where the valence and conduction band emanating from the antisymmetric (L_a) and symmetric (L_s) orbitals features a small band gap Δ. It has been shown that near the L points the bands mimic a linear dispersion characterized by a (3+1)-dimensional Dirac equation [87]. However, at a critical concentration of Sn doping (x $\sim$ 0.4), the band structure can be manipulated so that the band gap Δ at the L points closes, giving rise to a massless 3D Dirac fermion. As shown in figure 3.6b, with a gradual increase

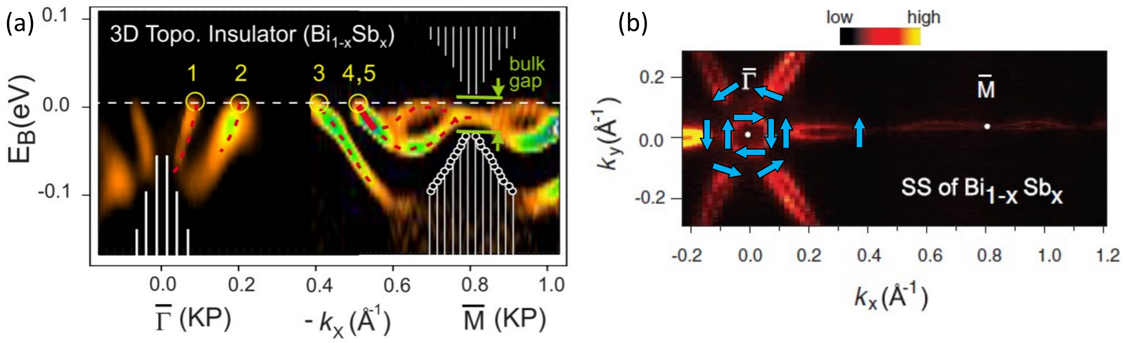

Figure 3.7: (a)Second derivative of the intensity describing the surface state dispersion of $Bi_{0.9}Sb_{0.1}$ along the $\bar{\Gamma}\bar{M}$. The red dotted lines indicate the SS that intersect the Fermi surface. The yellow circles indicate the Fermi crossings of the SSs. Here, the number of SSs crossing the Fermi surface between $\bar{\Gamma}$ and $\bar{M}$ is five. The odd number of crossings is a signature of the topologically non-trivial nature of the SSs. (b) Fermi surface contour featuring a vortex-like spin texture around the Γ point. Experimental evidence of the π Berry phase was obtained from Fermi-surface data. Reprinted parts (a) and (b) from ref. [16], Springer Nature Limited.

in the the Sn concentration *i.e.*, $x > 0.07$, the parity of the orbitals at the L points are reversed, and the valence band at the T point lowers below the conduction band at the L point, turning the material into an insulator. As the concentration of Sn increases further, at $x \sim 0.09$, the valence band at T goes below the valence band at L, forcing the material to feature a direct band gap with massive Dirac-like bulk bands. At higher Sn concentrations, $x > 0.22$, the valence band at a different high symmetry point shoots above the conduction band minima at the L point, restoring the semimetallic nature. Hsieh *et al.* [16] first demonstrated the 3D TI phase in $Bi_{0.9}Sb_{0.1}$ which is an insulator in the bulk. In figure 3.7a, the second-derivative of the intensity describing the surface state dispersion has been depicted, which shows 5 SSs (red dashed line) crossing the Fermi surface (yellow circles) between the high-symmetry points $\bar{\Gamma}$ and $\bar{M}$. This odd number of band crossings that is related to the $\mathcal{Z}_2$ topological invariant (as discussed in section 3.3) indicates that the gapless SSs are topologically non-trivial. These observations established $Bi_{0.9}Sb_{0.1}$ as a strong spin-orbit coupled topological insulator with $\nu_0 = 1$, featuring an odd number of Dirac cones. Following the experimental discovery of the 3D TI phase, the spin texture of the SSs was also measured using ARPES. Hsieh *et al.* [88] measured

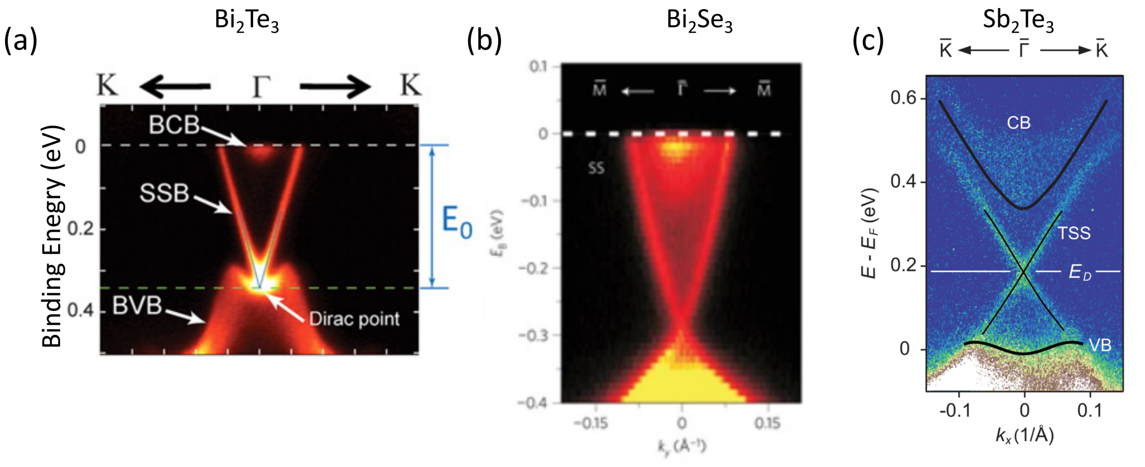

Figure 3.8: (a) Observation of Dirac cone from APRES measurement for (a) Bi_2Te_3, (b) Bi_2Se_3 and time-resolved ARPES for (c) Sb_2Te_3. Part (a) reprinted with permission from AAAS ref. [17]. Parts (b) reprinted from ref. [18], Springer Nature Limited. Part (c) adapted from ref. [89].

the spin polarization of the SSs, which strongly ascertains their spin-polarized and nondegenerate nature. As illustrated in figure 3.7b, the spin texture of the SS shows the spins rotating by 2π around the center Fermi surface, providing the first experimental evidence of the π Berry phase as theoretically predicted. Another important aspect of the SS of a 3D TI *i.e.* protection from backscattering was also established in $Bi_{0.92}Sb_{0.08}$ by combining STM/STS and ARPES techniques [90]. The successful demonstration of the 3D TI phase in $Bi_{1-x}Sb_x$ was extended to the chalcogenide family, including Bi_2Se_3 (figure 3.8b), Bi_2Te_3 (figure 3.8a) and Sb_2Te_3 (figure 3.8c). Unlike $Bi_{1-x}Sb_x$, the this family of 3D TIs was shown to possess a single Dirac cone located at the $\bar{\Gamma}$ point of the surface Brillouin zone with a rotating spin polarization around the Fermi-surface [17–19, 91]. Additionally, from the reports mentioned above, it was ascertained that the topological nature of these materials is associated with a band inversion induced by strong SOC at the Γ point of the bulk Brillouin zone. In the case of Bi_2Te_3, which possesses a smaller band gap (0.15 eV) as compared to Bi_2Se_3 (0.3 eV), it has been shown that the surface behaves differently from a conventional 3D TI. Both ARPES and STM/STS measurements have revealed a hexagonal warping of the SSs attributed to the low band gap and a strong trigonal potential [17, 92, 93].

3.5 Topological Crystalline Insulators

The previous sections dealt with topological edge or SSs in 2D and 3D TIs protected by $\mathcal{T}$ symmetry. It is important to note that the different symmetries play a crucial role in generating new topological states of matter. Hence the discovery of the topological insulating state and the role of the $\mathcal{T}$ symmetry cultivated the interest in exploring other symmetries like the particle-hole symmetry [94–96], known to give rise to the topological superconducting phase [34, 97] or the translation symmetry of spins giving rise to the magnetic topological insulating phase [98, 99]. In 2011, Liang Fu proposed that incorporating crystal symmetries, such as the mirror or rotational symmetry, could lead to a completely different topological class. He termed this new topological class as a topological crystalline insulator (TCI) [20] where the crystalline symmetries offer topological protection to the SSs. Unlike the TI, the TCI surface state can be easily destroyed if the crystal is distorted or has low symmetry, since the topology relies solely on the crystallographic symmetries. This also means that a TCI cannot be adiabatically connected to an atomic insulator solely by preserving the $\mathcal{T}$ symmetry because gradually removing atoms from a crystal to form an atomic insulator would mean breaking the crystalline order. Therefore, to understand the role of crystalline symmetries, initial theoretical works focused on the study of 3D model systems with 4-fold (C_4) or 6-fold (C_6) rotational symmetry [20]. Using the tight-binding formalism, the energy bands of electrons occupying the p- and d-orbital were derived for a tetragonal lattice with a unit cell consisting of two unique sites A and B (figure 3.9). It followed from the tight binding calculations [20] that the (001) surface, which preserves C_4 symmetry features doubly degenerate metallic surface states as depicted in figure 3.10b. The double degeneracy follows from the contributions arising from both the p_x and p_y orbitals at the high symmetry point $\overline{\mathrm{M}}$. The initial model used by Liang Fu did not consider SOC, however, the prediction of the TCI phase was done in a particular crystal with high SOC, which is discussed later in this section. In the model adopted by Fu [20], the presence of

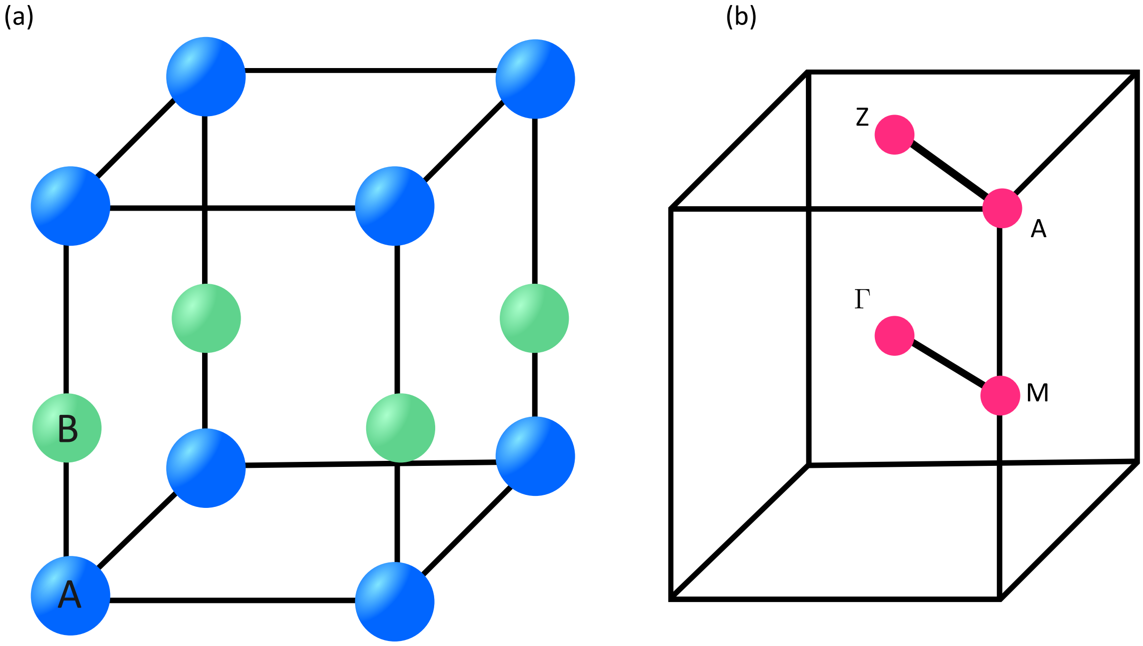

Figure 3.9: (a) Tetragonal lattice consisting of two unique lattice points A and B in the unit cell along the c-axis, (b) Brillouin zone corresponding to the lattice along with the high symmetry points at which the SSs are predicted to exist. Figure adapted from ref. [20].

$\mathcal{T}$ symmetry combined with C_4 symmetry renders these doubly degenerate SSs on the (001) surface to be topologically protected. Therefore, these SSs between two high symmetry points can connect in two possible ways, crossing the E_F either an even or an odd number of times. This follows from a similar discussion of weak and strong 3D TIs in the previous section. An even number of band crossings of the SSs suggests they are weakly protected as they can be easily pushed outside the bulk band gap by tuning the surface chemical potential. However, the same is not possible when the SS intercepts the E_F an odd number of times. As previously shown in the schematic in figure 3.5b,c the surface Fermi circle encloses an odd number of Dirac points. For the 3D TIs, these corresponded to the case of a strong TI. In the present case of a TCI, the odd number of SS crossings itself implies that they are topologically protected. The presence of these two types of crossing of the SSs corresponds to two topologically distinct phases, under the class of $\mathcal{T}$ invariant insulators with C_4 symmetry. Similar to the 2D and 3D TI characterized by a $\mathcal{Z}_2$ invariant, it was shown that the 3D $\mathcal{T}$ invariant insulators with C_4 symmetry can be defined by the topological invariant ν_0 and the gapless SSs on the (001) surface of these 3D band

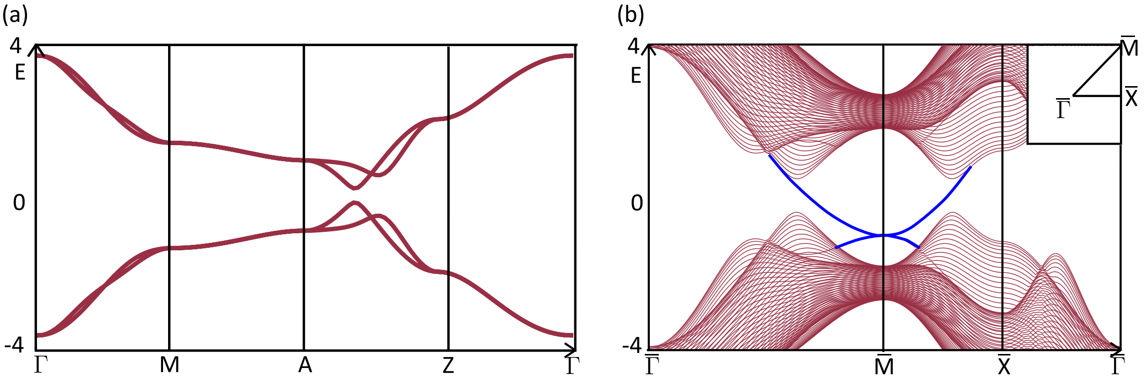

Figure 3.10: Schematic illustration (a) of the bulk bands derived from tight binding calculations along high symmetry directions corresponding to the tetrahedral lattice, (b) of the SSs (blue curves) on the (001) surface touching one another in a quadratic fashion. Figure adapted from ref. [20].

insulators have $\nu_0 = 1$.

Development of the TCI material class

Shortly after the discovery of the TCI phase for a generalized 3D tetrahedral lattice with $\mathcal{T}$ and C_4 symmetry, Hsieh *et al.* theoretically proposed the TCI phase in the semiconductor tin-telluride (SnTe) [21]. SnTe has a rocksalt structure with an interpenetrating lattice of Sn and Te as shown in figure 3.11a. It is an intermixing of a face-centered and body-centered cubic lattice. The 3D Brillouin zone corresponding to the SnTe lattice is sketched in figure 3.11b, resembling a truncated octahedron with 6 square faces and 8 hexagonal faces. It is a narrow band gap semiconductor where the band gap occurs at the center of the 8 hexagonal faces of the bulk Brillouin zone, which are the L valleys in the bulk Brillouin zone [100]. This implies that the conduction band minima and the valence band maxima occur at these L points. Since the SnTe crystal has inversion symmetry, each L point and its diagonally opposite L point are equivalent, leaving 4 unique L point momenta as depicted in figure 3.11b. Similar to conventional semiconductors, since Sn is more electropositive than Te, it is expected that the p-orbitals of Sn would contribute to the conduction band, whereas the p-orbitals of Te atoms contribute to the valence band, however, as demonstrated by electronic band structure calculations [21], the orbital nature of the cations and anions are reversed due to a band inversion at the conduction and valence band

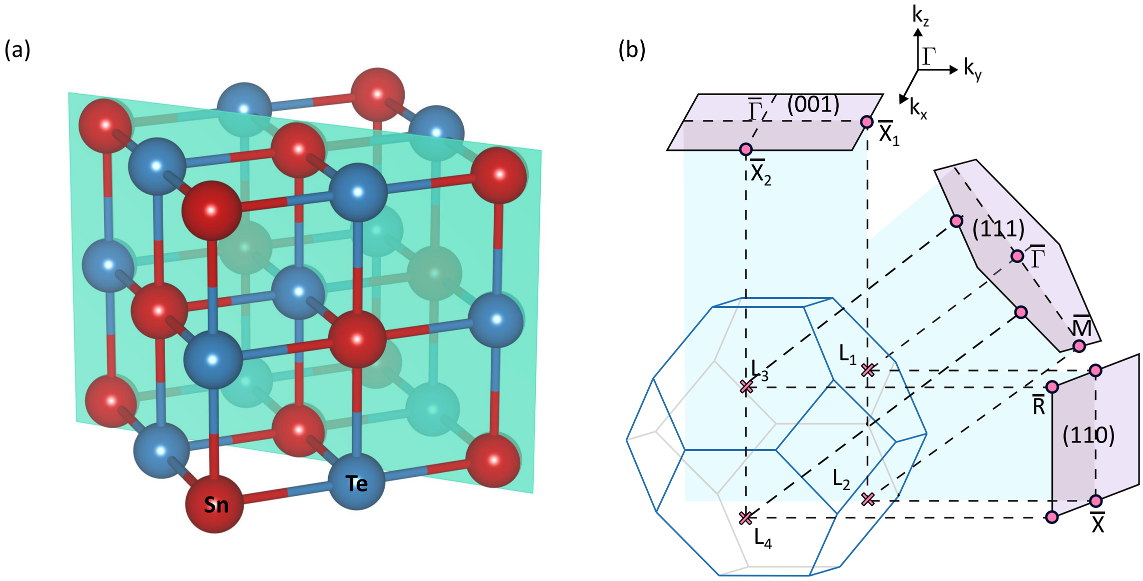

Figure 3.11: (a)Face-centered cubic structure of SnTe with Sn and Te atoms marked in red and blue, respectively. The plane shown in shamrock green corresponds to the $(1\bar{1}0)$ mirror plane. (b) Schematic illustration of the bulk Brillouin zone of the SnTe crystal structure along with its projections onto the (001), (111), and (110) surface Brillouin zones. L_1, L_2, L_3, and L_4 denote points in the bulk Brillouin zone at which the bulk semiconducting gap is located. For the (001) surface, the L_1 and L_2 are projected onto the $\overline{X}_1$ point located at the edge of the surface Brillouin zone, while points L_3 and L_4 are projected onto the $\overline{X}_2$ point. For the (111) surface, L_1 point is projected onto the $\overline{\Gamma}$ point while the L_2, L_3, and L_4 points are projected onto 3 different $\overline{M}$ points. For the (110) plane, L_1 and L_2 points are projected onto the $\overline{X}$ point while L_3 and L_4 points are projected onto the $\overline{R}$ point. The shaded blue planes are the mirror planes in momentum space for the respective surface terminations. Part (b) adapted from ref. [101].

edge [100]. A similar semiconductor in the same group, PbTe, possessing the same crystal structure as that of SnTe, is known to exhibit a normal band ordering where cationic orbitals from Pb contribute to the conduction band while the anionic ones from Te contribute to the valence band [102]. A schematic illustration of the above as obtained from first-principle electronic calculations has been sketched in figure 3.12, where it can be seen that on going from PbTe to SnTe, there is a parity reversal at the L point [21]. This also means that the band inversion occurs at all 4 unique L points in SnTe, indicating an even number of band inversions.

In the previous section on 3D TIs, it was emphasized that an odd number of band inversions driven by spin-orbit interactions is an essential factor for establishing the $\mathcal{Z}_2$ topological phase which means that in the present case, SnTe with an even

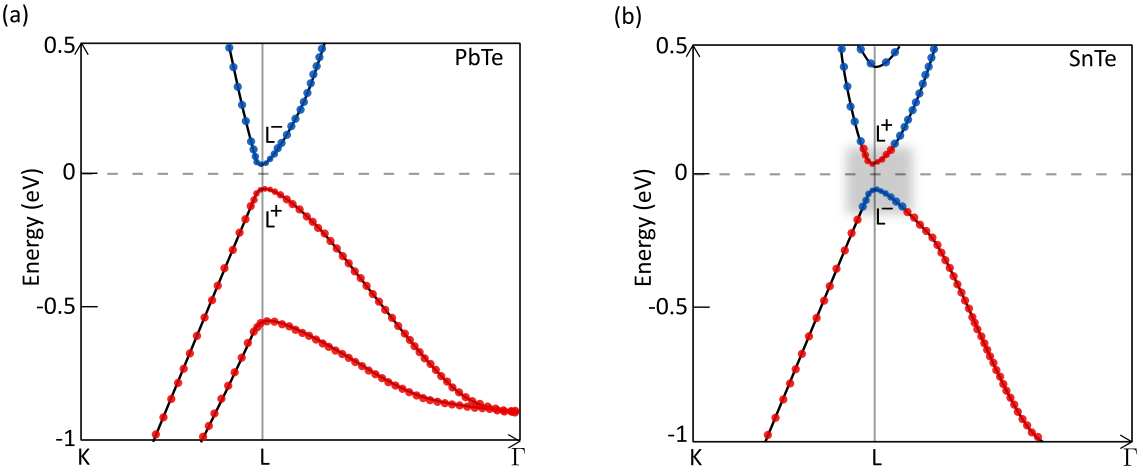

Figure 3.12: Schematic illustration of the electronic band structure of (a) PbTe exhibiting a normal ordering of the band structure where the L^- and L^+ states contribute to the conduction and valence band respectively, (b) SnTe where the shaded portion in grey indicates the region of the band inversion shown as a reversal of the role of the electronic states at the L point ($\mathrm{L}^+ \rightleftharpoons \mathrm{L}^-$). Figure adapted from ref. [21].

number of band inversions is not expected to be a $\mathcal{Z}_2$ TI in nature. However, it has been shown by Hsieh *et al.* that by invoking crystalline symmetries, which in this case is the mirror symmetry of SnTe's face-centered cubic lattice, an even number of band inversions can drive the system into the topological phase. It has been suggested that the set of {110} mirror planes in the real space (illustrated in shamrock green in figure 3.11a) has an important role to play here for there exists a plane $\Gamma\mathrm{L}_1\mathrm{L}_2$ (figure 3.11b) in the momentum space defined by the high symmetry points Γ, L_1 and L_2 on which the crystal momenta are invariant under reflection about the set of {110} mirror planes [21, 101, 103]. This establishes $\Gamma\mathrm{L}_1\mathrm{L}_2$ plane as the momentum space mirror invariant plane[1]. Previously, it has been demonstrated by Teo *et al.* [104] that for mirror symmetry invariant systems a characteristic invariant could be defined i.e. the Chern invariant $n_{\pm i}$. Under the mirror operation denoted by $\mathcal{M}$ where obeys the condition, $\mathcal{M}^2$ = -1 corresponding to spin 1/2 electrons, the Bloch wave functions on the mirror-invariant plane can be defined by the eigenvalues of $\mathrm{M} = \pm i$ namely, Ψ_{+i} and Ψ_{-i}. It is then possible to associate each wave function with the Chern invariant, $n_{\pm i}$. The difference of this Chern invariant defines a new topological invariant, which defines the mirror-invariant topological class, known as the mirror Chern number, $n_M = n_{+i} - n_{-i}$. The quantity n_M carries the same weightage as that of the $\mathcal{Z}_2$ invariant in 2D or 3D TIs. Just like the non-zero $\mathcal{Z}_2$ invariant gaurantees that any $\mathcal{T}$ invariant system is in the 2D or 3D TI phase, similarly a non-zero n_M ensures that any system characterized by mirror symmetry is in the topological crystalline insulating phase. To determine the mirror Chern number and establish that SnTe is a TCI, Hsieh *et al.* [21] and others [101, 103] solved the *k.p* Hamiltonian below:

---

[1] By similar arguments $\Gamma\mathrm{L}_3\mathrm{L}_4$ plane is another momentum space mirror invariant plane

$$H = m\sigma_z + v(k_1 s_2 - k_2 s_1)\sigma_x + v_3 k_3 \sigma_y \tag{3.4}$$

which has previously been established to determine the band structure of a crystal at the L point [105]. Here k_1, k_2, k_3 are a set of orthogonal coordinates in the momentum space where k_1 is perpendicular to the 110 mirror plane and k_3 is along the line joining the Γ and L point; v denotes the group velocity of the quasi-particles, $\sigma_z = \pm 1$ represents the p-orbitals from the cation (Pb or Sn) and anion (Te respectively) that contribute to the band and s_3 is the total angular momentum along the ΓL line. s_1 and s_2 are the angular momentum in the direction orthogonal to the ΓL line. The factor m in the Hamiltonian determines the ordering of the bands, where a positive m corresponds to normal band ordering, while a negative m corresponds to a switching of the cation and anion character at the conduction and valence band, indicating a band inversion. Solving the Hamiltonian above for the mirror invariant plane $\Gamma L_1 L_2$ corresponding to $k_1 = 0$, revealed that the mirror Chern number changes by 1 due to the band inversion at one of the L points in the mirror-invariant plane. A second L point within the $\Gamma L_1 L_2$ plane, where another band inversion occurs, contributes an additional change of 1 to the mirror Chern number. Therefore, for the $\Gamma L_1 L_2$ plane, the net contribution to the change in the Chern number from both L_1 and L_2 points is 2 in this case. Additionally, it has been demonstrated by Teo *et al.* that the sign of the Chern number is negative, which establishes that n_M = -2 for SnTe. Furthermore, from first-principle calculations [21] it was also shown that the band gap of SnTe varies monotonically with the lattice constant, where with decreasing lattice constant the band gap undergoes a transition from positive to negative values, passing through a zero band-gap point. The zero point crossing indicates that the band structure of SnTe undergoes a topological phase transition where the negative band gap region corresponds to the topologically non-trivial phase and establishes SnTe as a TCI with n_M = -2. As mentioned before, PbTe with a normal band ordering (m>0) being a trivial band-gap insulator has $n_M = 0$, hence proving that PbTe and both SnTe belong to unique topological classes.

The non-zero n_M of SnTe can have a significant impact on its electronic properties depending on the different surface terminations as theoretically demonstrated first by Hsieh *et al.* [21] and later by Liu *et al.* [101] and Wang *et al.* [103]. This motivated the theoretical study of the electronic properties of different surface terminations of SnTe that are expected to exhibit topological SSs owing to the non-zero n_M, provided these surfaces are mirror-invariant about the $\{110\}$ mirror plane. An inspection of the face-centered cubic structure of SnTe reveals that there exists 3 such surface terminations that respect the mirror symmetry about the $\{110\}$ mirror planes: the (001) surface termination which is mirror symmetric about two of the $\{110\}$ planes (plane shown in shamrock green in figure 3.11a and the plane perpendicular to it); the (110) surface which is mirror symmetric about the $\{1\bar{1}0\}$ mirror plane, and the (111) surface which is symmetric about three identical $\{1\bar{1}0\}$ mirror planes [21, 101]. Depending on the surface terminations, the different L points in the bulk Brillouin zone are projected to different or same $\mathcal{T}$ invariant surface momenta, namely, $\overline{\Gamma}$, $\overline{\mathrm{M}}$, $\overline{\mathrm{R}}$ and $\overline{\mathrm{X}}$. A description of these projections corresponding to the different surface terminations of SnTe is as follows: according to the schematic illustration of the SnTe Brillouin zone in figure 3.11b, it can be observed that for the (001) surface, the L_1 and L_2 points on the hexagonal face of the bulk Brillouin zone are projected onto the same $\mathcal{T}$ invariant surface momenta, $\overline{\mathrm{X}}_1$ point of the surface Brillouin zone. Similarly the L_3 and L_4 points are projected onto the same surface momenta $\overline{\mathrm{X}}_2$ which is related to $\overline{\mathrm{X}}_1$ by C_4 rotation about the (001) surface normal. For the (110) surface, the L_1 and L_2 points are projected onto the same $\mathcal{T}$ invariant surface momenta,

$\overline{\mathrm{X}}$ point of the surface Brillouin zone, while L_3 and L_4 points are projected onto the surface momenta $\overline{\mathrm{R}}$. For the (111) surface, the L_1 point is projected to the $\mathcal{T}$ invariant $\overline{\Gamma}$ point while L_2, L_3 and L_4 points are projected to 3 different $\mathcal{T}$ invariant $\overline{\mathrm{M}}$ points [21, 101, 106]. Liu *et al.* classified the SSs on the (111) surface as type-I and those on the (001) and (110) as type-II [101]. It was shown that the type-I SSs on the (111) surface can be obtained by simply solving the Hamiltonian in eq. 3.4 [101, 106]. This yields 4 Dirac cones on the (111) surface, located at unique surface momenta which are the surface projection of the 4 L points. In this case, the L valleys do not interact as the Dirac cones are projected to different surface momenta, and the in-plane translation symmetry prohibits them from doing so. On the other hand, for the type-II SSs on the (001) or (110) surfaces where the L points are projected onto the same in-plane surface momenta, it can be shown that one needs to consider interactions at the lattice scale between the different L valleys which can be accounted for by adding extra terms to the *k.p* Hamiltonian in eq. 3.4. In the context of the experimental results presented in the next chapter, only a qualitative derivation of the SSs on the (001) surface is outlined here. Detailed analyses of the (111) and (110) surfaces, which are outside the scope of this work, can be found in ref. [101, 106, 107].

Considering the invariance of the $\overline{\mathrm{X}}$ point on the (001) surface, under three point group operations, $\mathcal{M}_x$ (x → -x), $\mathcal{M}_y$ (y → -y) and C_2 (two-fold rotation about the surface normal) and the $\mathcal{T}$ operation Θ, it is possible to deduce the terms that describe the interaction between the L valleys at the lattice scale [101, 103]. On incorporating these terms in the *k.p* Hamiltonian in eq. 3.4, the resultant Hamiltonian describing the electronic structure at the $\overline{\mathrm{X}}$ for the (001) surface can be rewritten as:

$$H = (v_x k_x s_y - v_y k_y s_x) + m\tau_x + \delta s_x \tau_y \tag{3.5}$$

where the terms m and δ account for the interaction between the L valleys at the atomic scale. Before going on to describe the results of the Hamiltonian it is worthy

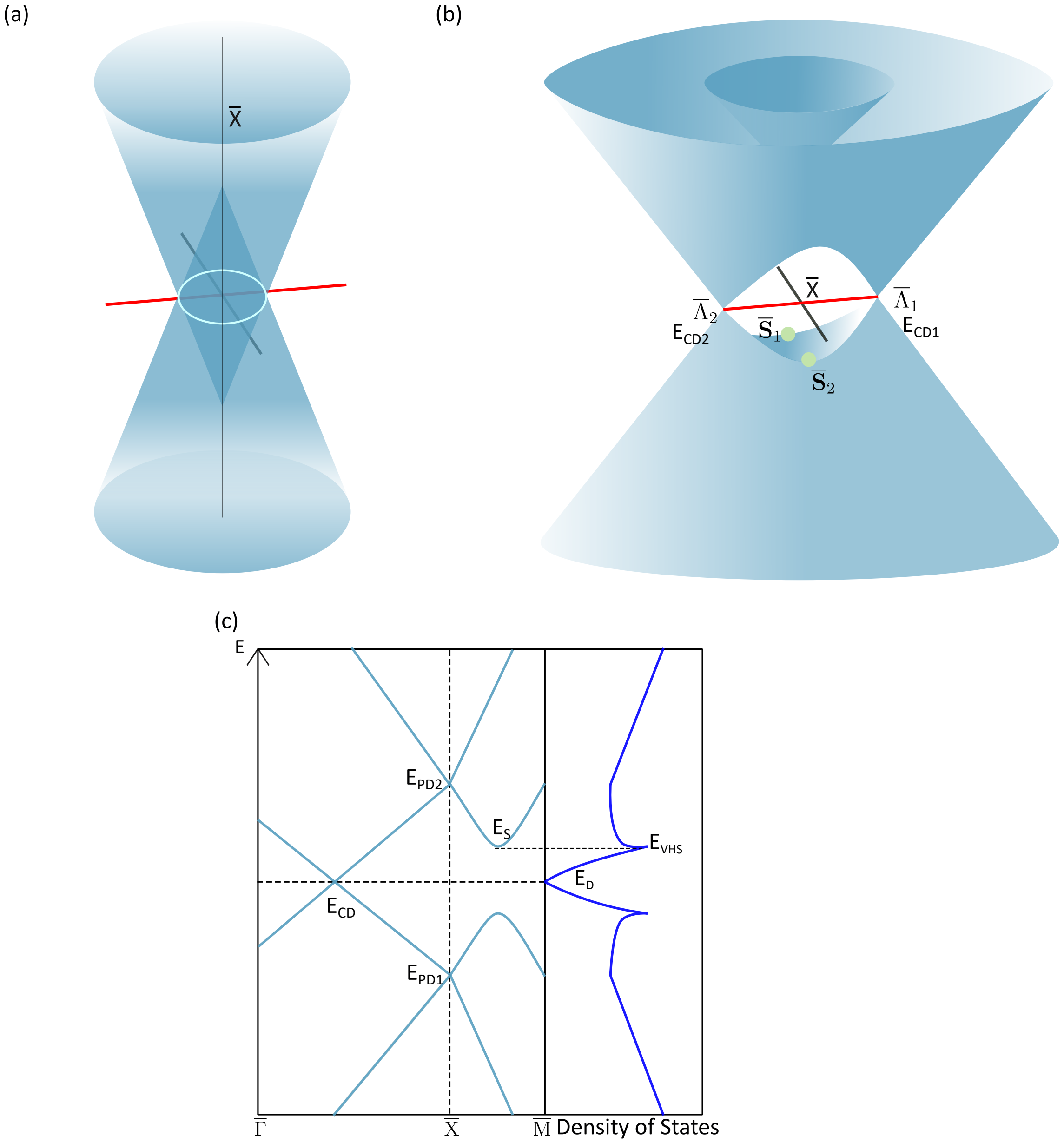
(a)
X̄
(b)
X̄
$\overline{\Lambda}_2$
E_{CD2}
$\overline{S}_1$
$\overline{S}_2$
$\overline{\Lambda}_1$
E_{CD1}
(c)
E
E_{PD2}
E_S
E_{VHS}
E_D
E_{CD}
E_{PD1}
$\overline{\Gamma}$
$\overline{X}$
$\overline{M}$
Density of States

Figure 3.13: (a)Schematic illustration of the band structure for the case where the parent Dirac cones do not interact. They intersect one another over an elliptical contour on the surface Brillouin zone, where the entire region within the elliptical region remains gapless. (b) Schematic illustration of the electronic band structure for the (001) surface depicting the low-energy child Dirac cones located at $\overline{\Lambda}_1$ and $\overline{\Lambda}_2$ on the surface Brillouin zone along the mirror line, formed out of the interaction between two high energy parent Dirac cones. Two saddle points S_1 and S_2 are also visible, located between the 2 child Dirac cones at energies close to the gap edge. (c) Energy dispersion showing one of the Dirac cones along $\overline{\Gamma}$-$\overline{X}$ while along $\overline{X}$-$\overline{M}$ the saddle points can be seen. The right side shows a plot of the DOS corresponding to the energy dispersion on the left, where at the energy of the child Dirac cone, there is a dip, and the saddle points lead to a Van Hove singularity on either side of the dip, which appear as kinks in the DOS. Parts (a) and (b,c) adapted from ref. [103] and ref. [101] respectively.

mentioning that the mirror plane in momentum space $\Gamma L_1 L_2$ (or $\Gamma L_3 L_4$) is projected on the (001) surface Brillouin zone along the $\overline{\Gamma}$-$\overline{X}_1$ (or $\overline{\Gamma}$-$\overline{X}_2$) direction. For simplicity, the $\overline{X}_1$ and $\overline{X}_2$ will be replaced by the generalized $\mathcal{T}$ invariant momentum $\overline{X}$. The line along the $\overline{\Gamma}$-$\overline{X}$, termed as the mirror line has a significant consequence since any set of Dirac cones that is present on this line is topologically protected by the mirror symmetry [21, 101, 103]. Therefore, on solving the Hamiltonian above, it was shown that there exists a pair of coaxial spin-polarized Dirac cones on the (001) surface along the mirror line $\overline{\Gamma}$-$\overline{X}$ originating from the crossing of two pairs of mirror SSs which are protected by the mirror symmetry and symmetrically separated about the $\overline{X}$ point as schematically illustrated in figure 3.13b. It is interesting to note that the crossing of the mirror SSs giving rise to the child Dirac cones originate from the interplay between two parent Dirac cones (located at the bulk L_1 and L_2 points) centered at the surface momenta $\overline{X}$ and separated in energy owing to their different band characters which are derived from either the Sn or Te atoms as sketched in figure 3.13b. In fact, it has been theoretically shown by Wang *et al.* that out of these two parent Dirac cones, the one with the Dirac point lower in energy has a Sn-like nature while the one higher in energy has a more Te-like character [103]. However, one should note that there exist two possibilities here, out of which only one is expected to capture the child Dirac surface bands: the first one, in which there is no interaction between the parent Dirac cones, and the other, in which the parent Dirac cones interact. First of all, when there are no interactions between the parent Dirac cones ($\delta = 0$), as shown in figure 3.13a, both the parent Dirac cones interpenetrate and cross one another over an elliptical contour in the surface Brillouin zone enclosing the $\overline{X}$ point and cutting the mirror line along $\overline{\Gamma}$-$\overline{X}$ only at two points located on either side of the $\overline{X}$ point. Between the two intersection points of the mirror line, the SSs are gapless in the entire elliptical region along the mirror line. It is therefore evident that in this case, the surface Dirac cones on the (001) surface cannot be obtained unless a gap opens over the elliptical contour. Consequently, it becomes important to consider the interactions between the parent

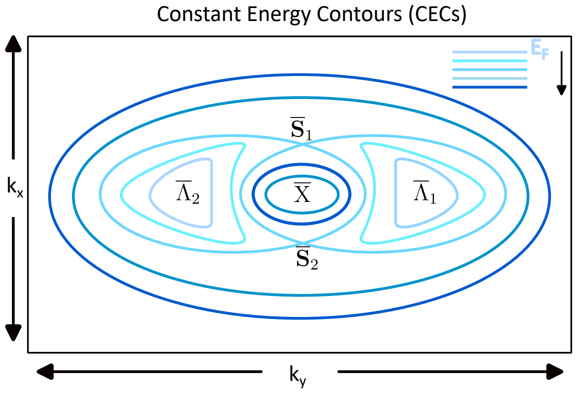

Figure 3.14: (a)Schematic illustration of the evolution of the constant energy contours undergoing a Lifshitz transition leading to a crossover from two disconnected energy pockets to a large hole pocket and a small electron pocket. Figure adapted from ref. [103].

Dirac cones ($\delta = 1$). As a result of the interactions, the SSs in the elliptical region where the two parent Dirac cones overlap become gapped, except at two points along the mirror line where the mirror symmetry prohibits the gap opening. These two points namely $\overline{\Lambda}_1$ and $\overline{\Lambda}_2$ host the mirror-symmetry protected child Dirac cones on the (001) surface as schematically illustrated in figure 3.13b. Figure 3.13c shows the energy dispersion of the (001) SnTe surface, where along the $\overline{\Gamma}$-$\overline{\mathrm{X}}$ line one of the child Dirac cones can be observed with the two aforementioned, parent Dirac cones located at the $\overline{\mathrm{X}}$ point. Since there are two $\overline{\mathrm{X}}$ points related to one another by C_4 symmetry, by solving the Hamiltonian and using similar arguments for the other, the $\overline{\mathrm{X}_2}$ point, it can be shown that there exists another pair of Dirac cones on the mirror line, $\overline{\Gamma}$-$\overline{\mathrm{X}}_2$ and symmetrically shifted about the $\overline{\mathrm{X}_2}$ point on the (001) surface of SnTe. This gives a total of 4 Dirac cones on the (001) surface of SnTe, which was an important discovery since, the even number of Dirac cones combined with the mirror symmetry of the (001) surface established that SnTe is a TCI with a non-zero mirror Chern number ($n_M = -2$).

Besides the discovery of the 4 Dirac cones on the (001) surface of SnTe, the theory also provided useful insights into the topology of the energy contours which were shown to evolve peculiarly as one goes away from the surface Dirac points towards higher and lower energies [21, 101, 103]. As sketched in figure 3.14, close to the E_F, the Fermi surface consists of two disconnected anisotropic Fermi pockets outside the $\overline{\mathrm{X}}$ point and centered about the $\overline{\Lambda}_1$ and $\overline{\Lambda}_2$ point. At energies lower than the E_F, the constant energy contour evolves, changing from two disconnected pockets to one large hole pocket and a small electron pocket centered at the $\overline{\mathrm{X}}$ point. This transition in the topology of the constant energy contours occurs via a Lifshitz transition where the disconnected pockets hybridize with one another leading to the saddle points $\overline{\mathrm{S}}_1$ and $\overline{\mathrm{S}}_2$ in the band dispersion. These saddle points occur along the $\overline{\mathrm{X}}$-$\overline{\mathrm{M}}$ where the surface band is gapped, leading to a divergence in the DOS at these points popularly known as Van Hove singularity as pictorially represented in figure 3.13c. which are known to play an important role in giving rise to interaction effects [108–110].

Based on the electronic band structure calculations, Wang *et al.* calculated the associated spin texture of the (001) surface Dirac cones [103]. For these calculations, the spin polarization of the different surface bands having a Sn or Te-like orbital nature was considered as qualitatively described below. Considering the upper cone region (conduction bands), it was shown that for the surface bands on the mirror line along $\overline{\Gamma}$-$\overline{\mathrm{X}}$ close to $\overline{\mathrm{X}}$ point, have a Te-like nature with spins rotating in a counterclockwise fashion. The region outside the $\overline{\mathrm{X}}$ point *i.e.* near the $\overline{\Lambda}_1$ and $\overline{\Lambda}_2$ point, the upper Dirac cones which have an Sn-like orbital nature, have spins rotating in a clockwise fashion. This leads to the scenario where the spin texture around the surface Dirac cones on the conduction band side is clockwise. On the valence band side of these surface Dirac cones, near the $\overline{\mathrm{X}}$ point, the orbital nature of the lower Dirac cones is Sn-like with a clockwise rotation of the spins while outside the $\overline{\mathrm{X}}$ point where the lower Dirac cones have a Te-like orbital nature, the spins rotate in a counterclockwise fashion. Consequently, both the lower surface Dirac cones in the valence band region have a counterclockwise spin texture. A schematic illustration of the preceding discussion showing the spin texture of the surface bands crossing at the $\overline{\Lambda}_1$ and $\overline{\Lambda}_2$ point is depicted in figure 3.15a. The discussion of the spin texture of the surface Dirac cones provides insight into the chirality of the Dirac cones. For

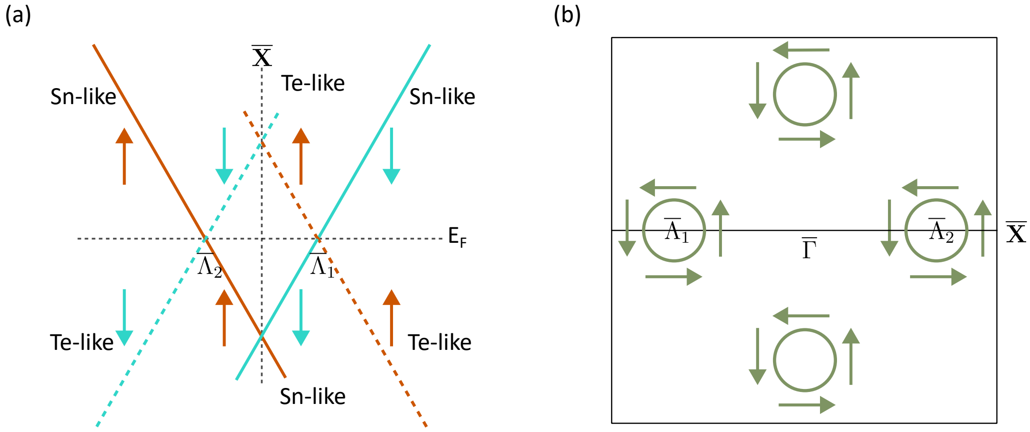

Figure 3.15: (a) Illustration of the spin-texture of the Sn and Te-like surface Dirac cones along the $\overline{\Gamma}$-$\overline{X}$-$\overline{\Gamma}$ direction displaying clockwise and counterclockwise rotation in the upper and lower Dirac cones, respectively. (b) Schematic of the spin texture for the lower Dirac cone showing a counterclockwise rotation corresponding to a mirror Chern number of -2. Figure adapted from ref. [103].

the (001) surface of SnTe, which features two pairs of Dirac cones, the spin texture reveals a counterclockwise rotation of the spins for all 4 Dirac cones, demonstrating a key point that all 4 Dirac cones on a TCI surface have the same chirality.

The theoretical prediction of the TCI phase by Hsieh *et al.* with an even number of Dirac cones on the (001) surface of SnTe was a phenomenal discovery, where combining topology with crystalline symmetries gave birth to this new topological state. However, it becomes much more captivating to observe these SSs in experiments and to be able to manipulate them, which could potentially lead to more practical applications. The first experimental realization of the TCI phase on the (001) surface of SnTe was performed by Tanaka *et al.* who synthesized SnTe single crystals and subsequently carried out ARPES measurements [22]. In their experiments, single crystals of SnTe were cleaved in situ exposing the (001) surface of SnTe and subsequent ARPES measurements revealed the existence of gapless SS crossings, mimicking a Dirac cone which was shifted from the edge of the surface Brillouin zone (referring to the $\overline{\Lambda}$ point). Furthermore, for comparison, ARPES measurements were also carried out on the trivial insulator PbTe, revealing the absence of any such gapless SSs, thereby providing strong experimental evidence of the well-established theoretical prediction that both SnTe and PbTe belong to two distinct classes. It is interesting to note that prior to the work by Tanaka *et al.*, photoemission studies on SnTe have been incapable of observing the surface Dirac surface bands owing to the formation of Sn vacancies on the surface, leading to a heavy p-doped nature of SnTe crystals [111]. As a result, the chemical potential was pinned deep inside the valence band, thereby not cutting across the SSs. This would imply that the potential SSs would be unoccupied, making them inaccessible for photoemission-based experiments, which heavily rely on the occupied electronic states. As mentioned in the study by Tanaka *et al.*, the Dirac SSs were closely aligned with the chemical potential, and, additionally, cleaving the sample led to Te vacancies causing a downward band bending, thereby making the Dirac SSs accessible. The type-I SSs on the (111) surface of SnTe were also experimentally demonstrated in ARPES measurements [112].

The theory by Hsieh *et al.* elegantly demonstrated the TCI phase and predicted mirror-symmetry-protected SSs in SnTe. Furthermore, it explored the impact of perturbations on the topological SSs, including strain or electric fields that break C_4 and mirror symmetries of the (001) surface. This would cause a structural distortion since the atoms would be displaced from their original positions. It has been shown that this distortion affects the surface Dirac cones inducing a gap opening in these gapless SS along one of the mirror lines while they remain intact along the other one and this would depend directly on the direction along which the distortion is applied [21, 113]. The opening up of a gap has been associated with the acquisition of a mass in the massless surface Dirac cones [21, 114]. Besides, SnTe is also known to readily undergo a rhombohedral distortion at low temperatures, exhibiting a ferroelectric behavior that has been demonstrated both theoretically and experimentally [21, 115, 116]. It has also been proposed that this gap opening in the presence of an applied magnetic field induces the Quantum Hall state in the SSs [21, 114]. From the above discussion, it is evident that there exist different ways in which the Dirac SSs can be tuned to realize novel phases suggesting the implementation of SnTe for device-based applications [117].

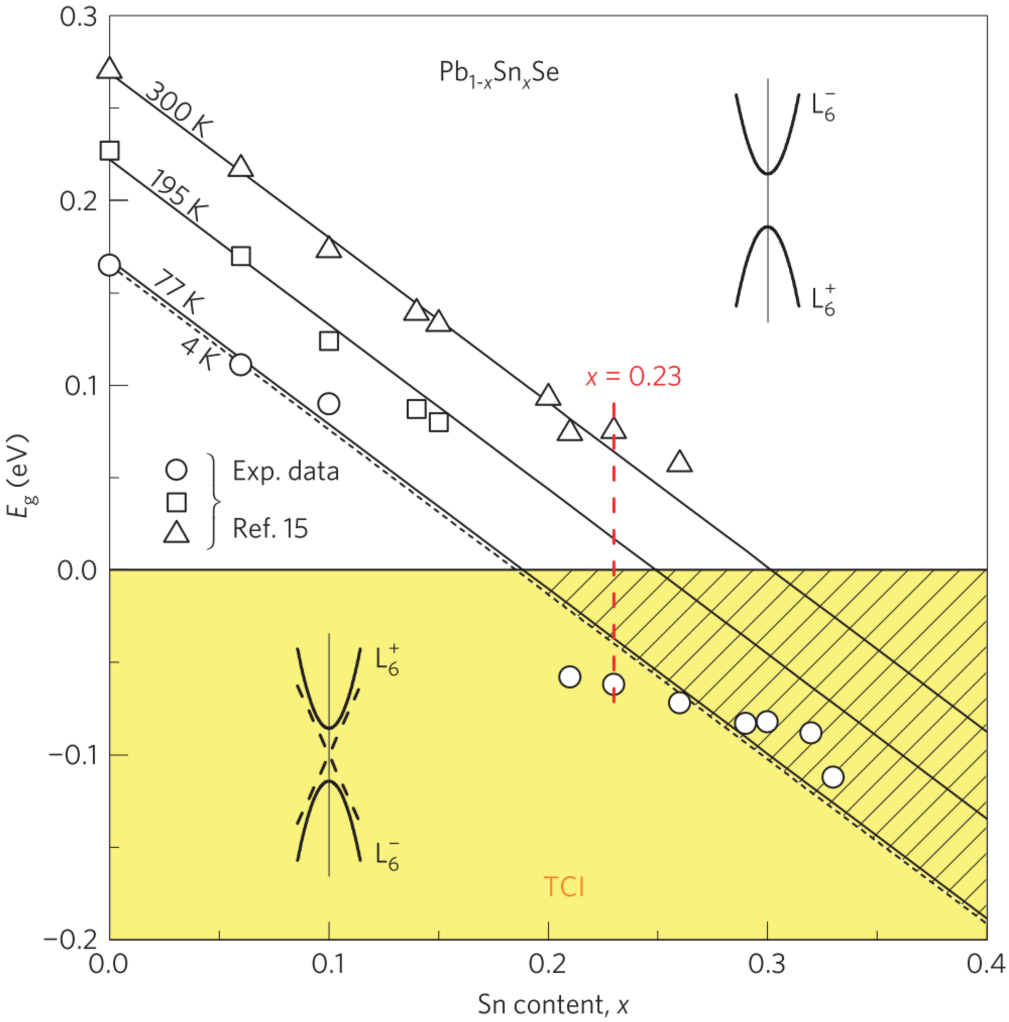

Figure 3.16: Evolution of the band gap for the substitutional alloy $Pb_{1-x}Sn_xSe$ at different temperatures. The white side is the region of the positive band gap or normal band ordering corresponding to the trivial insulator, like PbSe or PbTe. On the other hand, the region marked in yellow is the negative band gap region with a band inversion corresponding to a TCI. The lower right side of the diagram, with lines drawn across the yellow region, shows the composition range and temperature at which $Pb_{1-x}Sn_xSe$ is a TCI at ambient pressure. Figure reprinted from ref. [24], Springer Nature Limited.

Concurrent with the experimental discovery of SnTe as a TCI, broadening the TCI material class and addressing SnTe's heavy p-doping and ferroelectric transition (caused by structural distortion) were equally crucial. This demanded engineering new materials where the chemical potential can be easily tuned so that the Dirac SSs are occupied and the material is more resilient to structural distortion. It has long before been established that the ternary alloy formed by combining Pb, Sn, and Te (Se) yields the compound $Pb_{1-x}Sn_xTe$ (or $Pb_{1-x}Sn_xSe$) which is a narrow-gap band semiconductor with an inverted band gap at the L points [118–122]. These alloys are formed via a substitutional doping of Sn on the lattice sites of Pb in the trivial insulator PbTe (or PbSe), gradually replacing the Pb atoms as the concentration of Sn is progressively increased. The resultant compound comprises two sublattices *i.e.* Pb/Sn and Te (Se). Engineering the band gap by tuning the Pb/Sn ratio makes the inverted band gap phase accessible. This was shown using infrared absorption and p-n junction laser studies at different temperatures by A.J. Strauss [123]. This evolution of the band gap from the trivial to the TCI phase for $\mathrm{Pb}_{1-x}\mathrm{Sn}_x\mathrm{Se}$ is shown in figure 3.16 which highlights two regions one with a positive band gap (white) and the other with a negative band gap (yellow). It can be seen that at a lower composition of Sn, the alloy possesses a trivial band gap with a normal band ordering until the composition of the Sn reaches a critical value (x_c) at which the band gap closes and then reopens on further increasing the Sn concentration, inducing an inversion of the symmetry of the bands at the L point. Additionally, the study revealed that within a Sn concentration ranging between $\mathrm{x} = 0.18$ and $\mathrm{x} = 0.3$, the transition to the band inverted phase is driven by lowering the temperature from 300 K down to 4 K [24, 123]. It is important to note that below a Sn content of $\mathrm{x} < 0.4$, both $\mathrm{Pb}_{1-x}\mathrm{Sn}_x\mathrm{Te}$ and $\mathrm{Pb}_{1-x}\mathrm{Sn}_x\mathrm{Se}$ crystallize in the rock salt structure. Additionally, tuning the concentration to have an excess Pb content circumvents the problem of heavy p-doping in SnTe, shifting the chemical potential close to the conduction band minima so that the SSs are occupied. Band structure calculations performed on $\mathrm{Pb}_{1-x}\mathrm{Sn}_x\mathrm{Te}$ for different concentrations of Sn reveal a critical concentration of $\mathrm{x}_c = 0.381$ [24] to access the topological regime. For concentrations of Sn lower than x_c, the direct band gap was retrieved with a normal band ordering. In contrast, for $\mathrm{x} > \mathrm{x}\ _c$, the inverted band gap is obtained, which is expected to feature gapless states within the bulk bandgap along the mirror line $\overline{\Gamma}$-$\overline{\mathrm{X}}$. To experimentally demonstrate the presence of the topological SSs, Dziawa *et al.* synthesized $\mathrm{Pb}_{0.77}\mathrm{Sn}_{0.23}\mathrm{Se}$ ($\mathrm{x} = 0.23$) crystals and investigated the electronic properties of the (001) surface by ARPES at different temperatures [24]. Their photoemission measurements revealed both gapped and gapless SSs starting from T = 300 K down to T = 9 K. It was observed that the SSs transform from a gapped state to a Dirac cone-like SSs at temperatures below 100 K. This Dirac cone-like state associated with the child Dirac cones as previously discussed, became more prominent at T = 9 K. These Dirac cones were found to lie on the mirror line along $\overline{\Gamma}$-$\overline{\mathrm{X}}$, slightly shifted from the $\overline{\mathrm{X}}$ point whereas along any other direction, the SSs were found to be gapped at all temperatures.

Xu *et al.* demonstrated the TCI state by ARPES in the alloy, $\mathrm{Pb_{0.6}Sn_{0.4}Te}$ (x = 0.4), providing a comparison with the alloy $\mathrm{Pb_{0.8}Sn_{0.2}Se}$ [23]. For $\mathrm{Pb_{0.8}Sn_{0.2}Se}$, it was observed that the bands are gapped at E_F and there are no surface-state crossings at E_F. This implies that with a higher Pb content, $\mathrm{Pb_{0.8}Sn_{0.2}Se}$ has a normal band ordering with a band structure similar to that of the trivial insulator PbTe. However, for the alloy $\mathrm{Pb_{0.6}Sn_{0.4}Te}$, photoemission measurements at different photon energies were able to capture the SSs , which are symmetrically shifted from the $\overline{\mathrm{X}}$ point. Additionally, from their constant energy contour maps close to E_F they could image the first Brillouin zone which revealed 4 energy pockets, which is in line with the band inversion at the 4 L points in Pb_{1-x} $\mathrm{Sn}_x\mathrm{Te}$. From the spectroscopic mapping at different energies, they could experimentally demonstrate how the constant energy contours evolve from two disconnected energy pockets to a large and small energy pocket consistent with the theoretical prediction, as well as experimentally observed Lifshitz transition in the parent compound SnTe [21, 22, 101, 103]. Using spin-resolved ARPES measurements, it was shown that the SSs along the mirror line are spin-momentum locked with the spins polarized along the in-plane direction. In the out-of-plane direction, there was no spin polarization. This was found to be consistent with previous theoretical work on SnTe [103]. Additional comparison with the TI $\mathrm{GeBi_2Te_4}$, established the difference between the $\mathcal{Z}_2$ TI and TCI phase, where for the TI as expected, one single Dirac cone was located at the $\mathcal{T}$invariant momenta $\overline{\Gamma}$ due to a single (odd number in general) band inversion as opposed to $\mathrm{Pb_{0.6}Sn_{0.4}Se}$ where there is an even number of Dirac cones due to an even number of band inversions at the L points shifted away from the $\mathcal{T}$ invariant momenta $\overline{\mathrm{X}}$. Hence for the TI, the Fermi surface encloses the $\overline{\Gamma}$ point whereas for the TCI, it does not enclose any $\mathcal{T}$ momenta thereby also proving the insignificance of the $\mathcal{T}$ symmetry in the case of TCI where the surface state crossings are protected by the mirror symmetry. This provides additional evidence as to why the topological invariant for the $\mathcal{Z}_2$ TI does not act as a good Chern number, therefore demanding the invocation of the mirror Chern number as obtained from, theoretical predictions [21] and experimental demonstrations [19, 104].

The discovery of the TCI state in $\mathrm{Pb}_{1-x}\mathrm{Sn}_x\mathrm{Te}$ and $\mathrm{Pb}_{1-x}\mathrm{Sn}_x\mathrm{Se}$ opened a plethora of possibilities that were yet to be explored. Unlike ARPES, which requires precise alignment of the chemical potential with the Dirac SSs, STM, a surface-sensitive technique capable of probing both occupied and unoccupied states, does not rely on the electron occupation of the Dirac SSs. One such example is the study of quasiparticle scattering from the (001) SSs of p-doped SnTe nanoplates [124]. In these samples, the Dirac surface state was located 350 meV above the E_F, which could be directly observed in the LDOS measurements. LDOS mapping at different energies above and below the Dirac point energy revealed certain scattering patterns. The features observed in the fast-Fourier transform of these LDOS maps, which is a method to study QPI, were interpreted as arising from the scattering of the SSs among the Fermi pockets in the first Brillouin zone. Similar research work focused on investigating the QPI of the SSs of $\mathrm{Pb}_{0.77}\mathrm{Sn}_{0.23}\mathrm{Se}$ also exists in the literature [28]. A more detailed study employing QPI maps provided further insights into the orbital texture of $\mathrm{Pb}_{1-x}\mathrm{Sn}_x\mathrm{Se}$ and allowed the visualization of the theoretically predicted Lifshitz transition [29]. The influence of strain on the band structure of SnTe has also been investigated using STM/STS, and it has been shown that it is important to consider the orbital nature of the conduction and valence bands to account for the experimental features [125]. It is quite well known that strain can also break the mirror symmetry of a crystal and this was also shown in the case of $\mathrm{Pb}_{1-x}\mathrm{Sn}_x\mathrm{Se}$ where both massless Dirac SSs as well as symmetry broken mass acquired gap opening leading to massive Dirac SSs was experimentally observed

[25]. Apart from the above reports, there have been STM studies investigating the step edges on the (001) surface of $\mathrm{Pb}_{1-x}\mathrm{Sn}_x\mathrm{Se}$ [26, 30, 126]. For instance, in 2016, Sessi *et al.* demonstrated for the first time the presence of spin-polarized edge states in the half-unit cell step edges of $\mathrm{Pb}_{1-x}\mathrm{Sn}_x\mathrm{Se}$ [26]. The signature of the edge mode was a distinct peak at the step edge, coinciding with the Dirac point energy in $\mathrm{d}I/\mathrm{d}U$ measurements. Later, other works focused on the interaction between these topological edge modes, when two half-unit cell step edges are located close to one another [126]. Their experiments revealed the splitting of the one peak at the Dirac point energy into two peaks, the origin of which was attributed to the interplay of the Se p_x and p_y orbitals at the step edge. The next chapter will focus on the investigation of strong electron correlations at the unique step edges of $\mathrm{Pb}_{1-x}\mathrm{Sn}_x\mathrm{Se}$.

3.5.1 Strong Electron-Electron Correlations

The motivation for departing from the general discussion of topological materials to focus on strong electron correlations arises from the experimental results on a TCI that are presented in the next chapter. Electron-electron correlations play a vital role in condensed matter physics. It involves the competition between two conditions: one in which an electron is localized at a position in space and feels the Coulomb repulsion due to the conduction electrons present in the system, and the other case where due to the hybridization between the atomic orbitals, the electrons are delocalized in space, behaving as free electrons similar to Fermi gas. The delocalization of the electrons causes the lattice sites to be populated and depopulated, as the electrons are free to jump on and off that site, leading to charge fluctuation that can be minimized by a uniform distribution of the electrons across all the sites. However, the hopping of the electrons across different sites causes an increase in the Coulomb repulsion, which is energetically unfavorable [127]. These two conditions mentioned above can be characterized by two competing energy scales determining whether the electron correlations are strong or weak. To simplify the discussion, instead of considering a whole ensemble of electrons, let us consider only two electrons and try to understand how the interactions between them can modulate from strong to weak. The on-site energy of an electron due to Coulomb repulsion can be defined as $V = e^2/r$, where r is the separation between the two electrons. On the other hand, the hybridization between the orbitals can be described by the hopping element t, which describes the nearest-neighbor hopping between the lattice sites. So the ratio V/t allows us to determine whether the electron correlations are strong or weak. If $V/t >> 1$, the long-range Coulomb repulsion becomes significant, as the tendency of the electrons to hop across lattice sites diminishes, thereby reducing the charge fluctuations at the lattice sites. This condition, where electrons are localized, corresponds to the case of strong electron correlations. On the other hand, when $V/t << 1$, the onsite energy term is small while the hopping term is dominant, due to which there is an extensive overlap of the orbitals, allowing the electrons to move around freely across different sites. This can be better understood by considering the case of alkali atoms like Potassium, in which the strong overlap between s-orbitals, which are extended in space, implies that t is large and V is substantially small, hence electrons are weakly correlated [128]. This strong electron correlation facilitates the emergence of novel quantum states of matter which has been observed across many different systems such as Kondo systems [129–134], Heavy Fermion systems [135–137], Re-entrant superconductors [138, 139], Non-Fermi Liquid systems [140–143] etc.

4 Interaction effects at the step edges of $\mathbf{Pb_{1-x}Sn_xSe}$

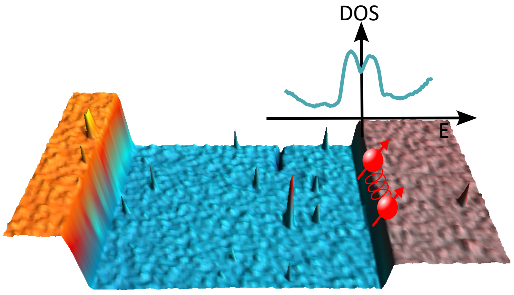

Electron-electron interactions at a TCI step edge

Following the introduction of the crystalline symmetry-protected topological class, the nature of the edge states in the TCI, $Pb_{1-x}Sn_xSe$ will be explored. The presence of unique steps on the (001) surface of $Pb_{0.7}Sn_{0.6}Se$ is demonstrated, followed by a discussion of the electronic properties of these step edges. It is shown that edge modes with a flat dispersion are exhibited by a particular type of step edge, providing a foundation for investigating novel correlated states. The emergence of these states will be demonstrated using STM/STS measurements. Theoretical modeling and analysis will elucidate the underlying physics, revealing a 1D flat band Stoner ferromagnetism at a specific step edge.

The results presented in this chapter have been published in *ACS Nano Letters* [144].

4.1 Experimental demonstration of edge states in $Pb_{1-x}Sn_xSe$

In the previous chapter, it was discussed that the 2D TIs are characterized by spin-momentum locked edge states, which are protected by the $\mathcal{T}$ symmetry. These edge states form dissipationless conducting channels that run along the edges of the sample. Using STM/STS measurements, the spatial detection of these edge modes has been realized in many topological systems [7, 8, 10, 145–147]. While these systems exhibiting the edge states are 2D TIs or the QSH insulators protected by $\mathcal{T}$ symmetry, it has also been demonstrated that such edge states exist in mirror symmetry protected 3D TCI $Pb_{1-x}Sn_xSe$. In 2016, Sessi *et al.* first demonstrated these spin-polarized edge states at the atomic step edges of $Pb_{0.67}Sn_{0.33}Se$ [26]. The experiments detailed in this chapter are fundamentally related to the edge states. Thus, a significant portion of the experimental work involved detecting these states using low-temperature STM and STS, which are discussed in this section.

The experiments were performed on crystals that are within the topological regime ($0.18 < x < 3$; refer to phase diagram in figure 3.16). Single crystals of $Pb_{0.7}Sn_{0.3}Se$ were cleaved in situ at room temperature under ultrahigh vacuum conditions using the procedure mentioned in section 2.3.1 and inserted into the STM head to cool it down. Once the sample is cooled down to the base temperature of the STM *i.e.* T= 1.8 K, topographic scans were performed on the freshly cleaved surface of $Pb_{0.7}Sn_{0.3}Se$ single crystals. The cleaving process involves breaking the bonds on the surface to remove a few layers of atoms from the top surface of the crystal. Figure 4.1a shows a constant-current topographic image acquired on a 450 nm x 450 nm sample region, revealing the (001) surface of $Pb_{0.7}Sn_{0.3}Se$, the termination that is easily procured when cleaving the bulk single crystals [26, 30, 126]. Figure 4.1b shows a 3D view of the 2D topographic image on the left. The inset in figure 4.1a shows an atomically resolved image with the Pb/Sn or Se atoms occupying the

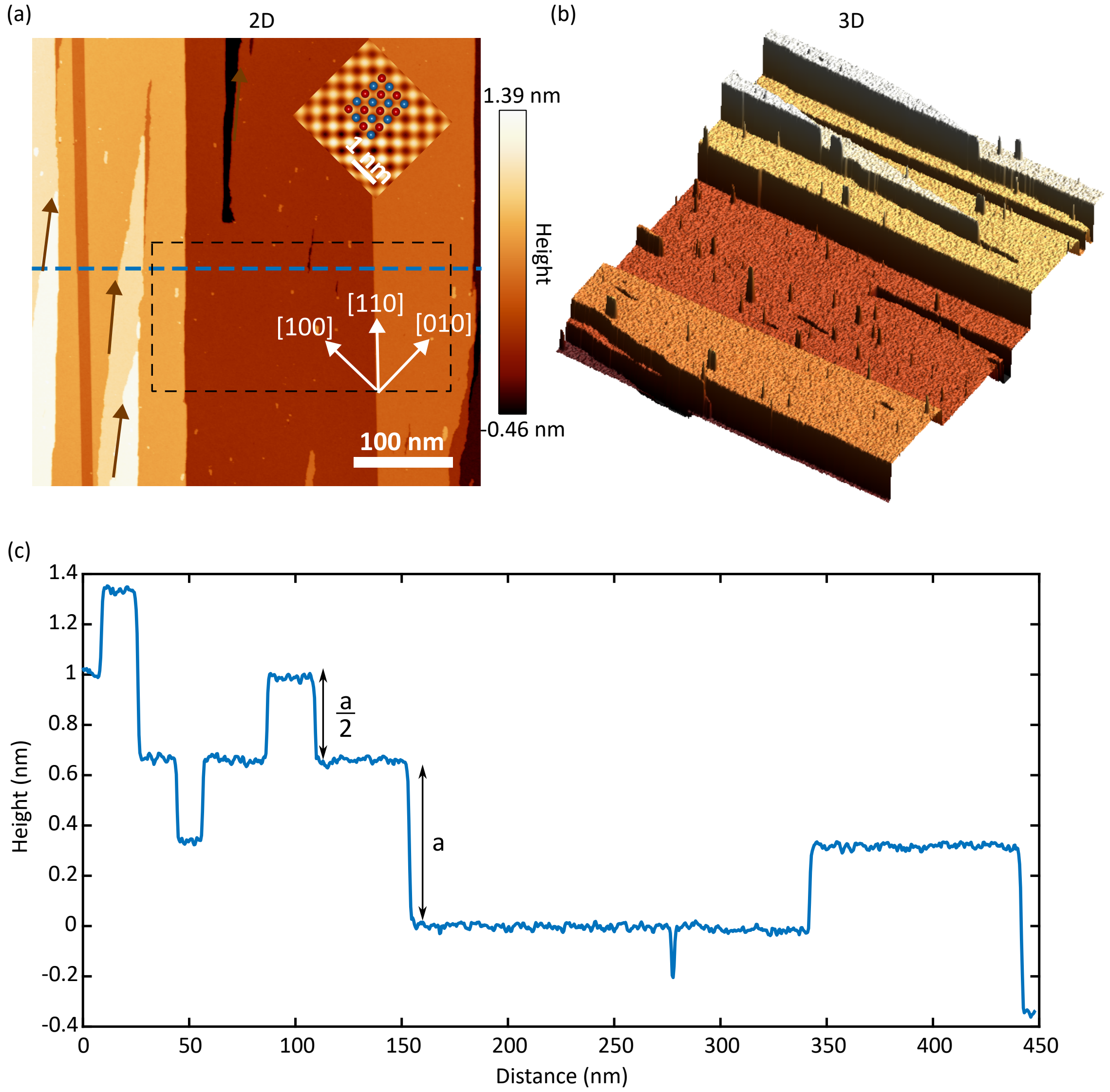

Figure 4.1: (a) Constant-current topographic image of the (001) surface of $Pb_{0.7}Sn_{0.3}Se$. Scanning parameters: $I_t = 50$ pA $V_b = 700$ mV. The inset shows an atomically resolved image acquired on a terrace. The in-plane atomic lattice has been laid on the top for a visual aid to the eye. Scanning parameters: $I_t = 100$ pA, $V_b = 300$ mV. (b) 3D view of the STM topography in (a). (c) Line profile acquired across the dashed line in (a) showing steps of different heights, corresponding to the integer and half-integer steps.

square lattice. The (001) surface lattice with Pb/Sn (red) and the Se (blue) atoms is laid on top of the atomically resolved image for a visual aid to the eye. However, it is to be noted that it is difficult to comment on the exact species of the atoms since STM is not chemically sensitive. There are some reports in the literature on the parent compound SnTe, claiming that when scanning at high positive bias voltages, since electrons tunnel from the occupied states of the tip to the unoccupied states or conduction band of SnTe, the Sn sublattice is better resolved and the same region when scanned at negative bias, the electrons tunnel from the occupied states of SnTe to the unoccupied states of the tip so the Te sublattice is revealed in the STM topography [124]. Gyeis *et al.* on the other hand demonstrated that at low negative bias (V_b = -50 mV), both the Pb/Sn and Se sublattices could be distinctly resolved in the $Pb_{0.77}Sn_{0.23}Se$ crystal where the Sn atoms were identified as small light dots in the topographic images [28]. The observed phenomenon was attributed to two factors: contrast reversal occurring at specific scanning biases and the presence of tip artifacts. Since, in the present case the atomically resolved image, in the inset, was acquired at a bias voltage of 300 mV, it can only be speculated that the Pb/Sn sublattice is resolved in the images, however, a more careful analysis would be required to assert firmly the chemical nature of the atoms observed. The white arrows indicate the high symmetry directions on the plane of the sample, obtained by analyzing the atomically resolved image.

As shown in figure 4.1a,b, the (001) surface of $Pb_{0.7}Sn_{0.3}Se$ hosts steps characterized by different heights, separated by atomically flat terraces. The ones running straight like a “highway” are oriented along the [100] direction of the face-centered cubic lattice. However, the presence of randomly oriented steps is also visible, like the ones marked with brown arrows on the topographic image in figure 4.1a. The fact that the steps are of unique height becomes more evident in the height profile shown in figure 4.1c, obtained along the blue dashed line on the topographic image. The experimentally measured step height of the larger step is $\sim$ 6.3 Å, which corresponds to the lattice constant of the $Pb_{0.7}Sn_{0.3}Se$ ($a \approx 6.3$ Å). These steps embody an even number of atomic layers resulting in a height that is an integer times the lattice constant, *i.e.* n.a, where n is an integer. The line profile further reveals a set of steps whose height is half the height of the unit cell step *i.e.* 0.32 Å. These steps, consisting of an odd number of atomic layers, can be categorized under the class of steps whose height is half-integer times the lattice constant ($[n+\frac{1}{2}].a$). An inspection of the surface lattice in figure 4.2 reveals that the integer and the half-integer step

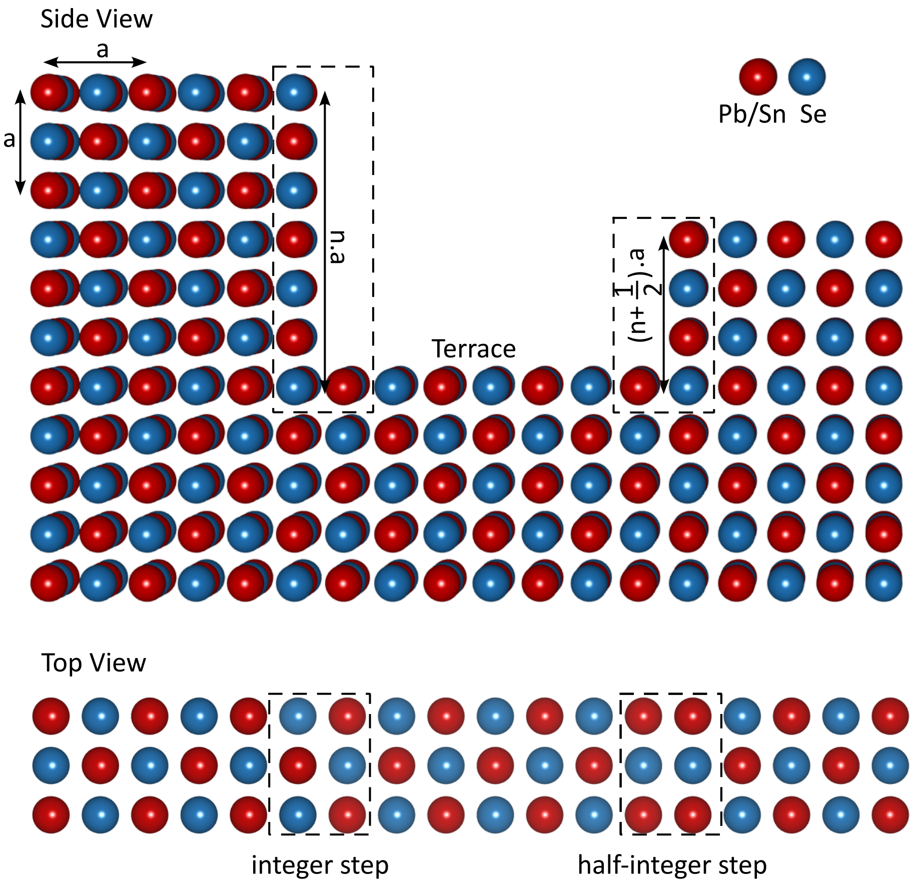

Figure 4.2: Top: Arrangement of atoms mimicking the side view of a unit-cell and a half-unit cell step separated by a terrace (after cleaving). Bottom: Top view of the cleaved surface demonstrates that the surface lattice's translation symmetry is maintained for the integer step while for the half-integer steps, it is broken due to the switching of the orbitals of Pb/Sn and Se.

edges are unique in the arrangement of the atoms across the step. Figure 4.2 shows a cartoon of the top view and the side view of an arrangement of atoms mimicking an integer step and a half-integer step separated by a terrace. On the terrace, the Pb/Sn (red) and Se (blue) atoms alternate accordingly in the lattice, maintaining the surface lattice symmetry. Similar behavior is observed while navigating across the integer step where the orbitals of Pb/Sn and Se are preserved, indicating the conservation of translation symmetry. Intriguingly, at the half-integer step, the orbital nature of Pb/Sn and Se are exchanged, thereby disrupting the translation symmetry of the surface lattice. From the cartoon in figure 4.2, the symmetry breaking of the surface lattice is significantly apparent, indicating a structural π shift across the half-integer step. This significantly impacts the electronic properties of the half-integer

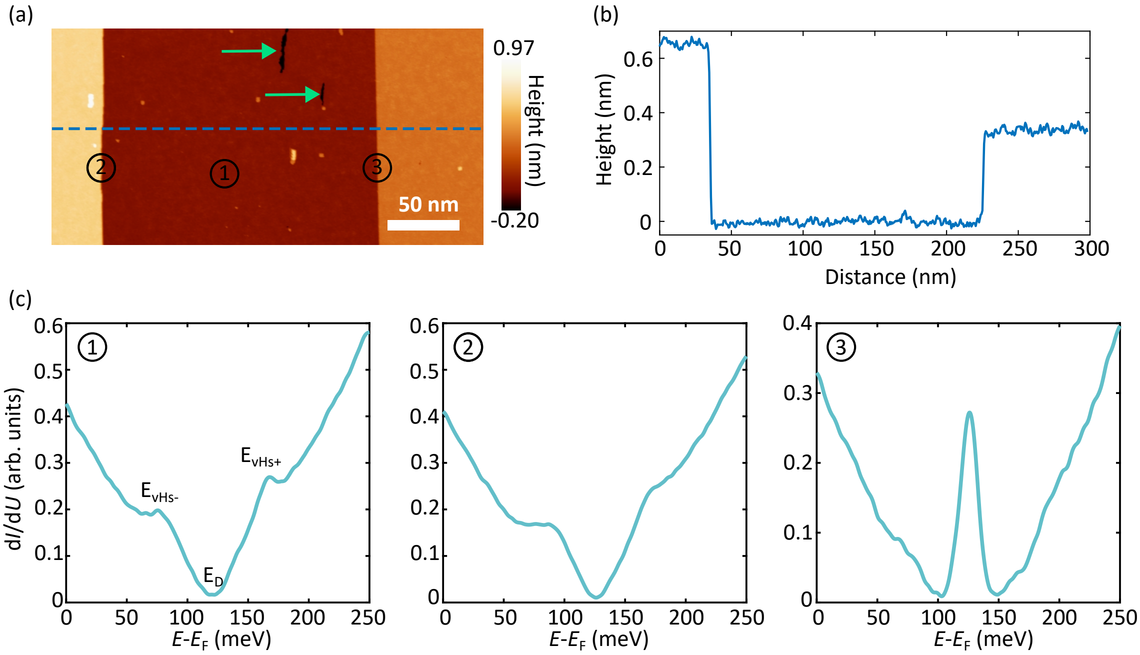

Figure 4.3: (a) STM topography of the (001) surface of $Pb_{1-x}Sn_xSe$ comprising a unit-cell step, a terrace, and a half-unit cell step. Scanning parameters: $I_t = 50$ pA, $V_b = 700$ meV. (b) Height profile across the dashed line in (a) shows the height of the unit-cell step and the half-unit cell step. (c) dI/dU spectrum acquired on the terrace (left), unit-cell step (middle), and half-unit cell step (right). Stabilization parameters for c: $I_t = 250$ pA, $V_b = 250$ mV, $V_{mod} = 5$ mV.

step, which forms the basis for the subsequent discussion of edge states.

The uniqueness of the (001) surface of $Pb_{0.7}Sn_{0.3}Se$ featuring atomically flat terraces, as well as steps of different heights characterized by unique surface lattice symmetry, motivates a meticulous examination of their electronic properties. To do so, a 300 nm x 100 nm topographic scan was acquired in a region marked by the dashed black rectangle in the overview image in figure 4.1a. The corresponding STM topography is shown in figure 4.3 , which includes a unit-cell step (left), a terrace (center), and a half-unit cell step (right). The line profile in figure 4.3b, obtained along the dashed blue line in the STM topography, reveals the height of even and odd steps. To probe the electronic properties of this sample region, dI/dU spectra were acquired at these unique locations indicated by the numbers 1, 2, and 3. The tip was stabilized at the following locations: middle of the terrace, at the unit-cell step edge, and the half-unit cell step edge, at a bias voltage $V_b = 250$ meV and a set point current, $I_t = 250$ pA and the feedback was subsequently switched off to

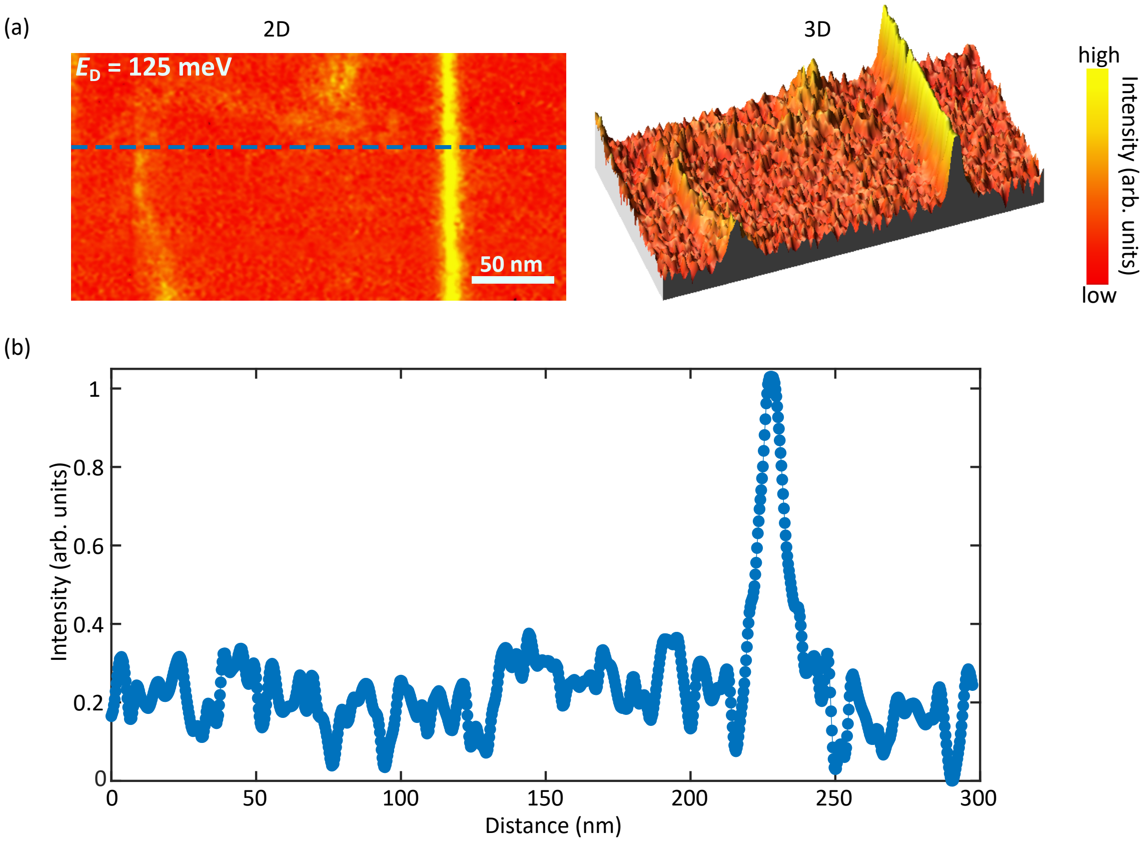

Figure 4.4: (a) dI/dU map acquired at the energy position of the Dirac point (E = 125 meV) on the topography in figure 4.3a. On the right, the 3D view of the dI/dU map shows a strong intensity distributed uniformly along the 1D step edge. Scanning parameters: I_t = 250 pA, V_b = 125 mV. (b) Intensity profile across the dashed line in (a) shows a peak at the location of the half-unit cell step.

acquire the spectra. As shown in the left panel of figure 4.3c, the dI/dU spectrum acquired on the terrace reveals a dip at E-E_F = 125 meV corresponding to the energy position of the Dirac point located near the $\mathcal{T}$ invariant momenta $\overline{X}$. Additionally, the spectrum reveals a pair of kinks straddling the Dirac point, marked as $E_{vHs-} = 75$ meV and $E_{vHs+} = 170$ meV, which corresponds to the Van Hove singularities (VHSs) arising from the saddle points above and below the Dirac point (refer to figure 3.13c). Having obtained the dI/dU spectrum on the terrace, the tip was navigated to the unit-cell step edge. The middle panel in figure 4.3 shows the LDOS at the unit-cell step edge exhibiting spectral features, reminiscent of the dI/dU spectrum obtained on the terrace, with the Dirac point locked at $E_D = E$-E_F = 125 meV. While the local LDOS at the terrace and the unit-cell step edge exhibit remarkable similarities, it is interesting to note that the dI/dU spectrum at the half-unit cell step edge features a peak in the DOS at the energy position of the Dirac point (right panel of figure 4.3c). It can be seen that the emergence of the peak in the LDOS is closely linked to the redistribution of the spectral features associated with the LDOS of the terrace (or the unit-cell step edge) over a broad energy spectrum. This is apparent from the vanishing of the kinks associated with the VHSs. As shown in figure 4.4a spatial mapping of the DOS at the energy of the Dirac point (E_D = 125 meV) acquired over the topographic region in figure 4.3a reveals an intense feature along the entire 1D half-unit cell step edge, which corresponds to the edge modes. From the 3D image in figure 4.4a, it can be inferred that this intensity remains constant along the entire length of the 1D channel and is evenly distributed on either side of the step, *i.e.* on the top and bottom of the step. The spatial width of the edge mode can be calculated from the intensity profile in figure 4.4b, acquired along the dashed line in the LDOS map, exhibiting a peak at the location of the half-unit cell step. A calculation of the FWHM of this peak allows extracting the spatial width of the edge modes, which is $\approx$ 9 nm. As evident from the intensity profile, the terrace and unit-cell step exhibit no such strong feature in LDOS mapping except for some spatial fluctuation of the DOS on the terrace, which could probably be related to the formation of charge puddles(bright patches). The differential conductance maps in figure 4.5 acquired close to the energy position of the van Hove singularities ($\mathrm{E}_{\mathrm{vHs-}}$ = 75 meV and $\mathrm{E}_{\mathrm{vHs+}}$ = 175 meV) show no such intensity features. Similarly, dI/dU maps acquired at energies (E = 100 meV, 150 meV; see figure 4.5) away from the energy of the edge mode (E_D = 125 meV) indicates the absence of any strong intensity feature along the half-unit cell step thereby reinforcing the correlation between the edge mode and the peak at E_D in the LDOS (see right panel of figure 4.3). The dI/dU map at E_D facilitates the extraction of additional information related to the electronic properties of the edge modes, such as the scattering of quasiparticles of the step edges. Firstly, the dI/dU map in figure 4.4a, does not feature any interference pattern like standing waves. Furthermore, the 2D fast-Fourier transform (FFT) of the LDOS map displayed in figure 4.6a does not reveal any features associated (e.g., standing

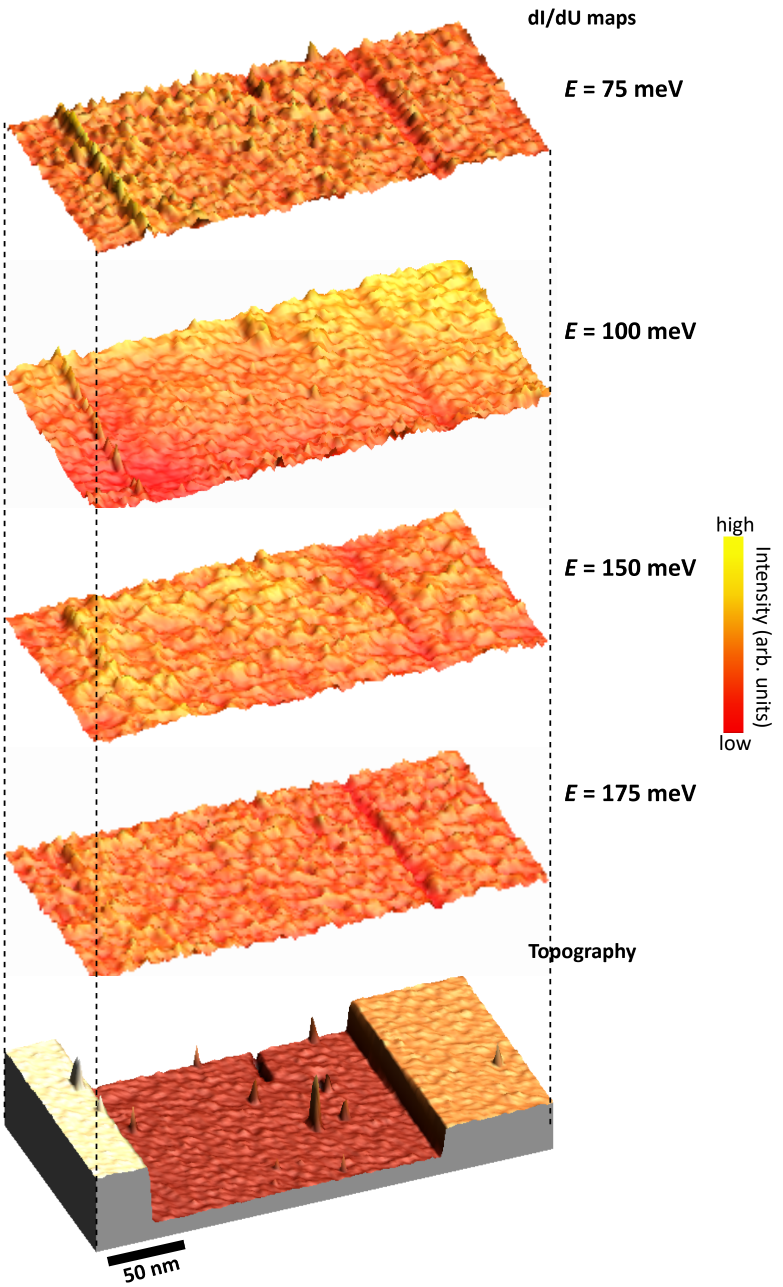

Figure 4.5: dI/dU maps acquired at energies below and above the Dirac point energy including the energies close to the saddle points (E_{VHS-} and E_{VHS+}) indicating the absence of any edge modes. Scanning parameters: I_t = 250 pA, V_b = 75 mV.

waves) with the formation of interference patterns due to the scattering from the defects or step edges. Such features are expected to manifest as peaks at discrete momenta in the Fourier space. The intensity profile of the Fourier transform of the DOS along the direction of the step edge is shown in figure 4.6b, providing a robust verification of the same, showing a monotonically decaying response with increasing wave vector, a signature consistent with the absence of QPI due to scattering. In the

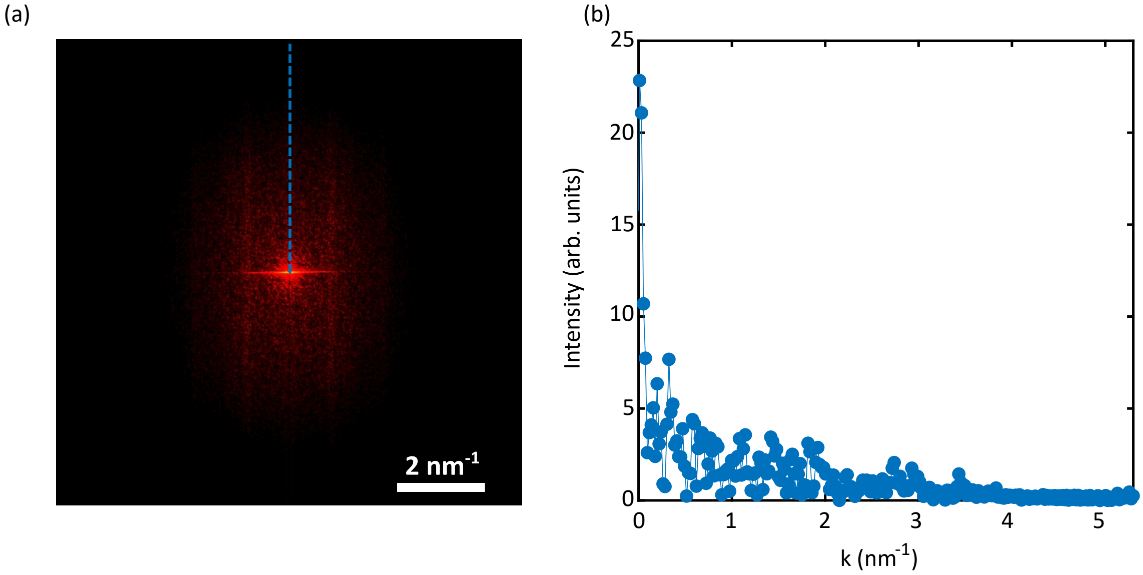

Figure 4.6: (a) 2D-FFT of the LDOS map at the energy of the edge modes. (b) The intensity profile of the 2D-FFT of the dI/dU signal along the half-unit cell step indicates a monotonic intensity decay with an increasing wave vector.

previous paragraph, it was pointed out that the unit-cell and half-unit-cell steps have different arrangements of atoms across the step. The translation symmetry of the surface lattice is maintained across the terrace as well as the unit-cell steps, so the LDOS is a replica of one another, however, the same is broken across the half-unit cell step, thereby inducing additional electronic states at the Dirac point, manifesting as a peak in the LDOS, giving rise to the 1D edge modes. In a more detailed study by Sessi *et al.*, it has been demonstrated that the appearance of the 1D edge states is strongly linked to the non-trivial electronic properties of the bulk [26]. In their report, DOS mapping was performed on crystals with varying concentrations of Sn so that the electronic properties of the entire phase diagram, ranging from the trivial to the inverted band gap region, could be mapped. It was demonstrated that the trivial insulator PbSe does not exhibit any edge states like feature as evident from their dI/dU maps. STS measurements were also performed on crystals having a critical concentration of Sn ($x_c = 0.24$) where the bands undergo a transition from the trivial to the inverted band phase. The measurements revealed a weak enhancement at E_D in the dI/dU signal at the half-integer step, indicating the onset of the edge modes. In contrast, no edge modes were detected at the integer steps. Interestingly, above the critical concentration of Sn (x = 0.33), which corresponds to the inverted band gap phase, a strong enhancement of the $\mathrm{d}I/\mathrm{d}U$ signal along the half-integer steps was detected, similar to those shown in figure 4.4a. This set of measurements established a one-to-one correspondence between the edge and the bulk, where the edge modes only appear when the bulk is topologically non-trivial. Additional measurements were performed to test the robustness of the 1D edge states to external perturbations. It was shown that even under an out-of-plane field of 11 T, the edge modes continue to exist, indicating the robustness of the mirror symmetry-protected edge state to $\mathcal{T}$ symmetry-breaking perturbations. Even at higher temperatures (T = 80 K), the edge states were captured in STM measurements, indicating their robustness against thermal fluctuations. The absence of scattering and the robustness of the edge states to external perturbations provide compelling evidence of the topological nature of the edge states. Section 4.3 will demonstrate, using a toy model, that the edge modes have a flat dispersion strictly localized along the 1D half-unit cell step edge. From now on, the peak at the half-unit cell step edge will be referred to as a 1D flat band for ease of discussion.

4.2 Tuning interactions in the 1D flat band by surface doping

In the previous section, the presence of intriguing features in the electronic band structure of the TCI, $\mathrm{Pb}_{0.7}\mathrm{Sn}_{0.3}\mathrm{Se}$, such as the VHS flanking the Dirac point and the flat band at the half-unit cell step edge, was demonstrated. The presence of VHS or flat bands in many systems, such as graphene, its twisted counterparts, heavy fermionic systems, kagome superconductors, are known to amplify electron-electron interactions [108–110, 135–137, 148–151]. These amplified interactions lead to electronic instabilities giving rise to a diverse array of quantum states such as unconventional superconductivity, Mott insulating phases, ferromagnetism, quantum spin liquids, etc. However, the VHS or the flat bands must be positioned close to the Fermi level for such novel effects to emerge, because when the flat band is proximitized to the Fermi level, the kinetic energy (bandwidth) is quenched, and the Coulomb interactions become dominant, thereby leading to strong electron-electron correlations which can cause instability in the flat bands giving rise to these novel quantum states. In conventional 3D TIs such as Bi_2Te_3, Bi2Se_3, or Sb_2Te_3, Coulomb interactions are negligible, so electron-electron interactions are usually ignored. In the present case of a 3D TCI, it is known that this material possesses a large dielectric constant [32] which implies that Coulomb interactions are irrelevant, however non-trivial band topology combined with the presence of VHS and flat bands might enhance electron-electron interactions leading to electronic instabilities in the bands and giving rise to correlated states. The realization of correlated effects necessitates the positioning of the Fermi level within the flat band, a condition that serves as the basis for the ensuing discussion.

As observed in the previous section on edge states, due to the p-doped nature of the $Pb_{0.7}Sn_{0.3}Se$ crystals, the 1D flat band at the step edge is located at $E_D =$ 125 meV, which is above the Fermi level. As a first step, it is therefore necessary to align the energy position of the 1D flat band with the Fermi level to observe how the 1D flat band gets affected. Different experimental possibilities exist for tuning the energy of these bands, such as electric gating, chemical gating, surface doping, etc. Here, an approach of surface doping was adopted since it was convenient to implement in the STM setup in which the experiments were performed. Small amounts of 3*d* transition elements were progressively dosed onto the crystal surface, with the crystal held at cryogenic temperatures (T = 12 K). This procedure is known to cause an n-type effect *i.e.*, a downward band bending implying a rigid shift towards negative energies. The idea behind depositing the atoms under cold conditions was to prevent the atoms from diffusing into the bulk, thereby preserving the effect of band bending on the SS. Furthermore, when the crystal is cold, the atoms do not agglomerate, preventing the formation of large clusters on the surface, which might cause instability in the STM tip during scanning. Here, 4 different

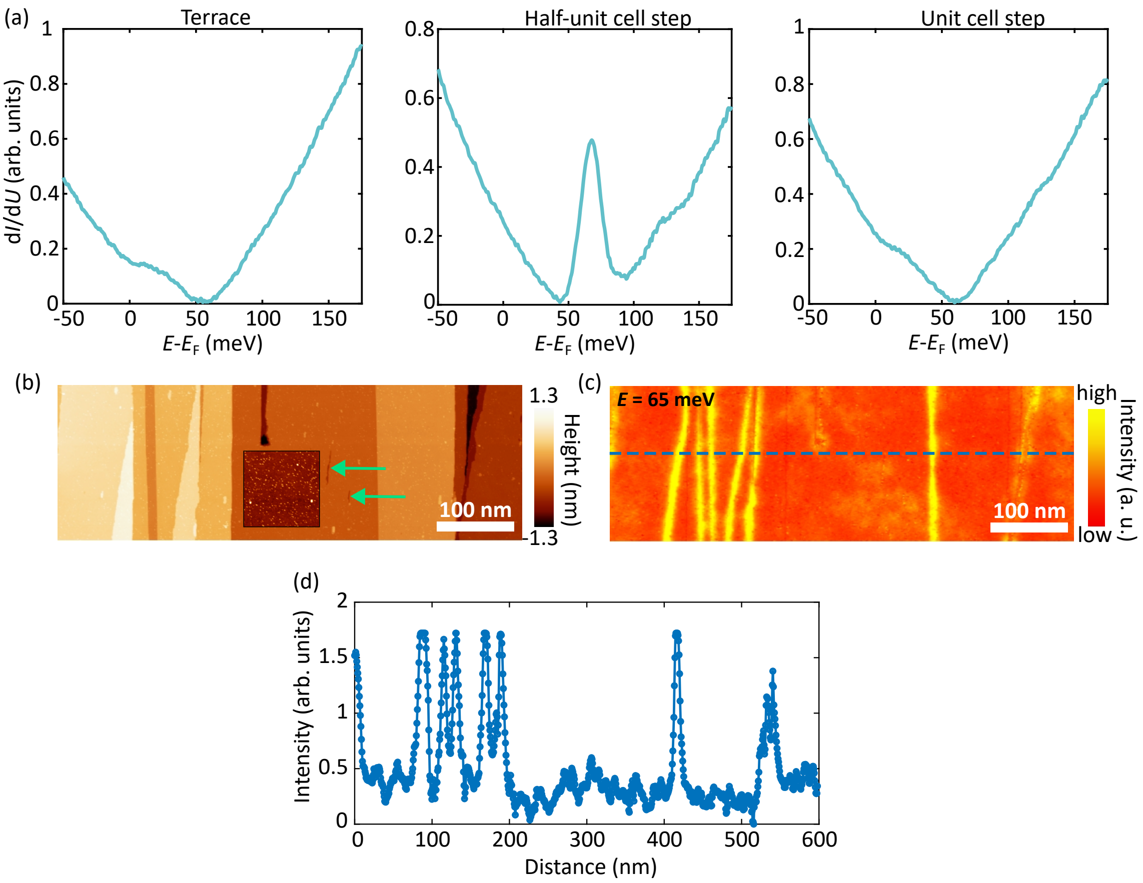

Figure 4.7: (a) dI/dU spectrum on the, left: terrace, middle: half-unit cell step, right: unit-cell step after the 1st step of Cr doping. The Dirac point along with the flat band is shifted to $E_\mathrm{D} \sim 65$ meV. (c) dI/dU map acquired over the STM topography in (b) showing the edge modes at the half-unit cell step. Scanning parameters: I$_t$ = 150 pA, V$_b$ = 40 mV. (d) Intensity profile along the dashed blue line in (c) demonstrates the presence of intense features only at the location of the half-unit cell step which corresponds to the edge modes. Here a.u. refers to arbitrary units. Stabilization parameters for a: I$_t$ = 250 pA, V$_b$ = 175 mV, V$_{mod}$ = 5 mV.

transition elements, namely Chromium, Manganese, Iron, and Copper, have been used as surface dopants to tune the Dirac point to the Fermi level. As the effects of Cr doping were investigated in detail, these results are presented first, followed by an examination of the effects of other transition metal dopants. It should be noted that while the influence of surface doping with Cr and Mn on the 1D flat band was studied as part of this thesis, the data for Fe and Cu were provided by collaborators from the University of Würzburg.

Figure 4.7b shows an STM topographic image of a similar region as in figure 4.3 but having more step edges, after the deposition of the Cr atoms onto the surface.

The Cr atoms can be visualized in the inset image, appearing as bright protrusions on the flat surface. Following the deposition of the Cr atoms, STS measurements are acquired at the 3 important locations. The dI/dU spectrum, acquired on the terrace as shown in figure 4.7a indicates a shift of the Dirac point to a lower energy ($E_\mathrm{D} \sim 65$ meV) , demonstrating a successful implementation of the surface doping technique. The dI/dU spectrum at the unit-cell step mirrors the spectra on the terrace with minor differences in the spectral weight at energies far away from the Dirac point. The middle panel in figure 4.7a shows that as the Dirac point shifts with doping, so does the 1D flat band, which is also positioned at E_D. DOS mapping performed at the energy of the flat band is reported in figure 4.7c, showing a strong intensity at all the half-unit cell steps, indicating a close resemblance of the features associated

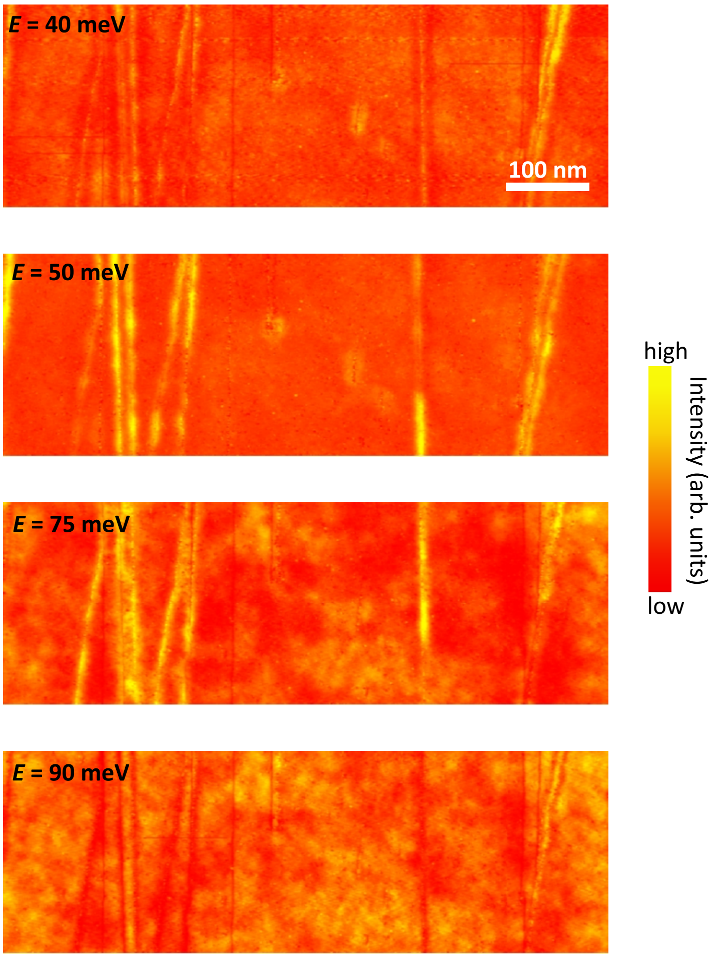

Figure 4.8: Spatial mapping of the DOS mapping at energies in the close vicinity ($E = 50$ meV and $E = 75$ meV) as well as far away ($E = 40$ meV and $E = 90$ meV) from the energy of the 1D flat band. Scanning parameters: $\mathrm{I}_t = 150$ pA.

with the pristine (undoped) samples. This further confirms the sustainability of the edge modes even in the Cr-doped samples, indicating the robustness of the edge modes to the magnetic dopants. An intensity profile extracted along the dashed line in figure 4.7b, is shown in figure 4.7c, indicating enhanced conductance manifesting as peaks exclusively at the half-unit cell steps. Figure 4.8 shows DOS mapping at energies in the close vicinity of the 1D flat band (E =50 meV and E =75 meV) revealing a substantial decay in the edge state intensity as expected. For energies far away from the flat band, the intensity of the edge modes is drastically suppressed (see DOS map at E = 40 meV and E = 90 meV in figure 4.8)

Following the 1^{st} surface doping step, a 2^{nd} doping step was performed to check the possibility of bringing the Dirac point even closer to the Fermi level. The STS results corresponding to this doping step will be presented now. As shown in the leftmost panel of figure 4.9a, the dI/dU spectrum on the terrace shows a further shift of the Dirac point towards the Fermi level. The Dirac point is positioned at $E_\mathrm{D} \sim 30$ meV. A similar shift is also observed in the case of the unit-cell step, however, the Dirac point is positioned close to $E_\mathrm{D} \sim 40$ meV. This difference in the energy of the Dirac point at the two locations possibly arises due to the fluctuation in chemical potential caused by either the intrinsic inhomogeneities in the crystal or the disorder created by the random distribution of dopants. Despite a slight difference in the energy of the Dirac point, it is important to note that the overall shape of the spectra is the same at both locations. While the dI/dU spectra at the terrace and the unit cell step are comparable for the 1^{st} and 2^{nd} Cr deposition step, notably as the flat band approaches closer to the Fermi level, the single peak of the 1D flat band splits into two peaks. This splitting is significant because it suggests the emergence of additional states. The DOS mapping corresponding to the 2 peaks at $E \sim 30$ meV and $E \sim 45$ meV and at the dip ($E \sim 35$ meV) are presented in figure 4.9b. Analysis of the dI/dU maps reveals that the edge states persist at the half-unit cell step across the energies of the peak and dip, however, a spatial fluctuation of the edge state energy is visible. This is captured by the intensity profile in figure 4.9c

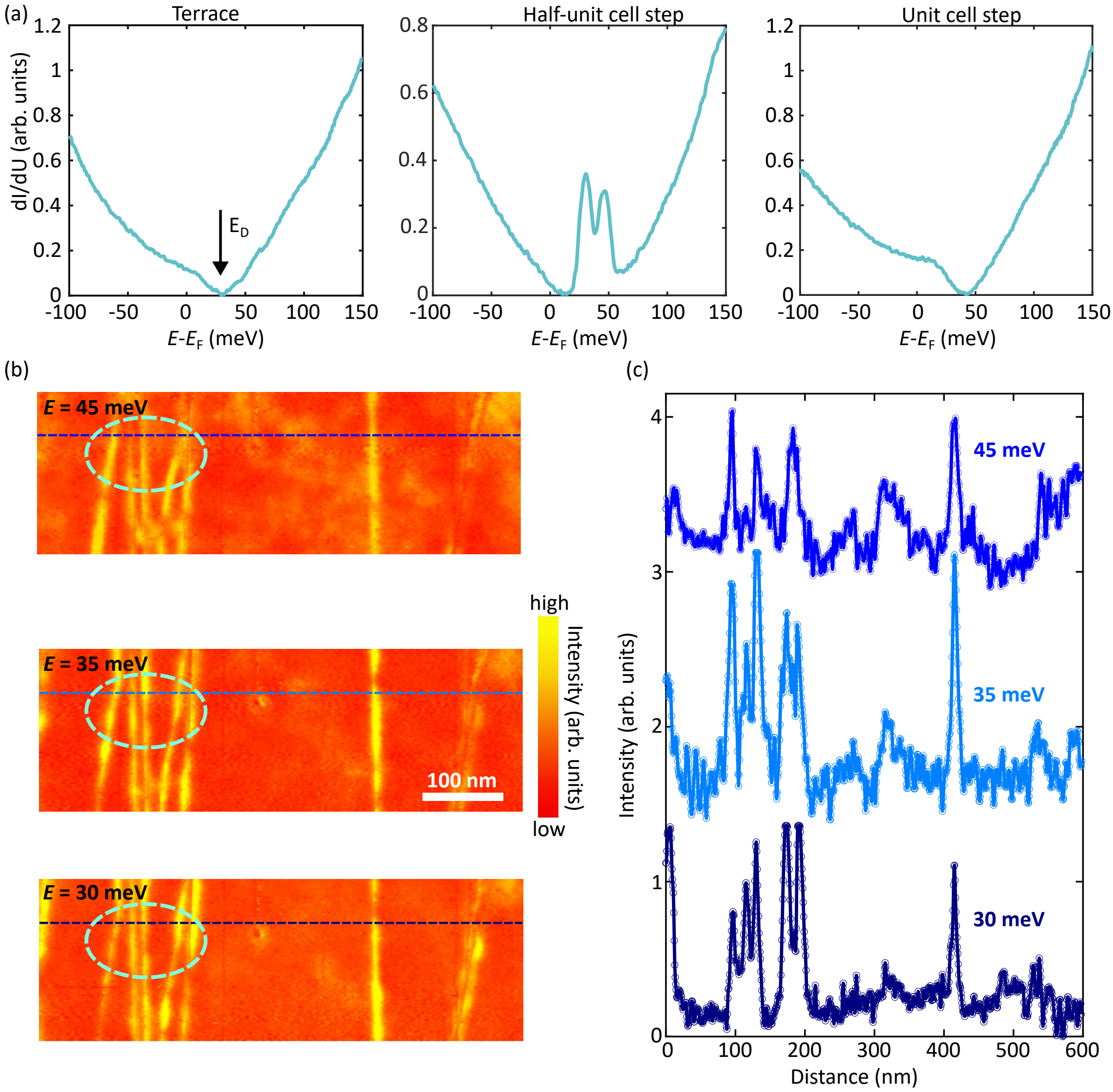

Figure 4.9: dI/dU spectrum on the left: terrace, middle: half-unit cell step, right: unit-cell step after the 2^{nd} step of Cr doping. The Dirac point is shifted to $E_{\mathrm{D}} \sim 30$ meV. Single peak of the 1D flat band splits into two peaks. (b) dI/dU map acquired over the STM topography in figure 4.7b at energy of the dip ($E \sim 35$ meV) and the two peaks ($E \sim 30$meV and $E \sim 45$ meV). Scanning parameters: $\mathrm{I}_t = 150$ pA. (c) Line profile acquired over the dashed lines in the dI/dU maps in (b) showing a variation of the intensity of edge modes at the same half-unit cell step at different energies. Stabilization parameters for a: $\mathrm{I}_t = 250$ pA, $\mathrm{V}_b = 150$ mV, $\mathrm{V}_{mod} = 5$ mV.

acquired along the same line in the dI/dU maps at the 3 different energies in figure 4.9b. For example, the series of half-unit cell step edges on the left and the ones to the right of the dI/dU maps reveal a spatial fluctuation of the intensity along the step edge. An energy-dependent intensity change can also be detected when focusing on a particular region (regions enclosed by the ellipse). As mentioned previously, the spatial fluctuation and the energy fluctuation of the energy of the edge states could

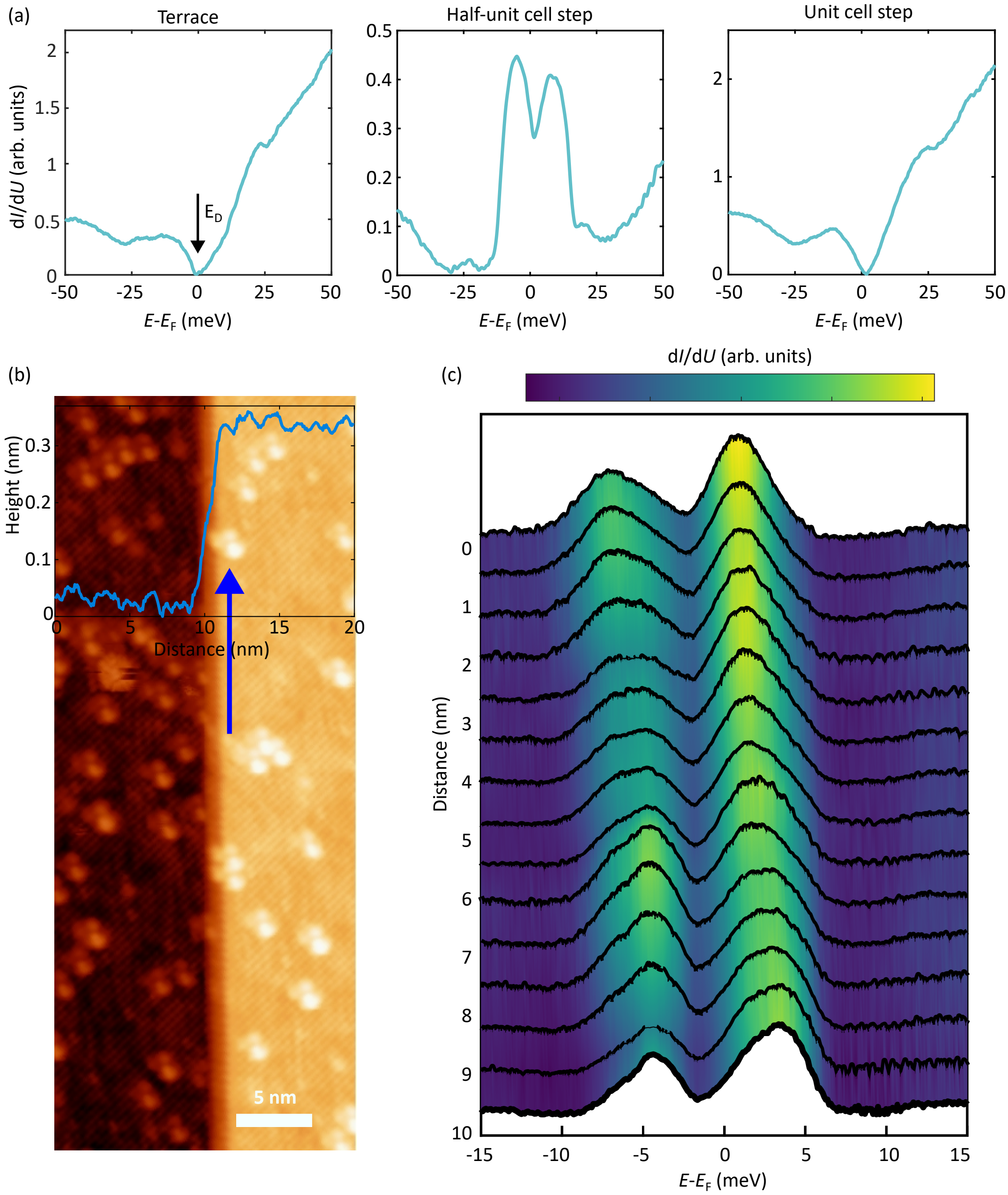

Figure 4.10: (a)dI/dU spectrum on the, left: terrace, middle: half-unit cell step, right: unit-cell step after the 3^{rd} step of Cr doping. The Dirac point is shifted to the immediate vicinity of E_F. Splitting of the flat band into a double peak structure persists. (c) Spatially resolved STS acquired at distinct points (blue line in b) along the structural π shift. Scanning parameters: I_t = 50 pA, V_b = 200 mV. Stabilization parameters for a: I_t = 250 pA, V_b = 50 mV, V_{mod} = 5 mV. Stabilization parameters for c: I_t = 250 pA, V_b = 15mV, V_{mod} = 1.5 mV.

be attributed to the disorder caused by the random distribution of Cr dopants as the doping is progressively increased. It is important to note that although the surface doping technique provides a means to tune the energy of the 1D flat band, it also introduces the major challenge of increasing disorder on the crystal surface with an increase in the concentration of the dopants. Given that the disorder increases with progressive doping, another doping step was still performed to adjust the Dirac point position even closer to the Fermi level by further increasing the concentration of Cr dopants. The effect of this doping step is presented in figure 4.10. As shown in the leftmost panel of figure 4.10a, this doping step allows shifting the Dirac point to the immediate vicinity of the Fermi level ($E_\mathrm{D} \sim 2$ meV). Similar to the previous two doping steps, the dI/dU spectrum on the terrace and unit cell step replicate one another due to the conserved translation symmetry of the surface lattice as well as the unit cell step. However, the two peaks still remain around E_F as shown in the middle panel of figure 4.10a. The STS further reveals suppression of the LDOS close to the Fermi level, indicating the onset of an instability in the 1D flat band. The energy position of the peaks was obtained by fitting them using a Gaussian profile. The peaks are positioned at $E_1 \sim$ -5 meV and $E_2 \sim$ 8.3meV respectively (see middle panel of figure 4.10a), yielding an energy splitting of $\Delta E = 12.74 \pm 0.02$ meV. It is crucial to emphasize that this surface doping method results in spatial fluctuations of the Dirac point, as shown in Figure 4.10c. This figure presents a spatially resolved STS acquired at distinct points along the half-unit cell step (indicated by the blue line). Even though these data reveal the existence of different broadening of the peaks and variations of the peak intensity, the splitting of the peaks and the dip at the Fermi level remain clearly distinguishable. Since the spectral shape observed on the unit-cell step after every Cr deposition step bears a close resemblance to the spectral shape observed in the pristine sample, it can be unequivocally affirmed that the splitting of the peak associated with the 1D flat band is related to the evolution of the electronic properties of the 1D flat band as a function of the doping. To examine how the splitting of the 1D flat band gets affected on doping below the Fermi level, the surface dopant concentration was further increased. Unexpectedly, as depicted in Figure 4.11, the peak splitting disappears, revealing the characteristic single peak associated with the 1D flat band. This suggests that the emergence of

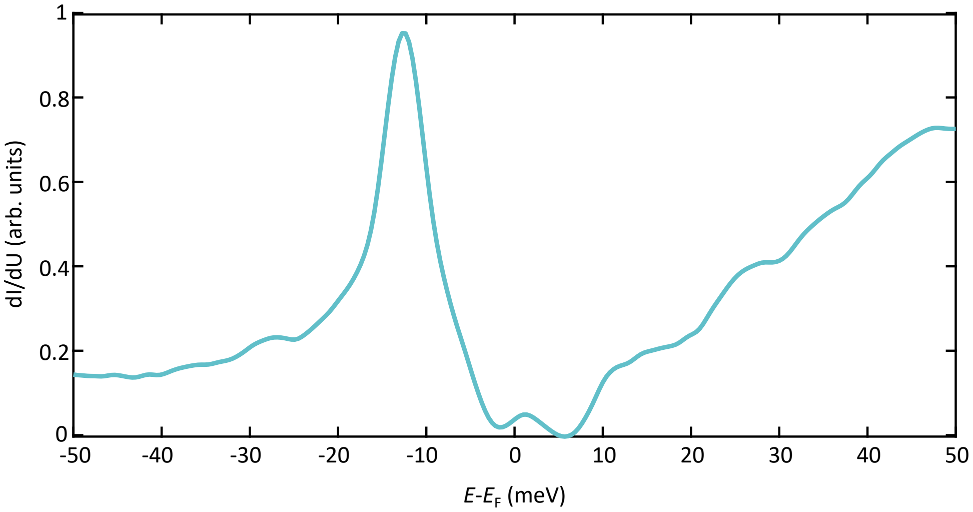

Figure 4.11: dI/dU spectrum on the half unit-cell step after shifting the Dirac point below the Fermi level, reveals the recovery of the single peak associated with the 1D flat band. Stabilization parameters: $I_t = 100$ pA, $V_b = 50$ mV, $V_{mod} = 5$ mV.

new states is closely linked to the proximity of the 1D flat band to the Fermi level, which disappears once the 1D flat band is shifted below the Fermi level.

The following discussion examines the effect of doping with other 3d transition elements (Mn, Fe, Cu) on the flat bands. An experimental approach similar to that of doping with Cr atoms was implemented to dope the pristine samples with Mn. Starting with the Dirac point and the 1D flat band located at $E_{\mathrm{D}} = 125$ meV, the pristine samples were progressively doped till the Dirac point was aligned close to the Fermi level. Figure 4.12b presents an STM topography where the Mn adatoms appear as bright protrusions. As demonstrated in figure 4.12a, analogous to the Cr doping, as the 1D flat band is tuned close to the Fermi level by doping Mn atoms onto the surface, the single peak of the 1D flat bands splits into a double peak structure. The inset provides a magnified view of the splitting. In this case, the energy splitting was obtained as, $\Delta E = 5.85 \pm 0.12$ meV. Following the trend observed for Cr doping, as the split flat band is doped below the Fermi level, the single peak of the 1D flat band is recovered.

Now, the results for doping the pristine samples with Fe will be presented. Figure 4.13b presents an STM topography where the Fe adatoms appear as bright protrusions. Following the trend observed for Cr and Mn doping, tuning the flat

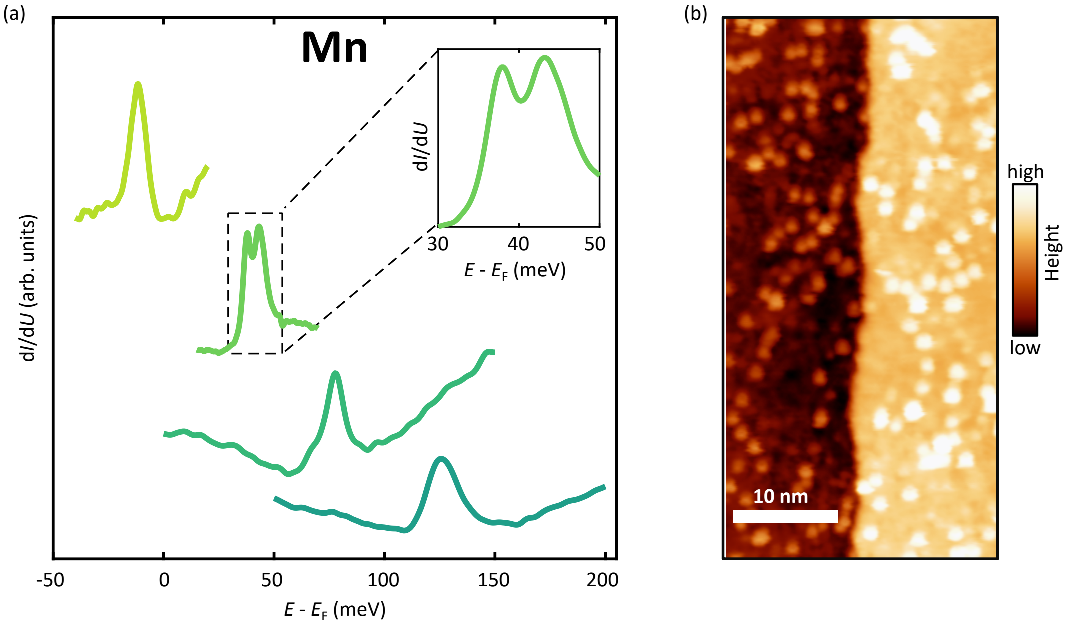

Figure 4.12: (a) STS spectra acquired at the half-unit cell step as a function of Mn doping. Close to E_F, the single peak of the 1D flat band splits into two peaks. The inset shows a magnified view of the splitting. As the Dirac point is shifted below the Fermi level , the splitting vanishes, and the single peak of the flat band is recovered. (b) STM topography illustrating the Mn adatoms on the surface. Scanning parameters: I_t = 30 pA, V_b = 650 mV. Stabilization parameters for a: I_t = 150 pA, V_b = 200 mV, 150 mV, 75 mV, 25 mV, V_{mod} = 5 mV.

band close to the Fermi level leads to the splitting of the single peak into a doublet as depicted in figure 4.13a. The inset provides a close-up view of the splitting within a narrower energy range. The energy splitting obtained in this case was $\Delta E = 6.01 \pm 0.07$ meV. This splitting disappears once the flat band is tuned below the Fermi level, indicating a revival of the original 1D flat band state. The same effect is observed when the pristine samples are doped with Cu. Figure 4.14b shows an STM topography of the Cu adatoms on the $\mathrm{Pb_{0.7}Sn_{0.3}Se}$ surface. As shown in figure 4.14a, a splitting of the 1D flat band into two distinct peaks occurs as it approaches the Fermi level with an energy splitting given by $\Delta E = 4.15 \pm 0.09$ meV. Adhering to the previous trends, once the flat band is shifted below the Fermi level, the splitting disappears.

Several control experiments were simultaneously conducted to ensure the observed phenomena's reliability against any potential artifacts. For example, to rule out any effect caused by the spatial inhomogeneities in the TCI surface, the same

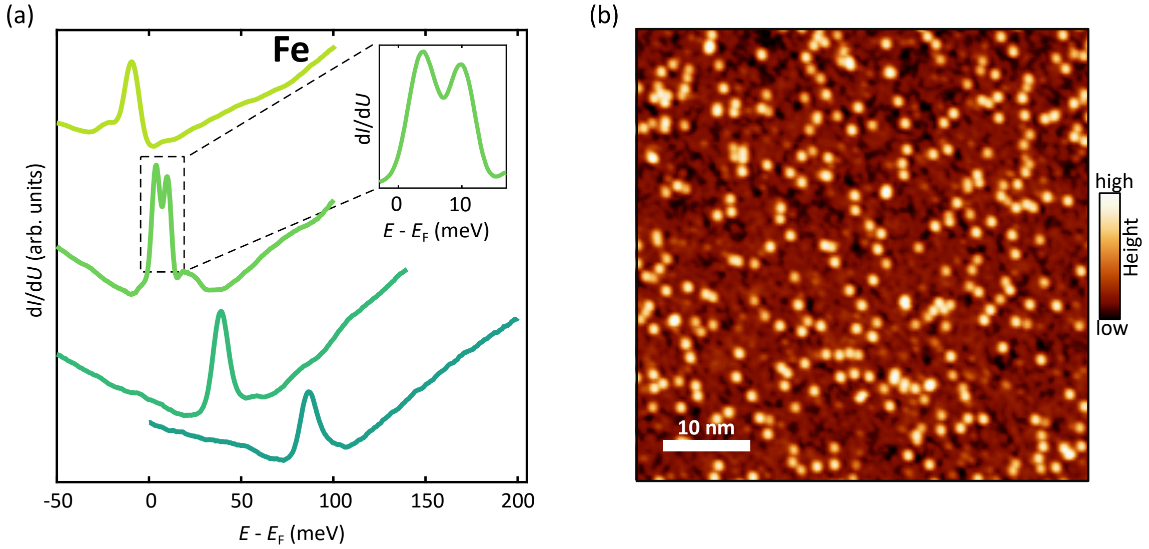

Figure 4.13: (a) STS spectra acquired at the half-unit cell step reveal the evolution of the 1D flat band structure as Fe doping increases. Near the Fermi level, a single peak splits into two distinct peaks. The inset shows a magnified view of the splitting. As the Dirac point is shifted below the Fermi level, the splitting vanishes, and the single peak of the flat band is recovered. (b) STM topography illustrating the Fe adatoms on the surface. Scanning parameters: I_t = 10 pA, V_b = 1 V. Stabilization parameters for a: I_t = 150 pA, V_b = 200 mV, 150 mV, 100 mV, 100 mV, V_{mod} = 2.5 mV.

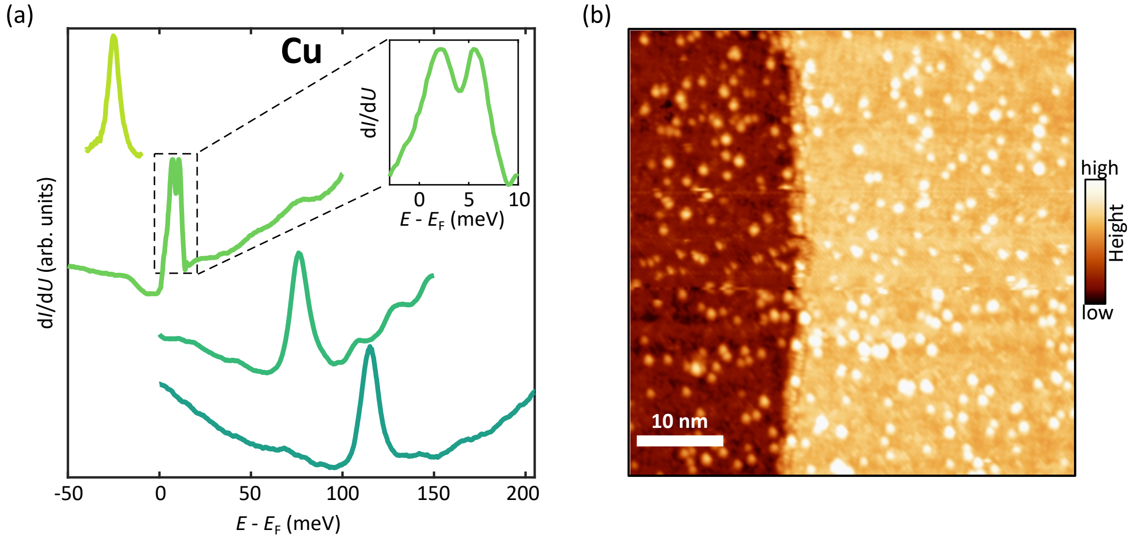

Figure 4.14: (a) STS spectra acquired at the half-unit cell step, evidencing a clear splitting of the 1D flat band as Cu doping increases. Two distinct peaks are visible close to E_F. As the Dirac point is tuned below the Fermi level, the double peak structure collapses into a single peak, indicating the recovery of the original 1D flat band state. (b) STM topography illustrating the Cu adatoms on the surface. Scanning parameters: I_t = 10 pA, V_b = 500 mV. Stabilization parameters for a: I_t = 150 pA, V_b = 200 mV, 150 mV, 100 mV, -40 mV, V_{mod} = 2.5 mV.

region of the sample was measured before and after the deposition of the atoms by following the defects as a guide to the eye (see figure 4.3a and 4.7b). As discussed above, it is evident that the splitting phenomenon of the 1D flat band into two distinct peaks exists for doping the pristine $\mathrm{Pb}_{1-x}\mathrm{Sn}_x\mathrm{Se}$ crystals with magnetic elements that have a high as well as a low magnetic moment ($\mu_{\mathrm{Cr}} > \mu_{\mathrm{Mn}} > \mu_{\mathrm{Fe}} > \mu_{\mathrm{Cu}}$). Figure 4.15a shows a distribution of the energy splitting as a function of the different magnetic dopants. The multiple data points for Cr correspond to the different experimental attempts indicating a distribution of the splitting magnitude, which is not associated with a particular element but can be ascribed to the intrinsic inhomogeneities in the sample as well as due to the disorder created by the random distribution of the dopants. This indicates that the splitting magnitude is not influenced by the magnetic moment of the dopant atoms. Figure 4.15b shows a comparison of the splitting magnitude for samples characterized by a varying concentration of Cr dopants. The inset highlights the STM topography of the regions where the respective $\mathrm{d}I/\mathrm{d}U$ spectra were acquired. An inverse scaling relation of the splitting magnitude with doping concentration (or disorder) is observed. For a doping concentration of two atoms per 20 nm^2 area (right panel of figure4.15b), the splitting magnitude significantly reduces to $\Delta E \sim 3$ meV, as compared to the case of just one atom within the same area (left panel of figure 4.15b). This data provides evidence that an increasing surface disorder has a detrimental effect on the splitting. It is important to note that under doping with alkali or non-magnetic atoms, which are also known to create a downward band bending, the splitting of the 1D flat band close to the Fermi level should be observed. The above discussion universally supports the previously drawn conclusion for doping with Cr atoms, that the evolution of the electronic properties of the 1D flat band close to the Fermi level, primarily drives the splitting of the peak associated with the 1D flat band.

While the splitting of the peak associated with the 1D flat band into a double peak structure was predominantly observed, frequently it was seen that each peak of this doublet was further split into another set of peaks, resulting in a total of

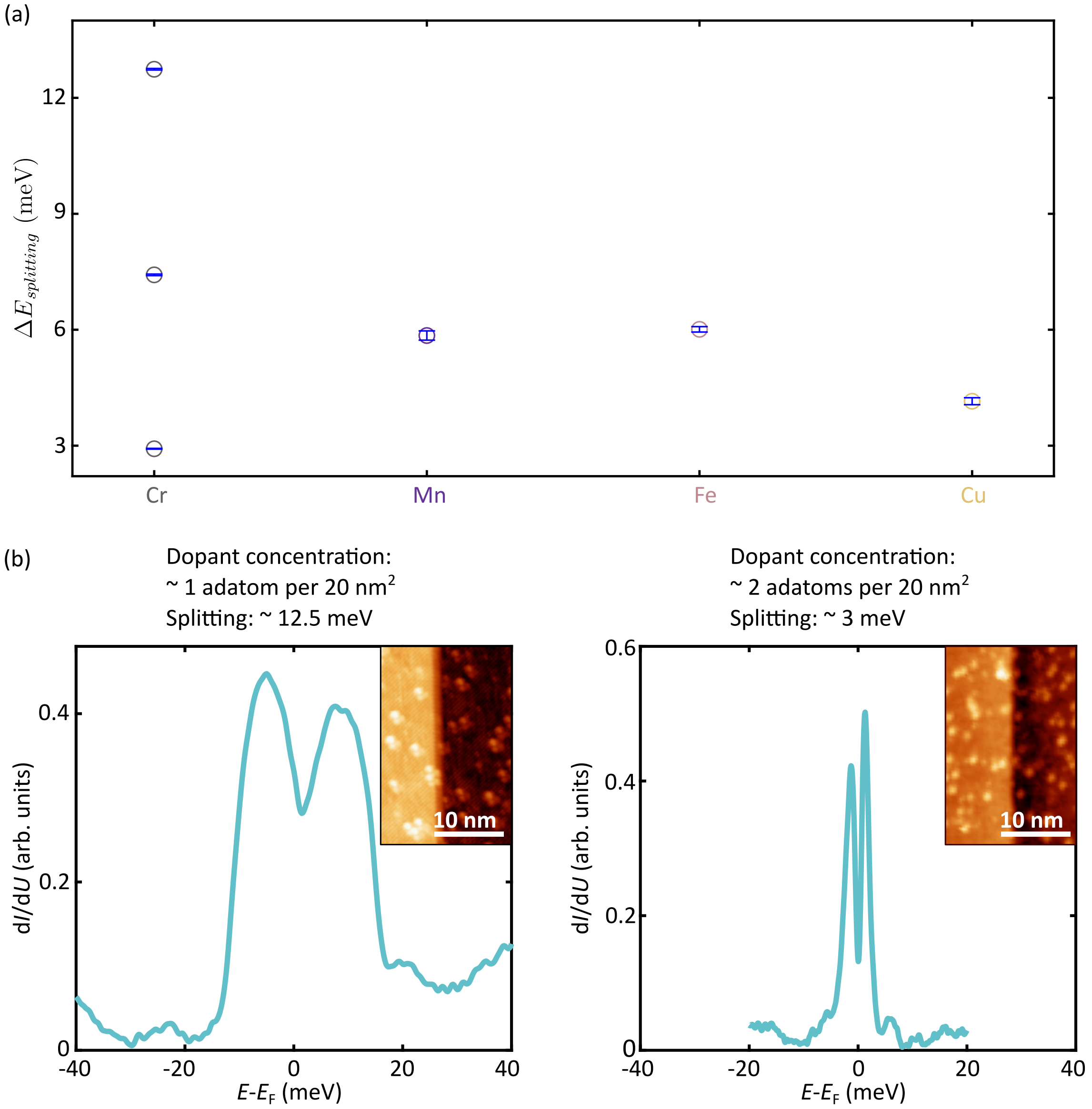

Figure 4.15: (a) Magnitude of the energy splitting as a function of the doping with Cr atoms. The peak positions are obtained by a Gaussian fitting of the dI/dU peaks. (b) Comparison of the splitting magnitude for a surface characterized by a varying concentration of surface dopants. A higher surface dopant concentration leads to a reduced splitting magnitude. Stabilization parameters for b: I_t = 150 pA, V_b = 40 mV, 20 mV, V_{mod} = 1.5 mV

four peaks. This is shown in figure 4.16, which reports STS spectra acquired at the different half-unit cell steps of the same as well as different samples, revealing the splitting of each peak into a doublet characterized by varying intensities. Interestingly, the spectra also feature a suppression of the LDOS at the Fermi level, potentially suggesting the previous speculation that it might be a correlation-driven instability. However, it is to be noted that while suppression of the LDOS at the

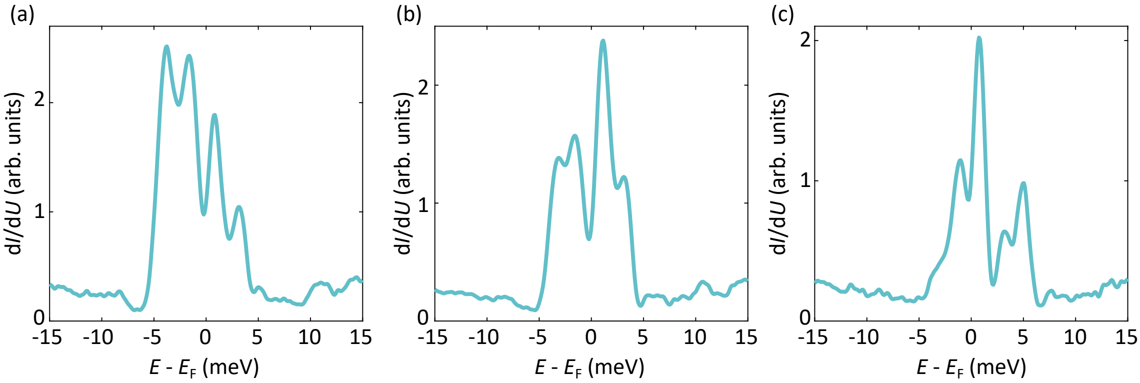

Figure 4.16: Splitting of each of the two peaks into a doublet resulting in a total of 4 peaks. The spectra are obtained at the different half-unit cell step edges of the same sample as well as different samples demonstrating peaks characterized by different intensities accompanied by a suppression of the LDOS at the Fermi. Stabilization parameters for a, b and c: $\mathrm{I}_t = 150$ pA, $\mathrm{V}_b = 15$ mV, $\mathrm{V}_{mod} = 1.5$ mV.

Fermi level is always observed, the splitting of each of the two peaks into a doublet is a subtle phenomenon that can easily be hindered due to Fermi broadening, intrinsic inhomogeneities in the crystal (bandwidth of the 1D flat band) as well as extrinsic ones such as the disorder induced by the random distribution of the dopants, which was shown to have a detrimental effect on the splitting. This explains the more frequent observation of the 2-peak scenario. However under ideal conditions *i.e.*, zero disorder, and absolute zero temperatures, the splitting of the 1D flat band into 4 peaks should always be detectable in the experiments. The following section will present a theoretical interpretation of the splitting of the 1D flat band into the 2-peak and 4-peak structure.

4.3 Theoretical interpretation of the 1D flat band splitting

This section begins by modeling the edge states through a toy model, followed by a theoretical explanation, supported by Hartree-Fock calculations, of how the 1D flat band's single peak splits into a multi-peak structure. These theoretical developments were conducted in collaboration with researchers from the University of Zurich and Julius-Maximilians-Universität Würzburg.

4.3.1 Theoretical understanding of the edge modes

The origin of the peak-like feature in the LDOS leading to the edge modes at the half-unit cell step can be explained by considering a toy model. In the introductory section, it was shown that the 4 Dirac cones on the (001) surface of $\mathrm{Pb}_{1-x}\mathrm{Sn}_x\mathrm{Se}$ can be derived by solving the perturbation Hamiltonian in eq. 3.4. The toy model employed here to explain the accumulation of the edge modes at the half-unit cell step incorporates the 4 Dirac cones in a way as illustrated in figure 4.17. The Hamiltonian corresponding to the toy model is as given below:

$$H = v_F[(p_y - \kappa_y)\sigma_x - (p_x - \kappa_x)\sigma_y] \tag{4.1}$$

where $p_j = -i\partial_j$ and σ_j are the Pauli spin matrices, v_F is the Fermi velocity and k_x is wave vector along the step edge. The valleys are labeled by the two pseudospin degrees of freedom τ_j and η_j. As was shown in ref. [152], the effect of the half-unit cell step was accounted for by the translation operator $-\tau_z$. It has been previously shown that the effect of the operation of $-\tau_z$ on the Hamiltonian $(-\tau_z\mathrm{H}-\tau_z)$ is to transform to a separate Hamiltonian that describes a terrace that is separated from another terrace by a single atomic step (half-unit cell step) [152], thereby defining two domains (terraces) separated by the domain wall (step edge). The distinction of the Hamiltonian on the terraces is accounted for by the term “m” which has an opposite sign on either domain as schematically shown in the schematic of a single atomic step on the right of figure 4.17. Here, a similar approach is undertaken where the exchange of valleys accounts for the sign of the “m” term as explained below. The toy model used here to explain the formation of the edge states considers that the two Dirac cones from the two valleys are shifted by k along the direction parallel to the step edge, *i.e.* k_x, characterized by τ values of opposite sign (red and blue color are used to distinguish the Dirac cones in the two valleys). This shift is considered to be opposite for the region $\mathrm{y} < 0$ (terrace A) and $\mathrm{y} < 0$ (terrace B) as schematically illustrated in figure 4.17. This implies that the valleys are exchanged across the $\mathrm{y} =$

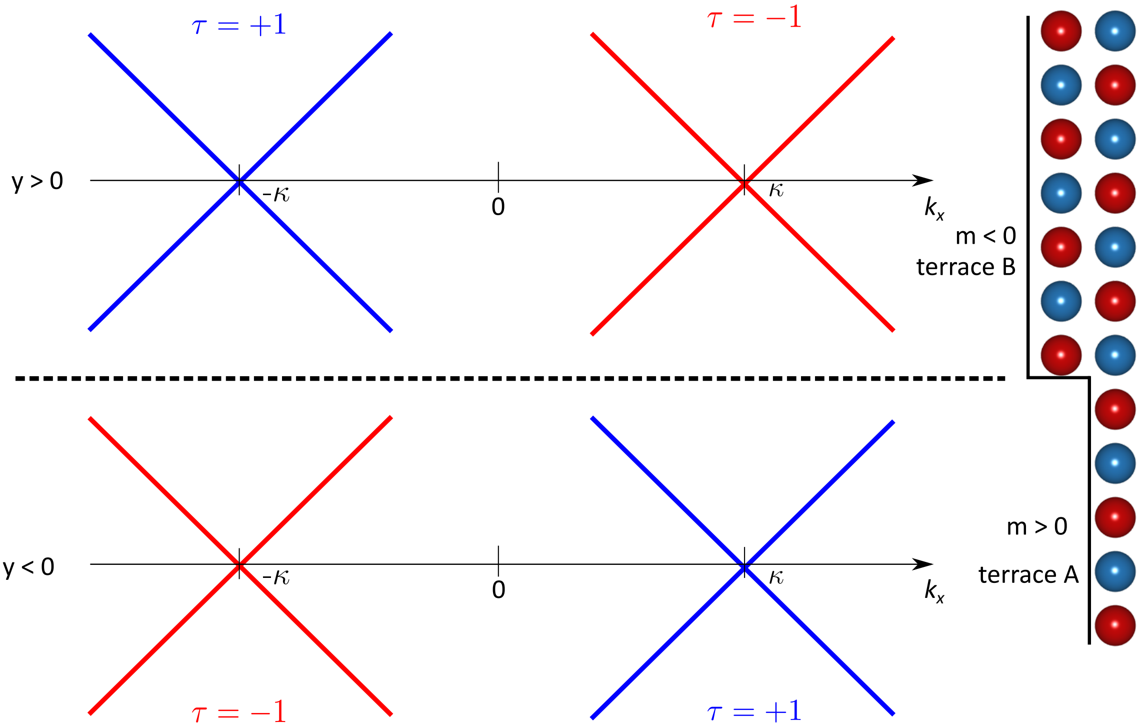

Figure 4.17: Schematic of the toy model corresponding to eq 4.1, showing the 4 Dirac cones shifted by an amount k along the x-axis. The shift is taken to be opposite for y< 0 and y> 0; in this way, the edge mode is obtained at y=0. The schematic of two terraces separated by an atomic step is illustrated on the right.

0 plane, thereby manifesting as a step edge at y = 0: $(\kappa_x, \kappa_y) = \kappa(\tau_z \text{sign}(y), \eta_z)$. The eigenstates of the Hamiltonian are defined by the eigenvalues σ_z, τ_z and η_z labeled as σ , τ and η. Solving the Hamiltonian yields two pairs of zero energy modes (zero energy here corresponds to the Dirac point [30]) with a very flat dispersion localized around y = 0 with opposite spin polarization in either valley, represented by the wave functions below:

$$\Psi_{k_x\tau\eta} \equiv e^{ik_x x} u_{k_x\tau\eta}(y) = e^{ik_x x + i\kappa\eta y} \begin{cases} e^{-|k_x - \tau\kappa| y}, & y > 0. \\ e^{|k_x + \tau\kappa| y}, & y < 0. \end{cases} \tag{4.2}$$

The above model predicts that the bands are completely flat, however, in ref. [26] and [30] it has been shown using a three-dimensional microscopic model, that breaking the particle-hole symmetry, causes a finite dispersion ($\sim$ a bandwidth of 100 meV) and shifts the bands away from zero energy, thereby motivating the following model

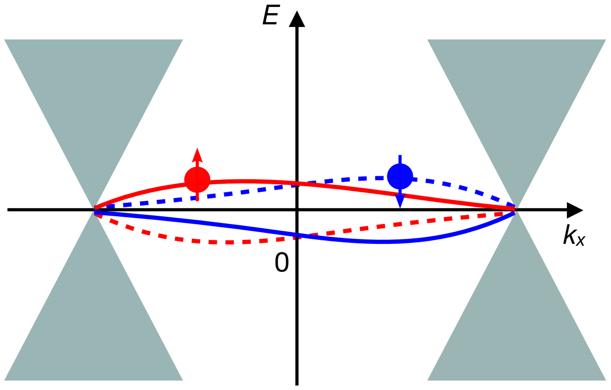

$$\Psi_{\tau\eta k_x} = e^{ik_x x + i\kappa\eta y} \begin{cases} e^{-|k_x - \tau\kappa| y}, & y > 0. \\ e^{|k_x + \tau\kappa| y}, & y < 0. \end{cases}$$

Figure 4.18: Schematic representation of the 4 edge modes with opposite spin polarization in the two valleys connecting the 2 Dirac states.

for the dispersion for a more realistic description of the edge modes:

$$\epsilon_{k_x \tau\eta} = W\eta\left(\tau cos\frac{\pi k_x}{2\kappa} + \frac{1}{5} sin\frac{\pi k_x}{\kappa}\right) \tag{4.3}$$

where W is the bandwidth. The inclusion of the dispersion term can be further substantiated by following the peak in the experimental LDOS, which is not very flat (a broadening can be observed) and has an effective bandwidth, $W \sim 18.29 \pm 0.49$ meV. After adding the dispersion term, the band structure reflects the one shown in the schematic illustration in figure 4.18 featuring the two pairs of narrow dispersing edge modes connecting the surface Dirac cones. These low-dispersing bands connecting the two Dirac SS account for a significant portion of the spectral weight at the half-unit cell step edge (see right panel of figure 4.3c). Within each valley, each of these bands is spin-polarized, however, the other valley contains its $\mathcal{T}$ counterpart, hence the net magnetization is zero. It is speculated that only one of the VHSs appears as a peak in the edge LDOS since the other VHS occurs where the flat band and the Dirac cone merge. Comparing the theoretical toy model for the narrow dispersing bands with the experimentally observed peak in the LDOS, it can be safely concluded that the half-unit cell step edge embodies flat bands running along the entire 1D channel.

4.3.2 1D flat-band Stoner ferromagnetism

The edge modes in the present system are very similar to those observed in zigzag graphene nanoribbons. In the case of graphene nanoribbons, it was initially theoretically predicted that the zigzag edge of graphene features edge states having a flat dispersion at the Fermi level [153, 154]. From the theoretical analysis of the charge density distribution, it was observed that the electron wave function was predominantly localized along the zigzag edge [155]. These localized states at the edge manifest as a sharp peak at zero bias in the DOS. The presence of the flat band at the edge, coupled with its proximity to E_F facilitates electron-electron interactions, potentially leading to a magnetic ground state. Fujita *et al.* utilized the Hubbard model for the zigzag edge of graphene and solved for the magnetic structure using the Hartree-Fock (HF) approximation, which is known to uncover the magnetic structure of a system [153]. The model revealed a ferromagnetic intra-edge coupling and an antiferromagnetic inter-edge coupling. While the intra-edge ferromagnetic coupling was attributed to the exchange interactions arising from the electron spins of the same sublattice, the inter-edge antiferromagnetic coupling was attributed to the magnetization arising from two different sublattices at either edge. Similarly, it was also demonstrated in mean-field approximations that the edge of nodal *d*-wave superconductors exhibits Majorana flat bands which are unstable in the presence of interactions due to their diverging DOS, leading to a ferromagnetic state along the edge which manifests as a splitting of the flat band [156].

Tao *et al.* experimentally demonstrated the presence of spin-polarized edge states in chiral (8,1) graphene nanoribbons using low-temperature STM/STS measurements [157]. These edge states were exclusively observed along the zigzag edge, manifesting as two energy-split peaks straddling the E_F in the STS measurements instead of a single peak. Theoretical calculations revealed that electron-electron interactions are responsible for driving a ferromagnetic coupling along the zigzag edge leading to a spin-polarization of the edge modes, and a subsequent splitting of the single peak associated with the flat band into a set of VHS at the graphene nanoribbon edge, indicating an instability at the Fermi level. The two peaks observed in the experiments near the Fermi level were identified with the pair of lowest-energy VHS flanking the Fermi level obtained from the theory. STM studies by Song *et al.* also demonstrated such splitting of peaks under an applied magnetic field in epitaxial Graphene by studying the Landau level spectra. It was shown that when the Fermi level lies within the four-fold degenerate $N = 1$ Landau level, strong electron-electron interactions lead to a significantly increased valley and electron spin splitting depending upon the filling factor (ν) of the bands [158].

Given the close resemblance between the observed edge states in $\mathrm{Pb}_{1-x}\mathrm{Sn}_x\mathrm{Se}$ and those found in the zigzag edge of chiral graphene nanoribbons, a similar theoretical approach was undertaken to account for the splitting of the 1D flat band. However, it is to be noted that there are a couple of differences between graphene and the TCI under investigation here. Firstly, the number of flat bands in the present case is double that of graphene nanoribbons *i.e.* four instead of two, and secondly, $\mathrm{Pb}_{1-x}\mathrm{Sn}_x\mathrm{Se}$ exhibits a strong SOC, so unlike graphene, the edges modes here are not spin-degenerate. It should also be noted that theoretical calculations [21] and experimental demonstrations [25] have revealed that under an external magnetic field, the SS of $\mathrm{Pb}_{1-x}\mathrm{Sn}_x\mathrm{Se}$ are driven into the integer QHS, exhibiting Landau level peaks. Therefore, the edge states under examination here share similar characteristics to those observed in Quantum Hall systems but without any applied magnetic field. This suggests that the Landau gauge orbitals of the form in eq. (4.4) can be used for the analysis.

$$\psi_{k_x\tau\eta}(x,y) \equiv \frac{1}{\sqrt{L_x}} e^{ik_x x} u_{k_x\tau\eta}(y) = \frac{1}{\sqrt{L_x}} e^{ik_x x + i\kappa\eta y} \begin{cases} e^{-|k_x - \tau\kappa| y}, & y > 0 \\ e^{|k_x + \tau\kappa| y}, & y < 0 \end{cases} \tag{4.4}$$

Here $-\kappa < k_x < \kappa$ and L_x is the length of the system in the x-direction. The

Hamiltonian of the form

$$H_{\text{HF}} = H_{\text{kin}} + H_{\text{int,HF}} \tag{4.5}$$

can be defined. The derivation of each term following the HF formalism in ref. [144] is provided below. The system has time-reversal and mirror symmetries and the effect of their operation on $\psi_{k_x\tau\eta}$ is provided below:

$$\mathcal{T} : \psi_{-k_x\bar{\tau}\bar{\eta}}(x,y) = \psi^*_{k_x\tau\eta}(x,y) \tag{4.6}$$

$$\mathcal{M}_y : \psi_{k_x\bar{\tau}\bar{\eta}}(x,y) = \psi_{k_x\tau\eta}(x,-y) \tag{4.7}$$

$$\mathcal{M}_x : \psi_{k_x\bar{\tau}\eta}(x,y) = \psi_{-k_x\tau\eta}(-x,y) \tag{4.8}$$

$$\mathcal{P} : \psi_{k_x\tau\bar{\eta}}(x,y) = \psi_{-k_x\tau\eta}(-x,-y) \tag{4.9}$$

It is to be noted that $\mathcal{T}$ operator flips both spin τ and valley η and changes $k_x \to -k_x$. The goal is to project the Coulomb interaction onto the Hilbert space of these edge states or the 1D flat bands. The interaction term accounting for the electron-electron interaction is as given below:

$$H_{\text{int}} = \frac{1}{2} V_{\alpha\beta\gamma\delta} c^\dagger_\alpha c^\dagger_\beta c_\delta c_\gamma, \tag{4.10}$$

where the short-hand label $\alpha = (k^\alpha_x, \tau^\alpha, \eta^\alpha)$ has been used, and the matrix elements obtained from the projection of the Coulomb interaction onto the flat bands (see eq. (4.2) and figure 4.18) are,

$$\begin{aligned} V_{\alpha\beta\gamma\delta} &= \langle \psi_\alpha \psi_\beta | \hat{V} | \psi_\delta \psi_\gamma \rangle \\ &= \int_{\vec{r},\vec{r}'} \psi^*_\alpha(\vec{r}) \psi^*_\beta(\vec{r}') V(\vec{r}-\vec{r}') \psi_\delta(\vec{r}) \psi_\gamma(\vec{r}') \\ &= \frac{1}{L_x^2} \sum_{q_x} \int_{q_y} \int_{\vec{r},\vec{r}'} e^{-ik^\alpha_x x - ik^\beta_x x' + ik^\delta_x x + ik^\gamma_x x' + iq_x(x-x') + iq_y(y-y')} V_q \times \\ & u^*_{k^\alpha_x \tau^\alpha \eta^\alpha}(y) u^*_{k^\beta_x \tau^\beta \eta^\beta}(y') u_{k^\delta_x \tau^\delta \eta^\delta}(y) u_{k^\gamma_x \tau^\gamma \eta^\gamma}(y'), \end{aligned} \tag{4.11}$$

where $V_q = \frac{2\pi}{L_x}\frac{e^2}{2\epsilon_0 q}$. The (unnormalized) form factors are defined as:

$$\tilde{\lambda}_{\alpha\delta}(k_x^\alpha, k_x^\delta, q_y) = \int_y u^*_{k_x^\alpha \tau^\alpha \eta^\alpha}(y) u_{k_x^\delta \tau^\delta \eta^\delta}(y) e^{iq_y y}. \tag{4.12}$$

The form factors can be derived analytically by using eq. (4.4) and they are obtained as given below:

$$\begin{aligned}\tilde{\lambda}_{\alpha\delta}(k_x^\alpha, k_x^\delta, q_y) = {} & \frac{i\kappa(\eta^\alpha - \eta^\delta) + iq_y + |k_x^\alpha - \tau^\alpha\kappa| + |k_x^\delta - \tau^\delta\kappa|}{(\kappa(\eta^\alpha - \eta^\delta) + q_y)^2 + (|k_x^\alpha - \tau^\alpha\kappa| + |k_x^\delta - \tau^\delta\kappa|)^2} \\ & + \frac{-i\kappa(\eta^\alpha - \eta^\delta) - iq_y + |k_x^\alpha + \tau^\alpha\kappa| + |k_x^\delta + \tau^\delta\kappa|}{(\kappa(\eta^\alpha - \eta^\delta) + q_y)^2 + (|k_x^\alpha + \tau^\alpha\kappa| + |k_x^\delta + \tau^\delta\kappa|)^2}.\end{aligned} \tag{4.13}$$

It is to be noted that the wave functions in eq. (4.4) are not normalized so the normalized form factors need to be calculated using

$$\lambda_{\alpha\delta}(k_x^\alpha, k_x^\delta, q_y) = \frac{\tilde{\lambda}_{\alpha\delta}(k_x^\alpha, k_x^\delta, q_y)}{\sqrt{\tilde{\lambda}_{\alpha\alpha}(k_x^\alpha, k_x^\alpha, 0)\tilde{\lambda}_{\delta\delta}(k_x^\delta, k_x^\delta, 0)}}. \tag{4.14}$$

The form factors have the form

$$\begin{aligned}\lambda(k_x^\alpha, k_x^\delta, q_y) = {} & (\Lambda^0(k_x^\alpha, k_x^\delta, q_y)\tau^0 + \Lambda^0(-k_x^\alpha, k_x^\delta, q_y)\tau^x)\eta_0 \\ & + (\Lambda^\times(k_x^\alpha, k_x^\delta, q_y)\tau^0 + \Lambda^\times(-k_x^\alpha, k_x^\delta, q_y)\tau^x)\eta_x.\end{aligned} \tag{4.15}$$

This transforms the matrix elements into,

$$V_{\alpha\beta\gamma\delta} = \sum_{q_x}\int_{q_y} \delta_{q_x - k_x^\alpha + k_x^\delta, 0}\delta_{-q_x - k_x^\beta + k_x^\gamma, 0}\lambda_{\alpha\delta}(k_x^\alpha, k_x^\delta, q_y)\lambda^*_{\gamma\beta}(k_x^\gamma, k_x^\beta, q_y)V(q_x, q_y) \tag{4.16}$$

$$= \delta_{k_x^\alpha + k_x^\beta = k_x^\gamma + k_x^\delta}\int_{q_y} \lambda_{\alpha\delta}(k_x^\alpha, k_x^\delta, q_y)\lambda^*_{\gamma\beta}(k_x^\gamma, k_x^\beta, q_y)V(k_x^\alpha - k_x^\delta, q_y), \tag{4.17}$$

where the Kronecker delta in the last line ensures the conservation of momentum in the x-direction. Next, a mean-field decoupling of the Hamiltonian below is performed

$$H_{\text{int,HF}} = V_{\alpha\beta\gamma\delta}(c^\dagger_\alpha c_\delta \langle c^\dagger_\beta c_\gamma\rangle - c^\dagger_\alpha c_\gamma \langle c^\dagger_\beta c_\delta\rangle). \tag{4.18}$$

A projector $P_{\alpha\beta} = \langle c_\alpha^\dagger c_\beta \rangle$ defines a Slater determinant. Considering the translational invariance along the x-direction, $P_{\alpha\beta}$ can be obtained as,

$$P_{\alpha\beta}(k_x^\alpha, k_x^\beta) = \langle c_\alpha^\dagger(k_x^\alpha) c_\beta(k_x^\beta) \rangle = \delta_{k_x^\alpha, k_x^\beta} \langle c_\alpha^\dagger(k_x^\alpha) c_\beta(k_x^\alpha) \rangle \equiv \delta_{k_x^\alpha, k_x^\beta} P_{\alpha\beta}(k_x^\alpha). \tag{4.19}$$

Considering the above simplification, the HF Hamiltonian reduces to

$$\begin{align} H_{\text{int,HF}} &= V_{\alpha\beta\gamma\delta}(c_\alpha^\dagger(k_x^\alpha) c_\delta(k_x^\alpha) P_{\beta\gamma}(k_x^\beta) \delta_{k_x^\beta, k_x^\gamma} - c_\alpha^\dagger(k_x^\alpha) c_\gamma(k_x^\alpha) P_{\beta\delta}(k_x^\beta) \delta_{k_x^\beta, k_x^\delta}) \tag{4.20} \\ &= V^D_{\alpha\beta\gamma\delta}(k_x^\alpha, k_x^\beta) P_{\beta\gamma}(k_x^\beta) c_\alpha^\dagger(k_x^\alpha) c_\delta(k_x^\alpha) - V^E_{\alpha\beta\gamma\delta}(k_x^\alpha, k_x^\beta) P_{\beta\delta}(k_x^\beta) c_\alpha^\dagger(k_x^\alpha) c_\gamma(k_x^\alpha), \tag{4.21} \end{align}$$

where the momentum-conserving Kronecker delta has been used. This allows for defining the direct and exchange matrix elements as given below:

$$\begin{align} V^D_{\alpha\beta\gamma\delta}(k_x^\alpha, k_x^\beta) &= \int_{q_y} \lambda_{\alpha\delta}(k_x^\alpha, k_x^\alpha, q_y) \lambda^*_{\gamma\beta}(k_x^\beta, k_x^\beta, q_y) V(0, q_y), \tag{4.22} \\ V^E_{\alpha\beta\gamma\delta}(k_x^\alpha, k_x^\beta) &= \int_{q_y} \lambda_{\alpha\delta}(k_x^\alpha, k_x^\beta, q_y) \lambda^*_{\gamma\beta}(k_x^\alpha, k_x^\beta, q_y) V(k_x^\alpha - k_x^\beta, q_y). \tag{4.23} \end{align}$$

To this interaction Hamiltonian, the kinetic component can be added

$$H_{\text{kin}} = \epsilon_\alpha(k_x) c_\alpha^\dagger(k_x) c_\alpha(k_x) \tag{4.24}$$

with the phenomenological band structure given by eq. (4.3) (modeled after the key features of the bandstructure found in [26]). Next, a mean-field approximation of the Hamiltonian (eq. (4.5)) was employed to narrow down the many-body problem into a single-body problem, and the HF calculations were performed to solve H_{HF} self-consistently. For details on the theory, refer to [144].

Given that, the observed electronic effects are confined to the surface, a 2D model is appropriate for describing the system, so the 2D Coulomb interaction term, $V = \frac{e^2}{2\epsilon_0 q}$ can be used here. Consideration of the 3D bulk would merely lead to a re-normalization of the dielectric constant. Based on the discussion above, the entire

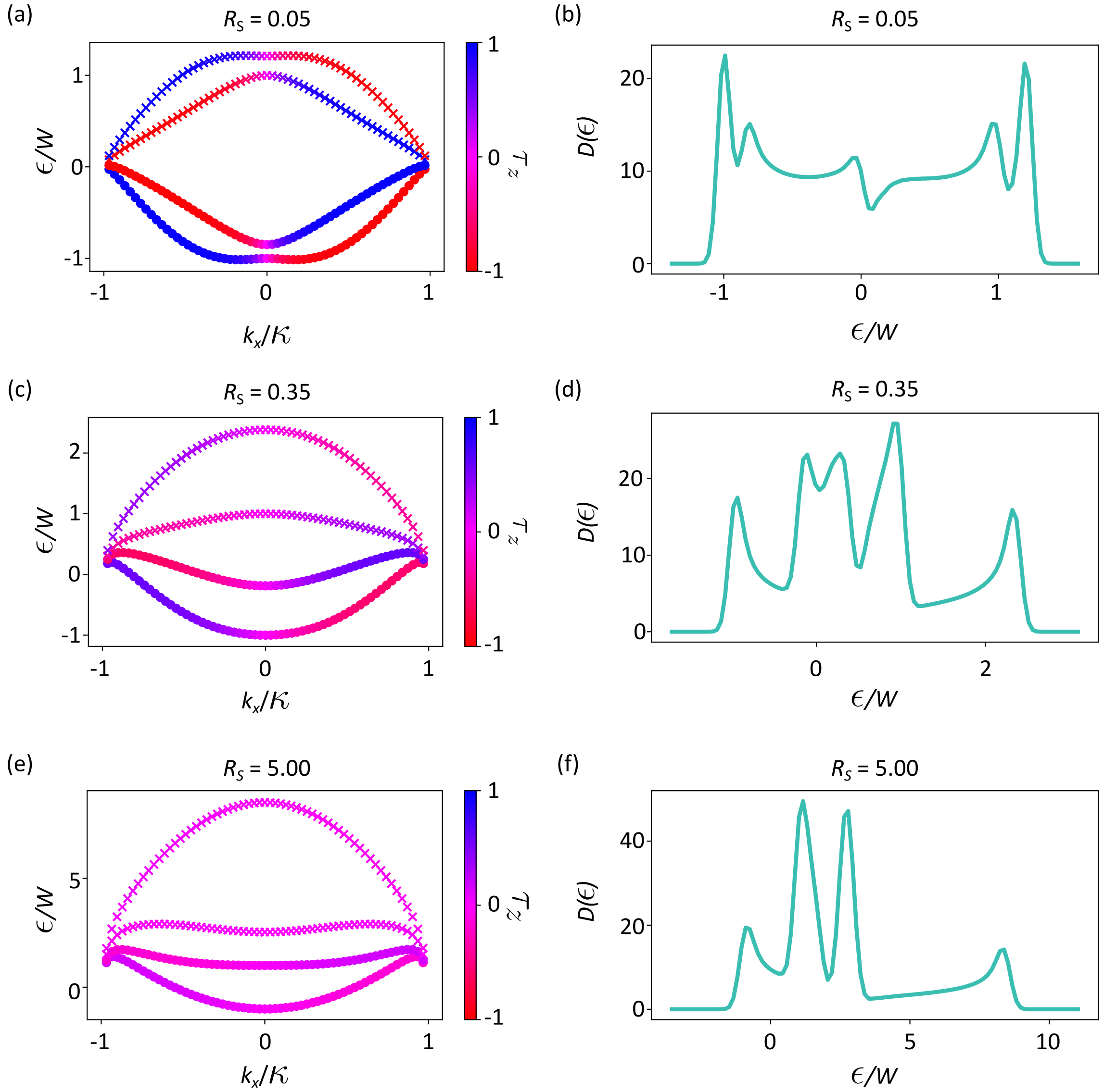

Figure 4.19: Results obtained from the Hartree-Fock calculations for varying strength of interaction quantified by the phenomenological parameter R_s. (a) R_s = 0.05 corresponds to weak interactions causing a splitting of the 1D flat band into 2 main peaks. (b) R_s = 0.35 corresponds to moderately strong interactions leading to a splitting of the 1D flat band into 4 peaks the separation of which is given by the interaction term V. (c) R_s = 5 corresponds to strong Coulomb interactions which cause complete hybridization between all the 4 bands with opposite spin, leading to 4 peaks in the DOS which are well separated in energy.

problem can be solved by considering the interplay between two energy scales, the kinetic energy scale related to the bandwidth W and the Coulomb energy scale, $V = \frac{e^2\kappa}{2\epsilon_0}$. This incorporates two dimensionless parameters in the model, $\bar{\kappa} = \kappa a$, and $R_s = V/W$, where the phenomenological parameter R_s denotes the strength of the interactions. Here, the role of $\bar{\kappa}$ is minimal, so it will not affect the results qualitatively, hence $\bar{\kappa}$ is fixed to 0.5 in line with ref. [26]. Therefore, the HF analysis results

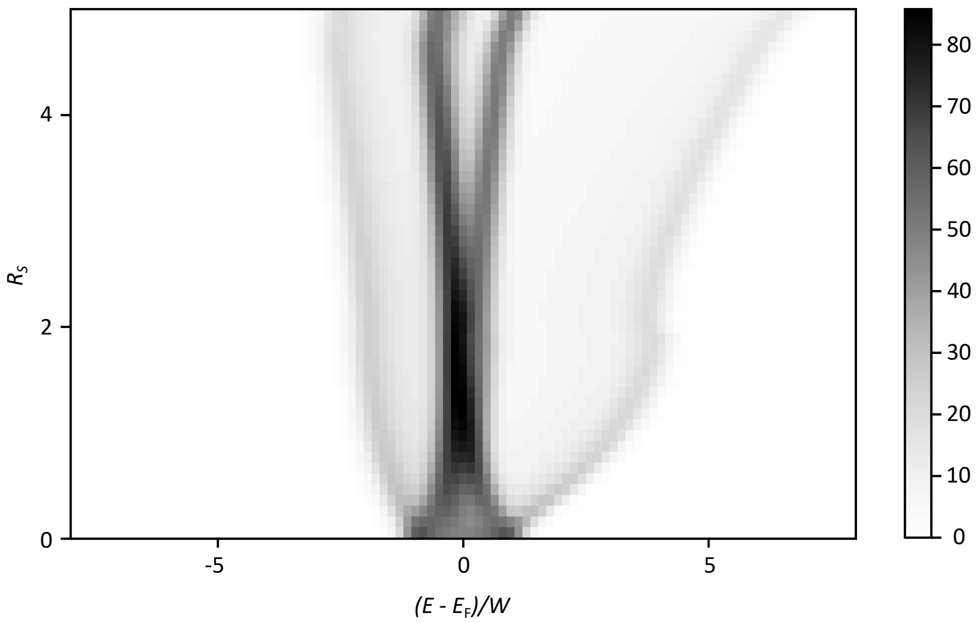

Figure 4.20: Continuous evolution of the splitting of the 1D flat band as a function of increasing interaction strength.

would depend solely on R_s. To solve the Hamiltonian, the filling factor is considered to be half. Now, the theoretical results will be presented for different values of R_s. As depicted in the energy dispersion in figure 4.19a, when the kinetic energy scale dominates *i.e.* $R_\mathrm{s} \ll 1$, the valence band (η = -1) subspace is entirely filled and Coulomb interactions cause a weak hybridization between the two bands with opposite spin polarization at the band crossings in both the valleys. This hybridization, although weak, spontaneously breaks $\mathcal{T}$ symmetry, causing the splitting of the 1D flat into two peaks, as depicted in the calculated DOS in figure 4.19b, where the peak-to-peak separation is given by W. When the kinetic energy and Coulomb energy scales are comparable *i.e.*, $R_\mathrm{s} \sim 1$, the separation between the conduction and valence band persists (∼W). However, the interactions being slightly stronger, the opposite spin bands in the conduction and valence bands are now fully hybridized, creating bonding and anti-bonding orbitals, separated by an amount V, leading to eventually 4 peaks in the DOS. The energy dispersion and the corresponding DOS are shown in figure 4.19c and d. Now, the final case will be discussed, where the Coulomb energy scale dominates and the kinetic energy scale is insignificant. As shown in figure 4.19e, when $R_\mathrm{s} \gg 1$, the large interactions lead to a complete intermixing between all four bands forming bonding and anti-bonding orbitals. However, due to the presence of spin and valley degrees of freedom, these bonding and anti-bonding orbitals can be formed in both cases, leading to the formation of 4 peaks in the DOS as depicted in figure 4.19, where the splitting is given by V. Figure 4.20 shows the gradual splitting of the peak with increasing strength of the interactions. When interactions are small, the peaks are positioned pretty close in energy, so it is challenging to detect them in the experiments due to the finite energy resolution, which explains the observation of two peaks frequently in the experiments. However, the increasing strength of interactions causes the peaks to be split far apart in energy, which makes their detection in the experiments easier, hence, the 4 peaks can be observed in the experimental LDOS.

Both experimental observation and theoretical calculations indicate that the bands in the vicinity of E_F have a flat dispersion, thereby characterized by a diverging DOS (D(E_F)). The localization of these bands close to the Fermi level makes them highly susceptible to electron-electron correlations. This is why, when the interactions (R_s) are invoked, the Stoner criteria $D(E_F)R_s{>}1$ is satisfied. According to the model developed by E. Stoner [159], the dispersion relation for spin-up and spin-down electrons can be written as,

$$E_\uparrow(k) = \epsilon(k) - R_s\frac{n_\uparrow - n_\downarrow}{n}, E_\downarrow(k) = \epsilon(k) + R_s\frac{n_\uparrow - n_\downarrow}{n} \tag{4.25}$$

where $\epsilon(k)$ corresponds to the dispersion of the spinless electrons without interactions, R_s is the interaction strength, $n_\uparrow$ and $n_\downarrow$ correspond to the number of up-spin and spin-down electrons in the entire system, and the total number of electrons is given by $n = n_\uparrow + n_\downarrow$. The second term in the above equation corresponds to the exchange energy term. With the total number of electrons in the system fixed, it is possible to calculate the net energy of the system using eq. (4.25), as a function of the spin polarization given by, $P_s{=}\frac{n_\uparrow - n_\downarrow}{n}$. In the event of a ground state with $P_s = 0$, a paramagnetic state will be favored, however as R_s becomes large, the condition

$D(E_F)R_s > 1$ is fulfilled, leading to a transition to a spin-polarized ground state even when $P_s = 0$. Therefore, the exchange energy term plays a crucial role, splitting the different spin states, resulting in spin-polarized states at the Fermi level. This spin polarization driven by the Stoner criterion eventually leads to a 1D flat band Stoner ferromagnetism along the half-unit cell 1D step edge of $\mathrm{Pb}_{1-x}\mathrm{Sn}_x\mathrm{Se}$.

4.4 Conclusion

Using a combination of low-temperature STM and STS, the step edges on the (001) surface of $\mathrm{Pb}_{0.7}\mathrm{Sn}_{0.3}\mathrm{Se}$ were investigated. The STS measurements reveal that the half-unit cell step edges embody 1D flat bands, manifesting as a peak in the LDOS at $E_\mathrm{D} = 125$ meV, above the Fermi level. By utilizing the surface doping technique, the single peak of the 1D flat band was shown to split into 2 or 4 peaks once the 1D flat band is tuned to the Fermi level, accompanied by the opening of a gap in the electronic spectrum at the Fermi level. A theoretical model was developed to describe the 1D edge modes hosting the 1D flat bands, and Hartree-Fock analysis was performed to investigate the effect of the interactions. From the theory, it was unveiled that the interactions act as symmetry-breaking perturbations. Since the bands are flat, this indicates a large DOS localized in a narrow energy window of E_F, which significantly strengthens electron-electron interactions. Depending on the strength of these interactions, defined as the ratio of the Coulomb energy and the kinetic energy, the single peak of the 1D flat band is split up to a maximum of 4 peaks due to the hybridization between the spin-polarized flat bands. These 4 states spontaneously break $\mathcal{T}$ symmetry, leadiong to a flat band Stoner ferromagnetism along the 1D edge, which also opens up additional correlation gaps as observed in the STM measurements.

Part IV

Unconventional topological superconductivity in a van der Waals heterostructure

5 Superconductivity and Magnetism

This chapter lays a theoretical groundwork starting with a historical context of superconductivity, followed by an introduction to conventional BCS theory and a progression towards p-wave superconductivity. A mathematical treatment, incorporating a gap function example, is presented to briefly introduce p-wave TSC. The distinction between chiral and helical p-wave superconducting phases is subsequently discussed. Finally, it concludes with a brief exploration of 2D van der Waals materials, establishing a foundation for the experimental findings presented in the next chapter.

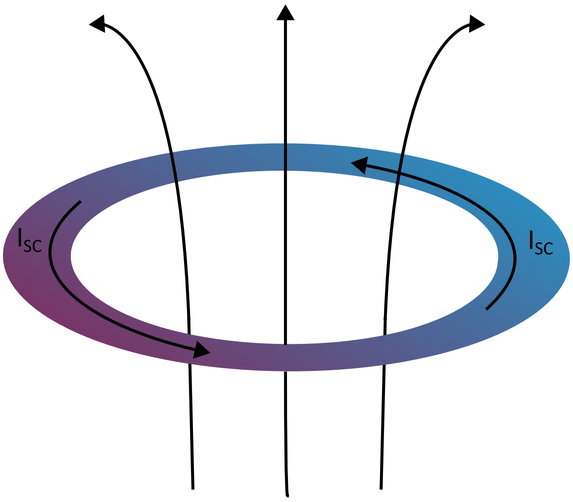

Persistent flow of supercurrents in a superconducting ring

5.1 Overview of Superconductivity

More than 100 years ago, the successful liquefaction of Helium by Kammerling Onnes and his sleepy young trainee established a novel research direction in condensed matter physics, which to date remains one of the most extensively studied research fields. Having achieved the means to liquefy Helium, which would allow reaching low temperatures of the order of a few Kelvin, opened up the possibility of exploring the resistivity of different solids as a function of temperature. In the early days, Onnes was highly interested in finding out the electrical response of metals when cooled down to absolute zero temperature. In his experiment, conducted on 8th April 1911, it was revealed that the resistivity of Mercury drops to "practically zero" (as inscribed in Onnes's lab notebook) when the temperature drops below 4.2 K, which was the first report of this quantum transition from a metallic state to a superconducting state [160]. Such a transition was also discovered around that time, in Pb and Sn. This quantum transition of vanishing resistivity at such temperatures had further implications. It was demonstrated that if a magnetically induced current is driven into a Pb coil cooled below its superconducting temperature, it can continue to flow without the external current source for many years. This current, termed "persistent current", was the first defining characteristic of superconductivity. Furthermore, this vanishing of resistivity was accompanied by an exclusion of a magnetic field by the superconducting host, implying a diamagnetic nature. This phenomenon of the expulsion of magnetic flux in the superconductor is popularly known as the Meissner effect [161] (see figure 5.1a). This magnetic flux expulsion occurs as the sample is cooled below its superconducting transition temperature (T_c). This suggests that above a certain critical value of the magnetic field (H_c), the flux lines would penetrate through the superconducting host, destroying its superconducting state. The transition from the normal to the superconducting state without a magnetic field is thermodynamically associated with condensation energy, which measures the energy saved on transitioning from the former to the latter. As

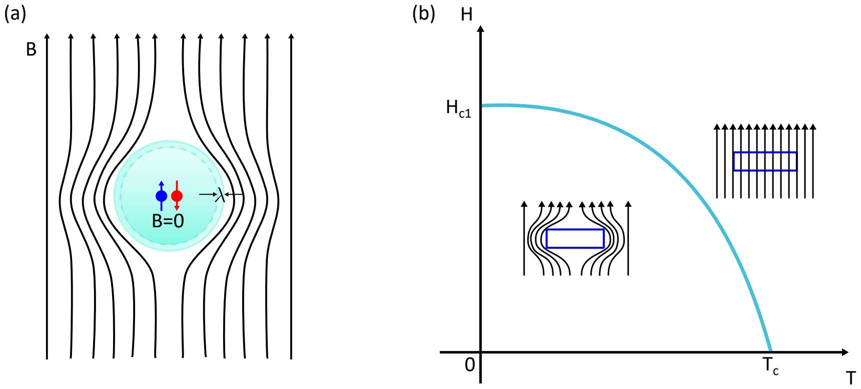

Figure 5.1: (a) Repulsion of magnetic field by a superconductor. The magnetic field penetrates up to a few nms within the edge of the superconductor. (b) Parabolic dependence of the critical field as a function of temperature characteristic to type-I superconductors.

shown in ref. [162], a scaling relation of H_c with temperature can be obtained by equating the condensation energy with the energy per unit volume associated with stabilizing a magnetic field given by $\frac{\mathrm{H}_c^2}{8\pi}$. This yields,

$$\frac{\mathrm{H}_c^2(\mathrm{T})}{8\pi} = F_n(\mathrm{T}) - F_s(\mathrm{T}) \tag{5.1}$$

where F_n and F_s are the free energies of the system in the normal and superconducting state, respectively. It has been shown that H_c follows a parabolic dependence on the temperature of the system,

$$\mathrm{H}_c(\mathrm{T}) = \mathrm{H}_c(0)[1 - (\frac{\mathrm{T}}{\mathrm{T}_c})^2] \tag{5.2}$$

The parabolic dependence of the critical field as a function of the temperature is schematically illustrated in figure 5.1b.

5.1.1 London penetration depth

In 1935, following the discovery of the Meissner effect (1933), Fritz and Heinz London formulated the London equations to describe the electromagnetic response of superconductors [163]. Their work introduced a phenomenological description that later found justification in quantum mechanics. The Londons' approach began by considering the canonical momentum of superconducting electrons, $\mathbf{p} = (m\mathbf{v}_s + \frac{e\mathbf{A}}{c})$, where m is the electron mass, $\mathbf{v}_s$ is the superfluid velocity, e is the electron charge, and $\mathbf{A}$ is the magnetic vector potential. In the absence of external fields, the average momentum vanishes $\langle\mathbf{p}\rangle$, leading to $\langle\mathbf{v}_s\rangle = \frac{-e\mathbf{A}}{mc}$. The supercurrent density $\mathbf{J}_s$ is the given by: $\mathbf{J}_s = n_s\mathrm{e}\langle\mathbf{v}_s\rangle =$ -$\frac{n_s e^2}{mc}\mathbf{A} = \frac{-\mathbf{A}}{\Lambda c}$, where n_s is the superfluid density and $\Lambda = \frac{m}{n_s e^2}$ is the London parameter.

The Londons drew an analogy to the Drude model but assumed a diverging mean free path. Their first equation describes the acceleration of superconducting electrons in an electric field $\mathbf{E}$:

$$\frac{\partial \mathbf{J}_s}{\partial t} = \frac{\mathbf{E}}{\Lambda} \tag{5.3}$$

which in the steady state, $\frac{\partial \mathbf{J}_s}{\partial t} = 0$, implying a vanishing $\mathbf{E}$ inside the superconductor, consistent with perfect conductivity. The second London equation relates the supercurrent to the magnetic field $\mathbf{h}$:

$$c\nabla \times (\Lambda \mathbf{J}_s) = -\mathbf{h} \tag{5.4}$$

By taking curl of the Maxwell's equation: $\nabla \times \mathbf{h} = (4\pi/c)\mathbf{J}$ and using the equation above, yields $\nabla^2\mathbf{h} = \frac{\mathbf{h}}{\lambda^2}$ where $\lambda^2 = \frac{mc^2}{4\pi n_s e^2}$ is the London penetration depth. This equation predicts that the magnetic field decays over a characteristic length λ, providing the first mathematical formulation of the Meissner effect.

For the derivation of the London equations, only the local effects of the electromagnetic fields were considered, i.e. the superconducting current density at a point was obtained by considering the field only at that particular point. Nevertheless, A.B. Pippard highlighted the importance of considering the non-local effects of electromagnetic fields through his discovery of the superconducting coherence length ξ_0. The necessity of considering non-local effects of the field arose while predicting an estimate for the maximum number of superconducting electrons possible in a system. It appeared that this number would be related to the total number of conduction electrons in a system in the extreme case of T → 0. In that case, an estimate of n_{max} could be obtained from London penetration depth at T = 0 given as: $\lambda_L(0) = (\frac{mc^2}{4\pi ne^2})^{1/2}$. It is evident that as the system's temperature approaches T$_c$, n_s would diminish causing $\lambda(\mathrm{T}_c)$ to diverge. However, experimental observations revealed a larger penetration depth for radio frequency fields in the superconducting state compared to the normal state, which challenged the conclusions derived by the London brothers. This excess penetration depth was accounted for by considering the non-local effects of the electromagnetic fields leading to the discovery of Pippard's coherence length.

5.1.2 Pippard's coherence length

In 1953 Pippard modified the London equation to solve the dilemma for increased field penetration in the superconducting state compared to the normal state by drawing an analogy from the generalized Ohm's law, $\mathbf{J}(\mathbf{r}) = \sigma\mathbf{E}(\mathbf{r})$ where he demonstrated that the supercurrent density $\mathbf{J_s}(\mathbf{r})$ at a point $\mathbf{r}$ in space would depend on the magnetic vector potential $\mathbf{A}(\mathbf{r}')$ enclosed by a sphere of radius $\mathbf{r_0}$ about the point $\mathbf{r}$ [164]. Pippard asserted that similar to normal electrons, the superconducting electrons can also be described by a wave function ψ_s with a wave packet of size ξ_0. These superconducting electrons that reside within k$_B$T$_c$ of E_F contribute to the intriguing physics that comes into play close to T$_c$. Combining this along with Heisenberg's uncertainty principle $\Delta x \Delta p \geq \hbar$, an estimate for the wave packet's size could be determined as follows: $\xi_0 = a\frac{\hbar v_F}{k_B T_c}$. The introduction of the term ξ_0, which was termed the coherence length, has similarities with the characteristic mean free path of charge carriers, 'l'. It was emphasized that the variation of the vector potential over ξ_0 ($\approx \mathbf{r_0}$) needs to be considered to obtain the correct supercurrent density, which ensures that the calculated λ is aligned with experimental observations [162]. This meant that any change of $\mathbf{A}(\mathbf{r}')$ over a length scale ξ_0, would affect $\mathbf{J_s}(\mathbf{r})$. Taking into account the above, it was proposed that $\mathbf{J_s}$ can be replaced by:

$$\mathbf{J}_{\mathrm{s}}(\mathbf{r}) = -\frac{3}{4\pi\xi_0\Lambda c}\int \frac{\mathbf{R}[\mathbf{R}\cdot\mathbf{A}(\mathbf{r}')]}{R^4}e^{-R/\xi}d\mathbf{r}' \tag{5.5}$$

where ξ is the coherence length of the superconducting carriers in the presence of scattering, $\mathbf{R}$ is the distance between the points at which $\mathbf{J}_s$ and $\mathbf{A}(r')$ are measured. A formal expression for the coherence length ξ in the presence of scattering centers was also formulated:

$$\frac{1}{\xi} = \frac{1}{\xi_0} + \frac{1}{l} \tag{5.6}$$

Eq. (5.5) solved the dilemma of increased London penetration depth for the radio-frequency field in the superconducting state compared to the normal state. From experiments on superconductors like tin and aluminum, it was observed that $\lambda \gg \lambda_L(0)$, since $\mathbf{A}(\mathbf{r}')$ does remain not constant over the entire ξ_0 rather it decreases over $\lambda \ll \xi_0$ which further leads to a reduction in supercurrent density $\mathbf{J}_{\mathrm{s}}(\mathbf{r})$ as evidenced by eq (5.5), hence an increased penetration depth for the field inside the superconductor.

5.1.3 The Ginzburg-Landau theory

Even though the phenomenon of superconductivity was understood, Ginzburg and Landau proposed the first phenomenological macroscopic model for superconductors in 1950. The theory developed by Ginzburg and Landau (GL theory) specifically concentrated on the description of the spatially varying superconducting carrier density close to the phase transition (T$_c$). Ginzburg and Landau proposed that the superconducting wave function ψ_s is an order parameter that describes the superconducting state. This order parameter was found to be related to the density of superconducting charge carriers as $n_s = |\Psi_s(r)|^2$. By applying a variational method, an expression similar to the Schrödinger equation in quantum mechanics was formulated for ψ_s:

$$\frac{1}{2m^*}\left(\frac{\hbar}{i}\nabla - \frac{e^*}{c}A\right)\psi + \beta|\psi|^2\psi = -\alpha(T)\psi \tag{5.7}$$

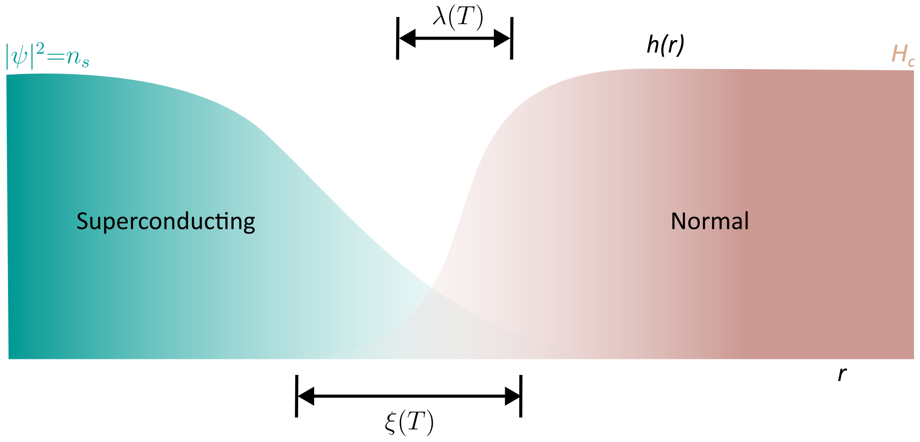

Figure 5.2: Schematic illustration of the intermediate state where the superconducting and normal phases coexist.

Following the analogy of the probability current J for a free particle in non-relativistic quantum mechanics, the corresponding supercurrent $\mathbf{J}_s$ was formulated:

$$\mathbf{J}_s = \frac{e^*\hbar}{2im^*}(\psi^*\nabla\psi - \psi\nabla\psi^*) - \frac{e^{*2}}{m^*c}|\psi|^2\mathbf{A} \tag{5.8}$$

where e^* and m^* are the effective charge (corresponding to 2e as discussed in section 5.1.4) and mass of the superconducting carriers respectively. One of the major successes of the theory was that it accounted for the non-local effects of electromagnetic fields (a modification of the equations proposed by London), similar to what Pippard's non-local electrodynamics proposed. The theory also proposed that the superconducting carrier density n_s would spatially vary in response to sufficiently strong fields (ref. to (5.7) and (5.8)). This inherently implies that the quantity ψ_s is not constant in space but exhibits spatial variations. A typical scenario would be the coexistence of a normal and superconducting state with an interface separating the two states as depicted in figure 5.2 which shows the superconducting state decaying over a coherence length ξ(T), while the magnetic field $h(r)$ exhibits spatial variation over the penetration depth λ(T) and increases to a constant value of H$_c$ in the normal state. A variation of ψ_s also suggests a spatial modulation of the superconducting gap, thereby challenging the notion of a spatially independent superconducting gap as postulated by the BCS theory (see following subsection). Subsequently, Gor'kov

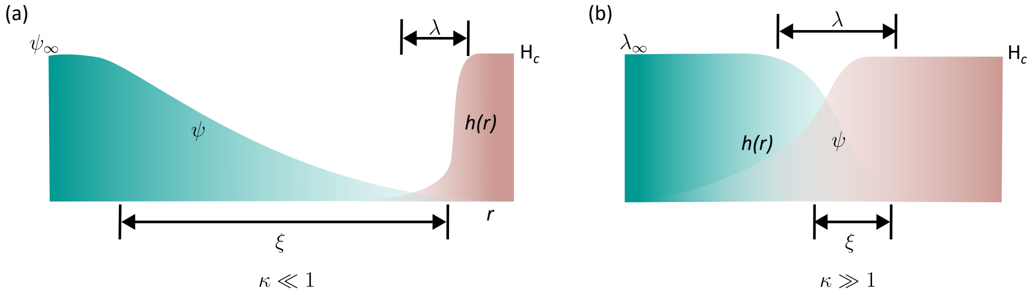

Figure 5.3: Schematic illustration of the variation of ψ and h for the case of: (a) $\kappa \ll 1$ corresponding to a type-I superconductor, (b) $\kappa \gg 1$ corresponding to a type-II superconductor.

in 1959 established that the GL theory represents a limiting case of BCS theory in the vicinity of T$_c$ with ψ_s directly corresponding to the spatially dependent gap function $\Delta(r)$ and valid only for a gradually varying ψ_s and electromagnetic fields [165]. The GL theory also defined a characteristic length scale over which ψ_s can vary without any energy cost:

$$\xi(T) = \frac{\hbar}{|2m^*\alpha(T)|^{1/2}} \tag{5.9}$$

which in the literature of superconductivity is known as GL "coherence length". It was demonstrated that the GL "coherence length" is a generalized version of Pippard's coherence length for the cases of T $\ll$ T$_c$ and T $\rightarrow$ T$_c$ [162]. A corresponding parameter called the GL parameter was defined, $\kappa = \frac{\lambda(T)}{\xi(T)}$. The quantity κ was used to distinguish between "pure" and "dirty" superconductors. For $\kappa \ll 1$, one is within the limit of "pure" superconductors. As shown in figure 5.3a, this is also the case for type-I superconductors, where the magnetic field strength beyond H_c kills the superconducting state due to the full field penetration (see figure 5.1b), however for smaller field strength there exists a region, $\xi - \lambda$ where besides the restriction of the field penetration, the superconducting order parameter does not recover to its full value *i.e.* $\psi \neq \psi_\infty$, thereby implying that the full condensation into the superconducting state does not occur leaving a portion of the sample in the normal state. This stabilizes a superconducting and normal state mixture with a positive surface energy, with a domain wall separating the two. The type-I superconductors mainly

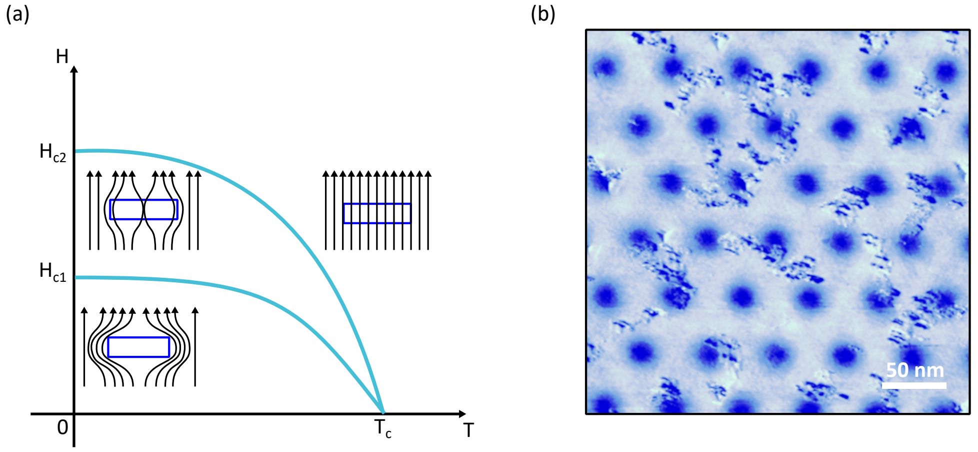

Figure 5.4: (a) Dependence of the critical field as a function of temperature in a type-II superconductor. (b) Vortex lattice on the type-II superconductor, NbSe$_2$.

include metals such as Lead (Pb), Tin (Sn), Zirconium (Zr), Aluminum (Al), etc.

While the type-I or "pure" superconductors with $\xi \gg \lambda$ were well understood back then, the idea of a "dirty" superconductor with $\kappa \gg 1$ was unknown. This was brought to attention in 1957 when Alexie Abrikosov questioned what would happen if the penetration depth was larger compared to the GL coherence length *i.e.* $\kappa \gg 1$. This is schematically illustrated in figure 5.3b. It was suggested in the GL theory that, beyond the lower critical field value H$_{c1}$, the superconducting state fails to maintain its perfect diamagnetic nature, leading to the formation of a mixed state where a superposition of the superconducting and normal regions coexist. This phenomenon is caused by the gradual increase of the magnetic flux up to a limiting value, the upper critical field H$_{c2}$ $= \sqrt{2}\kappa H_c$, that penetrates the sample forming an arrangement of regions, the core of which favors a metallic or "quasinormal" state [166]. Abrikosov termed this array of regions as vortices and showed that the flux through these regions was quantized: $\Phi_0 = \frac{hc}{2e} = 2.07 \times 10^{-7} G - cm^{-2}$. The intermediate state, characterized by the coexistence of superconducting and normal regions, occurs in type-II superconductors when the applied magnetic field exceeds the lower critical field H$_{c1}$ but is less than the upper critical field H$_{c2}$ (see figure 5.4a). STM measurements at low temperatures allow direct visualization of these vortex patterns, where the vortices stabilize into ground-state configurations, typically forming lattices of different symmetry. Figure 5.4b shows a vortex lattice on the type-II superconductor $\mathrm{NbSe_2}$ which follows the six-fold symmetry of the lattice. Some examples of elemental type-II superconductors are Niobium (Nb), Vanadium (V), Technetium (Te), and the more recent 2D ones involve $\mathrm{Bi_2Sr_2CaCu_2O}_{8+x}$ (Bi2212), $\mathrm{NbSe_2}$, PdTe2, etc.

5.1.4 The BCS theory

Until 1953, although many features, characteristic of the phenomena of superconductivity were known, the microscopic mechanism or the nature of the superconducting charge carriers remained elusive. While extracting the coherence length ξ_0 of these superconducting carriers, it was emphasized that the energy scale associated with the phenomena of superconductivity is expected to lie within $\mathrm{k}_B\mathrm{T}_c$ of E_F [162, 167]. In 1955, John Bardeen in an attempt to provide a mathematical description of the Meissner effect suggested that an energy of similar order, $\mathrm{k}_B\mathrm{T}_c$ would be required to destabilize the superconducting electrons from the Fermi sea causing them to behave like “normal”electrons, but in an excited state [168]. This would imply that the superconducting state drives an instability of the Fermi surface. Bardeen argued that an energy scale was associated with the Fermi surface instability, manifesting as an energy gap defining the superconducting condensate’s ground state (see figure 5.5). The first experimental evidence of an energy gap was found in the specific heat measurements on the elemental superconductor Vanadium [169] where below T_c, the specific heat decayed exponentially following the relation: $C_{es} \approx \gamma T_c a e^{-bT_c/T}$ where a and b are numerical constants. This exponential dependence on b $\sim$ 1.5 was related to the energy required to excite a quasiparticle, which was $\sim$ 1.5 $\mathrm{k}_B\mathrm{T}_c$. Some other experimental techniques also revealed an energy gap of 3 to 4 times k_B T_c suggesting the possibility of paired excitation [170, 171]. In 1956, Leon Cooper cleared all these dilemmas by theoretically demonstrating that electrons can exist as bound pairs due to non-trivial correlations and condense into a stable ground state with finite energy, not necessarily zero [172]. This was counterintuitive to the general notion that the Coulomb repulsion would oppose such pair formation between simi-

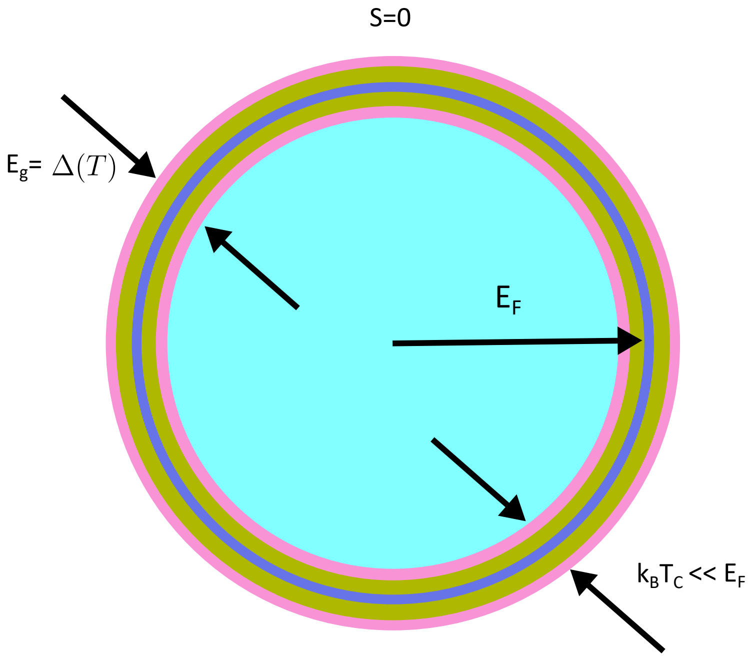

Figure 5.5: Instability of the Fermi surface manifests as an excitation gap given by $E_g = \Delta(T)$.

larly charged entities. Cooper showed that such an attraction between the electrons would typically exist on a length scale much larger than the atomic scale, typically of the order of a few 100 nanometres. The presence of an attractive interaction between electrons was supported by the fact that the attraction between electrons was mediated by the crystal lattice vibrations commonly known as phonons. Following these arguments, in 1957, Bardeen and Cooper, together with Schrieffer, presented their seminal work on the "*Theory of Superconductivity*" which would unravel many of the mysteries of the superconducting state [167]. This groundbreaking theory, commonly known as the Bardeen-Cooper-Schrieffer (BCS) theory, was awarded the Nobel Prize in 1972. This theoretical framework successfully explained the isotope effect in superconductors, first experimentally observed by Maxwell and Reynolds in 1950 [173]. Their measurements revealed an inverse relationship between the superconducting transition temperature T_c and the square root of the isotopic mass ($T_c \propto \sqrt{M}$), consistent with the phonon-mediated pairing mechanism of the BCS theory where an inverse scaling relation between the T_c and mass of the isotope was found. The remainder of this section provides a brief theoretical and mathematical overview of BCS theory. For detailed information on the BCS theory, see references

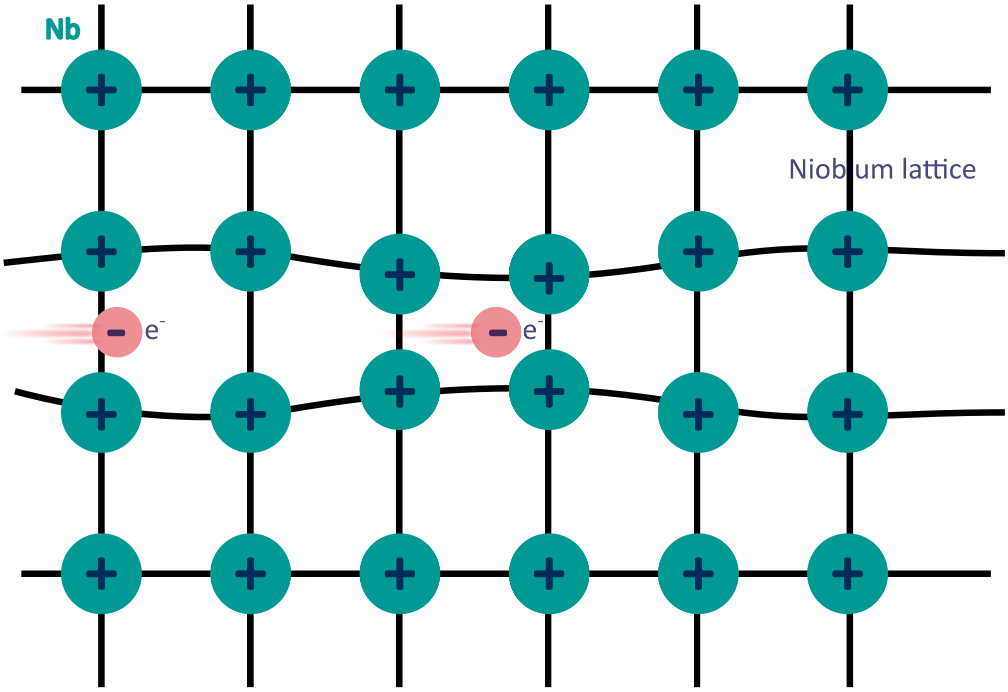

Figure 5.6: Schematic illustration of the pairing mechanism of electrons in a BCS superconductor mediated by the crystal lattice vibrations.

[167] and [162].

The BCS theory demonstrated that despite strong Coulomb repulsions, an effective attractive interaction between electrons can emerge through electron-phonon coupling. This enables electrons near the Fermi surface to form bound pairs with opposite momenta (k↑, -k↓) and antiparallel spins (S = 0). The phonon-mediated pairing interaction destabilizes the normal-state Fermi surface, creating an excitation gap with magnitude $\mathrm{E}_g(0) = 2\Delta(0) \approx 3.53\ \mathrm{k}_B\mathrm{T}_c$ at $\mathrm{T} \ll \mathrm{T}_c$, where where $\Delta(0)$ is the superconducting gap at absolute zero temperature. This gap vanishes as $\mathrm{T} \rightarrow \mathrm{T}_c$. These paired quasiparticles, known as Cooper pairs, serve as the charge carriers in the superconducting state. These Cooper pairs are spatially correlated over a characteristic length scale $\xi = \frac{\hbar v_F}{\pi\Delta(0)}$, called the BCS coherence length.

Qualitatively, the mechanism of Cooper pair formation can be understood by considering the interaction between the electron and the lattice. As illustrated in figure 5.6, when an electron moves through the lattice, it attracts nearby positive ions, creating a localized lattice distortion. This distortion generates a region of enhanced positive charge density that persists long enough to attract a second electron, provided the resulting electron-phonon attraction overcomes Coulomb repulsion. The two electrons then form a correlated pair that ultimately condenses into the superconducting ground state. While this picture describes a single pair, the superconducting state actually consists of a macroscopic phase-coherent condensate of such pairs. This collective nature makes the superconducting state robust against lattice vibrations (already suppressed at low temperatures) due to the finite energy required to break pairs. The Cooper pairs flow inside the superconductor without dissipation, giving rise to a supercurrent I_s.

In conventional s-wave superconductors described by BCS theory, the Cooper pairs form with a spin-singlet configuration (S = 0) and zero orbital angular momentum (L = 0), resulting in a spherically symmetric wavefunction. The orbital angular momentum fundamentally influences the superconducting properties. Unlike isotropic s-wave pairing, non-zero angular momentum states show directional dependence in their gap structures. In superconductors, the orbital angular momentum of Cooper pairs plays a role analogous to the orbital angular momentum in atomic systems, determining the spatial structure of the Cooper pair wavefunction (similar to how atomic orbitals define electron probability distributions). In fact, alternative pairing mechanisms can generate superconducting states with non-zero orbital angular momentum. p-wave superconductors exhibit L = 1 pairing with odd-parity wavefunctions and typically form spin-triplet states (S = 1), as proposed in systems like Sr_2RuO_4 [174]. In contrast, d-wave superconductors with L = 2 pairing maintain spin-singlet configurations but develop nodal gap structures, as observed in cuprate superconductors where the superconducting gap follows the symmetry [175]. The pairing symmetry (s-, p-, d-, or f-wave) reflects the quantized orbital angular momentum (L = 0, 1, 2, 3), which governs the nodal structure and anisotropy of the superconducting gap (see section 5.2). This chapter will address the topic of p-wave superconductivity in section 5.3.

5.1.4.1 Mathematical formalism of the BCS theory

In an attempt to determine the quasiparticle spectrum, the attractive interaction between electrons with opposite spin and zero momenta, which was the key finding of the BCS theory was described by the second-quantized Hamiltonian [162, 176],

$$H = \sum_{\vec{k},s} \xi_{\vec{k}} c^{\dagger}_{\vec{k},s} c_{\vec{k},s} + g \sum_{\vec{k},\vec{k}',\vec{q}} c^{\dagger}_{\vec{k}+\vec{q},\uparrow} c^{\dagger}_{\vec{k}'-\vec{q},\downarrow} c_{\vec{k}',\downarrow} c_{\vec{k},\uparrow} \tag{5.10}$$

where $c^{\dagger}_{\vec{k},s}$ ($c_{\vec{k},s}$) is the creation (annihilation) operator corresponding to an electron with spin s and momentum $\vec{k}$. The first term corresponds to the kinetic energy, which captures the parabolic band dispersion of a normal metal where $\xi_{\vec{k}}= \frac{\hbar^2}{2m}\left(\vec{k}^2 - k_F^2\right)$, measured w.r.t the chemical potential. The second term represents the attractive potential between the 2 spin-$\frac{1}{2}$ fermions. The term g is a random scattering matrix element related to the attractive potential $U(\vec{r}-\vec{r}')$ as follows: $U(\vec{r}-\vec{r}') = g\delta(\vec{r}-\vec{r}')$ ($g < 0$). In k-space, the interaction term $V_{\vec{k},\vec{k}'}$ can be obtained by a Fourier transform of $U(\vec{r})$: $V_{\vec{k},\vec{k}'} = V(\vec{q} = \vec{k} - \vec{k}') = \int d^3 r U(\vec{r}) = g$. The Hamltionian in eq. (5.10) can be simplified by considering only those terms in the scattering matrix g for which the electron pairing has $L = 0$, corresponding to the set of Bloch states $|\vec{k},\uparrow\rangle \otimes | -\vec{k},\downarrow\rangle|$. The simplified Hamiltonian is therefore given by,

$$H = \sum_{\vec{k},s} \xi_{\vec{k}} c^{\dagger}_{\vec{k},s} c_{\vec{k},s} + g \sum_{\vec{k},\vec{k}'} c^{\dagger}_{\vec{k}\uparrow} c^{\dagger}_{-\vec{k}\downarrow} c_{-\vec{k}'\downarrow} c_{\vec{k}'\uparrow} \tag{5.11}$$

The originally proposed BCS wave function representing the ground state of the Cooper pairs was given as:

$$|\Phi_{\mathrm{BCS}}\rangle = \prod_{\vec{k}} \left\{ u_{\vec{k}} + v_{\vec{k}} c^{\dagger}_{\vec{k}\uparrow} c^{\dagger}_{-\vec{k}\downarrow} \right\} |\mathrm{vac}\rangle \tag{5.12}$$

where $|\mathrm{vac}\rangle$ denotes the electrons in the normal state and $u_{\vec{k}}$ and $\nu_{\vec{k}}$ are numerical coefficients satisfying the relation $|u_{\vec{k}}|^2 + |\nu_{\vec{k}}|^2 = 1$ [162]. This mathematical constraint implies that the probability of occupation of a Cooper pair ($k \uparrow$,$-k \downarrow$) is $|\nu_{\vec{k}}|^2$, while

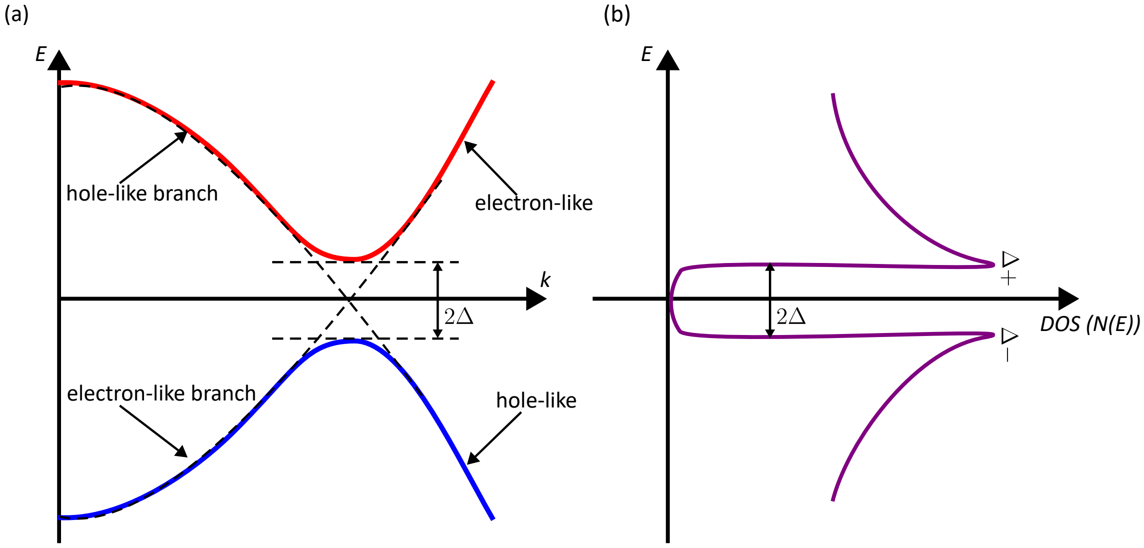

Figure 5.7: Schematic illustration of the (a) of the energy dispersion of the quasiparticles demonstrating the emergence of an energy gap around the Fermi energy (E_{F}) originating due to the hybridization of an electron-like (solid blue line) and hole-like branch (solid red line). The dashed lines correspond to the case of a normal metal which has $\Delta = 0$. (b) DOS features a pair of coherent electron-hole peaks separated by the excitation gap 2Δ. Panel (a) adapted from ref. [176].

the probability that it is empty is $|u_{\vec{k}}|^2 = 1 - |\nu_{\vec{k}}|^2$. The variational method employed in the original work by BCS [167] is mathematically pretty rigorous, so a more convenient approach to obtain the quasiparticle dispersion relation was proposed, which was the mean-field theoretical approach. This approach mitigates the complexity caused by the many-body interaction term in the Hamiltonian. For this, the off-diagonal term below in the mean-field matrix was proposed [176]:

$$b_{\vec{k}} = \left\langle c_{-\vec{k}\downarrow} c_{\vec{k}\uparrow} \right\rangle \tag{5.13}$$

where $b_{\vec{k}}$ relates states where the fermionic occupation differs by 2. The $b_{\vec{k}}$ can be interpreted as the momentum space wave function of the Cooper pairs. Using the mathematical jiggling, $c_{-\vec{k}\downarrow} c_{\vec{k}\uparrow} = b_{\vec{k}} + \left\{ c_{-\vec{k}\downarrow} c_{\vec{k}\uparrow} - b_{\vec{k}} \right\}$ in eq (5.11) and ignoring higher order terms, the model Hamiltonian can be written as:

$$H = \sum_{\vec{k},s} \xi_{\vec{k}} c^{\dagger}_{\vec{k},s} c_{\vec{k},s} + g \sum_{\vec{k},\vec{k}'} b^{*}_{\vec{k}'} c_{-\vec{k}\downarrow} c_{\vec{k}\uparrow} + b_{\vec{k}'} c^{\dagger}_{\vec{k}\uparrow} c^{\dagger}_{-\vec{k}\downarrow} - b^{*}_{\vec{k}} b_{\vec{k}'} \tag{5.14}$$

$$= \sum_{\vec{k},s} \xi_{\vec{k}} c^{\dagger}_{\vec{k},s} c_{\vec{k},s} - \sum_{\vec{k}} \left(\Delta^{*} c_{-\vec{k}\downarrow} c_{\vec{k}\uparrow} + \Delta c^{\dagger}_{\vec{k}\uparrow} c^{\dagger}_{-\vec{k}\downarrow} \right) - \Delta^{*} b_{\vec{k}} \tag{5.15}$$

where $\Delta = -g \sum_{\vec{k}} b_{\vec{k}'}$ is the superconducting gap equation. In the next step, a new fermionic operator $\gamma_{\vec{k}s}$ was introduced which had the form $\dot{\gamma}_{\vec{k},s} = i[H_{mf}, \gamma^{\dagger}_{\vec{k}s}] = E_{\vec{k}} \gamma^{\dagger}_{\vec{k},s}$. To determine the quasiparticle dispersion, the Hamiltonian needs to be diagonalized, which was achieved using the following transformation, as independently proposed by Nikolai Bogoliubov [177] and John Valatin [178]:

$$c_{\vec{k}\uparrow} = u^{*}_{\vec{k}} \gamma_{\vec{k}1} + \nu_{\vec{k}} \gamma^{\dagger}_{\vec{k}2} \quad \text{and} \quad c_{-\vec{k}\downarrow} = -\nu^{*}_{\vec{k}} \gamma_{\vec{k}1} + u_{\vec{k}} \gamma^{\dagger}_{\vec{k}2} \tag{5.16}$$

where $u_{\vec{k}}$ and $\nu_{\vec{k}}$ are the same indices in the variational ground state in eq (5.12) satisfying the condition $|u_{\vec{k}}|^2 + |\nu_{\vec{k}}|^2 = 1$ and the subscripts 1 and 2 correspond to electron-like and hole-like quasiparticles. Making the above substitution, the diagonalized Hamiltonian becomes,

$$H_{mf} = \sum_{\vec{k}} [\xi_{\vec{k}} - E_{\vec{k}} + \Delta b_{\vec{k}}] + \sum_{\vec{k}} E_{\vec{k}} (\gamma^{\dagger}_{\vec{k}1} \gamma_{\vec{k}1} + \gamma_{\vec{k}2} \gamma_{\vec{k}1}) \tag{5.17}$$

where $E_{\vec{k}} = \sqrt{\xi^2_{\vec{k}} + \Delta^2}$ is the energy of the Bogoliubov quasiparticles. The quasiparticle dispersion corresponding to H_{mf} consists of two branches originating from a normal metal's electron-like and hole-like parabolic bands. As shown in figure 5.7a, close to the Fermi energy, the attractive interaction g causes an instability manifesting as a gap of magnitude 2Δ. From the figure, it can be further inferred that the emergence of the gap is linked to the hybridization of the electron and hole-like branches, implying that the quasiparticles bear a mixed nature. The superconducting gap can be detected in STM measurements in the LDOS measurements. The BCS DOS, which is the number of quasiparticle states within a given energy interval, can be written as:

$$N_{BCS}(\xi) = \begin{cases} N_0 \frac{|\xi|}{\sqrt{\xi^2-\Delta^2}} & |\xi| \geq \Delta \\ 0 & |\xi| < \Delta \end{cases} \tag{5.18}$$

where N_0 is the DOS in the normal state. A typical DOS of a superconductor is illustrated in figure 5.7b.

Theoretically, the magnitude of this gap Δ can be obtained from the "gap equation":

$$\Delta = -g\sum_{\vec{k}} b_{\vec{k}} = -g\sum_{\vec{k}} u^*_{\vec{k}}\nu_{\vec{k}}[1-f(E_{\vec{k}})] = -g\sum_{\vec{k}} \frac{\Delta}{2E_{\vec{k}}}\tanh\left(\frac{E_{\vec{k}}}{k_BT}\right) \tag{5.19}$$

where $f(E) = 1/(1+e^{E/k_BT})$ is the fermi-Dirac distribution. It is important to note that this gap is solely temperature-dependent. In the limiting case of $\Delta \to 0$, the critical temperature T_c at which the gap vanishes can be obtained as follows,

$$\Delta = -g\Delta\sum_{\vec{k}} \frac{1}{2E_{\vec{k}}}\tanh\left(\frac{E_{\vec{k}}}{k_BT}\right) \quad \Rightarrow \quad 1 = -g\int d\xi \frac{N(\xi)}{2\xi}\tanh\left(\frac{\xi}{k_BT_c}\right) \tag{5.20}$$

where $N(\xi)$ represents the density of available electronic states at energy ξ. Since $\xi \to \pm\infty$, it is necessary to define a cutoff energy ε_c so that the integral does not diverge. This quantity ε_c must be much smaller than the bandwidth and should be defined around a small energy window around E_F within which the attractive interaction persists. Mathematically, this would imply $-\varepsilon_c \leq V^{ep}_{\vec{k},\vec{k}'} \leq \varepsilon_c$. Within this energy range, the electron density of states is expected to be constant, therefore, the integral can be written as:

$$1 = -gN_0\int_{-\varepsilon_c}^{+\varepsilon_c} \frac{d\xi)}{2\xi}\tanh\left(\frac{\xi}{k_BT_c}\right) \quad = -gN_0 \ln\frac{1.14\varepsilon_c}{k_BT_c} \tag{5.21}$$

from which the expression for T_c can be extracted: $k_B\mathrm{T}_c = 1.14\varepsilon_c e^{-1/|g|N_0}$. By using the above integral, the energy gap at T = 0 can also be obtained:

$$1 = -gN_0 \int_0^{\varepsilon_c} \frac{d\xi}{\sqrt{\xi^2 + \Delta^2}} \quad = -gN_0 \sinh^{-1} \frac{\varepsilon_c}{\Delta} \tag{5.22}$$

which yields $\Delta(\mathrm{T} = 0) \approx 2\varepsilon_c e^{-1/|g|N_0}$ =1.764 $\mathrm{k}_B\mathrm{T}_c$. Finally, the condensation energy at T = 0 can be obtained, corresponding to the energy gain associated with gap opening resulting from a modification of the quasiparticle states close to E_F. The condensation energy E_cond is therefore obtained as:

$$E_\mathrm{cond} = \sum_{\vec{k}} [\xi_{\vec{k}} - E_{\vec{k}} + \Delta b_{\vec{k}}] \approx -\frac{1}{2} N_0 |\Delta|^2 \tag{5.23}$$

The equation above demonstrates a clear dependence of the condensation energy on the density of states at the Fermi surface. A more comprehensive analysis of the BCS theory can be found in ref. [162].

5.2 The gap function for different pairing states

The gap function, defined as $\Delta_k = -g \sum_{\vec{k}} b_{\vec{k}}$ is a key parameter that determines the specific characteristics of the superconducting gap. The form of Δ_k is linked to the wave function of the Cooper pairs [167, 176]. It provides crucial information about the symmetry of the gap, revealing whether it is isotropic (independent of direction), anisotropic (varies with direction), or exhibits nodes (points or lines where the gap vanishes) for different pairing states. To gain a deeper insight into the gap structure, the wave function of the Cooper pairs $b_{\vec{k},s_1 s_2}$ can be written as a product of an orbital part and a spin part:

$$b_{\vec{k},s_1 s_2} = \phi(\vec{k}) \chi_{s_1 s_2} \tag{5.24}$$

where $\phi(\vec{k})$ is the orbital part and $\chi_{s_1 s_2}$ is the spin part corresponding to two electrons with spin angular momentum s_1 and s_2. Considering only the spin part of the Cooper pairs, composed of 2 spin-$\frac{1}{2}$ fermions, two spin states are possible depending on whether the total spin is S = 0 or S = 1. The S = 0 is the spin-singlet state,

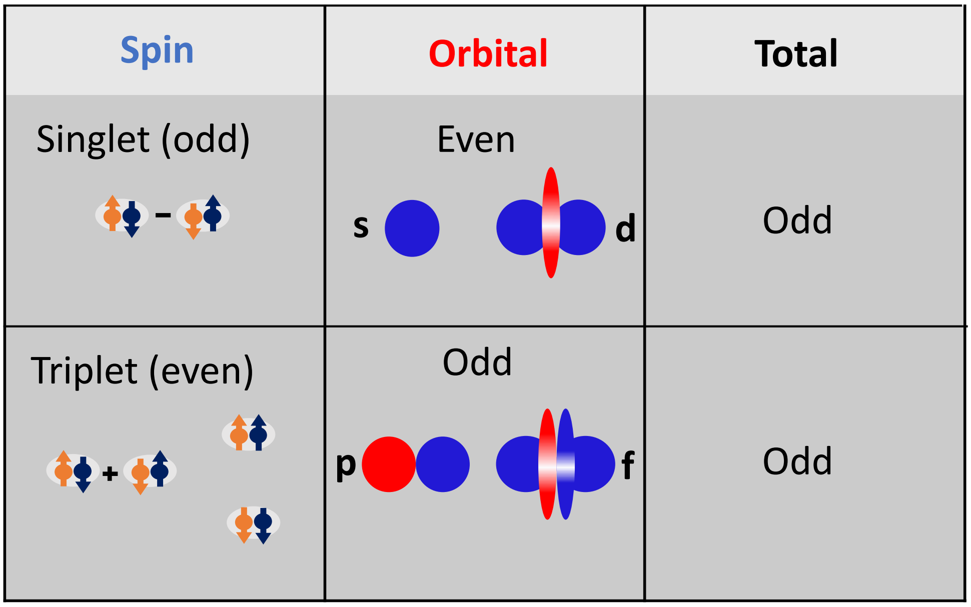

Figure 5.8: Classification of superconducting correlation following from the Pauli principle. With the spin part being antisymmetric (odd), the orbital part is symmetric (even), leading to an s-wave (L = 0) or d-wave (L = 2) orbital character. When the spin part is symmetric, the orbital part must be antisymmetric, resulting in a p-wave (L = 1) or f-wave (L = 3) orbital character.

described by the wave function:

$$\chi_{s_1 s_2} = \frac{1}{\sqrt{2}}(|\uparrow\downarrow\rangle - |\downarrow\uparrow\rangle) \tag{5.25}$$

which is antisymmetric under particle exchange. For the spin-triplet state corresponding to S = 1, three different states are possible depending on the spin projections (S_z= -1, 0, +1), which are described by the wave function:

$$\chi_{s_1 s_2} = \begin{cases} |\uparrow\uparrow\rangle \\ \frac{1}{\sqrt{2}}(|\uparrow\downarrow\rangle + |\downarrow\uparrow\rangle) \\ |\downarrow\downarrow\rangle \end{cases} \tag{5.26}$$

This wave function is symmetric under particle exchange. Since the Pauli exclusion principle demands that the total fermionic wave function of the Cooper pairs, $b_{\vec{k},s_1 s_2}$, be antisymmetric under the exchange of two identical fermions, two distinct possibilities arise depending on whether the spin state is a singlet or a triplet. For the

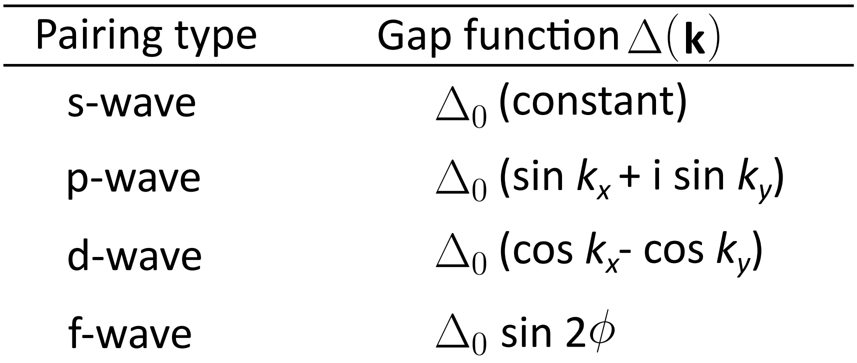

Pairing type	Gap function $\Delta(\mathbf{k})$
s-wave	Δ_0 (constant)
p-wave	Δ_0 ($\sin k_x + i \sin k_y$)
d-wave	Δ_0 ($\cos k_x - \cos k_y$)
f-wave	$\Delta_0 \sin 2\phi$

Figure 5.9: Examples of the form of the gap function for different pairing types. The s-wave superconductors exhibit an isotropic gap, while the p-wave superconductors can exhibit a nodal gap. The same is the case for d-wave superconductors, which can also exhibit a nodal gap. The f-wave superconductors are rare but have been proposed in some heavy fermion systems. Here the lattice constant has been set to $a = 1$ for simplicity ($k_x a = k_x$).

spin-singlet case, the Pauli exclusion principle demands that the orbital part have an even parity ($\phi(k) = \phi(-k)$), while for the spin-triplet case, the orbital part must have an odd parity (($\phi(k) = -\phi(-k)$). This constraint on $b_{\vec{k},s_1 s_2}$ also extends to the gap function $\Delta_{\vec{k},s_1 s_2}$ [176] in the following manner:

$$\Delta_{\vec{k},s_1 s_2} = -\Delta_{-\vec{k},s_2 s_1} = \begin{cases} \Delta_{-\vec{k},s_1 s_2} = -\Delta_{\vec{k},s_2 s_1} & \text{even orbital } - \text{odd spin} \\ -\Delta_{-\vec{k},s_1 s_2} = \Delta_{\vec{k},s_2 s_1} & \text{odd orbital } - \text{even spin} \end{cases} \tag{5.27}$$

In cases where the Cooper pair's orbital wave function possesses even parity and the spin configuration is a singlet, the superconducting state exhibits either s-wave or d-wave symmetry. Conversely, when the orbital parity is odd and the spin state is a triplet (the inverse scenario), the superconducting pairing is characterized as a p-wave or f-wave. Figure 5.8 provides a schematic representation of these correlations. This naming convention draws inspiration from the spatial shapes of atomic orbitals, reflecting a similar momentum dependence in the superconducting gap function. Examples of the gap functions of the different pairing symmetries are shown in figure 5.9 [167, 175, 179–182].

In the spin basis, the gap function can be represented in the form of a matrix

[162, 176]:

$$\widehat{\Delta}_{\vec{k}} = \begin{pmatrix} \Delta_{\vec{k},\uparrow\uparrow} & \Delta_{\vec{k},\uparrow\downarrow} \\ \Delta_{\vec{k},\downarrow\uparrow} & \Delta_{\vec{k},\downarrow\downarrow} \end{pmatrix} \tag{5.28}$$

Taking into account the equation above, the gap function matrix for the spin singlet can be expressed by just using the scalar function $\psi(\vec{k})$ ($\psi(\vec{k}) = \psi(-\vec{k})$) since the spatial part is symmetric. Substituting this into eq. 5.28 yields:

$$\widehat{\Delta}_{\vec{k}} = \begin{pmatrix} 0 & \psi(\vec{k}) \\ -\psi(\vec{k}) & 0 \end{pmatrix} = i\hat{\sigma}_y \psi(\vec{k}) \tag{5.29}$$

where $\hat{\sigma}_y$ is the y-component of the Pauli spin matrices. On the other hand, to represent the gap matrix for the odd parity case with spin-triplet pairing, a vector quantity with 3 components $\vec{d}(\vec{k}) = d_x(\vec{k})\hat{x} + d_y(\vec{k})\hat{y} + d_z(\vec{k})\hat{z}$ needs to be defined [176] allowing $\widehat{\Delta}_{\vec{k}}$ to be written as:

$$\widehat{\Delta}_{\vec{k}} = \begin{pmatrix} -d_x(\vec{k}) + id_y(\vec{k}) & d_z(\vec{k}) \\ d_z(\vec{k}) & d_x(\vec{k}) + id_y(\vec{k}) \end{pmatrix} = i(\vec{d}(\vec{k}) \cdot \hat{\vec{\sigma}})\hat{\sigma}_y \tag{5.30}$$

where $\vec{d}(\vec{k}) = -\vec{d}(-\vec{k})$ has an odd parity. From the gap matrices discussed above, it is possible to calculate a quantity defined as: $\widehat{\Delta}^{\dagger}_{\vec{k}}\widehat{\Delta}_{\vec{k}}$, the trace of which is proportional to the square of the gap function ($|\Delta\vec{k}|^2$)[176]:

$$\widehat{\Delta}^{\dagger}_{\vec{k}}\widehat{\Delta}_{\vec{k}} = \begin{cases} |\psi(\vec{k})|^2\widehat{\sigma}_0 & \text{spin singlet} \\ |\vec{d}|^2\widehat{\sigma}_0 + i(\vec{d} \times \vec{d^*}).\hat{\vec{\sigma}} & \text{spin triplet} \end{cases} \tag{5.31}$$

The corresponding gap function, which yields the quasiparticle spectrum, is therefore given by the equation below:

$$|\Delta_{\vec{k}}|^2 = \frac{1}{2}tr(\widehat{\Delta}^{\dagger}_{\vec{k}}\widehat{\Delta}_{\vec{k}}) \tag{5.32}$$

The nature of the superconducting gap function is dependent on the symmetry operations governing the spin-singlet and spin-triplet configurations, hence, it requires reviewing these symmetry operations. In the case of a s-wave superconductor or a conventional BCS superconductor, since the spins in a Cooper pair are paired with opposite spins (singlet pairing) and are located at opposite momenta, the crucial symmetry is the $\widehat{\mathcal{T}}$ symmetry [183]. This can be understood as follows: when the $\widehat{\mathcal{T}}$ operator is applied on a state $|k,\uparrow\rangle$, the corresponding $\widehat{\mathcal{T}}$ counterpart $|-k,\downarrow\rangle$ is obtained which is the partner state that together forms the Cooper pairs. Mathematically, this can be expressed as:

$$\mathcal{T}|k,\uparrow\rangle = |-k,\downarrow\rangle \tag{5.33}$$

However, for the spin-triplet pairing characteristic to p-wave superconductors, besides the $\widehat{\mathcal{T}}$ symmetry, the inversion symmetry ($\widehat{I}$) also needs to be invoked to generate the different spin-triplet configurations. When the $\widehat{I}$ and $\widehat{\mathcal{T}}$ operators are applied to the electronic state $|k,\uparrow\rangle$, the resulting partner state can be obtained as follows:

$$\widehat{I}|k,\uparrow\rangle = |-k,\uparrow\rangle, \quad \widehat{\mathcal{T}}|k,\uparrow\rangle = |-k,\downarrow\rangle, \quad \widehat{I}\widehat{\mathcal{T}}|k,\uparrow\rangle = |k,\downarrow\rangle \tag{5.34}$$

In general, to investigate the effect of $\widehat{\mathcal{T}}$ and $\widehat{I}$ operator on $\widehat{\Delta}_{\vec{k}}$, one needs to examine their effect on the fermionic creation and annihilation operators. In the case of $\widehat{\mathcal{T}}$ symmetry defined as $\widehat{\mathcal{T}} = -i\hat{\sigma}^y\widehat{C}$ with $\widehat{C}$ being a complex-conjugate operator, the effect of $\widehat{\mathcal{T}}$ operator on $c_{\vec{k},s}$ and $\widehat{\Delta}_{\vec{k}}$ can be given by the following equations:

$$\widehat{\mathcal{T}}c_{\vec{k},s} = \sum_{s'}(-i\hat{\sigma}^y)_{ss'}c^{\dagger}_{-\vec{k},s'} \quad \Rightarrow \quad \widehat{\mathcal{T}}\widehat{\Delta}_{\vec{k}} = \hat{\sigma}^y\widehat{\Delta}^{*}_{\vec{k}}\hat{\sigma}^y \tag{5.35}$$

In a similar way the effect of $\widehat{I}$ operator on $c_{\vec{k},s}$ and $\widehat{\Delta}_{\vec{k}}$ can be given by the following set of equations [176]:

$$\widehat{I}c_{\vec{k},s} = c_{-\vec{k},s} \quad \Rightarrow \quad \widehat{I}\widehat{\Delta}_{\vec{k}} = \widehat{\Delta}_{-\vec{k}} = \begin{cases} +\widehat{\Delta}_{\vec{k}}, & \mathrm{spin-singlet} \\ -\widehat{\Delta}_{\vec{k}}, & \mathrm{spin-triplet} \end{cases} \tag{5.36}$$

Besides the symmetries mentioned above, the effect of other symmetries on the $|\Delta_{\vec{k}}|$, namely rotations in real and spin space and U1-gauge symmetries, has also been examined[176]. For e.g., under spin rotation defined by the operator g, the singlet configuration remains unaffected since the net spin is 0, however the vector $\vec{d}$ in the spin-triplet case transforms under rotation according to the relation $g\vec{d}(\vec{k}) = \tilde{R}_S(g)\vec{d}(\vec{k})$, where $\tilde{R}_S$ denotes the rotation in the three-dimensional space. This leads to the following modification of the gap function in the spin space accordingly as a spin directed along $\vec{d}(\vec{k})$: $d_x\{-|\uparrow\uparrow\rangle + \downarrow\downarrow\rangle\} - id_y\{|\uparrow\uparrow\rangle + |\downarrow\downarrow\rangle\} + d_z\{|\uparrow\downarrow\rangle + |\downarrow\uparrow\rangle\}$.

Having thoroughly discussed the symmetries that constrain the form of the superconducting gap function, the specific form of the gap for s-wave and p-wave superconductors, such as its symmetry properties and nodal structure, can be investigated. For the spin-singlet state with L = 0 (s-wave) and protected by$\mathcal{T}$ symmetry, the gap function transforms to:

$$\Delta_{\vec{k}} = \Delta_0 = \psi(\vec{k}) \tag{5.37}$$

This implies that the gap function is a scalar quantity with an isotropic gap all along the Fermi surface, thereby establishing a single superconducting gap for the s-wave superconductors (ref. to figure 5.5 and 5.9). For the spin-triplet-pairing state, the gap structure is complex since its specific form is governed by the vector-$\vec{d}$. E.g., the gap function for the chiral p-wave state defined as $\vec{d}(\vec{k}) = \frac{\Delta_0}{k_F}(k_x \pm ik_y)$ (discussed in the subsection 5.3.1) takes the following form [176]:

$$|\Delta_{\vec{k}}|^2 = |\Delta_0|^2 \frac{k_x^2 + k_y^2}{k_F^2} \tag{5.38}$$

This state is known to have nodes in the superconducting gap for $\vec{k}$ || (0,0,±1) and has a net out-of-plane orbital angular momentum, $L_z = \pm 1$. In some cases, like for tetragonal crystals, the p_x and p_y gap functions are degenerate so one can form combinations of the type $p_x \pm ip_y$, the square of the modulus of which is isotropic. In the case of a cylindrical Fermi surface, this state exhibits no nodes, resulting in an optimized condensation energy for p-wave pairing [184].

5.3 p-wave superconductivity

Following the discovery of the BCS theory, the pairing mechanism for most of the superconductors in the early 1970s could be explained by the electron-phonon interaction, which leads to the formation of Cooper pairs with a singlet spin configuration and a net zero angular momentum. As mentioned previously, these superconductors were termed as s-wave or BCS superconductors. However, the discovery of superfluidity in ^{3}He in 1971 spurred extensive research into the possibility of a pairing state with non-zero angular momentum. Unlike the conventional s-wave superconductors, the Cooper pairs in ^{3}He possess a net angular momentum of L = 1 and a triplet-like spin configuration [176, 185]. As shown in the previous section, a net orbital angular momentum of 1 warrants their classification as p-wave superconductors. It was proposed that such a pairing with non-zero angular momentum would result from electron-electron interactions, which, despite being repulsive at short distances, are overall attractive. This would induce the formation of Cooper pairs with non-zero angular momentum. This implies that the conventional electron-phonon coupling could not explain the formation of non-zero momentum Cooper pairs. In the case of ^{3}He, the microscopic pairing mechanism was attributed to electron-paramagnon coupling (related to spin fluctuation mechanisms) or effects related to vdW origin [180, 186]. Due to the unconventional non-BCS-like pairing nature, the p-wave superconductors are also termed “unconventional superconductors”. The p-wave superconductors can be further classified into chiral p-wave and helical p-wave, depending on whether $\mathcal{T}$ is present or absent, which will be briefly discussed in the subsequent sections.

5.3.1 Mathematical formalism for a p-wave gap function

In the case of the s-wave superconductors, the gap function is a constant quantity, however for the case of a p-wave superconductor, the gap function can, for e.g., take the form $\Delta(\vec{k}) = \Delta_0$ (sin $k_x a$ +i sin k_ya) $= \Delta_0$ (sin k_x +i sin k_y) (for a = 1) , which for $k \to 0$, reduces to $\Delta(\vec{k}) = \Delta_0(k_x + ik_y)$. Substituting the form of this gap function into the BCS Hamiltonian, the Bogoliubov-de-Gennes (BdG) Hamiltonian [177, 187] corresponding to the p-wave state can be written as:

$$H_{BdG} = \begin{pmatrix} \frac{k^2}{2m} - \mu & \Delta_0(k_x + ik_y) \\ \Delta_0(k_x - ik_y) & \frac{k^2}{2m} - \mu \end{pmatrix} \tag{5.39}$$

where μ corresponds to the chemical potential. The energy eigenvalues of H_{BdG} can be obtained by solving the determinant $(H_{BdG}(k) - E\mathbb{I}) = 0$:

$$E^2 = \left(\frac{k^2}{2m} - \mu\right)^2 + |\Delta(\boldsymbol{k})|^2 = \left(\frac{k^2}{2m} - \mu\right)^2 + \Delta_0^2(k_x^2 + k_y^2). \tag{5.40}$$

From the above equation, it is evident that a gap-closing condition $(E = 0)$ occurs when:

$$\frac{k^2}{2m} = \mu \quad \text{and} \quad k_x = k_y = 0 \tag{5.41}$$

thereby suggesting that a topological phase transition occurs at $\mu = 0$. Notably, for both $\mu < 0$ and $\mu > 0$, the system is gapped, however, one of them is potentially topological while the other is trivial, which can be shown by calculating the Chern number corresponding to H_{BdG}. For this, H_{BdG} can be written as the product of the spin-triplet vector, $\vec{d}(k)$ and the Pauli matrices [4]:

$$H_{BdG}(k) = \vec{d}(k).\vec{\sigma}, \tag{5.42}$$

where $\vec{d}(k) = \left(\Delta_0 k_x, \Delta_0 k_y, \frac{k^2}{2m} - \mu\right)$ and $\vec{\sigma} = (\sigma_x, \sigma_y, \sigma_z)$ is the Pauli spin matrices. The Chern number corresponding to the H_{BdG} is defined as:

$$C = \frac{1}{4\pi}\int_{BZ} d^2k(\partial_{k_x}\hat{d} \times \partial_{k_y}\hat{d}) \cdot \hat{d}, \tag{5.43}$$

where $\hat{d} = \frac{\vec{d}}{|\vec{d}|}$ is the unit vector. On solving the integral, it can be obtained that $C = sgn(\mu)$, for $\mu > 0$. Notably for $\mu > 0$, $C = 1$. As previously discussed in sec. 3.1, a non-zero Chern number corresponds to non-trivial topology [1], hence $\mu > 0$, corresponds to the topologically non-trivial case, implying a topological p-wave pairing state. On the other hand, for $\mu < 0$, $C = 0$, corresponding to the case of an insulator. A key physical manifestation of the topologically non-trivial state (with Chern number $C = 1$) is the emergence of robust edge states at the boundary, as dictated by the bulk-boundary correspondence.

In the subsequent subsection, the discussion turns to the two variants of topological p-wave superconductivity: the chiral and helical p-wave state.

5.3.2 Chiral p-wave vs. Helical p-wave superconductors

The chiral p-wave superconducting state emerges when spin-triplet Cooper pairs with equal spins form, spontaneously breaking $\mathcal{T}$ symmetry. As the name implies, it shares key characteristics with the QHE described in section 3.1. Both systems support chiral edge modes, however, in the case of chiral p-wave superconductors, the chiral edge modes are formed by spin-polarized Cooper pairs, specifically the spin-triplet state $|\uparrow\uparrow\rangle$ or $|\downarrow\downarrow\rangle$. A schematic illustration of the chiral p-wave pairing is shown in figure 5.10a, where a Cooper pair with equal down spins rotates in an anticlockwise direction around the Fermi surface with a net Cooper pair orbital angular momentum indicated by the large arrow at the center. Notably, the chiral superconductors are topologically non-trivial [34], as evident from their intriguing non-BCS-like behavior; they are known to support features reminiscent of the topological character, such as the edge modes. The most common are the dispersive edge states crossing the Fermi energy and located inside the non-trivial gap of the chiral p-wave superconducting state. These states pinned at the Fermi energy are the zero energy states, occupied by the Majorana fermions [41, 184]. These zero-energy Majorana fermions propagate along the boundary of the superconductors in real space,

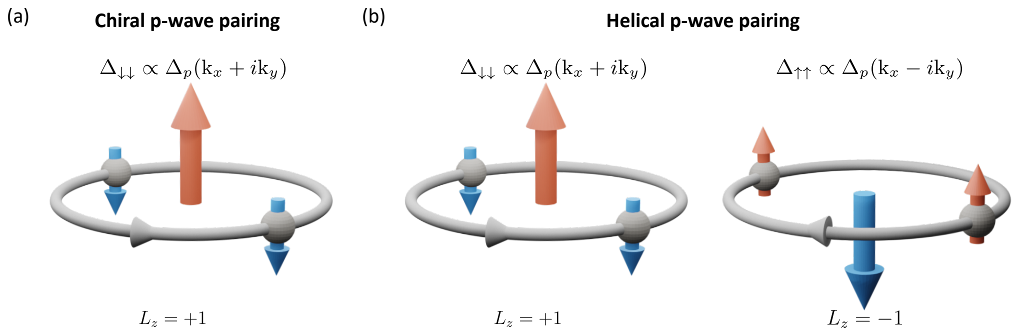
(a)
Chiral p-wave pairing
$\Delta_{\downarrow\downarrow} \propto \Delta_p(k_x + ik_y)$
$L_z = +1$
(b)
Helical p-wave pairing
$\Delta_{\downarrow\downarrow} \propto \Delta_p(k_x + ik_y)$
$\Delta_{\uparrow\uparrow} \propto \Delta_p(k_x - ik_y)$
$L_z = +1$
$L_z = -1$

Figure 5.10: Schematic illustration of the (a) chiral p-wave pairing state showing pairing between two down spin electrons moving in the anticlockwise direction with a net relative angular momentum $L_z = +1$, (b) helical p-wave pairing state where one chirality involves pairing between two down spin electrons moving in the anticlockwise direction carrying a net out-of-plane orbital angular momentum of +1 while the other chirality carries two up spin electrons in the clockwise direction with a net out-of-plane orbital angular momentum of -1, resulting in no net chirality.

leading to chiral edge currents. It is also known that chiral edge states combined with their non-trivial topology can give rise to quantized Hall conductance [41, 184, 188]. Another particularly intriguing aspect of chiral spin-triplet superconductors is the emergence of half-quantized vortices, each of which possesses a single localized Majorana zero-energy mode at its center [41, 180]. Given the unique properties of chiral p-wave superconductors, particularly the presence of robust Majorana zero modes, it can be concluded that these offer a promising foundation for the development of topological quantum computers, however, it is worth noting that the only firmly established chiral p-wave superconductor to date is ^{3}He. Other materials, that have proven to be promising candidates for chiral p-wave superconductivity and have been under extensive research, are UPt$_3$ [189–191] and Sr$_2$RuO$_4$ [192–194]. More recently, an STM study has also demonstrated chiral p-wave superconductivity in the heavy fermion candidate UTe$_2$ [195]. There also exist other ferromagnetic heavy fermion compounds such as UCoGe and UGe, which are promising candidates for chiral p-wave superconductors [190, 196, 197].

Besides the chiral p-wave state, there also exists the helical p-wave state, which was 1^{st} observed in the B-phase of superfluid ^{3}He [186]. The symmetry of the gap function for the helical state is given by the following $\vec{d}$ vector: $\vec{d} = k_x\hat{x} + k_y\hat{y}$. In the helical state, the up (↑) spins possess a positive chirality denoted as $k_x - ik_y$, while the down (↓) spins are in a state of negative chirality denoted as $-(k_x + ik_y)$ [184]. Qualitatively, the helical p-wave state can be viewed as two identical copies of the chiral p-wave state with opposite chiralities, resulting in no net chirality. Figure 5.10b shows a schematic illustration for a special case of the helical p-wave pairing state consisting of two opposite chiralities: in one case the down spin electrons pair up and move in an anticlockwise direction with an out-of-plane angular momentum of +1, while the other chirality involves pairing between two up spin electrons moving in a clockwise direction with a net out-of-plane angular momentum of -1. Similar to the chiral p-wave state, the helical p-wave state is also topologically non-trivial [34], but this state does not preserve $\mathcal{T}$ symmetry. Helical p-wave superconductivity was proposed in the compound BiH, where the Rashba SOC has been shown to drive the system from the chiral to the helical phase [198]. Theoretical studies have suggested a mixed helical p-wave pairing state in the mysterious unconventional superconductor Sr_2RuO_4 to account for the observation of polar Kerr effect. In this case, it was shown that this state would comprise two copies of the chiral p-wave but with different pairing amplitudes.

The discussion of helical p-wave superconductivity is motivated by the experimental results presented in Chapter 6, which will reveal a potentially intrinsic helical p-wave pairing state at the interface between a ferromagnetic insulator and a conventional s-wave superconductor. As will be demonstrated through combined experimental and theoretical analysis, this system exhibits a striking coexistence of two distinct pairing states: while the interface hosts a helical p-wave superconducting phase, the bulk regions away from the ferromagnetic interface maintain their s-wave character. Crucially, the boundary separating these topologically distinct phases gives rise to topologically protected helical edge states – a direct manifestation of the bulk-boundary correspondence principle in topological superconductors.

5.4 Rashba Spin-Orbit-Coupling

The Rashba spin-orbit coupling (SOC) is a relativistic quantum mechanical effect that arises in systems with structural inversion asymmetry, where an electric field gradient induces a momentum-dependent splitting of spin states. This phenomenon, first theoretically predicted by Emmanuel Rashba in 1960, has since become a cornerstone in the study of spin-dependent electronic properties in low-dimensional systems. The Rashba effect is characterized by a Hamiltonian of the form:

$$H_{Rashba} = \alpha_R(\mathbf{k} \times \vec{\sigma}) \cdot \hat{z}, \tag{5.44}$$

where α_R is the Rashba parameter, $\mathbf{k}$ is the electron momentum, $\vec{\sigma}$ represents the Pauli spin matrices, and $\hat{z}$ is the direction of the electric field gradient. This coupling between spin and momentum has profound implications for spintronics, topological materials, and superconductivity. The Rashba effect plays a pivotal role in the emergence of topological states of matter, such as topological insulators and topological superconductors. In topological insulators, the combination of Rashba SOC and time-reversal symmetry leads to the formation of robust surface states with spin-momentum locking [2, 19, 79, 88]. Similarly, in superconducting heterostructures, Rashba SOC can induce unconventional pairing symmetries, such as p-wave superconductivity, which are essential for realizing TSC and MBS, which will be the topic of discussion in the subsequent chapter.

5.5 2D van der Waals materials

The successful separation of graphene from bulk graphite constituted a significant milestone towards the development of 2D materials [199]. Since then, the field of 2D materials has expanded rapidly, leading to the discovery of a larger variety of materials with diverse properties, from insulators and semiconductors to metals, TIs, and superconductors [200–202]. The fascination with 2D materials arises from their unique properties which differ significantly from their 3D counterparts. The simplest example being graphene, a zero band gap semiconductor, on the contrary, graphite, its 3D counterpart, is a semimetal with overlapping bands. Within each atomic layer of a 2D material, the atoms are covalently bonded and free from any dangling bonds. On the contrary, the neighbouring layers are weakly bonded by the vdW interaction. This makes it feasible to precisely tune the electronic properties, including band-gap engineering through layer variation. The last decade has seen this method of layer variation being applied to the case of graphene, where different layers of graphene were twisted and combined to unravel novel quantum phenomena such as unconventional superconductivity [203–205], Hofstader butterfly effects [206, 207], interaction-driven ferromagnetism [208], etc.

Among the diverse 2D materials discovered [200, 209, 210], the 2D transition-metal dichalcogenides (TMDCs) have garnered significant attention owing to their rich variety of chemical composition and structural phases. This diversity results in a wide range of electronic properties, including the emergence of correlated phases such as superconductivity [210–218], charge density wave (CDW) [219–224], pair density wave (PDW) [225, 226] and spin density wave [227, 228]. The TMDCs are formed from the transition metals (group IV to group IX of the periodic table) bonded to elements of the chalcogen group such as that of Se, Te, and S. Different structural phases of TMDCs exist depending on the coordination of the transition metal atoms with the chalcogen atoms. The most common phases are the 2H phase, where the transition metal atoms are coordinated with six chalcogen atoms in a trigonal prismatic geometry, and the 1T phase, where the transition metal atoms are coordinated with six chalcogen atoms in an octahedral geometry. The family of 2D TMDCs is rapidly expanding, with numerous materials discovered, such as MoS_2, $NbSe_2$, TaS_2, $TiSe_2$, NbS_2, WTe_2, UTe_2, etc. The list is still growing with the ongoing advancement in materials research.

Beyond the above-mentioned discoveries in 2D materials, 2D magnetism has emerged as a particularly fascinating area. While 3D materials with Heisenberg-type spin are readily known to exhibit long-range magnetic ordering at a finite temperature, the magnetism for 2D materials is more complex, as the theory dictates that the magnetic ordering for Heisenberg- and Ising-type spins exists only above 2D and 1D, respectively [229–231]. Contrary to theoretical expectation, recent experimental evidence indicates that magneto-crystalline anisotropy [232–234], interfacial spin-orbit interactions [235], and magnetostatic dipole-dipole interactions [236] can indeed stabilize ferromagnetic or antiferromagnetic order in 2D materials. Early efforts to create 2D magnets initiated with the exfoliation of thin layers from the bulk single crystals of $FePS_3$, $NiPS_3$, and $CrSiTe_3$, however, the detection of magnetism relied on indirect techniques such as Raman Spectroscopy. The first direct experimental evidence of ferromagnetic ordering was found in atomically thin exfoliated layers of CrI_3 [233] and Fe_3GeTe_2 [232]. Since then, the range of 2D materials has expanded exhibiting different magnetic ground states such as ferromagnetism [232–234, 237–240], antiferromagnetism [241–243], 2D XY [74] and helimagnetism [124, 244].

In light of the experimental results presented in Chapter 6, the following subsections will explore the properties of the 2D in-plane ferromagnet $CrCl_3$ and the 2D vdW superconductor $NbSe_2$.

5.5.1 $CrCl_3$: a 2D in-plane van der Waals ferromagnet

$CrCl_3$ is a magnetic insulator which, in its bulk form, crystallizes in the layered rhombohedral structure with $R\overline{3}$ symmetry at low-temperature. The side view of the unit cell of $CrCl_3$ as shown in figure 5.11a is composed of covalently bonded Cl-Cr-Cl triple layers (dashed box in figure 5.11). The individual Cl-Cr-Cl triple layer forms the unit cell of a ML, where the layer of Cr atoms is sandwiched between two layers of Cl above and below it. Within each ML unit cell, the Cr atoms are octahedrally coordinated to 6 Cl atoms, 3 from the layer above and 3 from the layer

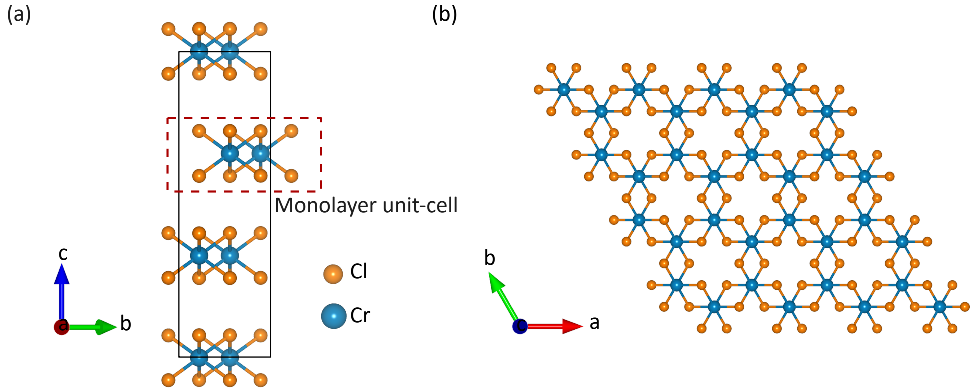

Figure 5.11: (a) Side view of the unit-cell of $CrCl_3$ composed of Cl-Cr-Cl triple layers. (b) The top view of the crystal structure illustrates the hexagonal lattice of Cr atoms.

below. These individual MLs within the unit cell of $CrCl_3$ are held together via the weak vdW interaction. Figure 5.11b shows the top view of the crystal structure, revealing a hexagonal arrangement of the Cr atoms. Bulk $CrCl_3$ is known to be an in-plane antiferromagnet with a Néel temperature of $T_N \sim 14$ K [245, 246]. This antiferromagnetic ordering results from the alternating magnetization of the individual MLs, which exhibit ferromagnetic ordering within the plane. Previous experimental investigations had successfully confirmed the presence of interlayer antiferromagnetic ordering in $CrCl_3$ down to the bilayer limit [245]. However, direct experimental evidence of in-plane ferromagnetism in $CrCl_3$ MLs remained elusive. This challenge stemmed from two primary factors: the difficulty in obtaining isolated MLs through exfoliation techniques and the inherent weakness of the magnetic signal in these MLs, which made it challenging to detect using conventional laboratory measurement techniques such as vibration sample magnetometry or superconducting quantum interference devices. Amilcar *et al.* has recently addressed these challenges by growing MLs of $CrCl_3$ on graphene/6H-SiC(0001) using MBE and performing x-ray magnetic circular dichroism (XMCD) measurements to demonstrate an in-plane ferromagnetic ordering with a 2D XY-like scaling behavior [74]. This behaviour in the $CrCl_3$ ML is unique as compared to other trihalide MLs, such as those of $CrBr_3$ and CrI_3, which favor an out-of-plane alignment of the magnetization [233, 247].

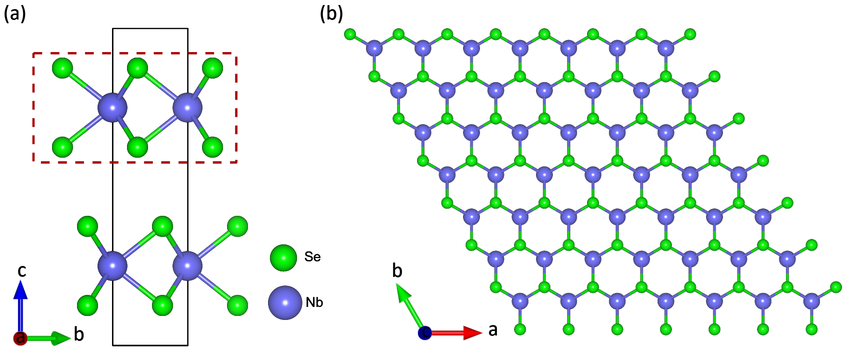

Figure 5.12: (a) Side view of the unit cell of $NbSe_2$. (b) Top view of the crystal structure showing a hexagonal arrangement of the Nb and Se atoms.

5.5.2 $NbSe_2$: a 2D van der Waals superconductor

$NbSe_2$ is a layered 2D TMDC that has garnered interest for its ability to exhibit multiple electronic phases. It is known to be metallic at room temperature and becomes superconducting below a certain critical temperature ($T_c = 7.2$ K). Furthermore, there exist different reports that suggest a multiband superconductivity in $NbSe_2$, revealing a two-gap feature in the DOS [233, 248, 249]. $NbSe_2$ also undergoes a transition to the CDW state at T = 33 K, preceding the superconducting state. One of the most intriguing aspects of $NbSe_2$ is the observed coexistence of charge density wave (CDW) and superconducting states at low temperatures, which has sparked considerable debate regarding its underlying cause.

Bulk $NbSe_2$ has a hexagonal crystal structure, with each unit cell composed of Se-Nb-Se MLs (as depicted by the dashed red box in figure 5.12a). The individual MLs are bonded to one another by the weak vdW interaction. Within a ML, the Nb atoms are coordinated to the Se atoms in a trigonal prismatic manner. The top view of the $NbSe_2$ lattice is illustrated in figure 5.12b, showing a hexagonal arrangement of the Nb and Se atoms. The electronic band structure of bulk $NbSe_2$ was initially studied using density functional theory (DFT) [250, 251] followed by successful demonstrations using ARPES [248]. The electronic band structure is derived from the Nb 4d atomic orbitals, which are subject to a crystal field splitting into three distinct groups due to the trigonal symmetry: d_{z^2}, $[d_{x^2-y^2}, d_{xy}]$, and $[d_{xz}, d_{yz}]$

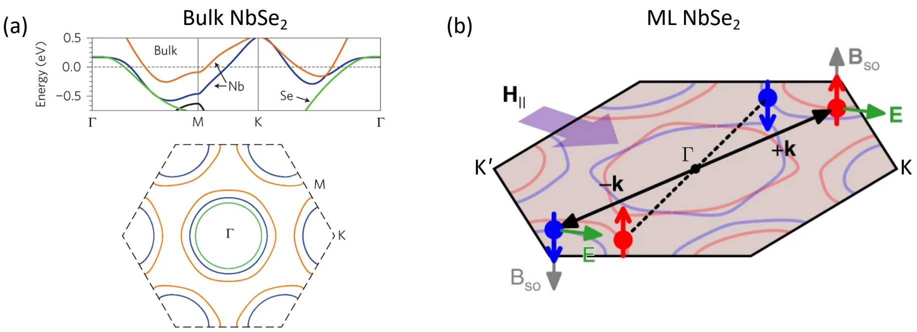

Figure 5.13: (a) (Top) Calculated band structure of bulk $NbSe_2$ showing 3 bands that cross the Fermi surface. (Bottom) Fermi surface of bulk $NbSe_2$ showing 3 pockets around the Γ point. (b) The Fermi surface of monolayer $NbSe_2$ illustrates electron pairing within one of the spin-split Fermi surfaces around the K and K′ points, with spins locked to the out-of-plane direction due to the effective magnetic field H_{SOC}. Parts (a) and (b) reprinted from ref. [253] and [254], respectively, Springer Nature Limited.

[252]. Figure 5.13a shows the bulk band structure of $NbSe_2$ where 3 bands cross the Fermi energy, 2 of which are derived from the Nb 4d orbitals and one from the Se p_z orbitals. The corresponding Fermi surface shows Fermi pockets around the Γ point and the inequivalent K and K′ points. The superconductivity in $NbSe_2$ arises from either intervalley pairing between electrons located at K and K′ points or intrapocket pairing at the Γ point.

Unlike bulk $NbSe_2$, which has a centrosymmetric crystal structure, ML $NbSe_2$ possesses out-of-plane mirror symmetry and lacks inversion symmetry, as illustrated in its crystal structure (see figure 5.12a). This structural asymmetry confines the crystal electric field (**E**) to the in-plane direction, as depicted in figure 5.13b. It is well-established that in crystals without inversion symmetry, an asymmetric form of spin-orbit coupling (SOC) is permitted [255]. This SOC generates an effective out-of-plane magnetic field, $H_{SOC}(\mathbf{k}) \propto \mathbf{k}\times \mathbf{E}$, which acts on electrons moving within the 2D plane. Consequently, the electron spins align out-of-plane, with opposite spins for opposite momenta. This spin-momentum locking leads to the formation of Cooper pairs between an electron at the K point and its time-reversed counterpart with opposite spin and momentum at the K′ point. Such pairing, where the electron spins are locked to their momentum and oriented out-of-plane, is referred to as Ising-type pairing. In monolayer $NbSe_2$, this pairing mechanism significantly influences the superconducting states, enabling in-plane critical fields that exceed the Pauli paramagnetic limit [224, 254].

6 Helical edge states in a van der Waals heterostructure

This chapter presents experimental evidence for the emergence of interfacial unconventional TSC in heterostructures formed by ML ferromagnetic $CrCl_3$ on superconducting $NbSe_2$ bulk crystals. Through high-resolution STM measurements, two remarkable phenomena have been demonstrated: (1) an enhanced robustness of the superconducting gap at the $CrCl_3/NbSe_2$ interface compared to bare $NbSe_2$ under out-of-plane magnetic fields, and (2) spatially localized enhancement of the zero-bias LDOS along $CrCl_3$ island edges. These observations, supported by theoretical calculations, provide strong evidence for the formation of an unconventional TSC state at the interface.

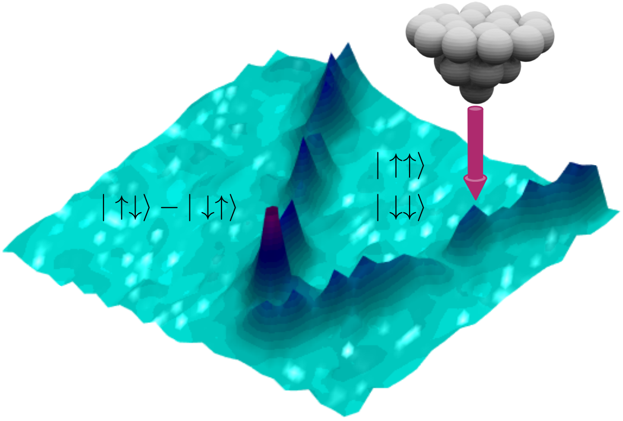
$|\uparrow\downarrow\rangle - |\downarrow\uparrow\rangle$
$|\uparrow\uparrow\rangle$
$|\downarrow\downarrow\rangle$

Topological edge states at the boundary between a s-wave and p-wave superconductor

The research outlined in this chapter is presently in the review process.

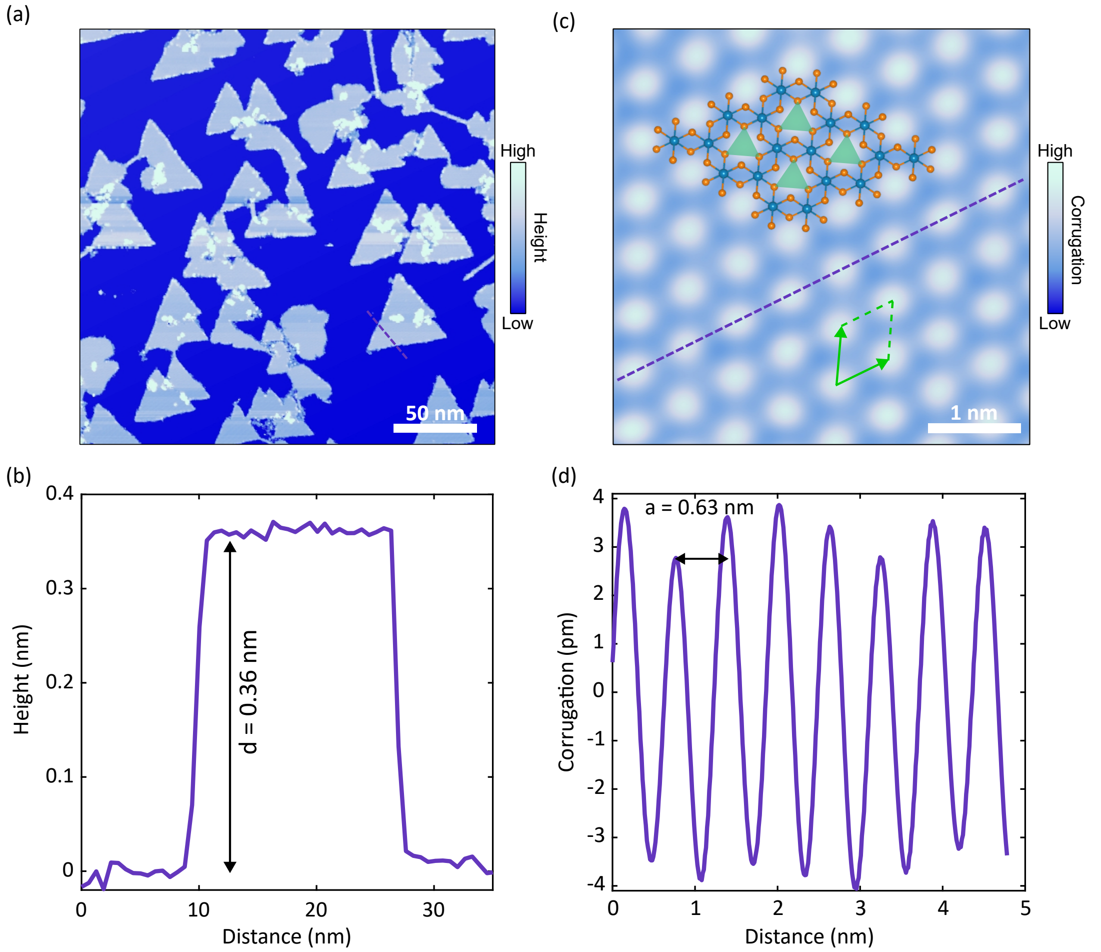

Figure 6.1: (a) STM topographic image of the $CrCl_3/NbSe_2$ heterostructure. Scanning parameters: $I_t = 15$ pA, $V_b = 1$ V. (b) Line profile acquired along the dashed purple line in (a) corresponds to the thickness of a ML island (d = 0.36 nm). (c) Atomically resolved STM topographic image on a $CrCl_3$ island where the bright protrusions are the z contrast from a trimer of Cl atoms indicated by the light green triangle on the overlaid crystal structure. The green parallelogram denotes the unit cell of the $CrCl_3$ lattice. Scanning parameters: $I_t = 25$ pA, $V_b = 1.5$ V. (d) Line profile along the dashed line in (c) shows the atomic corrugation. The measured in-plane lattice constant of the $CrCl_3$ ML is d = 0.63 nm.

6.1 STM topography of the vdW heterostructure $CrCl_3/NbSe_2$

Building upon the discussion of the individual 2D materials $CrCl_3$ and $NbSe_2$ in the previous chapter, the discussion now turns to their combined vdW heterostructure. This section provides a comprehensive investigation of the structural properties of the heterostructure formed when ML flakes of the in-plane ferromagnetic insulator

$CrCl_3$ are integrated with the 2D superconductor $NbSe_2$. The $CrCl_3/NbSe_2$ heterostructures are grown by MBE following the procedure discussed in sec. 2.3.3 and are probed using a low-temperature STM working at T= 1.8 K. Figure 6.1a displays a STM topographic image of the $CrCl_3/NbSe_2$ heterostructure, featuring triangularly-shaped $CrCl_3$ islands, where the triangular shape indicates the inherent three-fold $R\overline{3}$ symmetry of the underlying lattice. The line profile across a $CrCl_3$ island (dashed purple line in figure 6.1a) as shown in figure 6.1b indicates the height of the ML island, which is d = 0.36 nm at the measured bias voltage of 1V. In STM, the apparent height is influenced by the LDOS, meaning that varying the bias voltage can result in different measured heights for the same ML. For instance, when the same ML island was measured at a bias voltage of 1.5 V, the observed height increased to 0.55 nm. The atomically resolved image acquired on a $CrCl_3$ island is shown in figure 6.1c, where the round protrusions appearing as individual atoms reveal the combined z-contrast from 3 Cl atoms that form a trimer. The crystal structure is overlaid on the atomically resolved image to indicate the same (light green triangles connecting the 3 Cl atoms). Similar topographic effects have been observed in Cr-trihalides grown on different substrates [57, 256]. The green parallelogram depicts the unit cell of the $CrCl_3$ lattice. The atomic corrugation of the $CrCl_3$ lattice is depicted in Figure 6.1d, from which an in-plane lattice constant of a = 0.63 nm was deduced.

Having examined the structural properties of the $CrCl_3$ ML, the structural properties of the $NbSe_2$ surface will be discussed now. On the right of figure 6.2a, an atomically resolved image of the $NbSe_2$ surface is shown. The image reveals bright protrusions in a hexagonal arrangement that corresponds to the Se lattice with a lattice constant of $a_{Se} \sim 3.6$ Å. In addition to the atomic modulation, a periodic modulation of bright triangular (red circle) and round protrusions (grey circle) is observed, consistent with an incommensurate CDW, with a lattice constant of $a_{CDW} > 3a_{Se}$. The atomic corrugation acquired along the dashed line in figure 6.2a is elucidated in figure 6.2c, revealing the lattice periodicity of the CDW and the

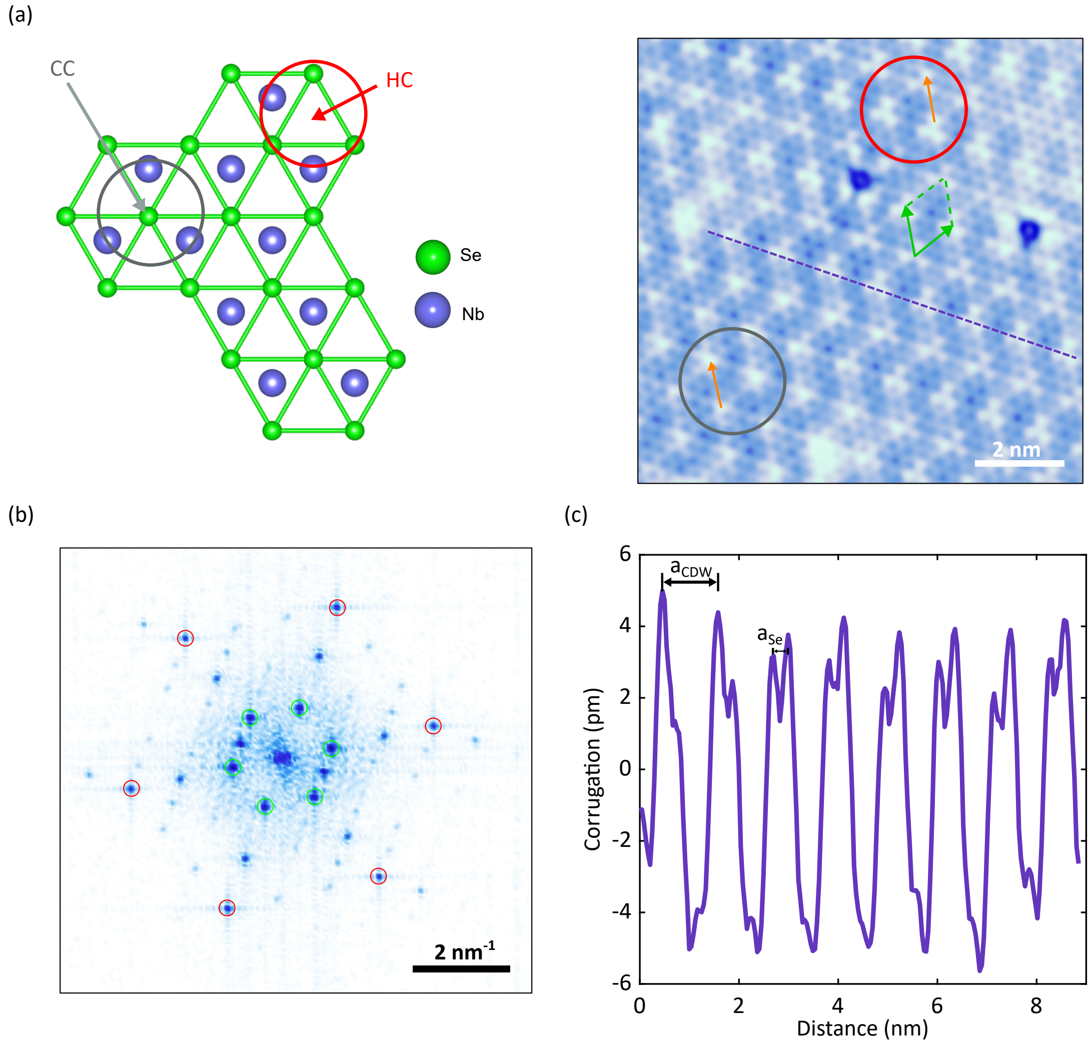

Figure 6.2: (a) (left) Top view of the crystal structure highlighting the two CDW centers: the chalcogen-centered (CC) and the hollow-centered (HC). (right) Atomically resolved STM topographic image of the NbSe$_2$ surface showing the Se lattice and the 2 types of CDW modulation. Scanning parameters: $I_t = 250$ pA, $V_b = 40$ mV. (b) 2D-FFT corresponding to the topographic image in (a) showing hexagonal spots of different order originating from the Se lattice (red circles) and the CDW (green circles). (c) Atomic corrugation of the NbSe$_2$ surface acquired along the purple dashed line in (a).

Se atoms. The green parallelogram denotes the unit cell of the CDW lattice. The bright triangular protrusions arise when the CDW maxima are centered at the hollow site enclosed by 3 Se atoms, while the round protrusions are a result of the CDW maxima centered on the chalcogen atom. This is schematically illustrated in the left panel of figure 6.2a which shows a top view of the NbSe$_2$ lattice, where the chalcogen-centered (CC) and hollow-centered (HC) CDW maxima are indicated. The 2D-FFT corresponding to the topography in figure 6.2a is presented in figure

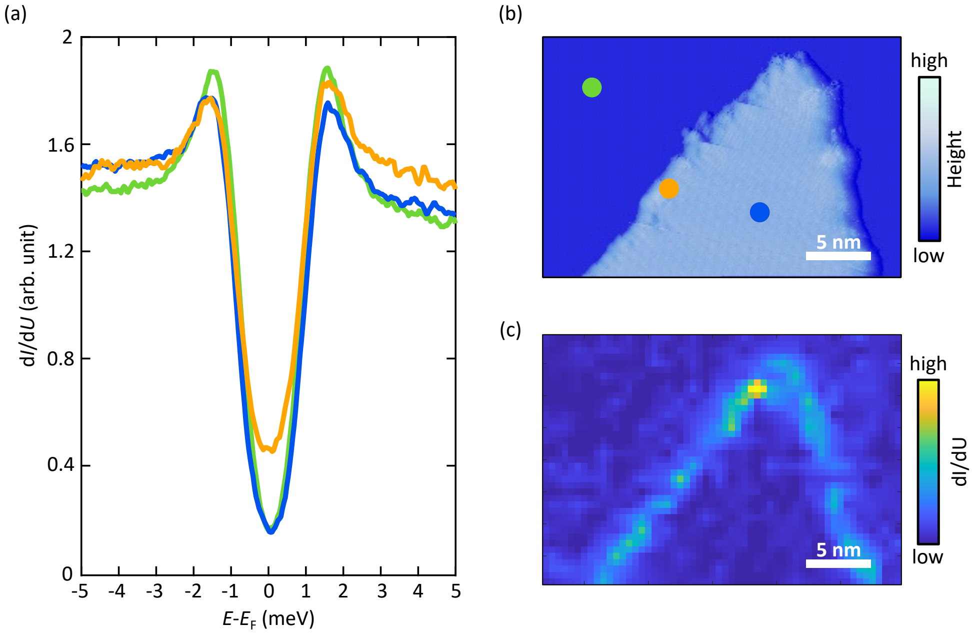

Figure 6.3: (a) Raw dI/dU spectra on the NbSe$_2$ substrate (green), on the CrCl$_3$ island (blue) and at the edge of the CrCl$_3$ island (yellow) in the low energy range acquired at the respective locations marked by colored circles on the STM topographic map of a ML CrCl3 island in (b). (c) Spatially resolved dI/dU map at zero bias, corresponding to the STM topographic map shown in (b), revealing the presence of edge modes. Scanning parameters for b: I_t = 25 pA, V_b = 1.5 V; Stabilization parameters for a and c: I_t = 100 pA, V_b = -5 mV, V_{mod} = 0.15 mV.

6.2c, revealing two sets of diffraction spots, where the inner (green circles) hexagonal diffraction spots reflect the CDW's 6-fold symmetry and the outer spots (red circles) correspond to the 6-fold symmetry of the Se lattice.

6.2 Edge states in the CrCl$_3$/NbSe$_2$ heterostructure

Following an introduction to the topographic features of the CrCl$_3$/NbSe$_2$ heterostructure, the electronic properties will be investigated now. The electronic properties of the heterostructure are examined using the STS technique. Figure 6.3a presents typical STS spectra obtained at various locations, as indicated by the colored circles in the STM topographic image in figure 6.3b. The dI/dU spectrum acquired on the bare NbSe$_2$ substrate (green in figure 6.3a) features a characteristic superconducting gap in the LDOS, indicative of s-wave superconductivity, evidenced

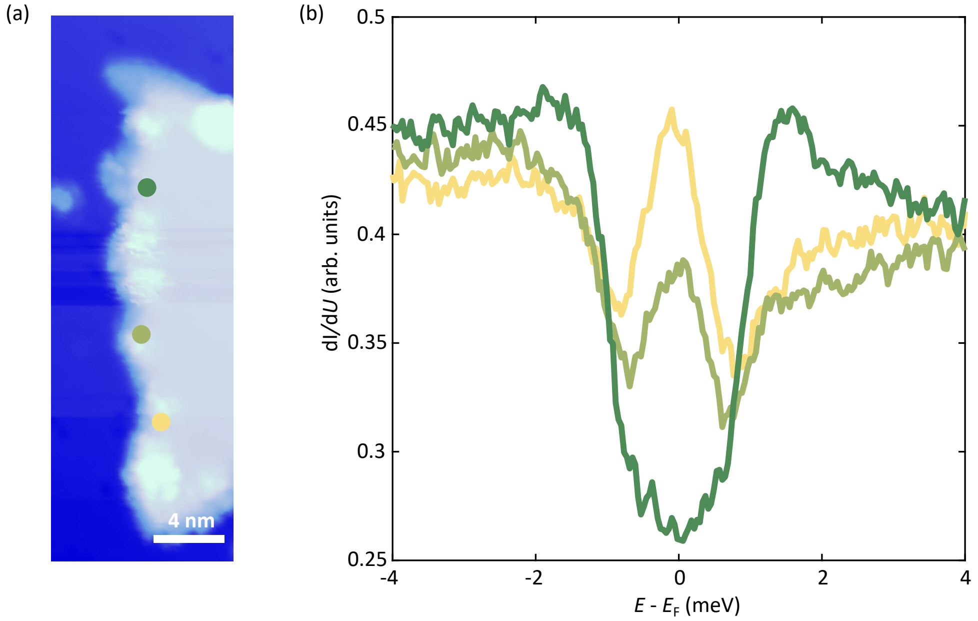

Figure 6.4: (a) STM topographic image of a section of a $CrCl_3$ island revealing many defects at the island edges, appearing as bright objects. Scanning parameters: $I_t = 20$ pA, $V_b = 1$ V (b) dI/dU spectra acquired on the defects marked by colored circles in (a) show a zero-bias peak. Away from the defect, the dip-like feature of the superconducting DOS (dark green curve) is recovered. Stabilization parameters for (b): $I_t = 200$ pA, $V_b = -5$ mV, $V_{mod} = 0.1$ mV.

by a dip at E_F. Notably, the dI/dU spectrum measured at the center of the $CrCl_3$ island (blue in figure 6.3a) also exhibits a superconducting gap, despite $CrCl_3$ being a magnetic insulator. While the spectra from $NbSe_2$ and the $CrCl_3$ island appear qualitatively similar, with only subtle variations, the spectra obtained at the edge of the $CrCl_3$ island reveal an enhancement in the spectral weight in the LDOS near E_F (yellow in 6.3a). This spectral feature indicates the presence of edge modes at the boundary of the $CrCl_3$ islands. In contrast to zero-dimensional (0D) Majorana modes, which are localized at the ends of 1D topological superconductors and manifest as a zero-bias anomaly, 2D topological superconductors are expected to host 1D propagating Majorana edge modes [50, 54, 56, 57]. These propagating modes, which can be either helical or chiral depending on the presence or absence of time-reversal symmetry, are characterized by a linear energy-momentum dispersion relation and a uniform DOS near E_F, resulting in a flat spectral weight within the superconducting energy gap [54]. It is important to note that the observation of an enhanced LDOS at E_F in the present case is different from what has been previously reported on a similar heterostructure consisting of $CrBr_3$ on top of $NbSe_2$ [57], where a zero-bias peak was observed at the edge of the $CrBr_3$ islands, which was attributed to MZM. Such a zero-bias peak likely arises from a localized bound state rather than a propagating edge state as has been shown in recent reports on the same heterostructure [257]. Indeed, zero-bias peaks have also been observed in the dI/dU spectra at certain positions along the edge of the $CrCl_3$ islands as shown in figure 6.4, which can be attributed to the presence of defect states located near the island edges. To investigate the spatially localized nature of the edge states, spectroscopic mapping was performed across a grid of 600 points on the topography in figure 6.3b. The resultant dI/dU map at zero energy as shown in figure 6.3c reveals a strong intensity along the boundary of the $CrCl_3$ island, which corresponds to the edge modes. Interestingly, the edge modes in the case of the $CrCl_3/NbSe_2$ heterostructure are continuous and connected, unlike the ones in the $CrBr_3/NbSe_2$ heterostructure, which are isolated and disconnected, thereby providing evidence of propagating 1D edge modes.

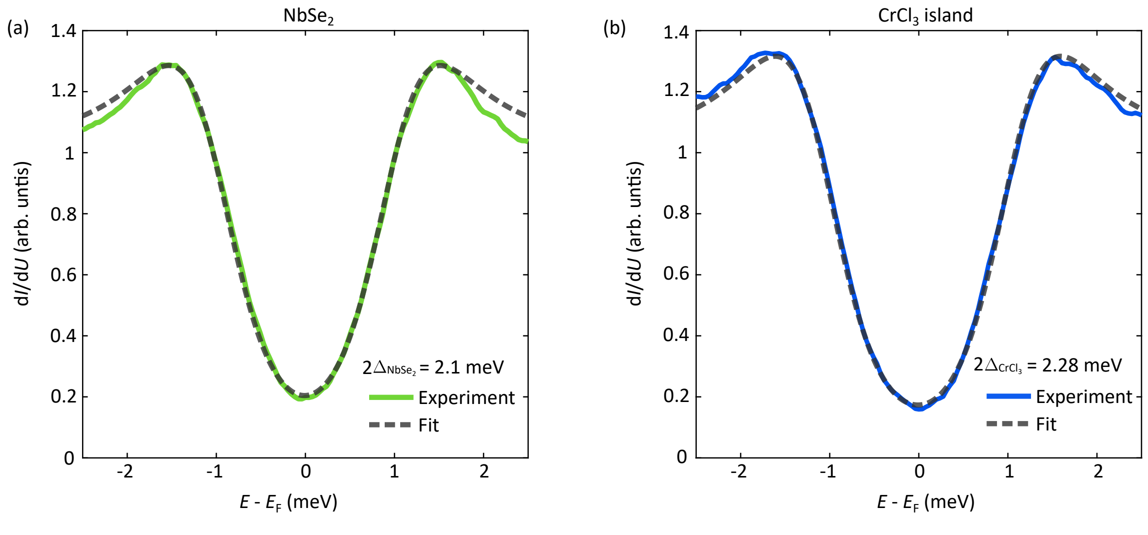

Figure 6.5: BCS fit using Dynes function, $\rho_s^{Dynes}(E,\Gamma)=\mathrm{Re}\left[\frac{|E|+i\Gamma}{\sqrt{(|E|+i\Gamma)^2-\Delta^2}}\right]$ where Γ is the broadening parameter associated with the lifetime of the quasiparticles and the finite experimental resolution. This is proportional to the dI/dU at zero temperature. The experimental dI/dU spectra were fitted using the following expression, $\frac{dI}{dU}=G_n\frac{d}{dU}\int_{-\infty}^{\infty}\rho_s^{\mathrm{Dynes}}(E,\Gamma)[f(E)-f(E-eV)]dE$, where G_n is the normal state conductance and $f(E)$ is the Fermi function. The corresponding fit yields a gap magnitude of a, $2\Delta_{\mathrm{NbSe_2}}=2.10$ meV on the $NbSe_2$ substrate and b, $2\Delta_{\mathrm{CrCl_3}}=2.28$ meV on the $CrCl_3$ island.

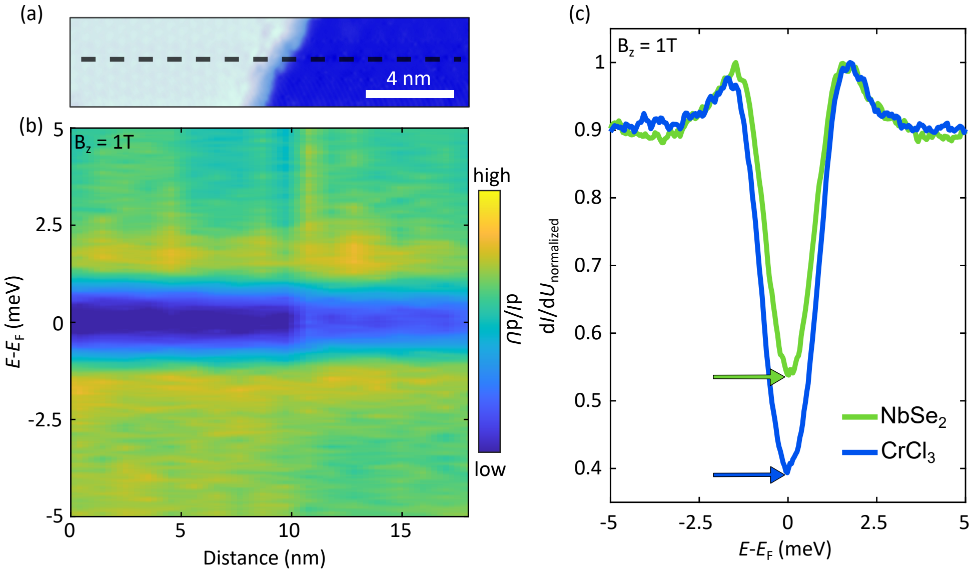

Figure 6.6: (a) STM topographic image of a section of a $CrCl_3$ ML. Scanning parameters: I_t = 25 pA, V_b =1.5 V. (b) dI/dU line spectroscopy acquired along the dashed line in (a) as a function of energy and tip position, under an out-of-plane magnetic field of 1T. (c) Normalized dI/dU spectra on the $NbSe_2$ substrate and the $CrCl_3$ island at an out-of-plane field of 1T showing a faster gap reduction in the former. Stabilization parameters for b and c: I_t = 100 pA, V_b = -5 mV, V_{mod} = 0.15 mV.

6.3 Robust interfacial superconductivity under an out-of-plane field

To study the nature of the interfacial superconductivity, the dI/dU spectra on $NbSe_2$ and the $CrCl_3$ island in figure 6.3 are fitted using the BCS-based Dynes function and the respective superconducting gaps have been extracted. The corresponding fits and the estimated superconducting gap size are shown in figure 6.5. The fitting unexpectedly reveals that the superconducting gap on the $CrCl_3$ island ($2\Delta_{\mathrm{CrCl_3}}$= 2.28 meV) is slightly larger ($\sim$ 8%) as compared to that of the $NbSe_2$ substrate ($2\Delta_{\mathrm{NbSe_2}}$= 2.10 meV). Contrary to popular belief, this is unusual, given that $CrCl_3$ is a magnetic insulator that should lead to a reduction of the superconducting energy gap. An even more intriguing aspect is how the superconducting gap evolves under an out-of-plane magnetic field. Figure 6.6b shows a dI/dU line spectroscopy along the dashed line in the topography in figure 6.6a as a function of energy and tip position under an out-of-plane magnetic field of 1 T. The resultant 2D color map, which displays the spatial distribution of the superconducting gap reveals that the gap on the $NbSe_2$ substrate decreases faster than that observed on the $CrCl_3$ island. Figure 6.6c further elucidates this behavior, which shows the spectra from the $CrCl_3$ island and the $NbSe_2$ substrate, normalized by the intensity of the coherence peaks, revealing a faster gap closure on the $NbSe_2$ substrate than that within the $CrCl_3$ island. These observed behaviors confirm the robustness of the superconducting gap on the $CrCl_3$ island as compared to that of the $NbSe_2$ substrate under an out-of-plane magnetic field. It should be noted, however, that the observed faster

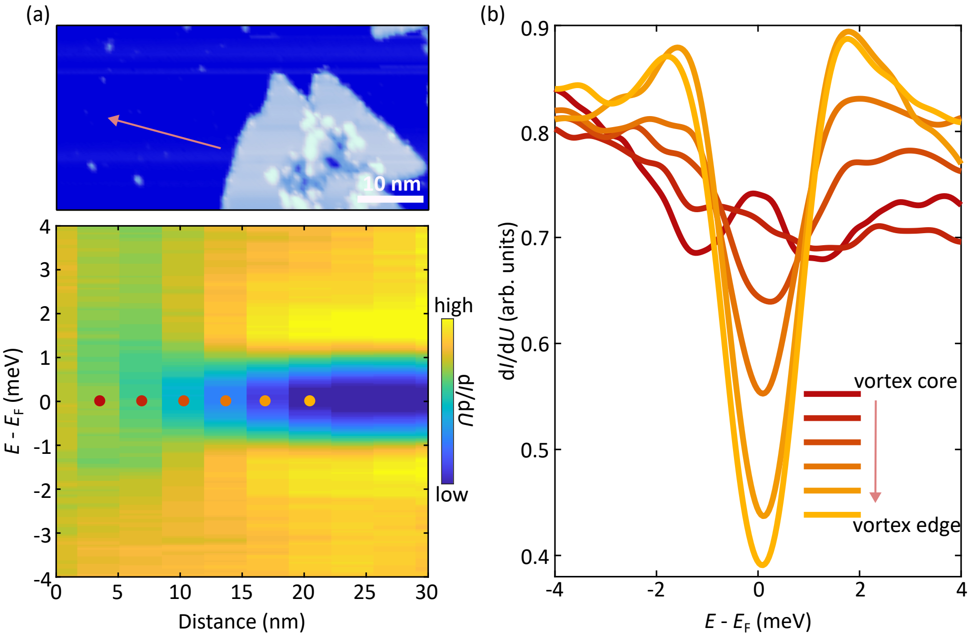

Figure 6.7: (a) Spectroscopic mapping along the arrow in the topographic image shows the evolution of the superconducting gap across a vortex nucleated on the $NbSe_2$ substrate under an applied out-of-plane field of 1 T. Colored circles denote the positions from the vortex core to the edge. (b) Corresponding $\mathrm{d}I/\mathrm{d}U$ spectra extracted from the spectroscopic map in (a) at the points marked by colored circles showing a progression from a zero-bias-peak at the core to a dip at the edge, demonstrating a significant spectral change within a length scale of $\sim$ 20 nm. Scanning parameter for (a): I_t = 20 pA, V_b = 1.5 V; Stabilization parameters for (a) and (b): I_t = 150 pA, V_b = -5 mV, V_{mod} = 0.1 mV.

gap reduction on the $NbSe_2$ substrate may not be solely intrinsic, and could arise from extrinsic effects such as vortex nucleation or trapped vortices [258]. Additional experiments were conducted on several islands to rule out such possible extrinsic origins, confirming that this enhancement is not due to vortices. For instance, an

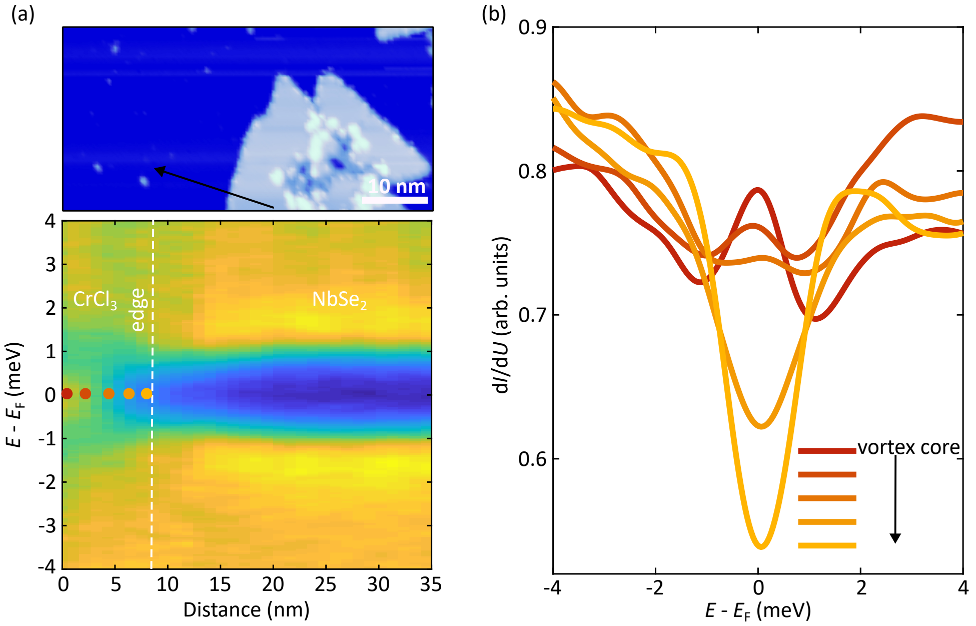

Figure 6.8: (a) Spectroscopic mapping along the arrow in the topographic image shows the evolution of the superconducting gap across a vortex nucleated in the vicinity of the edge of a $CrCl_3$ island under an applied out-of-plane field of 1 T. Colored circles denote the positions from the vortex core to the edge. (b) Corresponding $\mathrm{d}I/\mathrm{d}U$ spectra extracted from the spectroscopic map in (a) at the points marked by colored circles showing a progression from a zero-bias-peak at the core to a dip at the edge, demonstrating a substantial change in the spectral shape within a length scale of $\sim$ 8 nm. Scanning parameter for (a): I_t = 20 pA, V_b = 1.5 V; Stabilization parameters for (a) and (b): I_t = 150 pA, V_b = -5 mV, V_{mod} = 0.1 mV.

out-of-plane magnetic field of 1T was applied to generate a vortex on the $NbSe_2$ substrate. This is elucidated in figure 6.7a, which shows a $\mathrm{d}I/\mathrm{d}U$ spectroscopic mapping performed along the arrow in the topography (top panel of figure 6.7a), revealing a substantial modulation of the superconducting gap, as expected, as the tip traverses the entire length of 30 nm. The individual spectra acquired at the points marked by colored circles in the map are shown in figure 6.7b, which demonstrates that the spectral nature substantially changes from a zero-bias-peak close to the vortex core to a dip-like structure at the vortex edge. Notably, this change happens over a length scale of $\sim$ 20 nm. Similarly, a vortex was also nucleated on the $CrCl_3$ island as shown in figure 6.8a which shows a spectroscopic map acquired along the arrow in the topographic image (top panel in figure 6.8a) revealing a modulating superconducting gap on the $CrCl_3$ island as well as the edge. A critical observation from these measurements is that far away from the edge, on the $NbSe_2$ substrate, the gap becomes constant. The individual spectra extracted from the points indicated by the colored circles in the map are presented in figure 6.8b. Close to the vortex core located on the $CrCl_3$ island, the dI/dUspectrum exhibits a zero-bias peak in the LDOS, while a dip-like feature is observed close to the edge of the $CrCl_3$ island, corresponding to the vortex edge. The peak-to-dip-like transformation of the spectral shape occurs across a length scale of 8 nm. Unlike the spatial variation of the superconducting gap across a vortex, the gap remains constant across the $NbSe_2$ substrate and $CrCl_3$ island at comparable length scales, as previously evidenced by the spectroscopic map in Figure 6.6a. Specifically, the spectra exhibit a sharp step-like feature at the edge of the $CrCl_3$ island, which is not observed when vortices are formed (as shown in figure 6.7a and 6.8a). This feature above confirms that the rapid gap closure observed on the $NbSe_2$ substrate is primarily attributed to the spin Zeeman effect of the applied field, rather than orbital effects such as vortex formation.

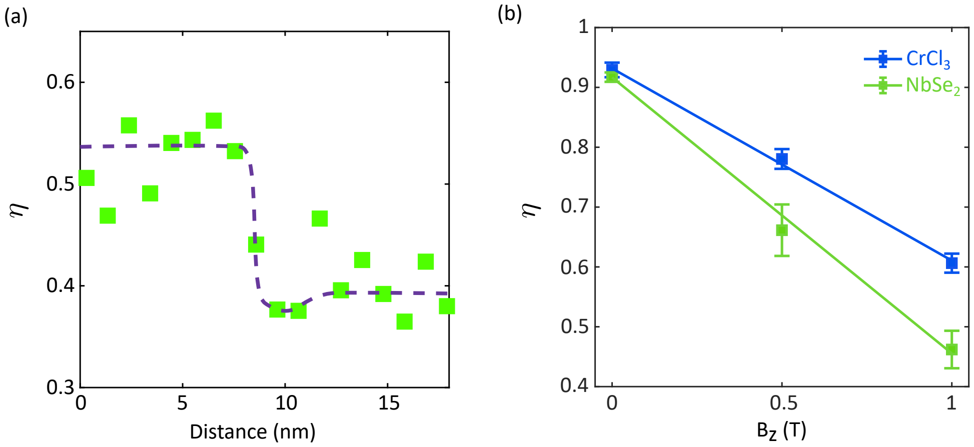

Figure 6.9: (a) η plotted along the 1D line cut in the topographic image in figure 6.6a. The dashed line acts as a guide to the eye, indicating a step-like feature. (b) η plotted as a function of the field, highlighting a progressive increase in the difference between η at the $CrCl_3$ island and the $NbSe_2$ substrate.

To ascertain the degree of relative robustness of the superconducting gap, a parameter η was defined:

$$\eta = \left[1 - (\mathrm{d}I/\mathrm{d}U)_{min}\right] \tag{6.1}$$

where $(\mathrm{d}I/\mathrm{d}U)_{min}$ is the minima of the spectra near E_F indicated by the green and blue arrows in figure 6.6b. The magnitude of this parameter correlates with superconducting robustness; a larger value indicates enhanced superconductivity robustness. Figure 6.9a shows a variation of the η along the dashed line in 6.6a, demonstrating robustness of the superconductivity at the $CrCl_3/NbSe_2$ interface as compared to that of the bare $NbSe_2$ substrate. Furthermore, the dashed line acting as a guide to the eye indicates a step jump in the value of η at the edge. Additionally, it was observed that on increasing the field, the difference between η at the $CrCl_3$ island and the $NbSe_2$ substrate increases progressively. From these experiments, it can be concluded that the superconductivity in $CrCl_3$ is resilient to out-of-plane magnetic fields as compared to that of $NbSe_2$.

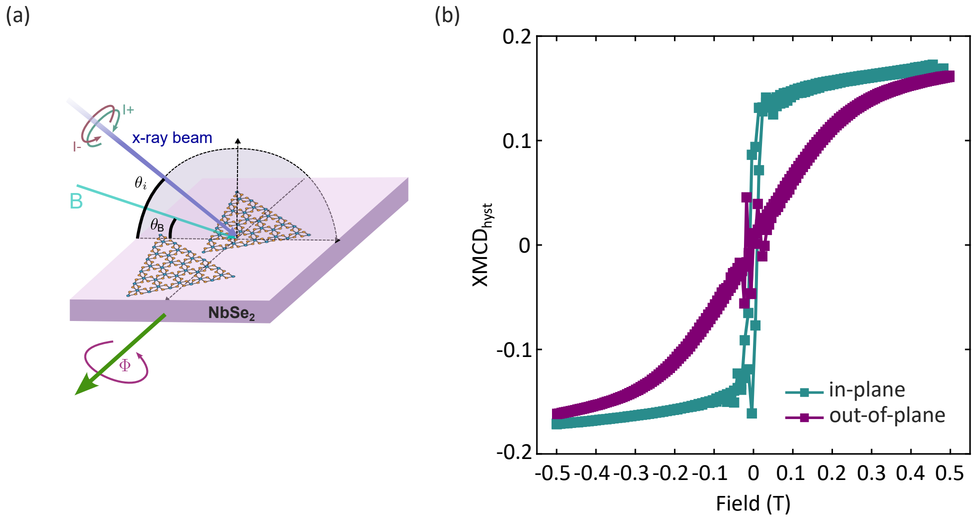

Figure 6.10: (a) Schematic of the XMCD setup. (b) Magnetic hysteresis loops under an in-plane (teal) and out-of-plane (purple) field.

6.4 XMCD measurements on the $CrCl_3/NbSe_2$ heterostructure

It has been previously shown that for $CrCl_3$ grown on graphene, the magnetization is oriented in the plane. To determine the magnetic anisotropy of $CrCl_3$ on the $NbSe_2$ substrate, XMCD measurements were performed at 1.5 K. Figure 6.10a presents a schematic representation of the XMCD experimental setup, depicting an x-ray beam with two opposite helicities directed onto the sample in the presence of an applied magnetic field. As shown in figure 6.10b, the in-plane and out-of-plane hysteresis loops were obtained by performing XMCD measurements on the Cr $L_{2,3}$ edge at grazing and normal incidence, respectively. From the hysteresis loops, it is evident that $CrCl_3$ on $NbSe_2$ exhibits an in-plane magnetization below the superconducting critical temperature of $NbSe_2$.

6.5 Theory of the edge states and the superconducting gap in the $CrCl_3/NbSe_2$ heterostructure

To provide a more comprehensive understanding of the preceding experimental results, this section presents theoretical modeling and calculations performed in collaboration with the theoretical research group of Prof. Marcel Franz at the University of British Columbia, including Benjamin Zhou and Niclas Heinsdorf.

The origin of the observed edge modes and the full superconducting gap in the bulk of the $CrCl_3/NbSe_2$ heterostructure is discussed now. Conventional TSC, which involves s-wave pairing and Rashba SOC, dictates that the magnetization **M** of the ferromagnet must be oriented out-of-plane to open a Zeeman gap at the Rashba-induced band crossing. In this case, TSC arises when the chemical potential lies within the Zeeman gap [40, 55–57, 259]. On the contrary, when **M** is in the plane, the normal-state-spectrum is known to remain gapless with the Rashba band crossing shifted in momentum space. In this case, the superconducting state does not allow a fully gapped TSC phase with an s-wave pairing [259]. In the present case, since $CrCl_3$ on $NbSe_2$ exhibits an in-plane magnetization, the observed fully gapped superconducting phase with gapless edge modes cannot be attributed to the conventional s-wave pairing-based TSC mechanism. However, it is essential to note that an in-plane **M** can also drive an s-wave superconductor into the chiral TSC phase if the Rashba and Dresselhaus SOCs (of the form $H_D = \lambda_D k_x \sigma_z$) are carefully tuned as demonstrated in the case of [110] quantum wells [259]. But in the present case, the three-fold symmetry of the $CrCl_3/NbSe_2$ heterostructure does not allow the above form of the H_D.

Furthermore, for the s-wave based TSC to occur, the exchange coupling J in the ferromagnetic layer must exceed the superconducting pairing gap (Δ). From the fit of the superconducting gap on the $NbSe_2$ substrate, $\Delta = 1.05$ meV, thereby necessitating $J > 1.05$ meV to enter the topological regime. However, first principle studies suggest that the exchange coupling between neighboring Cr atoms within a $CrCl_3$ ML is just of the order of, $J_{Cr-Cr} \sim 1$ meV [260, 261] while estimated values obtained from the spatial dependence of the interlayer exchange coupling [262] between the Cr and the Nb atoms in the topmost layer of the $NbSe_2$ substrate is of the order of, $J_{Cr-Nb} \sim 0.1$ meV. Since $J \simeq 0.1\Delta$, is significantly smaller than Δ, the necessary criterion for TSC, $J > \Delta$ is not met. Consequently, the observed topological edge modes in the $CrCl_3/NbSe_2$ heterostructure are very unlikely to originate from the conventional s-wave mechanism. The small exchange coupling between $CrCl_3$ and $NbSe_2$ also explains the remarkable resemblance exhibited by the experimental results presented here for the $CrCl_3/NbSe_2$ heterostructure with an in-plane M to those previously observed on the $CrBr_3/NbSe_2$ heterostructure with an out-of-plane M. This indicates that the orientation of $\mathbf{M}$ becomes irrelevant when J is negligible. The hypothesis of a negligible J is also confirmed by another independent STM research on the $CrBr_3/NbSe_2$ heterostructure, which reported negligible interaction between the ferromagnet and the superconductor [257]. This study reported the formation of discontinuous edge states, with the zero-bias peak split in segments along the edges of the $CrBr_3$ island. Due to the discrepancy between these observations and the expected signatures of chiral Majorana edge modes, the observed edge features were attributed to non-topological Yu-Shiba-Rusinov (YSR) states caused by atomic lattice reconstructions near the edges. In the case of the $CrCl_3/NbSe_2$ heterostructure, no such atomic reconstruction was observed and the edge states remain continuous in real space.

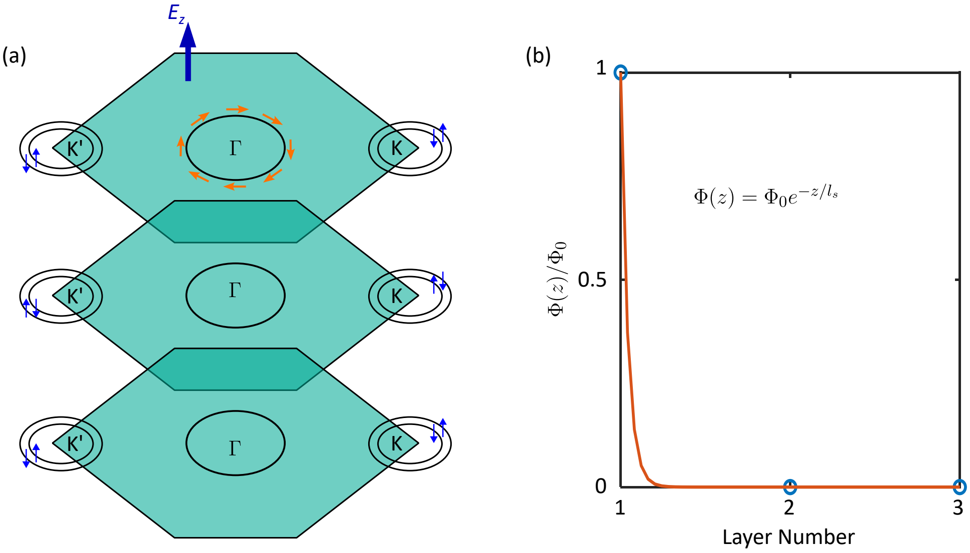

Figure 6.11: (a) Schematic of the Fermi pockets in multilayer $NbSe_2$ with the Ising SOC alternating between the layers and pinning the electron at the opposite K points in the opposite out-of-plane direction. Rashba SOC is predominantly observed near the Γ point of the valence band formed by Nb d_{z^2} orbitals. (b) Exponential decay of the modified electrostatic potential $\Phi(z)$ in $NbSe_2$ thin films due to Thomas-Fermi screening. The existence of the potential gradient only within the first layer since the screening length $l_s = 0.5$ Å is much smaller than the inter-layer distance of 10 Å.

Based on the preceding analysis, it can be concluded that the observed TSC phenomena at the $CrCl_3/NbSe_2$ interface originate from an unconventional pairing state possessing non-trivial bulk topology, which is independent of the orientation of **M**. As will be substantiated in the following discussion, these findings are most consistently explained by a Rashba spin-orbit-coupled helical p-wave pairing state. This topological superconducting phase provides a unified framework for understanding all the observed interfacial characteristics.

It is proposed that the $CrCl_3$ ML modifies the electrostatic potential at the interface Φ(z), inducing local perpendicular electric fields and enhancing interfacial Rashba SOC (of the form $H_R = \alpha_R \boldsymbol{g_k} \cdot \boldsymbol{\sigma}$) in the topmost $NbSe_2$ layer (see figure 6.11a). Figure 6.11a schematically illustrates the Fermi pockets of multilayer $NbSe_2$. The Ising SOC which is predominant at the K point, alternates between the layers, pinning the electron spins at the opposite K points in the opposite out-of-plane direction. Since the $NbSe_2$ thin films in the normal state are metallic, $\Phi(z)$ is subjected to screening and is expected to decay exponentially away from the $CrCl_3/NbSe_2$ interface into the bulk as shown in figure 6.11b. By applying the Thomas-Fermi approximation to a realistic lattice model for $NbSe_2$ thin films, a screening length of $l_s \approx 0.5$ Å was obtained along the direction perpendicular to the $CrCl_3/NbSe_2$ stack, which is much smaller than the distance between the individual $NbSe_2$ layers (c = 12 Å). This implies that the modified potential and the Rashba effects are significant only within the topmost $NbSe_2$ layer adjacent to the $CrCl_3$ ML.

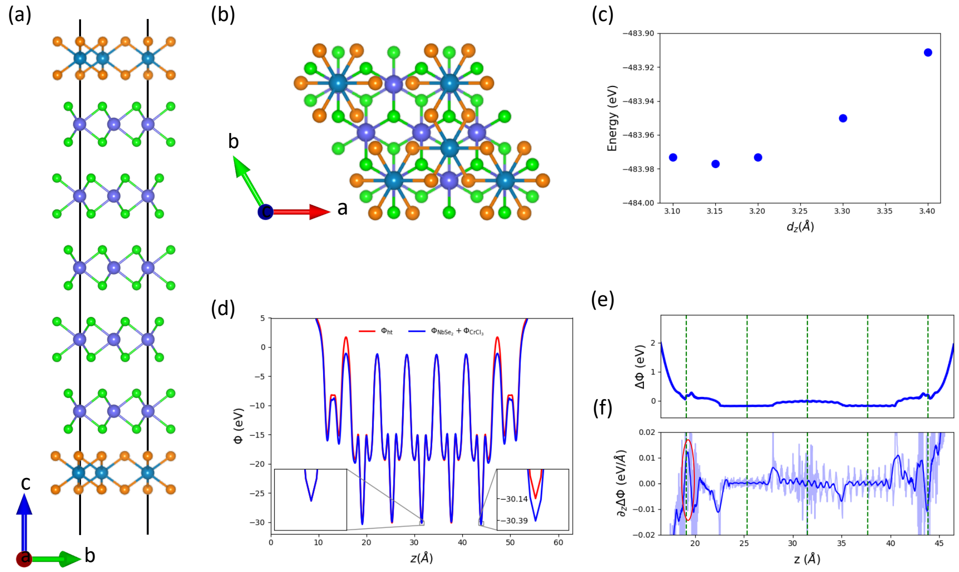

Figure 6.12: (a-b) The symmetric stack of $CrCl_3$ and $NbSe_2$ constructed to perform the DFT calculations. The Cr atoms are aligned with the Nb atoms. The interfacial distance was obtained as $d_z = 3.15$ Å. (c) Plot of the ground state energies of the unit cell as a function of varying d_z. The minimum is obtained at $d_z = 3.15$ Å. (d) The local potential averaged over the plane of the sample (*ab*-plane) as a function of z. The red curve corresponds to the potential of the heterostructure Φ_{ht} shown in (a-b), while the blue curve ($\Phi_{\mathrm{NbSe}_2} + \Phi_{\mathrm{CrCl}_3}$) is the sum of the local potentials of only $CrCl_3$ and $NbSe_2$. The potentials at the center Nb (left) and the interface Nb (right) are highlighted in the inset. In the bulk of the structure, the potential difference ($\Delta\Phi$) is 0, but at the interface $\Delta\Phi = 0.25$eV. (e) Plot of $\Delta\Phi$ as a function of z. The green dashed lines indicates the position of the Nb atoms. (f) Numerical differentiation of $\Delta\Phi$ (light blue) and the same data smoothened with a Savitzky-Golay filter. At the three Nb in the bulk of the slab, the effective electric field is approximately 0, but at the Nb closest to the interface $\partial_z\Delta\Phi \approx 0.0125$ ev/Å.

To estimate the strength of the Rashba parameter α_R, electronic band structure calculations were performed using density-functional theory (DFT). The details of the DFT calculations will be skipped, and only the results will be presented here for clarity. As shown in figure 6.12a,b, for the DFT computation, a slab structure was constructed consisting of a symmetric interface, with a ML $CrCl_3$ on the top and bottom of a 5-layer stack of $NbSe_2$ ($a = 3.44$ Å and $c = 31.47$ Å) such that the Cr atom is positioned on top of the Nb atom. For this, the ML $CrCl_3$ was stretched to fit the lattice parameter of the $NbSe_2$ supercell since there is a 12 % mismatch between the ML and the supercell. To find the equilibrium distance d_z between $NbSe_2$ and $CrCl_3$, defined as the z-coordinate difference between the outermost Se and innermost Cl atoms, ground state energies were computed for a range of d_z values, and a minimum was observed for $d_z \approx 3.15$ Å. This is demonstrated in figure 6.12c. To calculate the interface-induced potential gradient, the potential of the interfaced slab (Φ_{ht}) was compared with that of the sum of the individual potentials of the $CrCl_3$ ML ($\Phi_{\mathrm{CrCl_3}}$) and the $NbSe_2$ stack ($\Phi_{\mathrm{NbSe_2}}$). The local potentials are averaged over the ab plane of the crystal structure and the difference of the obtained potentials are defined as, $\Delta\Phi = \Phi_{ht} - (\Phi_{\mathrm{NbSe_2}} + \Phi_{\mathrm{CrCl_3}})$. Figure 6.12d show a combined plot of Φ_{ht} and $\Phi_{\mathrm{NbSe_2}} + \Phi_{\mathrm{CrCl_3}}$ as a function of the distance from the top of the stack. The inset shows a zoom-in of the vanishing potential difference for the Nb at the center as compared to the Nb at the interface with $\Delta\Phi \approx 0.275$ eV. Finally, the potential gradient along the stack, defined as $\partial_z\Delta\Phi$ is calculated as elucidated in figure 6.12f. The potential gradient leads to an effective electric field, $\partial_z\Delta\Phi \approx 0.0125$ eV/Å, at the z value where the interfacial Nb is located. This manifests as a sharp peak in the plot in figure 6.12f (marked by a red inverted ellipse). With the assumption that $NbSe_2$ must exhibit comparable electric-field dependence of the Rashba SOC as other TMDCs such as MoS_2 or WSe_2 [263], the Rashba parameter was estimated as $\alpha_R \approx$ 0.01-0.025 eV Å, which is approximately an order of magnitude larger than J and Δ. These calculations support the hypothesis of a strong Rashba coupling at the interface, rather than proximity-induced coupling J, possibly leading to an unconventional TSC state in the $CrCl_3/NbSe_2$ heterostructure.

Proceeding with the discussion of a strong Rashba coupling at the interface, DFT calculations have previously shown that, in TMDCs, Rashba SOC is substantial

Table 6.1: All possible fully-gapped superconducting order parameters for Γ-pocket (dominated by Nb d_{z^2}-orbitals in the topmost layer of $NbSe_2$), classified according to the irreducible representations (IRs) of the $C_{3\mathrm{v}}$ point group. The conventional d-vector notation has been employed with $\Delta(\boldsymbol{k}) = [\psi_s(\boldsymbol{k}) + \boldsymbol{d}_t(\boldsymbol{k}) \cdot \boldsymbol{\sigma}]i\sigma_y$ where ψ_s stands for the spin-singlet order parameter, while $\boldsymbol{d}_t$ is the spin-triplet vector. Only leading-order terms up to quadratic functions in $\boldsymbol{k}$ are considered. Shorthand notation $\boldsymbol{k}_\pm \equiv k_x \pm ik_y$ is used.

IR	Superconducting order parameters
A_1 (1D)	s-wave: $\psi_s = \Delta_{\mathrm{s,A_1}}$
	helical p-wave: $\boldsymbol{d}_t(\boldsymbol{k}) = \Delta_{\mathrm{p,A_1}}(k_y, -k_x, 0)$
E (2D)	spinless chiral $p \pm ip'$-wave: $\{\boldsymbol{d}_{t,1}(\boldsymbol{k}) = \Delta_{\mathrm{p,E,1}}(\boldsymbol{k}_+, +i\boldsymbol{k}_+, 0),\ \boldsymbol{d}_{t,2}(\boldsymbol{k}) = \Delta_{\mathrm{p,E,2}}(\boldsymbol{k}_-, -i\boldsymbol{k}_-, 0)\}$
	chiral $d \pm id'$-wave: $\{\psi_{s,1}(\boldsymbol{k}) = \Delta_{\mathrm{d,E,1}}\boldsymbol{k}_+^2,\ \psi_{s,2}(\boldsymbol{k}) = \Delta_{\mathrm{d,E,2}}\boldsymbol{k}_-^2\}$

only for states near the Γ-point, which are primarily composed of d_{z^2}-orbitals [263]. Conversely, Rashba SOC is negligible at the inequivalent K and $\mathrm{K}^{'}$ points, where high-angular-momentum $d_{x^2-y^2} \pm id_{xy}$ orbitals dominate and Ising SOC can be as strong as 100 meV [217, 264]. It is to be noted that superconductivity in $NbSe_2$ arises out of the intervalley pairing of electrons located at the inequivalent K-pockets as well as intravalley pairing within the Γ point. It is theoretically proposed here that the intervalley Ising SOC, which has been consistently observed in atomically thin films, is not influenced by the Rashba SOC. Consequently, since the Ising SOC is considered to be topologically trivial, the non-trivial topological properties are bound to arise from a novel form of unconventional pairing within the Γ pocket, where the Rashba SOC in d_{z^2} orbitals plays a critical role. It has been previously established that the Rashba SOC defined by the SOC vector $\boldsymbol{g_k} = \alpha_R(k_y, -k_x, 0)$ can play an essential role in enhancing the pairing instability in the spin-triplet channel, provided the spin-triplet **d**-vector is aligned with the SOC vector: $\boldsymbol{d_k} \parallel \boldsymbol{g_k}$ [198, 255, 265, 266]. This type of spin-triplet $\boldsymbol{d}$-vector indicates a helical p-wave pairing phase, with $(p_x - ip_y)$-wave pairing for spin-up electrons and $(p_x + ip_y)$-wave pairing for spin-down electrons (see schematic in figure 5.10). This type of helical p-wave phase exhibits a full superconducting gap, supports helical Majorana edge modes, and does not allow spontaneous out-of-plane magnetization, agreeing with the experimental results presented in the previous sections. Notably, the symmetry of the $CrCl_3/NbSe_2$ heterostructure which lies in the C_{3v} point group allows both the helical p-wave and s-wave pairing phases to coexist in the topmost layer, since they belong to the same A1 (trivial) irreducible representation of the C_{3v} point group (see Table 6.1). The topologically distinct nature of the two phases in the presence of $\mathcal{T}$ symmetry accounts for the observed gapless edge states at the boundary of the $CrCl_3$ islands.

To validate that the helical p-wave pairing in the d_{z^2}-governed Γ pocket supports a fully gapped TSC phase as observed in the experimental results, a tight binding model of $NbSe_2$ thin films was adopted with Rashba SOC and helical p-wave pairing induced in the d_{z^2} orbitals of the topmost layer (the one neaest to the $CrCl_3$ islands). The corresponding results are presented in the figure 6.13a,b, which shows

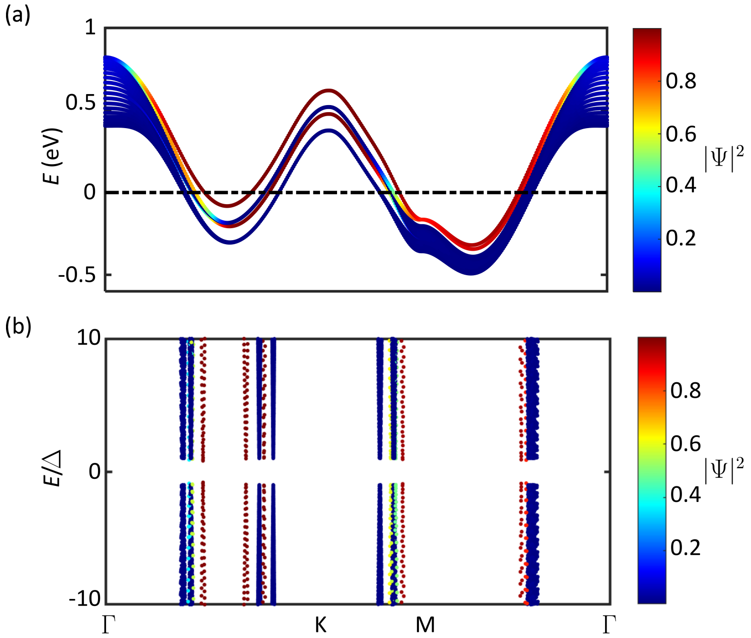

Figure 6.13: (a) The energy bands of a 20-layer $NbSe_2$ flake using a realistic tight-binding model, incorporating a potential offset and Rashba SOC on the first layer. The color bar displays the weight, $|\Psi^2|$, of the wave functions originating from the first layer. (b) The calculated bulk BdG spectrum for 20-layer thick $NbSe_2$ flakes with helical p-wave pairing in the d_{z^2} orbitals in the first layer. A full superconducting gap is exhibited by the spectrum.

the calculated Bogoliubov-de Gennes quasi-particle spectrum, revealing a full superconducting gap, consistent with the LDOS measurements in the STM experiments (see figure 6.3a). The topological nature of the helical p-wave state was further con-

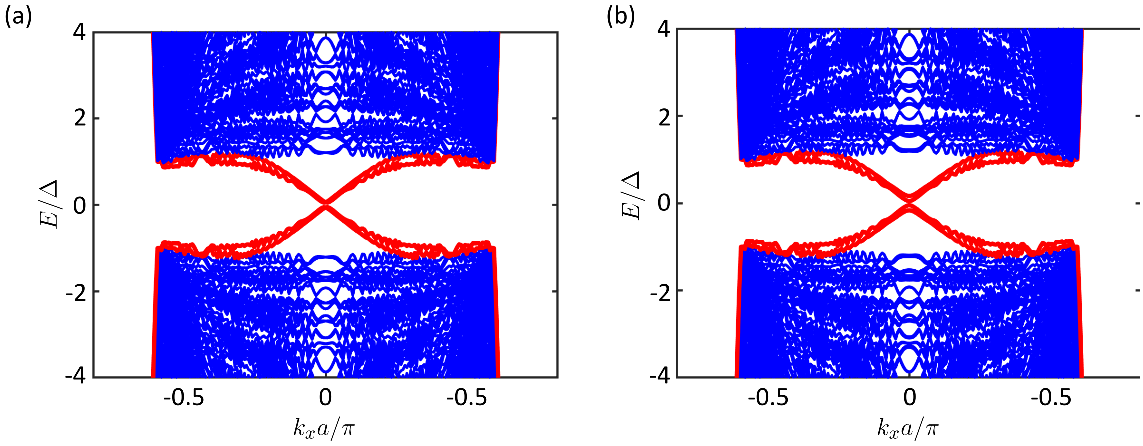

Figure 6.14: (a-b) Calculated edge state spectrum of multilayer NbSe$_2$ in a slab geometry with p-wave pairing at the interface and s-wave pairing on the rest of the system revealing helical edge states (a) without exchange coupling and (b) a small exchange $J \simeq 0.1\Delta$, arising from the neighboring ferromagnet.

firmed by conducting simulations on multilayer NbSe$_2$, revealing the presence of helical edge state in the excitation spectrum (see figure 6.14a). The $\mathcal{T}$ symmetry protects the crossing between the counter-propagating edge states. If a small exchange coupling $J \simeq 0.1\Delta$, arising from the neighboring ferromagnet, is added, the $\mathcal{T}$ symmetry is broken, leading to a small splitting, but the fundamental features of the edge state remain unaltered.

Alternatively, the observed TSC phase could be explained by the exotic spinless chiral $(p_x \pm ip_y)$ or $(d_{x^2-y^2} \pm id_{xy})$ pairing, as has been previously discussed in superconducting TMDCs [267, 268]. These fully gapped phases require spontaneous $\mathcal{T}$ symmetry breaking, selecting one chiral component from the C_{3v} E-representation (Table 6.1). However, this typically involves spontaneous out-of-plane magnetic order, which would have been revealed by the XMCD measurement. However, the lack of any such signals that would indicate an out-of-plane magnetic order in the XMCD measurements supports a non-magnetic TSC phase. This implies that the signatures of the TSC phase observed in the experiments presented above are very unlikely to originate from the exotic $\mathcal{T}$-broken TSC phase.

6.6 Conclusion

In summary, this chapter has unveiled compelling signatures of an unconventional superconducting phase emerging at the interface between ML ferromagnetic $CrCl_3$ islands and superconducting $NbSe_2$ substrate. Using the experimental approach, centered on high-resolution STM and STS, two striking characteristics of this ferromagnet/superconductor hybrid system was revealed: first, the interfacial superconducting state demonstrates unprecedented stability under strong magnetic fields, defying conventional expectations for such systems; second, a spatially localized pronounced zero-bias enhancement in the LDOS was detected at boundaries of the ferromagnetic island, strongly indicative of topologically protected edge states. Theoretical insights into these observations point towards a fascinating mechanism: interfacial Rashba SOC appears to stabilize a helical p-wave order parameter. This not only accounts for the system's exceptional resilience to magnetic perturbations but also naturally explains the emergence of helical edge modes.

Part V

Conclusion and Outlook

7 Conclusion and Outlook

This thesis has unveiled fundamental aspects of topological quantum phenomena, specifically through the identification of novel edge states arising from non-trivial band topology. Two key findings stand out: (1) the emergence of interaction-driven flat-band Stoner ferromagnetism in the topological edge states of $Pb_{0.7}Sn_{0.3}Se$, and (2) the realization of an unconventional TSC phase in the $CrCl_3/NbSe_2$ heterostructure, exhibiting both magnetic field resilience and signatures of topologically protected edge modes.

The edge modes arising at a step edge on the surface of the TCI $Pb_{0.7}Sn_{0.3}Se$ were investigated through a combination of high-resolution STM/STS and theoretical calculations. STM/STS measurements revealed the presence of edge modes at the half-unit cell step edge of $Pb_{0.7}Sn_{0.3}Se$. These edge modes manifest as a peak in the LDOS at the Dirac point, which is located above the Fermi level at 125 meV. Theoretical modeling suggests that this peak corresponds to four spin-polarized flat bands degenerate in energy, strictly localized at the 1D step edge. To study the effect of doping on the 1D flat band, different 3d transition elements were doped on the surface of the sample. It was observed that once the 1D flat band is energetically localized close to the Fermi level, the single peak splits into either 2 or 4 peaks. Additionally, the splitting of the peaks is accompanied by a suppression of the LDOS at the Fermi energy, indicating a gap opening in the spectrum. A continuum model description of these edge states was developed, and Hartree-Fock calculations were performed to examine the effects of electron-electron interactions in the flat bands. Depending on the strength of the interactions, the single peak associated with the

1D flat band splits into 2 or 4 peaks due to the hybridization between the spin-polarized flat bands. These new states spontaneously break $\mathcal{T}$ symmetry and lead to a 1D flat band Stoner ferromagnetism at the 1D half-unit cell step edge, which further induces correlation gaps, as observed in the STM measurements when the 1D flat band is doped to the Fermi energy. As a future outlook, it will be interesting to perform spin-resolved STM measurements at the half-unit cell step edges of $Pb_{0.7}Sn_{0.3}Se$ to validate the symmetry-breaking patterns predicted by Hartree-Fock calculations, which depend on the interaction strength. Furthermore, these step-edge flat bands exhibit similarities to the edge states in zigzag-terminated graphene nanoribbons, where it is known that the intra-edge coupling is ferromagnetic and the inter-edge coupling is antiferromagnetic [153, 154, 157]. While previous studies have demonstrated that two adjacent step-edges in a TCI can hybridize to form bonding and anti-bonding orbitals [126], the nature of magnetic coupling in such configurations remains an open question, which therefore warrants further investigation using spin-polarized STM measurements.

Employing the STM/STS technique, a unique material system was then explored: a 2D vdW heterostructure formed by a ML ferromagnetic insulator, $CrCl_3$, and a 2D superconductor, $NbSe_2$. Notably, a complete superconducting gap was detected at the $CrCl_3/NbSe_2$ interface. This gap exhibits resilience to an out-of-plane magnetic field, unlike the gap in the conventional s-wave superconductor $NbSe_2$, challenging the prevalent notion that ferromagnetism suppresses superconductivity. Additionally, DOS mapping reveals edge modes at the Fermi energy localized along the 1D boundary of the $CrCl_3$ islands. Theoretical modeling suggests that the $CrCl_3/NbSe_2$ interface develops an unconventional TSC state characterized by a helical p-wave pairing, stabilized by an interfacial Rashba SOC. This helical p-wave state is predicted to host a pair of counterpropagating edge modes, consistent with the observed zero-energy edge modes at the boundary of the $CrCl_3$ islands. However, it is crucial to acknowledge that interpreting the experimental observations through the lens of the p-wave hypothesis represents one potential explanation, since the pairing at the interface could be attributed to other pairing mechanisms as well. The STM/STS measurements presented here alone cannot definitively ascertain the precise pairing symmetry of this unconventional superconducting phase. Consequently, these findings necessitate in-depth theoretical analyses and further STM measurements using superconducting as well as spin-polarized tips to conclusively determine the nature of the observed unconventional TSC phase in the $CrCl_3/NbSe_2$ heterostructure.

Beyond the fundamental significance of the results presented in this thesis, these findings establish novel methodologies for quantum material design. The demonstrated ability to create, stabilize, and probe topological states through material engineering—whether via surface modifications or heterostructure assembly—opens exciting possibilities for future research on correlated topology and topological quantum computation. As the field progresses, the approaches developed here may prove instrumental in realizing more complex topological phases and ultimately harnessing their unique properties for quantum technologies.

Part VI

Appendix

Bibliography

1. Thouless, D. J. *et al.* Quantized Hall conductance in a two-dimensional periodic potential. *Physical Review Letters* **49,** 405 (1982).
2. Kane, C. L. *et al.* Quantum spin Hall effect in graphene. *Physical Review Letters* **95,** 226801 (2005).
3. Bernevig, B. A. *et al.* Quantum spin Hall effect. *Physical Review Letters* **96,** 106802 (2006).
4. Bernevig, B. A. *et al.* Quantum spin Hall effect and topological phase transition in HgTe quantum wells. *Science* **314,** 1757–1761 (2006).
5. Konig, M. *et al.* Quantum spin Hall insulator state in HgTe quantum wells. *Science* **318,** 766–770 (2007).
6. Kane, C. L. *et al.* Z_2 topological order and the quantum spin Hall effect. *Physical Review Letters* **95,** 146802 (2005).
7. Drozdov, I. K. *et al.* One-dimensional topological edge states of bismuth bilayers. *Nature Physics* **10,** 664–669 (2014).
8. Yang, F. *et al.* Spatial and energy distribution of topological edge states in single Bi(111) bilayer. *Physical Review Letters* **109,** 016801 (2012).
9. Wu, R. *et al.* Evidence for topological edge states in a large energy gap near the step edges on the surface of $ZrTe_5$. *Physical Review X* **6,** 021017 (2016).
10. Li, X.-B. *et al.* Experimental observation of topological edge states at the surface step edge of the topological insulator $ZrTe_5$. *Physical Review Letters* **116,** 176803 (2016).

11. Wang, X. *et al.* Observation of topological edge states in the quantum spin Hall insulator $Ta_2Pd_3Te_5$. *Physical Review B* **104,** L241408 (2021).
12. Reis, F. *et al.* Bismuthene on a SiC substrate: A candidate for a high-temperature quantum spin Hall material. *Science* **357,** 287–290 (2017).
13. Fu, L. *et al.* Topological insulators in three dimensions. *Physical Review Letters* **98,** 106803 (2007).
14. Moore, J. E. *et al.* Topological invariants of time-reversal-invariant band structures. *Physical Review B* **75,** 121306 (2007).
15. Roy, R. Topological phases and the quantum spin Hall effect in three dimensions. *Physical Review B* **79,** 195322 (2009).
16. Hsieh, D. *et al.* A topological Dirac insulator in a quantum spin Hall phase. *Nature* **452,** 970–974 (2008).
17. Chen, Y. *et al.* Experimental realization of a three-dimensional topological insulator, Bi_2Te_3. *Science* **325,** 178–181 (2009).
18. Xia, Y. *et al.* Observation of a large-gap topological-insulator class with a single Dirac cone on the surface. *Nature Physics* **5,** 398–402 (2009).
19. Hsieh, D. *et al.* Observation of time-reversal-protected single-Dirac-cone topological-insulator states in Bi_2Te_3 and Sb_2Te_3. *Physical Review Letters* **103,** 146401 (2009).
20. Fu, L. Topological crystalline insulators. *Physical Review Letters* **106,** 106802 (2011).
21. Hsieh, T. H. *et al.* Topological crystalline insulators in the SnTe material class. *Nature Communications* **3,** 982 (2012).
22. Tanaka, Y. *et al.* Experimental realization of a topological crystalline insulator in SnTe. *Nature Physics* **8,** 800–803 (2012).
23. Xu, S.-Y. *et al.* Observation of a topological crystalline insulator phase and topological phase transition in $Pb_{1-x}Sn_xTe$. *Nature Communications* **3,** 1192 (2012).

24. Dziawa, P. *et al.* Topological crystalline insulator states in $\mathrm{Pb}_{1-x}\mathrm{Sn}_x\mathrm{Se}$. *Nature Materials* **11,** 1023–1027 (2012).
25. Okada, Y. *et al.* Observation of Dirac node formation and mass acquisition in a topological crystalline insulator. *Science* **341,** 1496–1499 (2013).
26. Sessi, P. *et al.* Robust spin-polarized midgap states at step edges of topological crystalline insulators. *Science* **354,** 1269–1273 (2016).
27. Zeljkovic, I. *et al.* Dirac mass generation from crystal symmetry breaking on the surfaces of topological crystalline insulators. *Nature Materials* **14,** 318–324 (2015).
28. Gyenis, A. *et al.* Quasiparticle interference on the surface of the topological crystalline insulator $\mathrm{Pb}_{1-x}\mathrm{Sn}_x\mathrm{Se}$. *Physical Review B—Condensed Matter and Materials Physics* **88,** 125414 (2013).
29. Zeljkovic, I. *et al.* Mapping the unconventional orbital texture in topological crystalline insulators. *Nature Physics* **10,** 572–577 (2014).
30. Iaia, D. *et al.* Topological nature of step-edge states on the surface of the topological crystalline insulator $\mathrm{Pb}_{0.7}\mathrm{Sn}_{0.3}\mathrm{Se}$. *Physical Review B* **99,** 155116 (2019).
31. Baum, Y. *et al.* Magnetic instability on the surface of topological insulators. *Physical Review B—Condensed Matter and Materials Physics* **85,** 121105 (2012).
32. Dornhaus, R. *et al. Narrow-gap semiconductors* (Springer, 2006).
33. Kitaev, A. *Periodic table for topological insulators and superconductors AIP conference proceedings* **1134** (2009), 22–30.
34. Schnyder, A. P. *et al.* Classification of topological insulators and superconductors in three spatial dimensions. *Physical Review B* **78,** 195125 (2008).
35. Qi, X.-L. *et al.* Time-Reversal-Invariant Topological Superconductors and Superfluids in Two and Three Dimensions. *Physical Review Letters* **102,** 187001 (2009).

36. Sato, M. *et al.* Topological superconductors: a Review. *Reports on Progress in Physics* **80,** 076501 (2017).
37. Qi, X.-L. *et al.* Topological insulators and superconductors. *Reviews of modern physics* **83,** 1057–1110 (2011).
38. Sato, M. *et al.* Topological phases of noncentrosymmetric superconductors: Edge states, Majorana fermions, and non-Abelian statistics. *Physical Review B—Condensed Matter and Materials Physics* **79,** 094504 (2009).
39. Teo, J. C. *et al.* Majorana fermions and non-Abelian statistics in three dimensions. *Physical Review Letters* **104,** 046401 (2010).
40. Sau, J. D. *et al.* Controlling non-Abelian statistics of Majorana fermions in semiconductor nanowires. *Physical Review B—Condensed Matter and Materials Physics* **84,** 094505 (2011).
41. Read, N. *et al.* Paired states of fermions in two dimensions with breaking of parity and time-reversal symmetries and the fractional quantum Hall effect. *Physical Review B* **61,** 10267 (2000).
42. Fu, L. *et al.* Superconducting proximity effect and majorana fermions at the surface of a topological insulator. *Physical Review Letters* **100,** 096407 (2008).
43. Ivanov, D. A. Non-Abelian statistics of half-quantum vortices in p-wave superconductors. *Physical Review Letters* **86,** 268 (2001).
44. Xu, J.-P. *et al.* Experimental detection of a Majorana mode in the core of a magnetic vortex inside a topological insulator-superconductor $Bi_2Te_3/NbSe_2$ heterostructure. *Physical Review Letters* **114,** 017001 (2015).
45. Xu, J.-P. *et al.* Artificial topological superconductor by the proximity effect. *Physical Review Letters* **112,** 217001 (2014).
46. Sun, H.-H. *et al.* Majorana zero mode detected with spin selective Andreev reflection in the vortex of a topological superconductor. *Physical Review Letters* **116,** 257003 (2016).
47. Frolov, S. *et al.* Topological superconductivity in hybrid devices. *Nature Physics* **16,** 718–724 (2020).

48. Mourik, V. *et al.* Signatures of Majorana fermions in hybrid superconductor-semiconductor nanowire devices. *Science* **336,** 1003–1007 (2012).

49. Kitaev, A. Y. Unpaired Majorana fermions in quantumwires. *Physics-uspekhi* **44,** 131 (2001).

50. Nadj-Perge, S. *et al.* Observation of Majorana fermions in ferromagnetic atomic chains on a superconductor. *Science* **346,** 602–607 (2014).

51. Feldman, B. E. *et al.* High-resolution studies of the Majorana atomic chain platform. *Nature Physics* **13,** 286–291 (2017).

52. Kim, H. *et al.* Toward tailoring Majorana bound states in artificially constructed magnetic atom chains on elemental superconductors. *Science Advances* **4,** eaar5251 (2018).

53. Schneider, L. *et al.* Precursors of Majorana modes and their length-dependent energy oscillations probed at both ends of atomic Shiba chains. *Nature Nanotechnology* **17,** 384–389 (2022).

54. Jäck, B. *et al.* Detecting and distinguishing Majorana zero modes with the scanning tunnelling microscope. *Nature Reviews Physics* **3,** 541–554 (2021).

55. Sau, J. D. *et al.* Generic New Platform for Topological Quantum Computation Using Semiconductor Heterostructures. *Physical Review Letters* **104,** 040502 (2010).

56. Ménard, G. C. *et al.* Two-dimensional topological superconductivity in Pb/Co/ Si (111). *Nature Communications* **8,** 2040 (2017).

57. Kezilebieke, S. *et al.* Topological superconductivity in a van der Waals heterostructure. *Nature* **588,** 424–428 (2020).

58. Binnig, G. *et al.* Tunneling through a controllable vacuum gap. *Applied Physics Letters* **40,** 178 (1982).

59. Bardeen, J. Tunnelling from a many-particle point of view. *Physical review letters* **6,** 57 (1961).

60. Wiebe, J. *et al.* A 300 mK ultra-high vacuum scanning tunneling microscope for spin-resolved spectroscopy at high energy resolution. *Review of scientific instruments* **75,** 4871–4879 (2004).

61. Fein, A. *et al.* Scanning tunneling microscope for low temperature, high magnetic field, and spatially resolved spectroscopy. *Review of scientific instruments* **58,** 1806–1810 (1987).

62. Horcas, I. *et al.* WSXM: A software for scanning probe microscopy and a tool for nanotechnology. *Review of scientific instruments* **78** (2007).

63. Bryant, P. *et al.* Technique for shaping scanning tunneling microscope tips. *Review of scientific instruments* **58,** 1115–1115 (1987).

64. Ibe, J. P. *et al.* On the electrochemical etching of tips for scanning tunneling microscopy. *Journal of Vacuum Science & Technology A: Vacuum, Surfaces, and Films* **8,** 3570–3575 (1990).

65. Akama, Y. *et al.* New scanning tunneling microscopy tip for measuring surface topography. *Journal of Vacuum Science & Technology A: Vacuum, Surfaces, and Films* **8,** 429–433 (1990).

66. Wendel, M. *et al.* Sharpened electron beam deposited tips for high resolution atomic force microscope lithography and imaging. *Applied Physics Letters* **67,** 3732–3734 (1995).

67. Biegelsen, D. K. *et al.* Ion milled tips for scanning tunneling microscopy. *Applied Physics Letters* **50,** 696–698 (1987).

68. Biegelsen, D. *et al.* Simple ion milling preparation of <111> tungsten tips. *Applied Physics Letters* **54,** 1223–1225 (1989).

69. Basnet, G. *Fabrication of tungsten tips suitable for scanning probe microscopy by electrochemical etching methods* (University of Arkansas, 2013).

70. Meckler, S. *et al.* Real-Space Observation of a Right-Rotating Inhomogeneous Cycloidal Spin Spiral by Spin-Polarized Scanning Tunneling Microscopy in a Triple Axes Vector Magnet. *Physical Review Letters* **103,** 157201 (2009).

71. Ishibashi, T. *et al. In situ RHEED observation of MBE growth of organic thin films Organic Thin Films for Photonic Applications* (1995), MD–19.
72. Akinyele, D. *et al.* Fabrication Techniques Such As Molecular Beam Epitaxy. *Available at SSRN 4928834* (2024).
73. Lozovoy, K. A. *et al.* Kinetics of epitaxial formation of nanostructures by Frank–van der Merwe, Volmer–Weber and Stranski–Krastanow growth modes. *Surface and Coatings Technology* **384,** 125289 (2020).
74. Bedoya-Pinto, A. *et al.* Intrinsic 2D-XY ferromagnetism in a van der Waals monolayer. *Science* **374,** 616–620 (2021).
75. Haldane, F. D. M. Model for a quantum Hall effect without Landau levels: Condensed-matter realization of the "parity anomaly". *Physical Review Letters* **61,** 2015 (1988).
76. Halperin, B. I. Quantized Hall conductance, current-carrying edge states, and the existence of extended states in a two-dimensional disordered potential. *Physical Review B* **25,** 2185 (1982).
77. Klitzing, K. v. *et al.* New method for high-accuracy determination of the fine-structure constant based on quantized Hall resistance. *Physical Review Letters* **45,** 494 (1980).
78. Berry, M. V. Quantal phase factors accompanying adiabatic changes. *Proceedings of the Royal Society of London. A. Mathematical and Physical Sciences* **392,** 45–57 (1984).
79. Hasan, M. Z. *et al.* Colloquium: topological insulators. *Reviews of modern physics* **82,** 3045 (2010).
80. Wigner, E. *Group theory: and its application to the quantum mechanics of atomic spectra* (Elsevier, 2012).
81. Knez, I. *et al.* Evidence for helical edge modes in inverted InAs/GaSb quantum wells. *Physical review letters* **107,** 136603 (2011).

82. Shumiya, N. *et al.* Evidence of a room-temperature quantum spin Hall edge state in a higher-order topological insulator. *Nature Materials* **21,** 1111–1115 (2022).
83. Fu, L. *et al.* Topological insulators with inversion symmetry. *Physical Review B* **76,** 045302 (2007).
84. Nomura, K. *et al.* Topological delocalization of two-dimensional massless Dirac fermions. *Physical Review Letters* **99,** 146806 (2007).
85. Suzuura, H. *et al.* Crossover from symplectic to orthogonal class in a two-dimensional honeycomb lattice. *Physical Review Letters* **89,** 266603 (2002).
86. Liu, Y. *et al.* Electronic structure of the semimetals Bi*and*Sb. *Physical Review B* **52,** 1566 (1995).
87. Wolff, P. Matrix elements and selection rules for the two-band model of bismuth. *Journal of Physics and Chemistry of Solids* **25,** 1057–1068 (1964).
88. Hsieh, D. *et al.* Observation of unconventional quantum spin textures in topological insulators. *Science* **323,** 919–922 (2009).
89. Zhu, S. *et al.* Ultrafast electron dynamics at the Dirac node of the topological insulator Sb_2Te_3. *Scientific reports* **5,** 13213 (2015).
90. Roushan, P. *et al.* Topological surface states protected from backscattering by chiral spin texture. *Nature* **460,** 1106–1109 (2009).
91. Hsieh, D. *et al.* A tunable topological insulator in the spin helical Dirac transport regime. *Nature* **460,** 1101–1105 (2009).
92. Fu, L. Hexagonal warping effects in the surface states of the topological insulator Bi_2Te_3. *Physical Review Letters* **103,** 266801 (2009).
93. Alpichshev, Z. *et al.* STM imaging of electronic waves on the surface of Bi_2Te_3: topologically protected surface states and hexagonal warping effects. *Physical Review Letters* **104,** 016401 (2010).
94. Levin, M. *et al.* Particle-hole symmetry and the Pfaffian state. *Physical Review Letters* **99,** 236806 (2007).

95. Zirnbauer, M. R. Particle–hole symmetries in condensed matter. *Journal of Mathematical Physics* **62** (2021).
96. Vasseur, R. *et al.* Particle-hole symmetry, many-body localization, and topological edge modes. *Physical Review B* **93,** 134207 (2016).
97. Roy, R. Topological superfluids with time-reversal symmetry. *arXiv preprint arXiv:0803.2868* (2008).
98. Tokura, Y. *et al.* Magnetic topological insulators. *Nature Reviews Physics* **1,** 126–143 (2019).
99. Li, R. *et al.* Dynamical axion field in topological magnetic insulators. *Nature Physics* **6,** 284–288 (2010).
100. Rabii, S. Energy-band structure and electronic properties of SnTe. *Physical Review* **182,** 821 (1969).
101. Liu, J. *et al.* Two types of surface states in topological crystalline insulators. *Physical Review B* **88,** 241303 (2013).
102. Dimmock, J. O. *et al.* Band edge structure of PbS, PbSe, and PbTe. *Physical Review* **135,** A821 (1964).
103. Wang, Y. J. *et al.* Nontrivial spin texture of the coaxial Dirac cones on the surface of topological crystalline insulator SnTe. *Physical Review B* **87,** 235317 (2013).
104. Teo, J. C. *et al.* Surface states and topological invariants in three-dimensional topological insulators: Application to $\mathrm{Bi}_{1-x}\mathrm{Sb}_x$. *Physical Review B* **78,** 045426 (2008).
105. Mitchell, D. *et al.* Theoretical energy-band parameters for the lead salts. *Physical Review* **151,** 581 (1966).
106. Shi, Y. *et al.* (111) surface states of SnTe. *Physical Review B* **90,** 235114 (2014).
107. Wang, J. *et al.* Structural stability and topological surface states of the SnTe (111) surface. *Physical Review B* **89,** 125308 (2014).

108. Markiewicz, R. Phase separation near the Mott transition in $La_{2-x}Sr_xCuO_4$. *Journal of Physics: Condensed Matter* **2,** 665 (1990).

109. Kohn, W. *et al.* New mechanism for superconductivity. *Physical Review Letters* **15,** 524 (1965).

110. Rice, T. *et al.* New mechanism for a charge-density-wave instability. *Physical Review Letters* **35,** 120 (1975).

111. Littlewood, P. *et al.* Band structure of SnTe studied by photoemission spectroscopy. *Physical Review Letters* **105,** 086404 (2010).

112. Tanaka, Y. *et al.* Two types of Dirac-cone surface states on the (111) surface of the topological crystalline insulator SnTe. *Physical Review B* **88,** 235126 (2013).

113. Drüppel, M. *et al.* Strain tuning of Dirac states at the SnTe (001) surface. *Physical Review B* **90,** 155312 (2014).

114. Ando, Y. *et al.* Topological crystalline insulators and topological superconductors: From concepts to materials. *Annu. Rev. Condens. Matter Phys.* **6,** 361–381 (2015).

115. Chang, K. *et al.* Discovery of robust in-plane ferroelectricity in atomic-thick SnTe. *Science* **353,** 274–278 (2016).

116. Brillson, L. *et al.* Raman observation of the ferroelectric phase transition in SnTe. *Physical Review B* **9,** 1547 (1974).

117. Wang, H. *et al.* Spin Hall effect in prototype Rashba ferroelectrics GeTe and SnTe. *npj Computational Materials* **6,** 7 (2020).

118. Nimtz, G. *et al.* *Narrow-gap semiconductors* (Springer, 1983).

119. Khokhlov, D. *Lead chalcogenides: physics and applications* (Routledge, 2021).

120. Gao, X. *et al.* Investigation of band inversion in (Pb, Sn) Te alloys using ab initio calculations. *Physical Review B—Condensed Matter and Materials Physics* **77,** 033103 (2008).

121. Pankratov, O. *et al.* Supersymmetry in heterojunctions: Band-inverting contact on the basis of $Pb_{1-x}Sn_xTe$ and $Hg_{1-x}Cd_xTe$. *Solid state communications* **61,** 93–96 (1987).
122. Volkov, B. A. *et al.* Two-dimensional massless electrons in an inverted contact. *Soviet Journal of Experimental and Theoretical Physics Letters* **42,** 178 (1985).
123. Strauss, A. Inversion of conduction and valence bands in $Pb_{1-x}Sn_xSe$ alloys. *Physical Review* **157,** 608 (1967).
124. Zhang, D. *et al.* Quasiparticle scattering from topological crystalline insulator SnTe (001) surface states. *Physical Review B* **89,** 245445 (2014).
125. Walkup, D. *et al.* Interplay of orbital effects and nanoscale strain in topological crystalline insulators. *Nature Communications* **9,** 1550 (2018).
126. Jung, J. *et al.* Systematic investigation of the coupling between one-dimensional edge states of a topological crystalline insulator. *Physical Review Letters* **126,** 236402 (2021).
127. Edelstein, A. S. An overview of strongly correlated electron systems. *Journal of magnetism and magnetic materials* **256,** 430–448 (2003).
128. Fulde, P. *Correlated electrons in quantum matter* (World Scientific, 2012).
129. Daybell, M. *et al.* Sub-Kondo-Temperature Properties of Localized Moments in Metals. *Journal of Applied Physics* **40,** 1056–1060 (1969).
130. Edelstein, A. Observation of a Kondo effect in a concentrated system. *Physics Letters A* **27,** 614–615 (1968).
131. Lin, C. *et al.* Heavy-fermion behavior and the single-ion Kondo model. *Physical Review Letters* **58,** 1232 (1987).
132. Knorr, K. *et al.* Kondo effect in dilute alloy films of CuFe deposited at room and helium temperature. *Solid State Communications* **10,** 637–639 (1972).
133. Sugawara, T. *et al.* Kondo effect in single crystals of dilute Y-Ce alloys. *Journal of Low Temperature Physics* **4,** 657–667 (1971).
134. Baberschke, K. *et al.* ESR Study of the Kondo Effect in Au:Yb. *Physical Review Letters* **45,** 1512 (1980).

135. Fisk, Z. *et al.* Low-temperature properties of the heavy-fermion system UCd_{11}. *Physical Review B* **30,** 6360 (1984).
136. Nakamura, H. *et al.* Nuclear magnetic resonance in the antiferromagnetic heavy-fermion system UCu_5: spin reorientation at 1 K. *Journal of Physics: Condensed Matter* **6,** 10567 (1994).
137. Kim, J. *et al.* Specific heat in a magnetic field: A probe of the magnetic ground-state properties of heavy-fermion $\mathrm{Ce(Ru}_{2-x}\mathrm{Rh}_x\mathrm{)Si}_{2-y}\mathrm{Ge}_y$. *Physical Review B* **41,** 541 (1990).
138. Maple, M. *et al.* The re-entrant superconducting-normal phase boundary of the Kondo system (La, Ce) Al_2. *Solid State Communications* **11,** 829–834 (1972).
139. Huxley, A. *et al.* UGe_2: A ferromagnetic spin-triplet superconductor. *Physical Review B* **63,** 144519 (2001).
140. Aronson, M. *et al.* Non-Fermi-liquid scaling of the magnetic response in UCu_{5-x} Pd_x (x = 1, 1.5). *Physical Review Letters* **75,** 725 (1995).
141. Andraka, B. *et al.* Heavy-non-Fermi-liquid behavior in $\mathrm{U(Cu,Pd)}_5$. *Physical Review B* **47,** 3208 (1993).
142. Bauer, E. Non-Fermi-liquid behaviour of ytterbium compounds. *Journal of magnetism and magnetic materials* **196,** 873–877 (1999).
143. Tayama, T. *et al.* Unconventional heavy-fermion superconductor CeCoIn_5: dc magnetization study at temperatures down to 50 mK. *Physical Review B* **65,** 180504 (2002).
144. Wagner, G. *et al.* Interaction effects in a 1D flat band at a topological crystalline step edge. *Nano Letters* **23,** 2476–2482 (2023).
145. Pauly, C. *et al.* Subnanometre-wide electron channels protected by topology. *Nature Physics* **11,** 338–343 (2015).
146. Yin, J.-X. *et al.* Probing topological quantum matter with scanning tunnelling microscopy. *Nature Reviews Physics* **3,** 249–263 (2021).

147. Tang, S. *et al.* Quantum spin Hall state in monolayer 1T'-WTe_2. *Nature Physics* **13,** 683–687 (2017).

148. Hu, Y. *et al.* Rich nature of Van Hove singularities in Kagome superconductor CsV_3Sb_5. *Nature Communications* **13,** 2220 (2022).

149. Li, G. *et al.* Observation of Van Hove singularities in twisted graphene layers. *Nature Physics* **6,** 109–113 (2010).

150. Kerelsky, A. *et al.* Maximized electron interactions at the magic angle in twisted bilayer graphene. *Nature* **572,** 95–100 (2019).

151. Yuan, N. F. *et al.* Magic of high-order van Hove singularity. *Nature Communications* **10,** 5769 (2019).

152. Rechciński, R. *et al.* Topological states on uneven (Pb, Sn)Se (001) surfaces. *Physical Review B* **98,** 245302 (2018).

153. Fujita, M. *et al.* Peculiar localized state at zigzag graphite edge. *Journal of the Physical Society of Japan* **65,** 1920–1923 (1996).

154. Nakada, K. *et al.* Edge state in graphene ribbons: Nanometer size effect and edge shape dependence. *Physical Review B* **54,** 17954 (1996).

155. Kobayashi, K. Electronic structure of a stepped graphite surface. *Physical Review B* **48,** 1757 (1993).

156. Potter, A. C. *et al.* Edge ferromagnetism from majorana flat bands: Application to split tunneling-conductance peaks in high-T_c cuprate superconductors. *Physical Review Letters* **112,** 117002 (2014).

157. Tao, C. *et al.* Spatially resolving edge states of chiral graphene nanoribbons. *Nature Physics* **7,** 616–620 (2011).

158. Song, Y. J. *et al.* High-resolution tunneling spectroscopy of a graphene quartet. *Nature* **467,** 185–189 (2010).

159. Stoner, E. C. Collective electron ferromagnetism II. Energy and specific heat. *Proceedings of the Royal Society of London. Series A. Mathematical and Physical Sciences* **169,** 339–371 (1939).

160. Van Delft, D. *et al.* The discovery of superconductivity. *Physics today* **63,** 38–43 (2010).
161. Meissner, W. *et al.* A new effect at the onset of superconductivity. *Natural Sciences* **21,** 787–788 (1933).
162. Tinkham, M. *Introduction to superconductivity* (Courier Corporation, 2004).
163. London, F. *et al.* The electromagnetic equations of the supraconductor. *Proceedings of the Royal Society of London. Series A-Mathematical and Physical Sciences* **149,** 71–88 (1935).
164. Pippard, A. B. *et al.* An experimental and theoretical study of the relation between magnetic field and current in a superconductor. *Proceedings of the Royal Society of London. Series A. Mathematical and Physical Sciences* **216,** 547–568 (1953).
165. Gor'kov, L. P. Microscopic derivation of the Ginzburg-Landau equations in the theory of superconductivity. *Sov. Phys. JETP* **9,** 1364–1367 (1959).
166. Zh, A. A. Eksperim. i Teor. *Tiz* **32,** 1442 (1957).
167. Bardeen, J. *et al.* Theory of superconductivity. *Physical Review* **108,** 1175 (1957).
168. Bardeen, J. Theory of the Meissner effect in superconductors. *Physical Review* **97,** 1724 (1955).
169. Corak, W. *et al.* Exponential temperature dependence of the electronic specific heat of superconducting vanadium. *Physical Review* **96,** 1442 (1954).
170. Glover III, R. *et al.* Conductivity of Superconducting Films for Photon Energies between 0.3 and 40 kT_c. *Physical Review* **108,** 243 (1957).
171. Glover III, R. *et al.* Transmission of superconducting films at millimeter-microwave and far infrared frequencies. *Physical Review* **104,** 844 (1956).
172. Cooper, L. N. Bound electron pairs in a degenerate Fermi gas. *Physical Review* **104,** 1189 (1956).
173. Maxwell, E. Isotope effect in the superconductivity of mercury. *Physical Review* **78,** 477 (1950).

174. Rice, T. *et al.* $\mathrm{Sr}_2 Ru\mathrm{O}_4$: an electronic analogue of ^{3}He? *Journal of Physics: Condensed Matter* **7,** L643 (1995).

175. Scalapino, D. The case for $d_{x^2-y^2}$ pairing in the cuprate superconductors. *Physics Reports* **250** (1995).

176. Sigrist, M. *Introduction to unconventional superconductivity AIP Conference Proceedings* **789** (2005), 165–243.

177. Bogoljubov, N. N. *et al.* A new method in the theory of superconductivity. *Fortschritte der physik* **6,** 605–682 (1958).

178. Valatin, J. Comments on the theory of superconductivity. *Il Nuovo Cimento (1955-1965)* **7,** 843–857 (1958).

179. Mackenzie, A. P. *et al.* The superconductivity of $\mathrm{Sr_2RuO_4}$ and the physics of spin-triplet pairing. *Reviews of Modern Physics* **75,** 657 (2003).

180. Leggett, A. J. A theoretical description of the new phases of liquid ^{3}He. *Reviews of Modern Physics* **47,** 331 (1975).

181. Van Harlingen, D. Phase-sensitive tests of the symmetry of the pairing state in the high-temperature superconductors—Evidence for $d_{x^2-y^2}$ symmetry. *Reviews of Modern Physics* **67** (1995).

182. Sauls, J. The order parameter for the superconducting phases of UPt3. *Advances in Physics* **43,** 113–141 (1994).

183. Anderson, P. W. Theory of dirty superconductors. *Journal of Physics and Chemistry of Solids* **11,** 26–30 (1959).

184. Kallin, C. *et al.* Chiral superconductors. *Reports on Progress in Physics* **79,** 054502 (2016).

185. Volovik, G. E. *The universe in a helium droplet* (OUP Oxford, 2003).

186. Vollhardt, D. *et al.* *The Superfluid Phases of* ^{3}*He* 1990.

187. De Gennes, P.-G. *Superconductivity of metals and alloys* (CRC press, 2018).

188. Senthil, T. *et al.* Spin quantum Hall effect in unconventional superconductors. *Physical Review B* **60,** 4245 (1999).

189. Tsutsumi, Y. *et al.* A spin triplet superconductor UPt_3. *Journal of the Physical Society of Japan* **81,** 074717 (2012).

190. Avers, K. E. *et al.* Broken time-reversal symmetry in the topological superconductor UPt_3. *Nature Physics* **16,** 531–535 (2020).

191. Campos, P. G. *Visualization of chiral superconductivity in* UPt_3 PhD thesis (Université Grenoble Alpes [2020-....], 2021).

192. Maeno, Y. *et al.* Evaluation of spin-triplet superconductivity in Sr_2RuO_4. *Journal of the Physical Society of Japan* **81,** 011009 (2011).

193. Kallin, C. Chiral p-wave order in Sr_2RuO_4. *Reports on Progress in Physics* **75,** 042501 (2012).

194. Kallin, C. *et al.* Is Sr_2RuO_4 a chiral p-wave superconductor? *Journal of Physics: Condensed Matter* **21,** 164210 (2009).

195. Jiao, L. *et al.* Chiral superconductivity in heavy-fermion metal UTe_2. *Nature* **579,** 523–527 (2020).

196. Machida, K. Nonunitary triplet superconductivity tuned by field-controlled magnetization: URhGe, UCoGe, and UTe_2. *Physical Review B* **104,** 014514 (2021).

197. Aoki, D. *et al.* Review of U-based ferromagnetic superconductors: comparison between UGe_2, URhGe, and UCoGe. *Journal of the Physical Society of Japan* **88,** 022001 (2019).

198. Yang, L. *et al.* Chiral and helical p-wave superconductivity in doped bilayer BiH. *Physical Review B* **98,** 214522 (2018).

199. Novoselov, K. S. *et al.* Electric field effect in atomically thin carbon films. *Science* **306,** 666–669 (2004).

200. Novoselov, K. S. *et al.* 2D materials and van der Waals heterostructures. *Science* **353,** aac9439 (2016).

201. Novoselov, K. S. *et al.* Two-dimensional atomic crystals. *Proceedings of the National Academy of Sciences* **102,** 10451–10453 (2005).

202. Geim, A. K. *et al.* Van der Waals heterostructures. *Nature* **499,** 419–425 (2013).

203. Cao, Y. *et al.* Unconventional superconductivity in magic-angle graphene superlattices. *Nature* **556,** 43–50 (2018).

204. Oh, M. *et al.* Evidence for unconventional superconductivity in twisted bilayer graphene. *Nature* **600,** 240–245 (2021).

205. Yankowitz, M. *et al.* Tuning superconductivity in twisted bilayer graphene. *Science* **363,** 1059–1064 (2019).

206. Nuckolls, K. P. *et al.* Spectroscopy of the Fractal Hofstadter Energy Spectrum. *arXiv preprint arXiv:2501.04777* (2025).

207. Yu, J. *et al.* Correlated Hofstadter spectrum and flavour phase diagram in magic-angle twisted bilayer graphene. *Nature Physics* **18,** 825–831 (2022).

208. Sharpe, A. L. *et al.* Emergent ferromagnetism near three-quarters filling in twisted bilayer graphene. *Science* **365,** 605–608 (2019).

209. Liu, Y. *et al.* Van der Waals heterostructures and devices. *Nature Reviews Materials* **1,** 1–17 (2016).

210. Manzeli, S. *et al.* 2D transition metal dichalcogenides. *Nature Reviews Materials* **2,** 1–15 (2017).

211. Revolinsky, E. *et al.* Superconductivity in the niobium-selenium system. *Journal of Physics and Chemistry of Solids* **26,** 1029–1034 (1965).

212. Guillamón, I. *et al.* Superconducting density of states and vortex cores of 2H-NbS_2. *Physical Review Letters* **101,** 166407 (2008).

213. Nagata, S. *et al.* Superconductivity in the layered compound 2H-TaS_2. *Journal of Physics and Chemistry of Solids* **53,** 1259–1263 (1992).

214. Morosan, E. *et al.* Superconductivity in Cu_xTiSe_2. *Nature Physics* **2,** 544–550 (2006).

215. Sipos, B. *et al.* From Mott state to superconductivity in 1T-TaS_2. *Nature Materials* **7,** 960–965 (2008).

216. Lu, J. *et al.* Evidence for two-dimensional Ising superconductivity in gated MoS_2. *Science* **350,** 1353–1357 (2015).

217. He, W.-Y. *et al.* Magnetic field driven nodal topological superconductivity in monolayer transition metal dichalcogenides. *Communications Physics* **1,** 40 (2018).

218. Zhou, B. T. *et al.* Ising superconductivity and Majorana fermions in transition-metal dichalcogenides. *Physical Review B* **93,** 180501 (2016).

219. Wilson, J. *et al.* Charge-density waves in metallic, layered, transition-metal dichalcogenides. *Physical Review Letters* **32,** 882 (1974).

220. Wilson, J. A. *et al.* Charge-density waves and superlattices in the metallic layered transition metal dichalcogenides. *Advances in Physics* **24,** 117–201 (1975).

221. Moncton, D. E. *et al.* Neutron scattering study of the charge-density wave transitions in 2H-$TaSe_2$ and 2H-$NbSe_2$. *Physical Review B* **16,** 801 (1977).

222. Di Salvo Jr, F. J. *et al.* Charge-density waves in transition-metal compounds. *Physics Today* **32,** 32–38 (1979).

223. Calandra, M. Charge density waves go nano. *Nature Nanotechnology* **10,** 737–738 (2015).

224. Xi, X. *et al.* Strongly enhanced charge-density-wave order in monolayer $NbSe_2$. *Nature Nanotechnology* **10,** 765–769 (2015).

225. Gu, Q. *et al.* Detection of a pair density wave state in UTe_2. *Nature* **618,** 921–927 (2023).

226. Liu, X. *et al.* Discovery of a Cooper-pair density wave state in a transition-metal dichalcogenide. *Science* **372,** 1447–1452 (2021).

227. Güller, F. *et al.* Spin density wave instabilities in the NbS_2 monolayer. *Physical Review B* **93,** 094434 (2016).

228. Krishnamurthi, S. *et al.* Spin/charge density waves at the boundaries of transition metal dichalcogenides. *Physical Review B* **102,** 161106 (2020).

229. Stanley, H. *et al.* Possibility of a phase transition for the two-dimensional Heisenberg model. *Physical Review Letters* **17,** 913 (1966).

230. Stanley, H. E. Dependence of critical properties on dimensionality of spins. *Physical Review Letters* **20,** 589 (1968).

231. Mermin, N. D. *et al.* Absence of ferromagnetism or antiferromagnetism in one-or two-dimensional isotropic Heisenberg models. *Physical Review Letters* **17,** 1133 (1966).

232. Gong, C. *et al.* Discovery of intrinsic ferromagnetism in two-dimensional van der Waals crystals. *Nature* **546,** 265–269 (2017).

233. Huang, B. *et al.* Layer-dependent ferromagnetism in a van der Waals crystal down to the monolayer limit. *Nature* **546,** 270–273 (2017).

234. Deng, Y. *et al.* Gate-tunable room-temperature ferromagnetism in two-dimens- ional Fe_3GeTe_2. *Nature* **563,** 94–99 (2018).

235. Matsuoka, H. *et al.* Spin-orbit-induced Ising ferromagnetism at a van der Waals interface. *Nano Letters* **21,** 1807–1814 (2021).

236. Hussain, B. *et al.* Dipole-exchange spin waves in two-dimensional van der Waals ferromagnetic films and stripes. *Journal of Physics: Condensed Matter* **34,** 445801 (2022).

237. Fei, Z. *et al.* Two-dimensional itinerant ferromagnetism in atomically thin Fe_3GeTe_2. *Nature Materials* **17,** 778–782 (2018).

238. Bonilla, M. *et al.* Strong room-temperature ferromagnetism in VSe_2 monolayers on van der Waals substrates. *Nature Nanotechnology* **13,** 289–293 (2018).

239. Hu, X. *et al.* Enhanced ferromagnetism and tunable magnetism in Fe_3GeTe_2 monolayer by strain engineering. *ACS applied materials & interfaces* **12,** 26367–26373 (2020).

240. Tan, C. *et al.* Hard magnetic properties in nanoflake van der Waals Fe_3GeTe_2. *Nature Communications* **9,** 1554 (2018).

241. Lee, J.-U. *et al.* Ising-type magnetic ordering in atomically thin $FePS_3$. *Nano Letters* **16,** 7433–7438 (2016).

242. Kang, S. *et al.* Coherent many-body exciton in van der Waals antiferromagnet $NiPS_3$. *Nature* **583,** 785–789 (2020).

243. Kim, K. *et al.* Antiferromagnetic ordering in van der Waals 2D magnetic material $MnPS_3$ probed by Raman spectroscopy. *2D Materials* **6,** 041001 (2019).

244. Occhialini, C. A. *et al.* Signatures of pressure-enhanced helimagnetic order in van der Waals multiferroic NiI_2. *arXiv preprint arXiv:2306.11720* (2023).

245. Cai, X. *et al.* Atomically thin $CrCl_3$: an in-plane layered antiferromagnetic insulator. *Nano Letters* **19,** 3993–3998 (2019).

246. McGuire, M. A. *et al.* Magnetic behavior and spin-lattice coupling in cleavable van der Waals layered $CrCl_3$ crystals. *Physical Review Materials* **1,** 014001 (2017).

247. Zhang, Z. *et al.* Direct photoluminescence probing of ferromagnetism in monolayer two-dimensional $CrBr_3$. *Nano Letters* **19,** 3138–3142 (2019).

248. Yokoya, T. *et al.* Fermi surface sheet-dependent superconductivity in 2H-$NbSe_2$. *Science* **294,** 2518–2520 (2001).

249. Rodrigo, J. *et al.* STM study of multiband superconductivity in $NbSe_2$ using a superconducting tip. *Physica C: Superconductivity* **404,** 306–310 (2004).

250. Mattheiss, L. Energy Bands for 2H-$NbSe_2$ and 2H-MoS_2. *Physical Review Letters* **30,** 784 (1973).

251. Johannes, M. *et al.* Fermi-surface nesting and the origin of the charge-density wave in $NbSe_2$. *Physical Review B—Condensed Matter and Materials Physics* **73,** 205102 (2006).

252. Wickramaratne, D. *et al.* Ising superconductivity and magnetism in $NbSe_2$. *Physical Review X* **10,** 041003 (2020).

253. Ugeda, M. M. *et al.* Characterization of collective ground states in single-layer $NbSe_2$. *Nature Physics* **12,** 92–97 (2016).

254. De la Barrera, S. C. *et al.* Tuning Ising superconductivity with layer and spin–orbit coupling in two-dimensional transition-metal dichalcogenides. *Nature Communications* **9,** 1427 (2018).

255. Frigeri, P. A. *et al.* Spin susceptibility in superconductors without inversion symmetry. *New Journal of Physics* **6,** 115 (2004).

256. Chen, W. *et al.* Direct observation of van der Waals stacking–dependent interlayer magnetism. *Science* **366,** 983–987 (2019).

257. Li, Y. *et al.* Observation of Yu-Shiba-Rusinov-like states at the edge of $CrBr_3/NbSe_2$ heterostructure. *Nature Communications* **15,** 10121 (2024).

258. Galvis, J. *et al.* Tilted vortex cores and superconducting gap anisotropy in 2H-$NbSe_2$. *Communications Physics* **1,** 30 (2018).

259. Alicea, J. Majorana fermions in a tunable semiconductor device. *Physical Review B—Condensed Matter and Materials Physics* **81,** 125318 (2010).

260. Xue, F. *et al.* Two-dimensional ferromagnetic van der Waals $CrCl_3$ monolayer with enhanced anisotropy and Curie temperature. *Physical Review B* **100,** 224429 (2019).

261. Lu, X. *et al.* Meron-like topological spin defects in monolayer $CrCl_3$. *Nature Communications* **11,** 4724 (2020).

262. Larson, B. *et al.* Theory of exchange interactions and chemical trends in diluted magnetic semiconductors. *Physical Review B* **37,** 4137 (1988).

263. Yao, Q.-F. *et al.* Manipulation of the large Rashba spin splitting in polar two-dimensional transition-metal dichalcogenides. *Physical Review B* **95,** 165401 (2017).

264. Liu, G.-B. *et al.* Three-band tight-binding model for monolayers of group-VIB transition metal dichalcogenides. *Physical Review B—Condensed Matter and Materials Physics* **88,** 085433 (2013).

265. Bauer, E. *et al.* *Non-centrosymmetric superconductors: introduction and overvi- ew* (Springer Science & Business Media, 2012).

266. Yip, S. Noncentrosymmetric superconductors. *Annu. Rev. Condens. Matter Phys.* **5,** 15–33 (2014).

267. Yuan, N. F. *et al.* Possible topological superconducting phases of MoS_2. *Physical Review Letters* **113,** 097001 (2014).

268. Hsu, Y.-T. *et al.* Topological superconductivity in monolayer transition metal dichalcogenides. *Nature Communications* **8,** 14985 (2017).

List of Publications

Publications related to the dissertation:

1. **S. Das***, B. Zhou*, A. Padhi*, J. Ji, N. Heinsdorf, T. Chen, P. Rigvedi, F. Küster, W. Li, P. Gargiani, M. Valvidares, M. Franz, B. Pal, S.S.P. Parkin. "Unconventional topological superconductivity in $CrCl_3/NbSe_2$ heterostructures". Manuscript under review.(* - **equal contributions**)

2. G. Wagner*, **S. Das***, J. Jung, A. Odobesko, F. Küster, F. Keller, J. Korczak, A. Szczerbakow, T. Story, S.S.P. Parkin, R. Thomale, T. Neupert, M. Bode, P. Sessi.
   "Interaction Effects in a 1D Flat Band at a Topological Crystalline Step Edge". ***Nano Lett.*** 23(7), 2476-2482 (2023). (* - **equal contributions**)

Other Publications during PhD:

1. A.K. Gopi*, A.K. Srivastava*, A.K. Sharma*, A. Chakraborty, **S. Das**, H. Deniz, A. Ernst, B.K. Hazra, H.L. Meyerheim, S.S.P. Parkin.
   "Thickness-Tunable Zoology of Magnetic Spin Textures Observed in Fe_5GeTe_2". ***ACS Nano*** 18(7), 5335-5343 (2024). (* - **equal contributions**)

2. M.O. Soldini*, F. Küster*, G. Wagner, **S. Das**, A. Aldarawsheh, R. Thomale, S. Lounis, S.S.P. Parkin, P. Sessi, T. Neupert.
   "Two-dimensional Shiba lattices as a possible platform for crystalline topologi-

cal superconductivity". ***Nat. Phys.*** 19, 1848–1854 (2023). (* - **equal contributions**)

3. F. Küster, **S. Das**, S.S.P. Parkin, P. Sessi.
   "Yu-Shiba-Rusinov tips: imaging spins at the atomic scale with full magnetic sensitivity". arXiv preprint arXiv:2307.09534 (2023)

4. A. Chakraborty*, A.K. Srivastava*, A.K Sharma, A.K. Gopi, K. Mohseni, A. Ernst, H. Deniz, B.K. Hazra, **S. Das**, P. Sessi, I. Kostanovskiy, T. Ma, H.L. Meyerheim, S.S.P. Parkin.
   "Magnetic skyrmions in a thickness tunable 2D ferromagnet from a defect driven Dzyaloshinskii–Moriya interaction". ***Adv. Mater.*** 34(11), 2108637 (2022). (* - **equal contributions**)

5. K. Chang*, J.W.D. Villanova*, J. Ji*, **S. Das**, F. Küster, S.B. Lopez, P. Sessi, S.S.P, Parkin.
   "Vortex-Oriented Ferroelectric Domains in SnTe/PbTe Monolayer Lateral Heterostructures". ***Adv. Mater.*** 33(32), 2102267 (2021). (* - **equal contributions**)

6. S. Galeski, T. Ehmcke, R. Wawrzyńczak, P.M. Lozano, K. Cho, A. Sharma, **S. Das**, F. Küster, P. Sessi, M. Brando, R. Küchler, A.s Markou, M. König, P. Swekis, C. Felser, Y. Sassa, Q. Li, G. Gu, M.V. Zimmermann, O. Ivashko, D.I. Gorbunov, S. Zherlitsyn, T. Förster, S.S.P. Parkin, J. Wosnitza, T. Meng, J. Gooth.
   "Origin of the quasi-quantized Hall effect in $ZrTe_5$". ***Nat. Commun.*** 12, 3197 (2021).

7. S.K. Yadav, **S. Das**, N. Prasad, B.K. Barick, S. Arora, D.S. Sutar, S. Dhar.
   "Ammonia assisted low temperature growth of In_2O_3 (111) epitaxial films on c-sapphire substrates by chemical vapor deposition technique". ***J. Vac. Sci. Technol. A*** 38, 033414 (2020).

8. S. Ding, A. Ross, R. Lebrun, S. Becker, K. Lee, I. Boventer, **S. Das**, Y. Kurokawa, S. Gupta, J. Yang, G. Jakob, M. Kläui.
   "Interfacial Dzyaloshinskii-Moriya interaction and chiral magnetic textures in a ferrimagnetic insulator". ***Phys. Rev. B*** 100, 100406(R), (2019).

Curriculum Vitae

Personal Details

Name	Souvik Das
Nationality	Indian

Education

08/2019–12/2025	Max Planck Institute of Microstructure Physics, Halle, Germany NISE Department **Doctoral Student**
09/2018–07/2019	Johannes Gutenberg Universität, Mainz, Germany Institüt für Physik **Research Internship Programme**
07/2016–08/2018	Indian Institute of Technology Bombay, Mumbai, India Department of Physics **Master of Science in Physics** Master's Project: Study of Epitaxial Indium Oxide thin films on c-plane Sapphire deposited by Chemical Vapour Deposition
06/2013–07/2016	St. Xavier's College (Autonomous), University of Calcutta Department of Physics **Bachelor of Science (Honours) Physics** Bachelor's Project: Nature of Singularities in a Scalar Field Collapse

Declaration/ Selbstständigkeitserklärung

I, Souvik Das, hereby declare that this thesis is entirely my own work, and has been written without the help of others, that I only used the mentioned sources and indicated all kinds of citations correctly.

Ich, Souvik Das, erkläre hiermit, dass ich diese Arbeit selbstständig und ohne fremde Hilfe verfasst, andere als die von mir angegebenen Quellen nicht benutzt und die den benutzten Werken wörtlich oder inhaltlich entnommenen Stellen als solche kenntlich gemacht habe.